



TECHNISCHE UNIVERSITÄT MÜNCHEN

Lehrstuhl für Werkstoffe und Werkstoffprüfung im Bauwesen

EXPERIMENTAL INVESTIGATION OF GAS DIFFUSIVITY AND CO₂- BINDING CAPACITY OF CEMENTITIOUS MATERIALS

Mouna BOUMAAZA

Vollständiger Abdruck der von der Ingenieur fakultät Bau Geo Umwelt der Technischen Universität München zur Erlangung des akademischen Grades eines

Doktor-Ingenieurs

genehmigten Dissertation.

Prüfer der Dissertation:

1. Dr. Véronique BAROGHEL-BOUNY
2. Dr. Hong WONG
3. Prof. Dr. Amiri OUALI
4. Prof. Dr. Nele DE BELIE
5. Prof. Dr. Abdelkarim AÏT-MOKHTAR
6. Prof.Dr.-Ing. Christoph GEHLEN
7. Dr.Ing. Bruno HUET
8. Dr.Ing. Philippe TURCRY

Die Dissertation wurde am 14.02.2020 bei der Technischen Universität eingereicht und durch die Ingenieur fakultät Bau Geo Umwelt am 09.03.2020 angenommen.



Université de La Rochelle - Laboratoire des Sciences de l'Ingénieur pour l'Environnement

And

Technische Universität München - Ingenieur fakultät Bau Geo Umwelt

A thesis submitted to attain the degree of doctor of philosophy

in Civil Engineering

EXPERIMENTAL INVESTIGATION OF GAS DIFFUSIVITY AND CO₂- BINDING CAPACITY OF CEMENTITIOUS MATERIALS

By:

Mouna BOUMAAZA

Defense date: 24th June 2020

Jury

Véronique BAROGHEL-BOUNY	Dr. HDR. IFSTTAR Champs sur marne. France	Reviewer
Hong WONG	Dr. associate professor. Imperial College London UK.	Reviewer
Amiri OUALI	Prof. Nantes university	President of the jury
Nele DE BELIE	Prof. Ghent University. Belgium	Examiner
Abdelkarim AÏT-MOKHTAR	Prof. La Rochelle Université. France	Supervisor
Christoph GEHLEN	Prof. Technische Universität München. Germany	Supervisor
Bruno HUET	Dr. Ing. LafargeHolcim Saint Quentin Fallavier. France	Supervisor
Philippe TURCRY	Dr. Associate Professor. La Rochelle Université. France	Supervisor

PREFACE

This thesis was developed in collaboration (joint-supervision agreement) between the University of La Rochelle (France), and the Technical University of Munich (Germany). The financial support came from LafargeHolcim research center (Swiss-French Company) and l'Association Nationale de la recherche et de la Technologie ANRT (France).

Institution: LafargeHolcim research center.

Doctoral schools: ED618 Euclide La Rochelle University, and Technical University of Munich

Laboratories: Laboratoire des Sciences de l'Ingénieur pour l'Environnement (LaSIE), and Centrum Baustoffe und Materialprüfung (cbm)

PhD specialty: Civil engineering (Joint PhD).

Advisors:

Prof. Dr-Ing Abdelkarim AÏT-MOKHTAR: La Rochelle University

Dr-Ing Bruno HUET: LafargeHolcim research center

Prof. Dr-Ing Christoph GEHLEN: Technical University of Munich

MCF. Dr-Ing Philippe TURCRY: La Rochelle University

ACKNOWLEDGEMENTS

The work behind this dissertation has been possible owing to collaborations, inspiring discussions, and genuine support from many people, from three different affiliations, and I would like to express my gratitude to each one of them.

First, deep thanks go to the members of my thesis committee for their time, constructive advices and valuable feedback on this thesis work.

I would like to express my gratitude to my advisors: Prof. AïT-Mokhtar, Prof. Gehlen, Dr. Turcry, and Dr. Huet who provided me extensive professional guidance. Their precious scientific support was indispensable to the achievement of this research. I am grateful for having the opportunity to work with passionate researchers; their overwhelming and encouraging attitude is sincerely appreciated.

This work was supported by a grant from LafargeHolcim innovation Center, and ANRT (Association nationale de la recherche et la technologie, France). This support is most gratefully acknowledged. I am also grateful to LafargeHolcim innovation center scientific committee for initiating and supporting this thesis project. Many thanks and appreciations go to La Rochelle University for the Mobility scholarship that greatly helped financing my research stay abroad.

From LafargeHolcim innovation center, I am grateful to my officemates Gérard PHAM, Quentin OE, Guillaume POMMIER and my friend Bao CHEN for their constant support, for providing a positive environment of work, for always bringing good mood and for their constant help in all the laboratory work. A very special gratitude goes to Gabriel PHAM for giving me all personal and professional support and guidance which made me complete my mission in LafargeHolcim Innovation center. I am extremely thankful to him for his generous availability and precious support; he willingly follows the whole process of my thesis work and provides big help in the laboratory work. Thank you, Cassandre Le Galliard, for spending your internship helping me with my thesis work, I enjoyed supervising your internship work. My thanks and appreciation go to all the Durability and Modeling team members especially Sebastien, Alain, Didier, and Aleth who have always offered their help and support. Thanks to the staff in the analytical support team for their valuable help.

Big thanks go to my colleagues and friends at cbm institute in TUM for their warm welcome during my stay in Munich. Thank you, Charlotte, for your nice office company, kind support, and warm way of sharing your experience and knowledge. Special thanks go to Fabian, Mareike, Nicolai, Thomas, Danial and Carla for their kindness and friendly welcome at the

institute. Thank you, Sylvia, Eduardo, Gregory for fun chats, laughter and coffee sharing. My sincere thanks go to Prof. Heinz, Dr. Irbe, Dr.Ing Osterminski, and B.Sc. Ph.D. Bedoe for the helpful and inspiring discussions and suggestions. Also, I would like to thank the Kern center in TUM for their big help.

Deep thanks to my colleagues at La Rochelle University, where I spent the last period of my thesis work. Anass, Suelen, Jean-David, Yunlu, and Marwan, thank you for your helpful advices, kind welcome to the university and fun chats.

A special thanks to the technical and administrative staff for always being helpful and accommodating when I most needed them: Mrs Sara Scapol (LafargeHoclim), Dr.-Ing Annette Spengler and Mrs Francesca Girotti (TUM, cbm), and Mrs Jennifer De La Corte Gomez and Mrs Isabelle Hirsch (La Rochelle university).

Finally, I would not have managed to finalize this work without the genuine support from my beloved friends. Thank you for listening to my frustrations and for your full support and love. I would also like to thank my parents, brother and dear aunt for their love and belief in me. Most of all, I thank you Yassine for your love, patience, and your everyday reminder of what is really important to me.

ABSTRACT

The current standardized methods used to investigate the carbonation performance of concrete are based on the direct determination of the pH variation on the surface of a concrete specimen exposed to ambient or higher CO₂ concentration. These methods are either time-consuming (natural carbonation) or of a questionable accuracy (accelerated carbonation). The carbonation physicochemical process involves two major mechanisms: gaseous CO₂ diffusion into the cementitious material's porous network and its dissolution and reaction with CaO of the hardened cement paste. Most carbonation depth prediction models require the CO₂-effective diffusion coefficient and the amount of carbonatable products as input parameters. Hence the aim of this work is to develop two simple and reliable test methods to determine these two properties in a reliable and cost-effective manner.

First we developed and validated a test method to determine the oxygen-effective diffusion coefficient (D_{e,O_2}) of nine different hardened cement pastes preconditioned at different relative humidity levels, and 44 concrete mixtures. The influence of the hydration duration, water-per-binder ratio, accelerated carbonation, and binder type on the oxygen diffusivity was investigated. The dependence of the D_{e,O_2} on the tested concrete specimen thickness was investigated at the dry state and after conditioning at 93%RH. The D_{e,O_2} was determined before and after full carbonation of six concrete mixtures previously conditioned at different RH. A correlation between oxygen permeability and diffusivity is investigated on 44 concrete mixtures.

A second test method is developed to determine the instantaneous CO₂ binding rate and the amount of carbonatable products of powdered hydrated cement pastes and synthetic anhydrous and hydrates. The samples were carbonated in open systems at ambient CO₂ concentration and controlled relative humidity, and then the system switches into a closed configuration while the measurement of the CO₂-uptake is performed over a short period of time. The test method allows for the measurement of the carbonation reaction rate and capacity; and their evolution as function of time under different RH. The developed method shows advantages for being nondestructive, allowing the samples to carbonate at controlled CO₂ concentration and humidity, and providing measurements with low cost equipment. A good agreement between the test method results and thermogravimetric analysis was observed, which highlights the reliability and accuracy of the developed test method.

The results obtained from the gaseous diffusion coefficient and carbonatable products test methods were used as inputs for carbonation depth prediction models. A correlation was investigated between the measured carbonation depth on different concrete and hydrated cement pastes mixtures by means of phenolphthalein solution under both natural and accelerated exposure. The results were compared with the calculated carbonation depth using our experimental results.

Keywords: Carbonation, test methods, oxygen-effective diffusion coefficient, amount of carbonatable products, carbonation depth

RESUME

Actuellement, les méthodes d'essais normalisées, couramment utilisées pour étudier la carbonatation du béton, s'appuient sur l'évaluation de la chute du pH (<9) de la solution interstitielle d'un échantillon de béton exposé à des concentrations ambiantes ou très élevées de CO_2 (2% à 50% en volume). Ces méthodes sont souvent critiquées car soit, elles nécessitent beaucoup de temps (plus d'une année pour la carbonatation naturelle), soit elles sont coûteuses et d'une faible fiabilité (la carbonatation accélérée, notamment quand la concentration de CO_2 est supérieure à 3% CO_2).

Deux mécanismes principaux pilotent la carbonatation : le transport diffusif du dioxyde de carbone gazeux, qui est régi par le coefficient de diffusion effectif de cette espèce dans le milieu poreux, et la consommation de CO_2 par la quantité de produits carbonatables présente dans la matrice cimentaire. Ces deux propriétés du matériau sont requises pour les modèles prédictifs de la profondeur de carbonatation des matériaux cimentaires. L'objectif de ce travail est donc de développer deux méthodes d'essai simples et fiables pour déterminer ces deux propriétés.

D'abord, nous avons développé et validé une méthode d'essai permettant de déterminer le coefficient de diffusion effectif d'oxygène (D_{e,O_2}) de neuf pâtes de ciment durcies et 44 bétons pré-conditionnés à différentes humidités relatives. L'influence de la durée d'hydratation, du rapport eau sur liant, de la carbonatation accélérée (1% CO_2) et du type de liant sur la diffusivité de l'oxygène est étudiée sur des bétons et pâtes de ciment durcies. L'influence de l'épaisseur de l'échantillon de béton testé sur le D_{e,O_2} est évaluée à l'état sec et après conditionnement des bétons à une humidité relative de 93%. La corrélation entre la perméabilité à l'oxygène et le coefficient de diffusion effective d'oxygène est étudiée sur 44 mélanges de béton.

Une deuxième méthode d'essai est développée pour étudier le taux instantané de fixation de CO_2 et la quantité de produits carbonatables de pâtes de ciment hydratées, de phases pures d'hydrates et anhydres synthétisées. Les échantillons ont été carbonatés dans des systèmes ouverts sous humidités relatives contrôlées et concentration ambiante de CO_2 , puis le système bascule en configuration fermée pour mesurer la quantité de CO_2 fixée par le matériau testé pendant une courte période. Cette méthode d'essai permet de déterminer l'évolution en fonction de temps du taux instantané de réaction de carbonatation et de la capacité de fixation de CO_2 sous différents environnements. Un bon accord entre les résultats de la nouvelle méthode d'essai et l'analyse thermogravimétrique a été observé, ce qui met en évidence la fiabilité et la précision de la méthode de test développée.

Les résultats obtenus des essais de diffusion et les quantités de produits carbonatables sont intégrés dans des modèles de prédiction de la profondeur de carbonatation. Ces profondeurs de carbonatation ont été comparées aux profondeurs de carbonatation déterminées directement sur les mêmes matériaux par pulvérisation de phénolphtaléine, en carbonatation naturelle et accélérée.

Mots clés: Carbonatation, méthodes d'essais, quantité de produits carbonatables, coefficient de diffusion effective d'oxygène, profondeur de carbonatation

ZUSAMMENFASSUNG

Die zurzeit verwendeten Methoden zur Untersuchung des Karbonatisierungs-widerstandes von Beton basieren auf der direkten Bestimmung des pH-Wertes der oberflächennahen Betonrandzone, die zuvor einer bestimmten Prüflagerung ausgesetzt war (relative Luftfeuchte, spezifische CO₂-Konzentrationen). Diese Methoden sind jedoch entweder sehr zeitaufwändig (natürliche Karbonatisierung) oder von fraglicher Praxisnähe (beschleunigte Karbonatisierung). Der physikalisch-chemische Karbonatisierungsprozess beinhaltet zwei Hauptmechanismen: die Diffusion von gasförmigem CO₂ in das poröse Netzwerk des Betons und dessen Auflösung und Reaktion mit CaO der ausgehärteten Zementsteins. Die meisten Modelle zur Vorhersage der Karbonatisierungstiefe erfordern den effektiven CO₂-Diffusionskoeffizienten und die Menge an karbonisierbarer Masse als Eingabeparameter. Ziel dieser Arbeit ist es, zwei einfache und zuverlässige Testmethoden zu entwickeln, um diese beiden Eigenschaften zuverlässig und kostengünstig zu bestimmen.

Nach Entwicklung und Validierung einer geeigneten Testmethode zur Messung von Sauerstoffdiffusionskoeffizienten (D_{e,O_2}), wurden diese an neun verschiedenen Zementproben gemessen, die bei unterschiedlichen relativen Luftfeuchten vorkonditioniert wurden. Anschließend wurden 44 verschiedene Betonmischungen geprüft. Bei diesen wurde die Hydratationsdauer und der Wasserbindemittelwert variiert. Die Abhängigkeit des Sauerstoffdiffusionskoeffizienten D_{e,O_2} von der getesteten Betonprobendicke wurde im trockenen Zustand und nach Konditionierung bei 93% relativer Luftfeuchtigkeit untersucht. Der Sauerstoffkoeffizient D_{e,O_2} wurde vor und nach der vollständigen Carbonisierung von sechs Betonmischungen bestimmt, die zuvor bei unterschiedlicher relativer Luftfeuchtigkeit vorkonditioniert worden waren.

Eine zweite Testmethode wurde entwickelt, um die momentane CO₂-Bindekapazität und die Menge an karbonisierbarer Masse aus pulverförmigen Zementhydratpasten und synthetischen wasserfreien Produkten und Hydraten zu bestimmen. Die Proben wurden zunächst in offenen Systemen bei einer CO₂-Konzentration in der Umgebung und einer kontrollierten relativen Luftfeuchtigkeit gegeben, um danach dann in eine geschlossene Konfiguration umzuwechseln. So konnte man die CO₂-Aufnahme über einen kurzen Zeitraum nachverfolgen. Die Testmethode ermöglicht die Messung der Karbonatisierungsreaktionsrate und -kapazität in Abhängigkeit der Zeit unter verschiedenen relativen Luftfeuchten der Umgebungsluft. Es wurde eine gute Übereinstimmung zwischen den Ergebnissen der Testmethode und der thermogravimetrischen Analyse festgestellt, was die Zuverlässigkeit und Genauigkeit der entwickelten Untersuchungsmethodik unterstreicht.

Die Ergebnisse beider Tests wurden als Input für Vorhersagemodelle für den zeitabhängigen Karbonatisierungsfortschritt von Beton verwendet. Es wurde eine Korrelation zwischen der gemessenen Karbonatisierungstiefe an verschiedenen Beton- und Zementhydratmischungen mittels Phenolphthaleinlösung untersucht, wobei u. a. Karbonatisierungstiefen bestimmt nach natürlicher Lagerung mit berechneten/vorhergesagten Karbonatisierungstiefen, die mithilfe der vorgestellten Modellierung und Inputdaten aus Test miteinander verglichen wurden.

Schlüsselwörter: Karbonatisierung, Testmethoden, Sauerstoffdiffusionskoeffizient, Menge der karbonisierbaren Masse, Karbonisierungstiefe

TABLE OF CONTENTS

INTRODUCTION.....	1
I. CHAPTER I: THE CARBONATION PROCESS AND ITS CONSEQUENCES ON THE REINFORCED CONCRETE.....	4
1.1 Carbonation physicochemical process.....	4
1.1.1 Gas diffusivity.....	4
1.1.2 Chemical reaction.....	6
i) Carbonation reaction of the main cement phases.....	6
ii) Carbonation products	8
1.2 Consequences of carbonation	10
1.2.1 Effect of carbonation on microstructural properties	10
i) Total porosity	10
ii) Pore size distribution (PSD).....	10
1.2.2 Effect of carbonation on other properties	12
i) Water retention capacity	12
ii) Permeability	12
1.2.3 Effect of carbonation on the gas diffusivity	13
1.2.4 Corrosion initiation	14
II. CHAPTER II: STATE OF THE ART ON THE PREDICTION OF THE CARBONATION RATE	17
2.1 Determination of the carbonation rate from the pH-indicator test.....	17
2.2 Determination of the carbonation rate from material properties	20
2.2.1 Gas diffusion coefficient.....	20
2.2.2 CO ₂ -binding capacity	26
2.3 Carbonation rate prediction models	28
2.3.1 Square root of time model	29
2.3.2 Papadakis' model	30
2.3.3 Gehlen's model	31
III. CHAPTER III: TEST PROTOCOLS AND MATERIALS.....	35
3.1 Microstructure characterization.....	35

3.1.1	Water porosity	35
3.1.2	Mercury Intrusion Porosimetry (MIP)	35
3.1.3	Scanning Electron Microscopy (SEM)	35
3.2	Physical properties.....	36
3.2.1	Degree of water saturation	36
3.2.2	BET surface area	37
3.2.3	Helium pycnometry	37
3.2.4	Apparent oxygen permeability.....	37
3.3	Chemical composition	38
3.3.1	Thermogravimetric analysis (TGA)	38
3.3.2	X-ray diffraction (XRD).....	39
3.4	Carbonation tests.....	39
3.4.1	Natural carbonation	39
3.4.2	Accelerated carbonation	40
3.5	Synthetic anhydrous and hydrates.....	41
3.6	Hardened cement pastes (HCP).....	42
3.7	Concrete	43
3.7.1	Concrete mixtures tested to O ₂ permeability and O ₂ diffusivity	46
3.7.2	Concrete mixtures used to investigate the influence of the specimen thickness on D _{e,O2}	47
3.7.3	Concrete mixtures tested to the influence of accelerated carbonation on D _{e,O2}	47
IV.	CHAPTER IV: MAIN RESULTS.....	49
4.1	Gas diffusivity of cementitious materials	49
4.1.1	Test method	49
	i) The design of the diffusion cell	49
	ii) Test method protocol and validation.....	52
	iii) CO ₂ diffusion coefficient vs. O ₂ diffusion coefficient	54
4.1.2	Hardened cement pastes diffusivity.....	56
	i) Influence of the hydration duration and degree of water saturation on D _{e,O2}	56
	ii) Influence of the water-per-binder ratio on D _{e,O2}	57
	iii) Influence of accelerated carbonation on D _{e,O2}	57
	iv) Influence of the pore size distribution on D _{e,O2}	59
4.1.3	Concrete diffusivity	61
	i) Influence of concrete specimen thickness on D _{e,O2}	61
	ii) Influence of accelerated carbonation on D _{e,O2} of concrete	66

iii)	Oxygen permeability vs oxygen diffusivity	69
4.2	CO₂-binding capacity	71
4.2.1	Test method	71
i)	Equipment	71
ii)	Test protocol	73
iii)	Experimental data analysis	74
4.2.2	CO ₂ binding capacity of the synthetic cement phases	75
4.2.3	CO ₂ binding capacity of hydrated cement pastes	79
4.2.4	Comparison with TGA results	80
V.	CHAPTER V: DISCUSSION.....	82
5.1	Limits and advantages of the developed test methods	82
5.1.1	Gas diffusion coefficient test method	82
5.1.2	CO ₂ -binding capacity test method.....	83
5.2	Materials properties	84
5.2.1	Influence of different parameters on D_{e,O_2}	84
5.2.2	CO ₂ -binding capacity and rate at different RH	86
5.3	Comparison of experimental results to Millington's model.....	88
5.4	Comparison of experimental results to literature models	89
5.4.1	Prediction of the HCP carbonation depth	89
5.4.2	Prediction of the concrete carbonation depth.....	92
i)	Papadakis' model	92
ii)	Gehlen's model	94
iii)	Differences in the carbonation tests protocols.....	97
5.5	Comparison between the carbonation test methods	98
	CONCLUSIONS.....	100
	PERSPECTIVES.....	102
	APPENDED DOCUMENTS	103
1	PAPER I: A NEW TEST METHOD TO DETERMINE THE GASEOUS OXYGEN DIFFUSION COEFFICIENT OF CEMENT PASTES AS A FUNCTION OF HYDRATION DURATION, MICROSTRUCTURE, AND RELATIVE HUMIDITY	104

2 PAPER II: INFLUENCE OF CARBONATION ON THE MICROSTRUCTURE AND THE GAS DIFFUSIVITY OF HARDENED CEMENT PASTES.....	127
3 PAPER III: THE CO₂-BINDING CAPACITY OF SYNTHETIC ANHYDROUS AND HYDRATES: VALIDATION OF A TEST METHOD BASED ON THE INSTANTANEOUS REACTION RATE.....	152
EXTENDED ABSTRACT IN FRENCH.....	181
REFERENCES.....	194
APPENDICES.....	208

Introduction

Concrete structures should fulfill their mechanical and durability functions during the specified service life without unforeseen costs or repairs. Therefore, concrete must resist to the damage process to which it is exposed in order to ensure that. Durability problems are caused by either external harmful species (e.g. chloride ingress, acid attacks, sulfur, carbon dioxide) or internal reactions within the concrete itself (e.g. alkali aggregate, expansion caused by differed ettringite formation). Sometimes, concrete structures fail to achieve the specified service life, or reach it at high cost of repair and maintenance [1].

Carbonation of concrete affects all above ground concrete structures (two-thirds of all concrete structures [2]). When CO₂ diffuses into the concrete structure, it dissolves and reacts with the phases of the hydrated binder. Carbonation reactions lead to a decrease in the pH and result in changes in the microstructure and moisture content. The decrease in pH leads to a risk of corrosion of reinforcing steel. This causes repair and maintenance costs. In the UK alone, about £20 billion of yearly expenditure [3]. In France, the maintenance and repair costs of a concrete structure represent 0.25% of the concrete structure building cost [4].

Therefore, carbonation resistance of concrete is a key-property that should be determined with sufficient accuracy, reliability and efficiency. The correct understanding and determination of carbonation related properties is not only necessary for the prediction of long-term durability of reinforced concrete structures, but it is also essential for maintenance and repair works on existing structures.

Concrete carbonation has a depth progressing from the surface of the concrete inwards. This depth is currently determined based on different standards [5]. These standards rely on direct measurements of the pH variation due to carbonation of concrete specimen after a certain preconditioning period and exposure to a certain concentration of CO₂. The carbonation depth is determined by means of pH-color indicators giving the latter at the limit of the colorless part. Under natural carbonation exposure (0.04 vol.-% CO₂), the test is criticized for being time-consuming (>1 year). When the specimens are tested under accelerated conditions (1, 3 or 50 vol.-% CO₂), the results representativeness of the real carbonation process is questionable. Furthermore, there is currently no international or European agreement on the pre-conditioning protocol, the CO₂ concentration, and the geometry of the specimens exposed to accelerated carbonation.

Numerous models have been developed to predict the carbonation depth of cementitious material e.g. [6]. Most of these models require as input parameters the gaseous CO₂-effective diffusion coefficient and the amount of carbonatable products of the hardened cement paste. Therefore, these properties are of high relevance regarding carbonation. So far, there are no standardized test methods to determine them. A reliable determination of these two properties using simple, reliable, time-saving, and cost-effective test methods would facilitate the validation of the existing models, the prediction of the carbonation depth, and the quality control of standardized and innovative cementitious materials.

The CO₂-effective diffusion coefficient is usually deduced from empirical relationships determined from tests on mixtures made of Portland cement [7]. The literature is not rich in experimental studies of gas-diffusion coefficient (relatively to other methods such as permeability and chloride ingress), and the existing procedures that can be found in the literature are based on different principles [8], [9], [10]. Thus, the first objective of this work is to develop an experimental device for determining the gas-effective diffusion coefficient of different cementitious materials preconditioned at different relative humidity levels. Once validated, this technique is used to investigate the influence of different parameters on the gas-effective diffusion coefficient: material composition, hydration duration, degree of water saturation (relative humidity), accelerated carbonation and concrete specimen size.

The uptake of gaseous carbon dioxide due to the carbonation reaction of calcium-bearing phases in a cement paste is a parameter controlling the carbonation depth progress within concrete. The CO₂-binding capacity of cementitious materials indicates how much CO₂, within a defined carbonation time, is being taken up. This allows determining the amount of carbonatable products within the hardened cement paste. This parameter can be theoretically calculated if the cement composition is known [11]. However, the real amount of carbonatable products is found to be not in line with these calculations (paper III). The experimental determination of the real amount of bound-CO₂ is currently investigated by means of expensive devices (e.g. thermogravimetric analysis TGA) or inaccurate measurements (mass variation). Therefore, the second part of the thesis work focuses on the experimental investigation of the CO₂-binding capacity of the main cement phases and hydrated cement pastes exposed to natural carbonation under different relative humidity levels. A new method is proposed, and the results reliability is checked by a comparison to TGA results.

The developed test methods are used to test different binders with Portland cement and supplementary cementitious materials SCMs such as fly ash, slag, limestone, metakaolin and silica fume, which is of high importance as the use of supplementary cementitious materials in the cement industry has become a common practice to reduce the embodied energy and the

carbon dioxide emissions of concrete.

This manuscript is divided into five chapters. First, the basics for a better understanding of the carbonation process and its consequences on different materials' properties are presented based on literature findings. The second chapter describes the current state of knowledge on the carbonation tests based on the pH variation and the microstructural properties determination. The third chapter gives information on the tested materials and presents the test methods used to investigate the physical, chemical and microstructural properties of the tested materials. The fourth chapter presents a detailed description of the developed test methods that allows for the determination of the oxygen-effective diffusion coefficient and the CO₂-binding capacity. The influence of different parameters (such as relative humidity, carbonation, hydration duration) on these two properties is presented in detail. The fifth chapter presents a discussion of the thesis work findings with regards to the literature findings, gives the limits and advantages of the developed test methods, and analyses of the experimental data obtained on the tested materials. In this chapter, the carbonation depths given by two carbonation depth prediction models using our experimental results are compared to the carbonation depths determined by means of phenolphthalein solution on the same materials exposed to natural and accelerated carbonation.

I. Chapter I: The carbonation process and its consequences on the reinforced concrete

This chapter gives a description of the physicochemical process of carbonation, the main mechanisms that control carbonation, and the consequences of carbonation on the cementitious materials microstructure and transport properties based on previous results from the literature.

1.1 Carbonation physicochemical process

Carbonation is an irreversible diffusion-reaction process leading to the neutralization of the pore solution that protects the reinforcement from corrosion [12], [13]. The process includes the diffusion of CO₂ in the gaseous phase into the concrete pores, and its reaction with the dissolved calcium from some cement phases in the pore solution [14]. Two properties are of interest with regards to carbonation: the gaseous CO₂-effective diffusion coefficient [3], [4], and the total molar concentration of CaO in the hardened cement paste, in the form of carbonatable products.

1.1.1 Gas diffusivity

In a porous medium, diffusion-based phenomenon are described by an effective diffusion coefficient. The effective diffusion coefficient is based on the average cross-sectional area open to diffusion and the distance traveled by molecules in the porous medium. The latter is proportional to the self-diffusion coefficient but is reduced by a factor that takes into account the reduced cross-sectional area (or porosity) available for diffusion, the tortuosity and constrictivity factors of the pore space.

Fick's laws are the most popular approach to evaluate gas diffusion. Fick's first law describes the correlation between the diffusive flux of a gas component and its concentration gradient: the rate of transfer of a diffusing substance through unit area of a section is proportional to the concentration gradient measured normally to the section. The negative sign in this equation arises because diffusion occurs in the direction opposite to the direction of increasing concentration [17]. Fick's second law relates the unsteady diffusive flux to the concentration gradient. Neglecting the absorption process and the gas solubility in the pore solution [18], and considering a one dimensional diffusion of gas molecules, these laws can be written as:

Fick's first law:
$$J = -D_{e,g} \frac{\partial C}{\partial x}$$
 Equation 1

Fick's second law:
$$\frac{\partial C}{\partial t} = \frac{\partial}{\partial x} \left(D_{e,g} \frac{\partial C}{\partial x} \right)$$
 Equation 2

C [mol.m⁻³] is the gas concentration, J [mol.m⁻².s⁻¹] is the diffusion flux, $D_{e,g}$ [m².s⁻¹] is the gas-effective diffusion coefficient.

The majority of carbonation models that have been published up until now are based on Fick's laws of diffusion [13][6]. Therefore, in the following, Fick's second law of diffusion will be used to analyze our experimental data.

As gas molecules travel through the porous media, two mechanisms can occur with a distinct diffusion coefficient for each of them. These mechanisms depend on the characteristic of the diffusing gas species and the microstructure of the porous medium.

- Molecular diffusion (Bulk diffusion): Occurs predominantly when molecule–molecule collisions dominate over molecule–pore wall collisions. Different species of a mixture move relatively to each other under the influence of concentration gradients.
- Knudsen diffusion (Free diffusion): molecules of different species move entirely independently of each other. This occurs mainly when molecule–molecule collisions can be ignored compared to molecule–pore wall collisions.

The predominant diffusion mechanism depends on the Knudsen number which is the ratio between the mean free path λ [nm] (72 nm in the case of gaseous oxygen) and the pore diameter d_p [nm]:

$$K_n = \frac{\lambda}{d_p}$$
 Equation 3

- Knudsen diffusion is predominant when the Knudsen number is amply large ($K_n > 10$).
- Molecular diffusion is predominant when the Knudsen number is negligible ($K_n < 10^{-2}$), since the molecules collide with each other more frequently than with the pore walls.

A third diffusion mechanism can occur when both Knudsen and molecular diffusion coexist ($10^{-2} < K_n < 10$). Table 1 gives an expression of the effective diffusion coefficients in these three cases [9]. Note that it is reported that for concrete materials, Knudsen diffusion contributes primarily for pores smaller than 50 nm. Ordinary diffusion occurs when the mean free path of gas molecules is relatively short compared to the pores size and it is typically

shown in large pores [19].

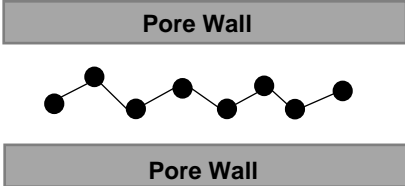
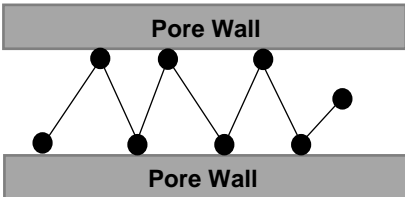
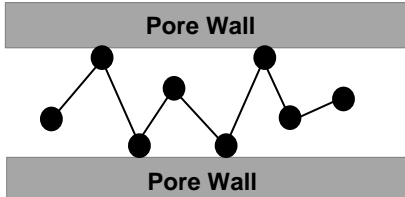
Mechanism	Diffusion coefficient [9]
<p>Molecular diffusion</p> 	$D_{ij,e} = \frac{\Phi}{\tau} D_{ij,0}$ <ul style="list-style-type: none"> - $D_{ij,e}$ [m²/s] is the diffusion coefficient of the gas i in the gas j - Φ [-] is the porosity available for transport - τ [-] the tortuosity factor - $D_{ij,0}$ [m²/s] is the binary diffusion coefficient of the gases i and j
<p>Pure Knudsen diffusion</p> 	$D_{K,e} = \frac{\Phi}{\tau} \frac{d_p}{3} \left(\frac{8RT}{\pi M_i} \right)^{\frac{1}{2}}$ <ul style="list-style-type: none"> - $D_{K,e}$ [m²/s] is the diffusion under Knudsen regime - Φ [-] the porosity available for transport - τ [-] the tortuosity factor - d_p [m] is the mean pore size - M_i [g/mol] the molecular mass of the diffusing gas - R [g.m².K⁻¹.mol⁻¹.s⁻²], T [K] are the gas constant and temperature respectively
<p>Knudsen + molecular diffusion</p> 	$\frac{1}{D'_i} = \frac{1}{D_{ij,e}} + \frac{1}{D_{K,e}}$ <ul style="list-style-type: none"> - D'_i [m²/s] is the diffusion coefficient under both Knudsen and molecular diffusion

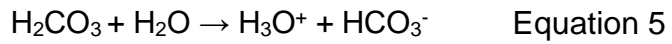
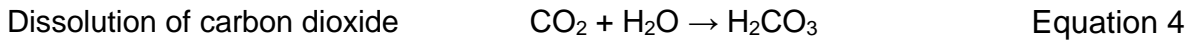
Table 1: Mechanisms of gas diffusion in a porous media

1.1.2 Chemical reaction

i) Carbonation reaction of the main cement phases

Once the diffusion of carbon dioxide takes place, the gaseous CO₂ dissolves in the moist pores under suitable water content conditions. Part of the dissolved CO₂ is converted to carbonic acid, H₂CO₃, or its dissociation forms: hydrogen carbonates HCO₃⁻ or carbonate

CO_3^{2-} depending on the pH of the pore solution. (See Equation 4, Equation 5, Equation 6, and Figure 1).



Carbonic acids dissociation forms

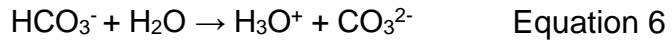


Figure 1 shows that the dissociation forms of CO_2 are directly related to the pH value of the pore solution. During the carbonation of concrete, the pH of the pore solution decreases from a basic value (about 13.5) to a value close to 9 [20]. Therefore, CO_3^{2-} and HCO_3^- are the dissolved carbonate species majorly present in cementitious materials' pore solution during carbonation.

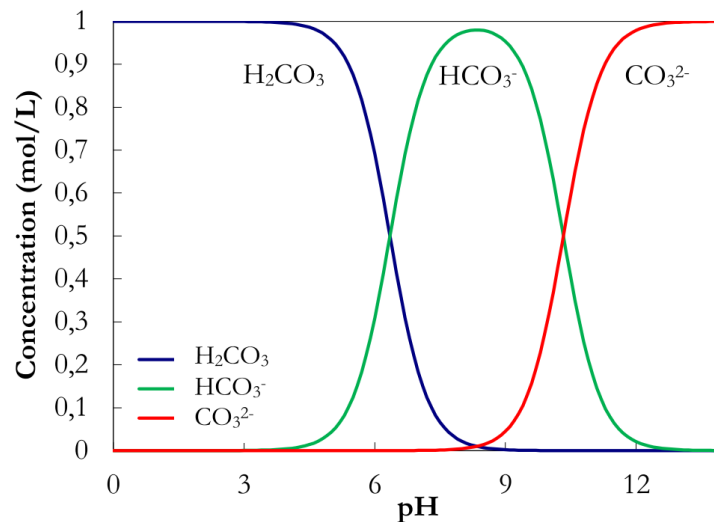


Figure 1: Distributions of the dissociation forms of carbonic acid [20]

The Ca^+ ions dissolved in the pore solution from the Ca-bearing phases in a hardened cement paste (HCP) react with the dissolved CO_2 to form CaCO_3 . The amount of released calcium ions depends on the amount of Ca-containing phases in the cement paste (carbonatable products) and their solubility. The carbonation reactions of the main phases in the HCP are shown in Table 2 [21][22].

Cement phase	Reaction with CO ₂
Portlandite	$\text{Ca(OH)}_2 + \text{CO}_2 \rightarrow \text{CaCO}_3 + \text{H}_2\text{O}$
Calcium Silicate	$\text{C}_x\text{S}_y\text{H}_z + (\text{x-x}')\text{CO}_2 \rightarrow \text{C}_{x'}\text{S}_y\text{H}_{z'} + (\text{x-x}')\text{CaCO}_3 + (\text{z-z}')\text{H}_2\text{O}$
Ettringite	$3\text{CaO} \cdot \text{Al}_2\text{O}_3 \cdot 3\text{CaSO}_4 \cdot 32\text{H}_2\text{O} + 3\text{CO}_2 \rightarrow 3\text{CaCO}_3 + 2\text{Al(OH)}_3 + 3\text{CaSO}_4 \cdot 2\text{H}_2\text{O} + \text{XH}_2\text{O}$
Monosulfoaluminate	$3\text{CaO} \cdot \text{Al}_2\text{O}_3 \cdot \text{CaSO}_4 \cdot 12\text{H}_2\text{O} + 4\text{CO}_2 \rightarrow 4\text{CaCO}_3 + \text{Al(OH)}_3 + \text{SO}_4$
Alite	$\text{C}_3\text{S} + \text{y H}_2\text{O} + (\text{3-x})\text{CO}_2 \rightarrow \text{xCSH} + (\text{3-x})\text{CaCO}_3$
Belite	$\text{C}_2\text{S} + \text{y H}_2\text{O} + (\text{2-x})\text{CO}_2 \rightarrow \text{xCSH} + (\text{2-x})\text{CaCO}_3$

Table 2 : Carbonation reactions of the main cement phases [25, 26]

Figure 2 gives a schematic description of the carbonation reaction of CH and C-S-H. Binders with higher amounts of carbonatable products (e.g., CH and C-S-H) have a higher CO₂-binding capacity, and are more resistant to carbonation, if the latter is defined mainly as a carbonation depth or front. Indeed the carbonation front is proportional to the inverse square root of the amount of carbonatable products [6].

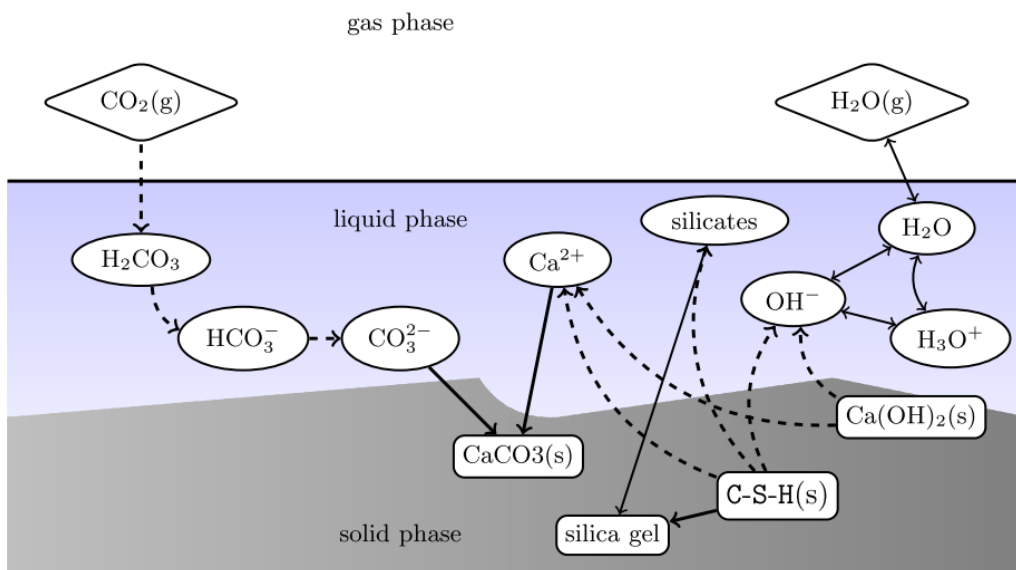


Figure 2: Main chemical species involved in the carbonation reaction [24]

ii) Carbonation products

The carbonation reaction takes place in stages and several intermediate reactions occur. However, one of the final products is always one or many polymorphs of CaCO₃, which are precipitated in the porous network. Different polymorphs of calcium carbonate exist: anhydrous crystalline polymorphs (calcite, aragonite and vaterite), hydrated forms (monohydrocalcite, crystalline hexahydrate (ikaite, CaCO₃·6H₂O)) and amorphous calcium carbonate hydrates [25], [26]. Indeed, calcium carbonate can also be found under amorphous form and crystallizes with time to calcite or aragonite [27]. Note that during carbonation, the first calcium carbonate formed is amorphous calcium carbonate [27].

According to Radha et al. [27], the most unstable CaCO_3 polymorph is the amorphous calcium carbonate, followed by the crystalline forms: vaterite then aragonite and finally calcite which is the most stable. The properties of the anhydrous crystalline CaCO_3 polymorphs are shown in Table 3.

Mineral	Density [$\text{g}\cdot\text{cm}^{-3}$]	Molar volume [cm^3]	Crystal shape	Variation of volume [%]
Calcite	2.71	36.93	Prismatic	11.2
Aragonite	2.93	34.16	Fibrous	2.9
Vaterite	2.54	39.40	Spherical	18.7

Table 3 : Properties of the calcite polymorphs [28]

Figure 3 shows SEM images of the shape of calcite (trigonal), vaterite (hexagonal) and aragonite (orthorhombic).

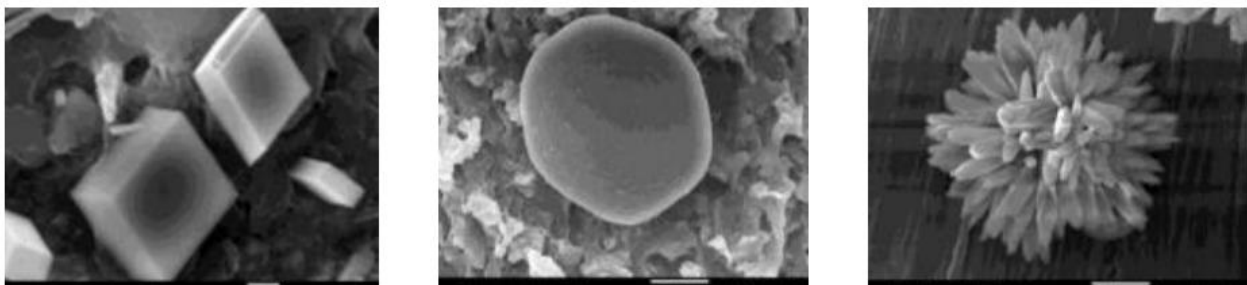


Figure 3 : SEM images of calcite (left), vaterite (center) and aragonite (right) [29]

The precipitation of a certain calcium carbonate polymorph during the carbonation reaction is reported to be dependent upon various factors like the concentration of carbon dioxide, the relative humidity, pH, Ca per Si ratio of C-S-H phase, duration of exposure and the phase of the hydrated cement paste involved in the carbonation reaction [30], [25], [31], [32], [33]. However, the exact conditions that favors the precipitation of these polymorphs are not well understood [34]. Morandea [24] suggests that aragonite probably forms during carbonation of C-S-H phase with low C/S, vaterite results from the carbonation of C-S-H with high C/S ratio and calcite comes from the carbonation of CH. However, thermodynamic laws indicate that all the polymorphs will eventually transform into the most stable phase: calcite [31].

Another product of carbonation is silica gel in the case of C-S-H carbonation, aluminum hydroxide in the case of aluminate carbonation, and the carbonation of the anhydrous alite and belite results in the formation of C-S-H as well [21][35].

1.2 Consequences of carbonation

1.2.1 Effect of carbonation on microstructural properties

i) Total porosity

As seen in Table 3, carbonation products cause a high volume variation since their volume is higher than the primary reactants. Therefore, carbonation is expected to result in a reduction of the concrete total porosity. Indeed, under natural carbonation conditions, Soja et al. [36] found a decrease by around 4% in the MIP (Mercury intrusion porosimetry) total porosity of hardened cement pastes (CEM II/B-LL). The same conclusion is drawn by Van de Heede et al. [37] on high-volume fly ash and fly ash plus silica fume binder systems under natural and accelerated carbonation (1% and 10% CO₂).

Pham et al. [38] investigated the change in the water porosity of CEM I mortars after accelerated carbonation (20% CO₂) and found a total porosity decreased by almost 5%. The reduction of porosity due to the carbonation reaction is also observed in the case of Portland cement and blended cement concretes [39]. Morandea [24] attributes the decrease in the total porosity more to the decalcification of C-S-H phases than to the carbonation of portlandite. It is worth noting that due to the porosity decrease, carbonation is also reported to increase the compressive strength of concrete by 20 - 50% [40].

ii) Pore size distribution (PSD)

Carbonation also influences the cement paste pore size distribution. Miragliotta [41] observed a decrease in the microporosity upon carbonation especially when the CO₂ concentration increases. Pham et al. [38] investigated the influence of accelerated carbonation (20% CO₂, 65% RH, 20°C) on the pore size distribution of CEM I and CEM II pastes and mortars using nitrogen adsorption. Pham et al. [38] found that carbonation caused a decrease in the volume of microspores (radius <2 nm) for all materials, and a significant increase in the volume of the meso-pores (2 nm < radius < 10 nm) for CEM II based materials. Only a slight increase in the meso-pores volume is seen for CEM I mortars, while a clear decrease in the volume of these pores is observed for CEM I pastes. In agreement with these findings, Lawrence et al. [42] found that due to carbonation of lime mortars there is an increase in the volume of pores with 100 nm diameter, and an increase in the volume of pores with diameters below 30 nm. Ngala et al. [43] state that the redistribution of the pore sizes of hardened cement pastes is linked to the binder type: the proportion of large capillary pores (diameter ≈ 30 nm) is slightly increased for the OPC pastes but much more significantly for the fly ash and slag pastes. Villain et al.

[44] investigated the changes in the pore size distribution with the water-per-cement ratio. For cement pastes with $W/C = 0.3$ a reduction of the amount of pores of diameter between 100 and 12.5 nm is observed. The pastes with higher water to cement ratios indicate an increase in the volume for pores of diameter between 100 and 50 nm. The volume of pores with a diameter lower than 12.5 nm seems to be unchanged upon carbonation. Figure 4 shows results of Soja el al [36] on the pore size distribution in CEM I and CEM II/B-M pastes before carbonation (t_0), after preconditioning for 12 months in a CO_2 -free environment ($t_0 + 12m$ no CO_2), and after exposure to natural carbonation for 12 months ($t_0 + 12m$ at 400ppm CO_2). Soja el al [36] suggests that the porosity redistribution during CO_2 -free exposure is due to drying. After carbonation, a coarsening of the pore size distribution is seen in Figure 4.

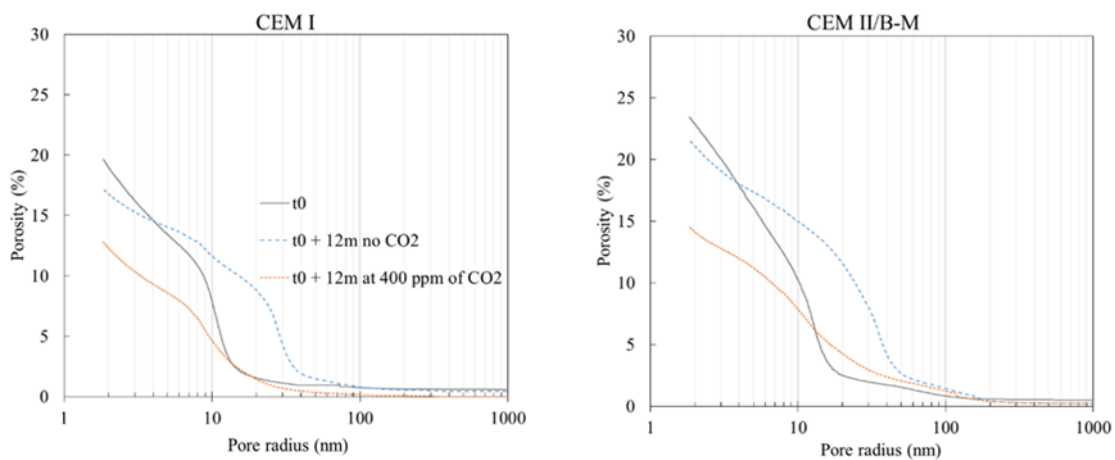


Figure 4: Porosity analysis of Portland (CEM I) and blended cements (CEM II/B-M) exposed to 70 % RH and 400 or 0 ppm of CO_2 ; exposure for 12 months after 28 day (t_0) of curing, [36]

While there is an agreement in the literature about the fact that the decrease in the pores volume (2-10 nm) is due to clogging due to calcite [38] formed from the carbonation of portlandite, the increase in the capillary pore volume (10 nm to 100 micrometer) is explained differently. Thiéry el al [45] (ref from [46]) suggests that the increase of macro capillarities corresponds to the disappearance of the clusters of CH crystals replaced by a packing of $CaCO_3$ crystals leaving new voids. Other authors have attributed this increase to carbonation shrinkage [47]. Indeed Omikrine-Metalssi el al [48] found that carbonation led to an increase of shrinkage (hence a probable increase of cracking). Brunauer et al. [49] attributed the increase in the capillary porosity volume to the cracks in the $CaCO_3$ that surrounds the portlandite crystals. In agreement with these results, Ranaivomanana [50] explains the formation of additional macro-porosity after carbonation by the removal of the silica gel released after decalcification of C-S-H that causes micro-cracks. These results reveal that the change in the pore size distribution of cementitious materials upon carbonation depends on the materials

composition (CH and C-S-H content) and water-binder ratio. Therefore, the microstructure changes must be investigated on various materials with different water-binder ratios, before definite conclusions can be drawn.

1.2.2 Effect of carbonation on other properties

i) Water retention capacity

As a consequence of the pore size distribution changes after carbonation, the water retention capacity of cementitious materials, which is directly related to their porous structure, varies upon carbonation. Auroy et al. [51] found that after accelerated carbonation (3% CO₂), the water retention capacity of the CEM I paste only hardly changed, while the water retention capacity of blended cement pastes (CEM III /A and CEM V/A) strongly decreased. The same findings are assessed by Ranaivomanana [50] after accelerated carbonation (50% CO₂) of CEM I and CEM V/A concretes.

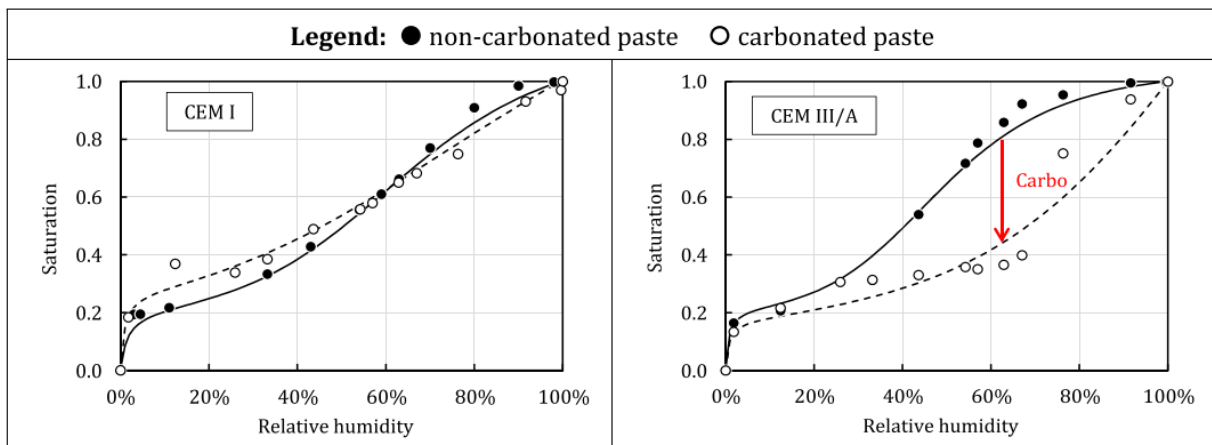


Figure 5: Desorption isotherms of CEM I and CEM III/A pastes (from [52] and [51])

Hyvert [53] investigated the sorption/desorption isotherms of CEM I, CEM II, and CEM III mortars and found that at 65% RH the degree of water saturation of the non-carbonated materials is 15% to 21% higher. The desorption isotherms show that the degree of water saturation of carbonated CEM I and CEM II mortars is almost 10% higher at relative humidity level lower than 50%, while at higher relative humidity level (>50%) non-carbonated mortars are more water saturated than carbonated mortars. The recent work of Dutzer et al. [52] (Figure 5) shows that carbonation (3 vol.% of CO₂) induced cracking which are more important for blended cement pastes than CEM I pastes, which could explain the decrease in water retention capacity of these materials.

ii) Permeability

Ranaivomanana [50] found that the ethanol and gaseous oxygen permeability of concrete with

CEM I only slightly decreased after accelerated (50 vol.% of CO₂) carbonation (by a factor of 0.8 and 0.1 respectively) despite the important decrease in the total porosity. However, for CEM V/A ethanol and gas permeability increased by a factor of 6 and 2.5, respectively. In agreement with these findings, Borges et al. [54] measured the oxygen permeability of a CEM I paste and a CEM I paste with slag (75% and 90% clinker replacement) and found that the CEM I paste permeability only slightly varied after carbonation (5 vol.% of CO₂) whereas the slag paste oxygen permeability increased significantly. Furthermore Tracz et al. [55] assessed the nitrogen permeability before and after carbonation of hardened cement pastes and found that the permeability decrease ranged from 15% to 42% depending on the W/C ratio.

However, according to Thiéry et al. [45], for CEM I concrete with a high w/c-ratio (0.84) the permeability (evaluated using inverse analysis method) increased after carbonation by one order of magnitude.

Auroy et al. [51] explains the variation of gas permeability upon carbonation (3 vol.% of CO₂) by a competition between porosity clogging due to the precipitation of CaCO₃ and carbonation induced micro-cracking. In fact, both parameters depend on the initial mineralogical composition.

1.2.3 Effect of carbonation on the gas diffusivity

Soja et al. [36] determined the oxygen-effective diffusion coefficient for CEM II/B-LL pastes before and after exposure to natural carbonation using the experimental setup described in (Paper I). These paste diffusion coefficients slightly decreased (by a factor of 1.6 at the most) after 12 months of natural carbonation. No definite conclusion can be drawn from these results because: only one replicate was tested in both states, the 1.6 factor could be due to averaging error.

Dutzer et al. [52] investigated the influence of accelerated carbonation (3 vol.% of CO₂) on the helium diffusivity of CEM I, CEM III/A, CEM V/A and a low alkalinity paste (LAC) at different water saturation degrees. The experimental setup used for this investigation is described in [9]. As shown in Figure 6, the He diffusion coefficient decreases for CEM I pastes and increases by more than one order of magnitude (LAC paste) for blended cements. Dutzer et al. [52] explains these results by accelerated carbonation-induced cracking, which are found to be more important for blended cement pastes than for CEM I pastes.

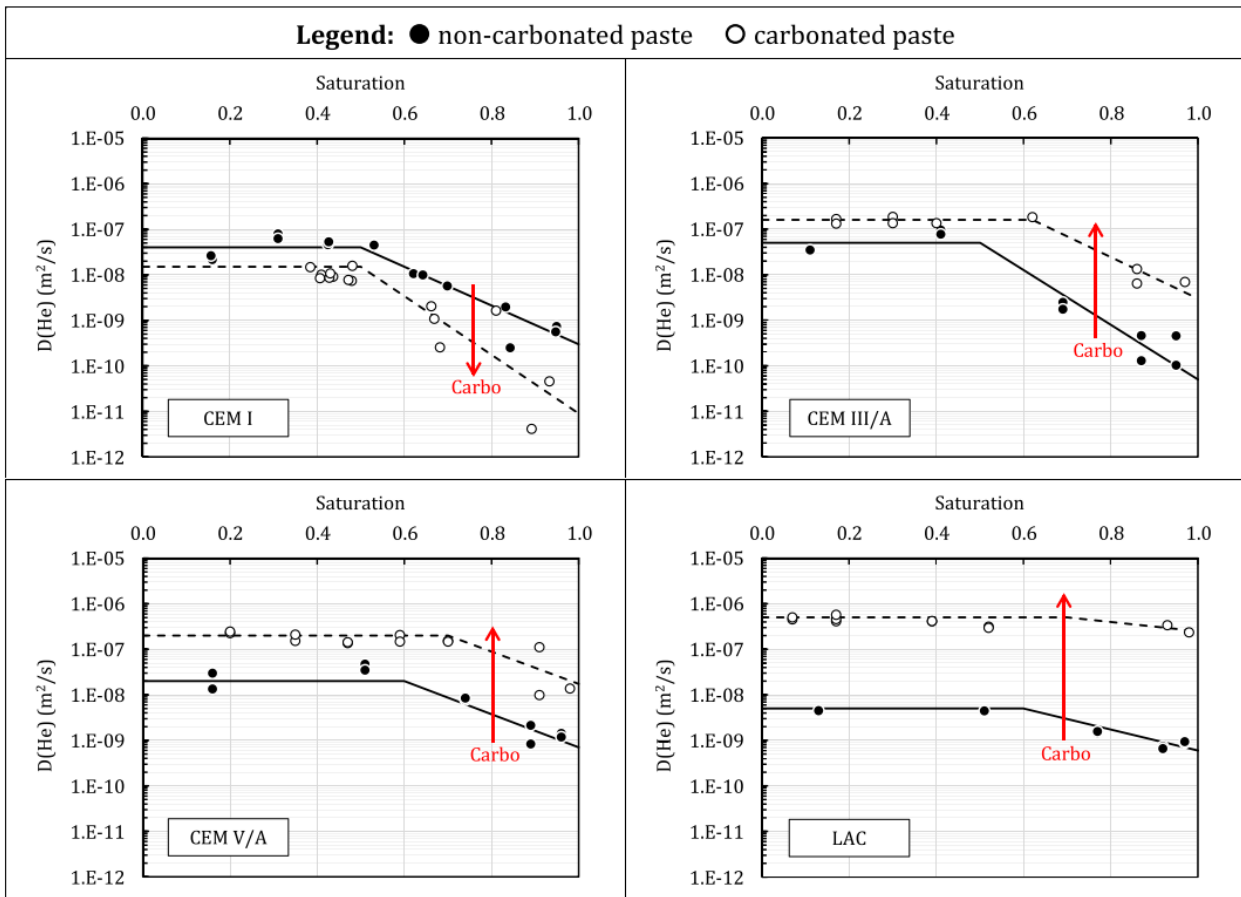


Figure 6: Helium diffusion coefficient of the non-carbonated and carbonated pastes [52]

Bertin [46] determined the oxygen-effective diffusion coefficient of CEM I and CEM I + 60% Slag (cured for 6 months) upon carbonation (at 3 vol.% of CO_2 65% RH) using the experimental setup described in Paper I. The oxygen diffusivity of CEM I decreased upon carbonation by almost one order of magnitude while it increased by more than one order of magnitude for slag blended pastes. The influence of carbonation on three concrete types made with CEM I, CEM I + 30 % fly ash and CEM I + 60% slag is also investigated using the experimental setup described in [56] at the dry state only (oven-drying at 45°C). The oxygen diffusivity decreased by a factor of about 4 and 2 for CEM I and fly ash concrete while it increased by almost a factor of 2 for slag concrete. Bertin [46] explained the decrease in O_2 diffusivity by the decrease in the total porosity and its increase by the fact that the pore structure becomes coarser and its connectivity increases after carbonation due to the decalcification of C-S-H.

1.2.4 Corrosion initiation

Steel reinforcement in non-carbonated concrete corrodes at very slow rates ($<0.1 \mu\text{m} / \text{year}$) [57], thanks to the passivation layer formed by the high alkalinity of the hardened cement paste. The carbonation reaction gives rise to a neutralization of the pore solution to pH below

9 [13],[47]. Therefore, the steel in concrete is no longer protected and begins to corrode because the thin nanometric layer of impermeable $\text{Fe}(\text{OH})_3$ created around the steel reinforcements is destroyed. As seen in Figure 7, depending on the electrical potential, the reinforcements may be in the zone where $\text{Fe}(\text{OH})_3$ is no longer predominant but Fe^{2+} is. This change is seen when the pH is lower than 9.

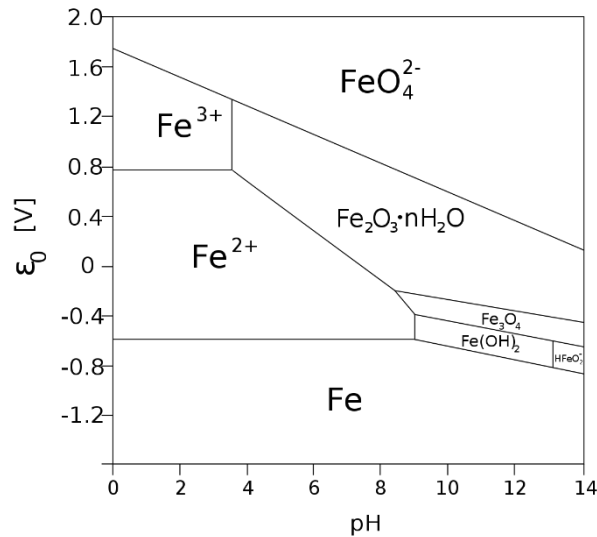


Figure 7: Pourbaix diagram

The fundamentals of corrosion of the reinforcement have been dealt with by several researchers [13], [58], [57]. According to Tuutti [13], corrosion is considered as a two-stage process (Figure 8). The initiation period (t_i) (which takes years in the case of carbonation), is the stage during which CO_2 progresses in a time-dependent manner into the depth at which it encounters the reinforcement in concrete. The propagation stage (t_p) is the period after the depassivation when active corrosion takes place. The addition of the two periods represents concrete service life (t_{sr}).

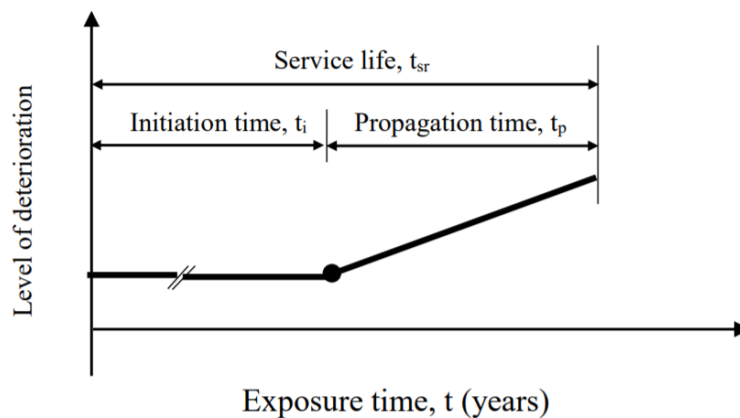


Figure 8: Corrosion service life of reinforced concrete (RC) structure [1]

Corrosion results in a formation of expansive corrosion products (rust) that occupy a bigger volume than the original non-corroded steel [59]. Rust creates tensile stresses on the

surrounding concrete, leading to cracking and spalling of the concrete cover, which is a usual consequence of steel corrosion in concrete [60]. Afterwards, the reinforcement is exposed to external environment. Without suitable repair measures, this procedure leads from limitations of serviceability to loss of load-bearing capacity of concrete structures [61]. Equation 7 gives the balanced equation of the entire corrosion process.



In some cases, the deterioration is visible within a few years of construction in the form of cover concrete cracking (Figure 9). This is one of the limit state indicators in defining the end of functional service life for existing reinforced concrete structures undergoing corrosion.



Figure 9: example of carbonation-induced corrosion (Olympic Arena, Munich) [62]

Regarding the carbonation-induced corrosion, it is worth noting that even though theoretically, corrosion starts when the carbonation front reaches the reinforcement [58], Yoon et al. [63] observed corrosion of the reinforcement before the apparent carbonation depth has reached the rebar. Hussain et al. [64] suggest that corrosion starts when the carbonation depth reaches 80% of the concrete cover.

Concrete cover depth and composition influence the ease of carbon dioxide, oxygen and moisture ingress into the concrete, thus the corrosion rate of the rebar. A significant portion of a reinforced concrete structure service life may be lost if the concrete carbonation properties are not determined with enough accuracy.

II. Chapter II: State of the art on the prediction of the carbonation rate

This section gives an overview of the available standardized and non-standardized experimental methods related to carbonation. Advantages and limitations of the different techniques are discussed. A presentation of two models commonly used to predict the carbonation depth of cementitious materials is also given.

2.1 Determination of the carbonation rate from the pH-indicator test

The determination of the carbonation depth is usually achieved by means of pH indicators (thymolphthalein, phenolphthalein, m-nitrophenol, etc.). The materials are tested to carbonation under two types of exposure conditions: natural exposure (around 0.04 vol.% of CO₂ and uncontrolled ambience) or under controlled relative humidity, temperature, and CO₂ concentration [1]. The carbonation depth, which is judged to be the colorless part on the specimen, is measured on the broken faces of the samples obtained by splitting and is the average of different distance measurements to the central points on the face. The carbonation rate is obtained by determining carbonation depths at different exposure times.

Although the exposure to natural carbonation is considered to be the most accurate method for determining the carbonation rate of cementitious materials, it is highly criticized for its time-consuming nature. Therefore, accelerated carbonation tests are usually performed by increasing the CO₂ concentration on the exposed surface of the specimen. This way, the carbonation depth under accelerated conditions is higher than the depth under natural carbonation. Indeed Limbachiya et al. [65] state that the carbonation depth determined under accelerated carbonation (3.5 vol.% of CO₂) for one week equals the carbonation depth determined for one year under natural exposure.

According to Henry's law [66], the amount of dissolved gas in a liquid C [mol.L⁻¹] is directly proportional to its partial pressure above the liquid p [atm]. This relationship is described in Equation 8. Henry's constant k_H [atm.L.mol⁻¹] is a temperature-dependent constant.

$$p = k_H C$$

Equation 8

The equipment needed to perform these tests is: a climate chamber with controlled RH, T, and CO₂ concentration, a specimen splitting equipment, and a pH-indicator solution. The climate chamber required for these measurements is costly and requires expensive safety equipment especially when accelerated carbonation tests are performed with high CO₂ concentration (case of the standard XP P18-458 with 50 vol.% of CO₂ concentration [5]).

Regarding the accuracy of the accelerated carbonation test, we have on one hand, Dhir et al. [67] who suggest that accelerated carbonation at 4 vol.% of CO₂ can provide an indication of long term carbonation behavior of concrete since a good agreement between the carbonation at natural and accelerated (4 vol.% of CO₂) conditions is observed. In agreement with these findings, Shah et al. [35] found that the micro-structural and phase assemblage changes under accelerated conditions (3 vol.% of CO₂) and natural carbonation exposure are similar. Leemann et al. [68] show that the carbonation resistance of mortars carbonated at 1 vol.% and 4 vol.% of CO₂ concentration is practically the same.

On the other hand, Yan [69] found that accelerated carbonation test results are significantly lower than the carbonation depths calculated theoretically. This is mainly due to the clogging of the pore system due to the water release due to carbonation. Increasing the CO₂ concentration could result in a transmitted quantity of CO₂ higher than the bound CO₂ by the material carbonation [20]. As a result, the rate of carbonation decreases gradually with the increase of CO₂ concentration. Furthermore, Bernal et al. [70] found that the reaction products during accelerated and natural carbonation of alkali-activated binders are notably different (bicarbonate favored at high CO₂ partial pressure), and the pH drop of the pore solution is much more important during the accelerated carbonation. Hyvert et al. [71] and Castellote et al. [72] agree on the fact that the C-S-H degree of carbonation depends on the CO₂ concentration during the carbonation reaction.

Accelerated carbonation reliability is also criticized for the following reasons: (i) European inter-laboratory tests carried out by CEN (European Committee for Standardization) showed that the test had a poor repeatability [73] (ii) the method depends only on the pH change and therefore the influence may not be clearly identified if carbonation only partially occurs, or if carbonation occurs but with pH beyond the scope changeable by indicator. Nevertheless, it is a simple and easy method in a visual aspect for testing carbonation, which makes it widely used.

As for the accelerated carbonation test, there is a variety of test protocols (see Table 4). Differences occur regarding the CO₂ concentration while the relative humidity of the test is

usually carried out at a relative humidity level that ranges between 55-70% RH under which the progress of carbonation is reported to reach a maximum [74].

Regulation / recommendation / standards	Test conditions
XP P18-458 (France) [5]	CO ₂ : 50 ± 5 vol.% RH: 65 ± 5 % T: 20 ± 2°C 0, 7, 14 and 28 days
DAfStb Heft 510 [15] (German recommendation not an official German regulation)	CO ₂ : 2 vol.% RH: 65 % T: 20 °C 28 days
BS EN 14629 (Great Britain) [75]	CO ₂ : 1 vol.% RH: 60 ± 10 % T: 21± 2°C 0 and 56 days
BS 1881-210 (2013) (Great Britain) [76]	CO ₂ : 4 ± 0.50 vol.% RH: 55 ± 5 % T: 20 ± 5°C 56, 63, and 70 days
ISO 1920-12:2015 [77]	CO ₂ : 3 ± 0.5 vol.% RH: 55 ± 5 % RH T: 22 ± 2°C 70 days
SIA 262/1 (Switzerland) [78]	CO ₂ : 4 ± 0.1 vol.% RH: 57 ± 3 % T: 20 ± 2°C 0, 7, 28 and 63 days
NT Build 357 (Nordtest) [79]	CO ₂ : 3 vol.% RH: 60 ± 5 % T: 20 ± 2°C 0 and 56 days
LNEC E391 (Portugal) [59] Concrete. Determination of accelerated carbonation	CO ₂ : 5 ± 0.1 vol.% RH: 60 ± 5 % T: 23 ± 3°C 14, 76, 166 and 351 days
<u>CUR</u> -Aanbeveling 48:2010 (Netherland Recommendation) Geschiktheidsonderzoek van nieuwe cementen voor toepassing in beton	CO ₂ : 2 vol.% RH: 65 °% T: 20 °C 28, 56 days
GB T50082-2009 (China) Standard test methods of long-term performance and durability of ordinary concrete [80]	CO ₂ : 20 ± 3vol.% RH: 70 ± 5 % T: 20 ± 2°C 2, 7, 14, 28 days

Table 4: Accelerated carbonation test methods in different countries (CO₂ concentration, relative humidity, temperature and test durations)

The accuracy and reliability problems of the accelerated carbonation test limit its use to set the concrete performance. However, shortly an European agreement (EN 12390-12:2018-10 [81]) on a suitable test method for determining the carbonation resistance under accelerated conditions has been achieved: CO₂: 3 ± 0.1 vol.-% ; RH: 57 ± 3 %; T: 20 ± 2°C; testing age

0, 7, 28 and 70 days.

A reliable prediction of the carbonation rate under natural exposure from the accelerated carbonation test requires a mathematical relationship between both test results which is challenging and sets the limit of the accelerated test method. Note that Rafai et al. [82] compared the pH-indicator results to other test methods such as TGA and volumetric dosage of CO₂, and found that, besides the fact that it is unable to determine the amount of carbonates in a concrete, the phenolphthalein solution leads to an underestimation of the carbonation front.

2.2 Determination of the carbonation rate from material properties

Besides the above mentioned test methods, another way to predict the carbonation rate of cementitious materials can be achieved by means of the experimental determination of the carbonation rate prediction models' input parameters [8], [9]. The CO₂-effective diffusion coefficient and the amount of carbonatable products are the key material properties to model the of carbonation rate. These properties are also appropriate durability indicators that could be used in performance based and probabilistic durability design of concrete structures. When determining these two properties, it is important to consider the strong dependence on the degree of water saturation of the material (Paper I), [9], [85]. Pores that are well saturated almost totally prevent the CO₂-diffusion [86], and dry pores prevent the dissolution of gaseous CO₂ and reactive CaO.

2.2.1 Gas diffusion coefficient

The gas diffusion coefficient is a material property of high relevance regarding service life prediction models [15], [6]. However, there is so far no standardized test method for the determination of this property. In comparison to other transport properties such as permeability and sorptivity, the literature is not rich with innovative experimental techniques for the determination of the gas-effective diffusion coefficient of cementitious materials. The test methods developed by some researchers are based on different principles, use different gas species, allow for the performance of the test under different relative humidity levels, and their reliability and detection limit are poorly documented.

One way to determine the gas-diffusivity is based on monitoring the time evolution of the gas concentration in a downstream chamber due to the diffusion through the tested sample. The

concentration is measured by means of a gas sensor. Test methods based on this technique (“accumulation”) (Figure 10 (a)) rely on the measurement of the concentration of the diffusing gas 1, which can also be a mixture of gases, inside the lower chamber by means of the gas 1 analyzer, after diffusing through the sample. Note that the concentration of the gas 1 in the upper chamber is usually kept constant. The experimental data collected in this case are the concentration of the diffusing gas 1 as a function of time. These raw data are fitted to Fick’s Laws described in section 1.1.1. An advantage of this test method is that the transient state can be considered in the data analysis. Based on this technique, Houst [87] developed an experimental setup for determining the gaseous oxygen diffusion coefficient of mortars and concretes, and Namoulniara [88] developed a test method that allows to determine the CO₂ - effective diffusion coefficient of dry mortars. This test method is further improved by Gendron [89]. Namoulniara [88] and Gendron [89] use CO₂ as the diffusing specie through mortars and hardened cement pastes since it is the gas of interest regarding carbonation. However, partially saturated materials are not tested since with the presence of water CO₂ reacts with the hydration products causing precipitation of calcium carbonates which modifies the materials’ microstructure and the diffusion process during the test itself. Indeed, Gendron [89] uses CO₂ diffusion tests on partially water-saturated specimens to investigate carbonation rate. No information about the reliability, accuracy or cost-efficiency on these test methods is given. Table 5 gives a summary of the existing test methods based on this principle.

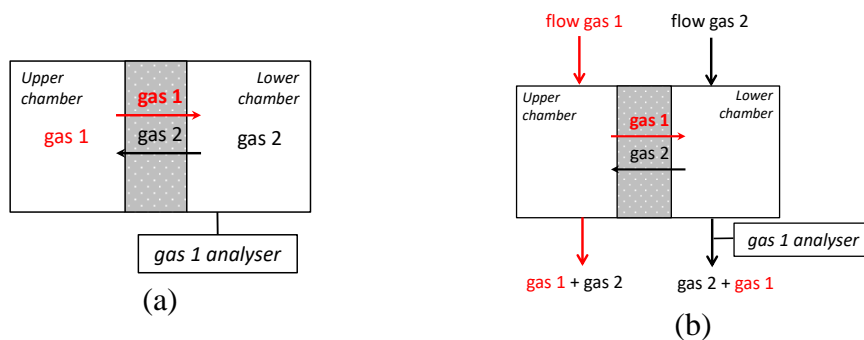


Figure 10: The procedures for gas diffusion setups found in the literature [90]

A second type of procedure is shown in Figure 10 (b). One face of the specimen is exposed to a flow of gas 2 and the other one is exposed to a steam of the diffusing gas 1. The gases flow rates are maintained constant. The concentration of the gas 1 in the mix (gas 2 + gas 1) at the output of the lower chamber is monitored using an analyzer. This concentration increases gradually until the steady state is reached. Knowing the concentration of the gas 1 and its flow rate, Fick’s first law of diffusion (Equation 1) can be used to calculate the effective diffusion coefficient. Using this principle only the steady state is taken into consideration in the determination of the diffusion coefficient. Note that Lawrence [8] test method for the

determination of oxygen-effective diffusion coefficient is based on this principle. This experimental setup is also used by Leemann et al. [91] and Wong et al. [56]. Table 6 gives a summary of the existing test methods based on this principle.

Different diffusing gas species used in the development of these experimental setups are found in the literature. Lawrence [8], Leemann et al. [91], Wong et al. [56], and Houst [87] diffusion tests are based on the determination of pure oxygen diffusion coefficient, since oxygen is inert with most of the hydration products. Consequently, the materials microstructure will not be altered during the test itself, and the determination of this gas-effective diffusivity is possible for partially saturated materials. The CO₂-effective diffusivity, which is the property of interest regarding carbonation, is then determined from O₂-effective diffusion coefficient [91]. Note that O₂-diffusion coefficient is of high interest regarding corrosion, since the corrosion rate of reinforcing bars is partly controlled by the diffusion of oxygen into concrete [13]. Sercombe et al. [9], Boher [92], Vu [93] and Dutzer et al. [52] used Hydrogen, Helium or Xenon as the diffusing specie, mainly because they do not react with the pore structure of cement pastes.

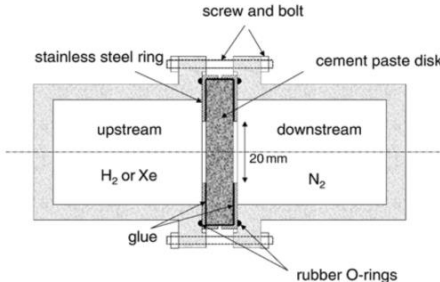

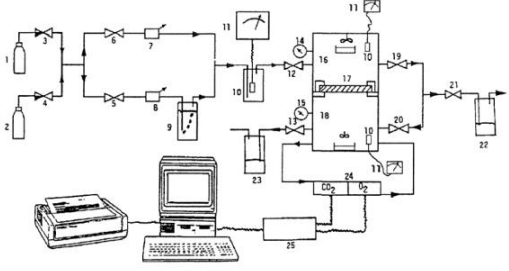

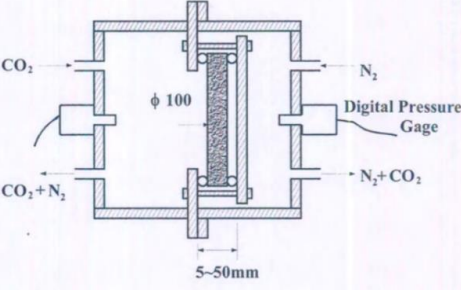
Reference	Experimental setup sketch	Gas type	The lower value of the gas diffusivity [m ² /s]
Sercombe et al. [9] Boher [92] Vu [93] Dutzer et al. [52]		He, Xe	3.10 ⁻¹²
Benavente et al. [94]		CO ₂	10 ⁻⁹
Houst[87]	 <p data-bbox="544 1133 1082 1267"> 1. gaz : 78% N₂ - 20% O₂ - 2% CO₂ 2. gaz: 100% N₂ 3-6. vannes 7-8. débitmètres 9. flacon laveur contenant H₂O 10. sonde de mesure h.r. 11. indicateur h.r. 12-13. vannes 14-15. manomètres 16. chambre supérieure 17. échantillons 18. chambre inférieure 19-21. vannes 22-23. flacons destinés à prévenir l'introduction d'air ambiant 24. analyseurs de gaz 25. système d'acquisition de données </p>	CO ₂ and O ₂	Not reported
Namouniara [95] Gendron [89]		CO ₂	10 ⁻¹²
Jung et al. [96] Soukup et al. [97] Papadakis et al. [6] Originally by Wicke and Kallenbach and modified by Graham [98]		CO ₂	Not reported

Table 5: Summary of gas diffusion coefficient measurement methods based on the “accumulation” principle

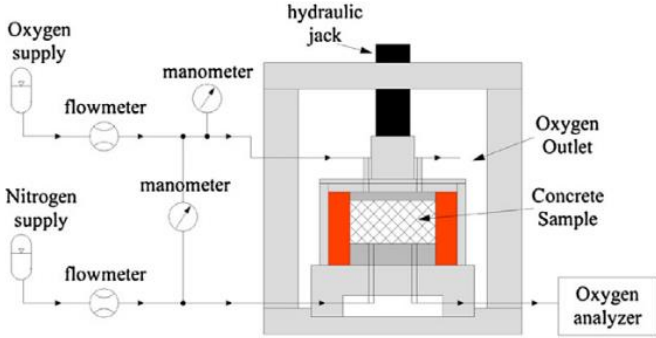
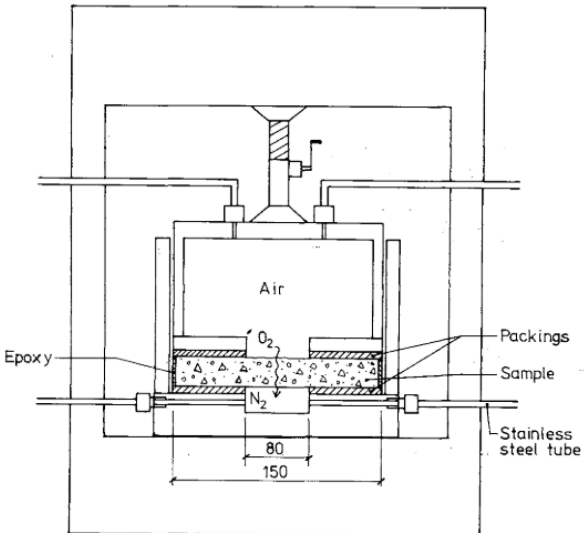
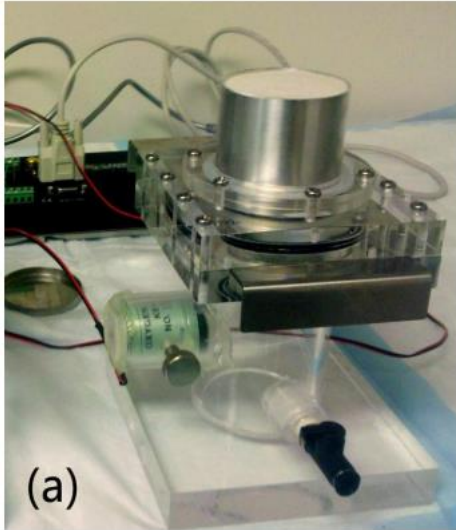
reference	Experimental setup sketch	Gas type	The lower value of the gas diffusivity [m ² /s]
Lawrence [8] Wong et al. [56] Leemann et al. [91] Villain et al. [99]		O ₂ and CO ₂	Not reported
Tuutti [13]		O ₂	Not reported
Peng et al. [100]		O ₂	5·10 ⁻⁹

Table 6: Summary of gas diffusion coefficient measurement methods based on the ‘flow’ analysis

The CO₂-effective diffusion coefficient of cementitious materials can also be predicted from empirical models [101]. As stated in section 1.1.1, the effective diffusion coefficient in a porous

media is correlated to the self-diffusion coefficient D_{0,CO_2} , the total porosity, the degree of water saturation, and a parameter f called the “form factor”.

$$D_{e,CO_2} = \phi * (1 - SI) * f * D_{0,CO_2} \quad \text{Equation 9}$$

The form factor f takes into account the tortuosity, constrictivity and connectivity of the porous network. These parameters describe respectively: the increase of the path that the diffusing specie must follow in the porous network, the pore sections variation, and the degree to which a porous network is connected. Note that the quantification of these parameters is challenging.

Efforts have been carried out in the literature to determine an expression of the diffusion coefficient (see Table 7). Papadakis et al. [83] (Equation 10) present an expression of the effective diffusion coefficient of carbon dioxide as a function of the relative humidity of the air (RH) and the porosity Φ_p of the hydrated cement paste and an experimental parameter $B = 1.2 \pm 0.1 \cdot 10^{-3} \text{ m/s}^{1/2}$. Equation 10 was determined from experimental results obtained on a Portland cement mortar.

Based on this model, Millington [102] (Equation 11) suggested a new model based on the degree of water saturation SI , the diffusion coefficient of carbon dioxide in air D_{0,CO_2} , the total porosity of the material Φ and two parameters a and b . Currie [103] (Equation 12) modified and enlarged former expression of the gas-effective diffusion coefficient by further explicitly considering the constrictivity β , and tortuosity τ , which is defined as the ratio of the length of the curve to the distance between the ends of it.

Model	
$D_{e,CO_2} = (\phi_p * (1 - RH) * B)^2$	Equation 10
$D_{e,CO_2} = (\phi)^a (1 - SI)^b D_{0,CO_2}$	Equation 11
$D_{e,CO_2} = \phi (1 - SI) \frac{\beta}{\tau^2} D_{0,CO_2}$	Equation 12

Table 7: Some models of CO₂-effective diffusion coefficient

2.2.2 CO₂-binding capacity

The second parameter that controls the carbonation process is the amount of available reactive carbonatable products. Indeed, according to Papadakis et al. [6], the carbonation rate is inversely proportional to the square root of the amount of carbonatable products in the material. From the composition of the cementitious material, one can calculate a theoretical amount of the major phases contributing to the carbonation reaction in the cement paste (CH, C-S-H, AFt, AFm, etc.). Huntzinger et al. [104] suggest that the theoretical CO₂ consumption (as a percentage of dry mass) in a hydrated Portland cement paste can be calculated as follows:

$$\begin{aligned} \%CO_2 = & 0.785(\%CaO - 0.56 \%CaCO_3 - 0.7\%SO_3) + 1.091\%MgO + 0.71\%Na_2O \\ & + 0.468\%K_2O \end{aligned} \quad \text{Equation 13}$$

Where the %CO₂ refers to the mass of CO₂ consumed in the carbonation reaction compared to the original unreacted mass of the sample. The stoichiometric mass factors shown in Equation 13 assume that all of the CaO (except that bound in CaSO₄ and CaCO₃) will react to form CaCO₃, all the MgO will react to form MgCO₃, and all of Na₂O and K₂O will convert to Na₂CO₃ and K₂CO₃. The mass factors for K₂O and Na₂O are doubled if bicarbonates form instead of carbonates.

Equation 13 is valid under the assumption that all the magnesium oxide, sodium oxide, potassium oxide, and all the calcium oxide in the cement, excluding that in calcium carbonate and calcium sulfur, are available to react with carbon dioxide to form carbonates. The major limit of this model is the fact that for cements blended with pozzolanic additions, other phases (e.g. Mg(OH)₂, K(OH) and Na(OH)) may also contribute to the carbonation through a variety of reaction pathways [105].

Thermogravimetric technique (TGA) is a valuable tool to quantify the amount of calcium carbonate in cementitious materials [106]. This method consists of heating a powdered hardened cement paste sample at a constant rate from room temperature to a temperature usually higher than 1000°C. The mass variation of the sample is monitored as a function of the temperature increasing. The carbonates formed during the carbonation reaction have certain temperature decomposition ranges, which allows for the quantification of the amount of carbonates (which is expressed relatively to the mass at 1000°C), and consequently the CO₂ binding capacity. TGA is a technique that, although limited in scope to those reactions taking place with a change in weight, gives results that are intrinsically quantitative. According to

Villain et al. [107] the mass loss due to calcium carbonates decomposition ranges between 580°C - 1000°C.

Note that there is no agreement in the literature concerning the temperature range of decomposition of calcium carbonates [108]. Thiéry et al. [39] identified three temperature ranges for a completed carbonation, which are summarized in Table 8. The authors pointed out that a strict separation of the individual modifications is difficult, since the temperature ranges overlap. They show also a preferential formation of calcite from the carbonation of Ca(OH)₂. The less well crystallized and thermodynamically more unstable forms of CaCO₃ are attributed to the carbonation of the C-S-H phases.

Decomposition temperature range	CaCO ₃ state
I (780 – 990 °C)	well crystallized CaCO ₃ (calcite)
II (680 – 780 °C)	thermally unstable, less well crystallized calcite the thermal transformation of the metastable CaCO ₃ phases Vaterite and Aragonite at about 440 - 470°C
III (550 – 680 °C)	amorphous CaCO ₃

Table 8: Decomposition temperatures of the CaCO₃ polymorphs [39]

Note that TGA technique is commonly used alongside complimentary techniques such as X-ray diffraction (XRD/Rietveld), which is a technique for studying the crystalline materials [109]. CaCO₃ polymorphs such as vaterite or aragonite can hardly be identified by means of TGA. X-ray diffraction gives differentiated results in this case.

The major limits of these techniques are as follows: i) they are expensive; ii) the CO₂ contained in the amorphous carbonated pastes is not considered by XRD; iii) the CO₂ mass loss due to some carbonates (e.g. MgCO₃) has a temperature range that may overlap the portlandite's and the bound water in the C-S-H gel pores in TGA [107]; iv) the overlapping of XRD reflections makes identification of individual phases difficult in a multi-phase hydrated material [108].

Another way to quantify the amount of carbonatable products of cementitious materials is by studying its CO₂-uptake. Indeed, the potential for capturing CO₂ from the atmosphere by concrete carbonation is widely discussed in the literature. However, these discussions are mainly carried out in the field of life cycle analysis of concrete structures during their service life [110], [111], [112], [101]. The uses of the measurement of CO₂-uptake due to carbonation

of cementitious materials in order to quantify the amount of carbonatable products and to study the carbonation reaction kinetics are only scarcely documented. To our knowledge, the main work with this approach is the one of Van Balen et al. [113], who developed an experimental setup that consists of exposing a lime sample to 15% or 50% CO₂ at a certain relative humidity level in a closed loop (Figure 11).

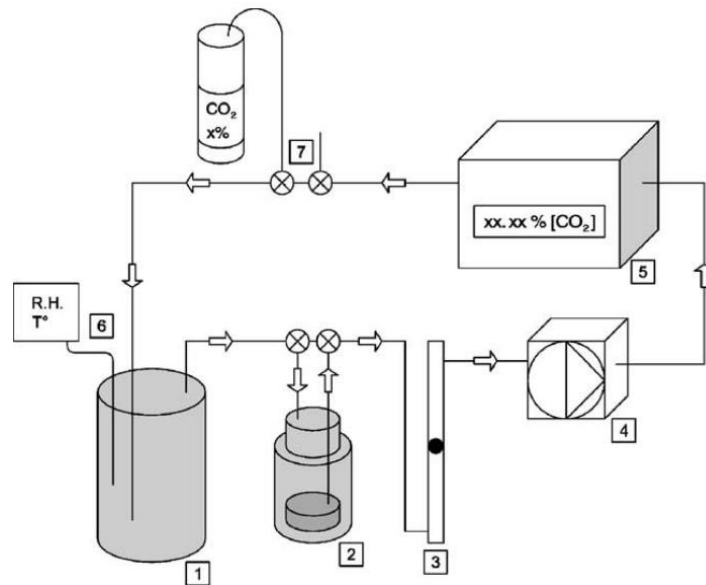


Figure 11: CO₂-uptake measurement device developed by van Balen et al. [113]

The carbonation reaction rate is measured continuously by the reduction of carbon dioxide concentration in a closed system (Figure 11). The tested sample is spread thinly over a plastic cup inside the sample holder ((2) Figure 11), exposed to air with a certain CO₂ concentration regulated at a certain relative humidity (1), the flow meter (3) sets the flow speed at 1.5L/min. Monitoring of the CO₂ concentration is performed using the sensor (5), (4) is a hermetically sealed pump and (7) are valves that control the direction of the flow and the amount of CO₂ concentration.

2.3 Carbonation rate prediction models

Several carbonation depth models have been developed in the literature [7][114][115]. In LaSIE laboratory, several research works have been conducted in order to develop a carbonation rate prediction model based on the physicochemical properties of the material. Miragliotta [41] studied the carbonation process on the concrete surface and developed a carbonation depth prediction model based on upscaling methods. Later, Delmi [116] focused on modeling the coupling between carbonation process and moisture exchanges between cement-based materials and their ambience of exposure. Omikrine-Metalssi [117] aimed at

modeling the coupling hydration-water exchanges by the resolution of the equations of mass conservation. Younsi [118] studied the influence of drying on the accelerated carbonation kinetics of blended cement concrete highly substituted by fly ash (50% in mass) and slag (75% in mass). Recently Gendron [89] and Omikrine-Metalssi et al. [119] proposed a carbonation depth prediction model that takes into account the evolution of total porosity, water saturation, amount of CH, C-S-H and CaCO₃ during carbonation. In the following, only two carbonation depths which are the most commonly used are described and used in this thesis work.

2.3.1 Square root of time model

Carbonation begins at exposed surfaces and spreads inwards at a rate proportional to the square root of time [21] in an environment protected from rain. Previous experimental studies [13], of concrete carbonation have established that the thickness of the affected layer can be modeled by the following simple model:

$$X_c = A * \sqrt{t} \quad \text{Equation 14}$$

X_c [mm] is the carbonation depth, A [mm/ $\sqrt{\text{year}}$] is the carbonation rate, and t [year] is the exposure time. A can be determined empirically based on accelerated and natural carbonation tests or predicted from the physicochemical properties of the tested material.

Based on Fick's first law of diffusion, Equation 14 can be written as a function of the mass of the diffusing CO₂ dg [kg/m²], the CO₂ concentration difference between air and the carbonation front ΔC [kg/m³], the carbonated layer thickness x [m] and the effective diffusion coefficient of carbon dioxide D_{e,CO_2} [m²/s] [87] as seen in Equation 15. The CO₂ amount required to carbonate the carbonatable substances can be determined according to Equation 16, where dV [m³] is the specimen volume and a [kg/m³] is the amount of carbonatable products. In a unitary approach, $dV = dx$. The substitution of Equation 16 in Equation 15 leads to Equation 17 for which the integration gives the carbonated layer thickness as a function of the gas diffusivity and the amount of carbonatable products (Equation 18).

$$dg = -D_{e,\text{CO}_2} \frac{\Delta C}{x} dt \quad \text{Equation 15}$$

$$dg = a dV = a dx \quad \text{Equation 16}$$

$$a x dx = -D_{e,\text{CO}_2} \Delta C dt \quad \text{Equation 17}$$

$$x^2 = 2 D_{e,\text{CO}_2} \frac{\Delta C}{a} dt \quad \text{Equation 18}$$

$$A = \sqrt{\frac{2 D_{e,CO_2} \Delta C}{a}}$$

Equation 19

The main assumptions of the determination of the carbonation rate A (as seen in Equation 19) are the following:

- The carbonation reaction is instantaneous; therefore, the model is only valid for RH > 50%.
- The carbonation process is described based on an assumption of the existence of two layers carbonated and non-carbonated, which implies the sharp carbonation front existence.
- The water content, diffusion coefficient and concentration gradient between the surface and the carbonation front are assumed constant.

The majority of carbonation models that have been published up until now are based on Fick's 1st law of diffusion [13], [15]. For outdoor conditions, predictions from Equation 14 and Equation 18 always overestimate the carbonation depth. Consequently, in those conditions, these models are reported not to be sufficiently valid [15]. This result is to be expected since the concrete pores at the surface subjected to rain would be more water saturated which hinders the transport of gaseous carbon dioxide in the porous system. Moreover, this kind of models does not take into account the microstructure changes due to carbonation such as porosity clogging which modifies the diffusion coefficient.

2.3.2 Papadakis' model

Papadakis et al. [6] developed an analytical model based on the physicochemical processes of carbonation. The model assumptions imply the formation of a sharp carbonation front and consider the cementitious material homogeneous, fully hydrated and in hydric equilibrium with the ambient environment. These assumptions are the ones previously exposed for the square root of time models.

The application range of this model is further developed in [83] using experimental results carried out on CEM I concrete. The carbonation depth was determined by means of phenolphthalein solution under accelerated carbonation conditions (50 vol.% of CO₂, 65% RH) from 1 to 20 days. The CO₂-diffusion coefficient is determined for carbonated samples, and the nitrogen diffusion coefficient is determined for non-carbonated samples using Wick-Kallenbach experimental setup described in [18].

The model predicts the carbonation depth X_c [m] according to the square root of time, the CO_2 concentration at the surface of the sample $[\text{CO}_2]$ [mol.m⁻³], the effective diffusion coefficient of CO_2 D_{e,CO_2} [m².s⁻¹], the exposure time to carbonation t [s], and the amount of carbonatable products [mol.m⁻³]. The latter is calculated from the amount of CH, C-S-H gel, C_2S and C_3S . The general formula for calculating the carbonation depth is given in Equation 20:

$$X_c = \sqrt{\frac{2 D_{e,\text{CO}_2} [\text{CO}_2]}{[\text{CH}] + 3[\text{CSH}] + 3[\text{C}_3\text{S}] + 2[\text{C}_2\text{S}]} t} \quad \text{Equation 20}$$

Major limits of this model are: (i) the model does not take into account water transfers; (ii) the model is only valid in an environment sheltered from rain; (iii) the assumption of a sharp carbonation front (iv) the model is based on the diffusivity of carbonated CEM I concrete only and needs to be validated for blended cement concretes (v) the amount of Ca-bearing phases that can be carbonated depends on the RH which is not accounted in Papadakis' approach (vi) the C-S-H are considered to be in the form $\text{C}_3\text{-S}_2\text{-H}_3$ [83]. Note that the model is valid only when the relative humidity is above 50%, that is to say that the kinetically limiting step is the diffusion of CO_2 through the porous network.

2.3.3 Gehlen's model

For concrete structures protected from rain, models such as Papadakis' could give rather good results (especially for OPC concrete) [6]. However, in unsheltered environment, the carbonation rate no longer obeys the square root law [15].

Therefore, the CEB Task Group V (1997) [6] developed an empirical approach, based on the squared-root of time model representation, that applies to structural components sheltered and subjected to rain. This approach is based on the introduction of a parameter called 'the weather function'. This weather function globally describes the effect of wetting events which will partly block further ingress of CO_2 .

Based on this approach, Gehlen [15] developed a carbonation depth prediction model that takes into account the environmental and executional effects on the CO_2 -diffusion coefficient, shown in Equation 21. This model can also be found in the fib model code [84].

$$X_c = \sqrt{2 \cdot k_e \cdot k_c \cdot R_{\text{NAC},0}^{-1} \cdot C_a \cdot \sqrt{t} \cdot W(t)} \quad \text{Equation 21}$$

$R_{NAC,0}^{-1}$ [mm².year⁻¹.kg⁻¹.m³] is the inverse natural carbonation resistance of concrete, determined in a standard test on specimens exposed to a standard climate (relative humidity 65 ± 5 % RH, temperature 20 ± 2 °C, CO₂ concentration 0.04 ± 0.005 vol.% and at atmospheric pressure). C_a [kg/m³] is the CO₂ concentration of the ambient air.

In the case of accelerated carbonation tests, Gehlen [15] introduced a parameter k_t for converting carbonation resistances that are determined under accelerated conditions (ACC) into resistances that are determined under natural carbonation conditions (NAC) ε_t is an error term in the unit of $R_{ACC,0}^{-1}$ for taking account of test-related errors in the determination of $R_{ACC,0}^{-1}$, and k_t [-] is a regression parameter. Note that $R_{ACC,0}^{-1}$ is determined under CO₂ 2% vol.% during 28 days under $T=20^\circ\text{C}$ and $RH_{ref} = 65\%$. Gehlen [15] suggests: $k_t = 1.25 \pm 0.35$ and $\varepsilon_t = 0 \pm 0.2$.

$$R_{NAC,0}^{-1} = k_t \cdot R_{ACC,0}^{-1} + \varepsilon_t \quad \text{Equation 22}$$

The different model parameters take into account the impact of different environmental and intrinsic conditions on the carbonation progress. The weather function $W(t)$ [-] takes into account the effect of re-wetting events.

$$W(t) = \left(\frac{t_0}{t}\right)^{\frac{(p_{wr} \cdot ToW)^{b_w}}{2}} \quad \text{Equation 23}$$

- t_0 [day]: is the time reference at which the carbonation experiments started.
- t [day]: the time of the carbonation exposure.
- ToW [days] (time of wetness) is the number of days with a precipitation quantity higher than 2.5 mm/day in a year.
- p_{wr} [-] is the probability of wind-driven rain. It considers the exposure orientation of vertical components to wind-driven rain.
- b_w [-] is a regression exponent with a value of 0.428 ± 0.170 [15].

The parameter k_e [-] describes the effect of relative humidity of exposure on the gaseous CO₂-diffusion coefficient.

$$k_e = \frac{(1 - RH_{\text{actual}}^5)^{2.5}}{(1 - RH_{\text{ref}}^5)^{2.5}} \quad \text{Equation 24}$$

- RH_{actual} [-] the average relative humidity in the location of the structural component.
- RH_{ref} [-] is the relative humidity set as the reference humidity during the basic examination.

The parameter k_c [-] considers for the effect of curing/execution on the carbonation resistance, taking 7 days as the curing date of reference.

$$k_c = \left(\frac{7}{t_c}\right)^{b_c} \quad \text{Equation 25}$$

- t_c [days]: is the curing time.
- b_c [-]: regression exponent (-0.567 ± 0.024) [15].

The major advantage of this model is its validity for all cement types and a large range of environments. In [120], Equation 21 was little revised, mainly to transfer the so-called inverse carbonation resistance $R^{-1}_{\text{NAC},0}$ [$\text{mm}^2 \cdot \text{year}^{-1} \cdot \text{kg}^{-1} \cdot \text{m}^3$] into a more common used carbonation rate k_{NAC} [$\text{mm} \cdot \text{year}^{-0.5}$]. k_{NAC} is the carbonation rate for standard test conditions ($W(t) = 1$, $k_e = 1$, $k_c = 1$, $k_a = 1$, relative humidity 65 ± 5 % RH, temperature 20 ± 2 °C, CO_2 concentration 0.04 ± 0.005 vol.% CO_2 at atmospheric pressure). k_a is a function describing the effect of CO_2 concentration in the ambient air [-], C_i [$\text{kg} \cdot \text{m}^{-3}$] is the CO_2 concentration during concrete testing.

$$X_c = k_{\text{NAC}} \cdot \sqrt{2 \cdot k_e \cdot k_a \cdot k_c} \cdot W(t) \cdot \sqrt{t} \quad \text{Equation 26}$$

$$k_a = \frac{C_a}{C_i} \quad \text{Equation 27}$$

The limits of the model are as follows:

- The model is empirical; it combines different parameters obtained from experimental data fit.

- Distribution of rainy days during the year is not taken into account.
- The number of days with a precipitation quantity higher than 2.5 mm/day in a year (ToW) is not easy to find in the literature.
- The correlation between natural and accelerated carbonation is only established for the following accelerated test procedure: 7 days of wet curing at 20°C then 21 days of curing at RH=65% and T=20°C before 28 days of 2% CO₂ exposure. This correlation must be adapted for other accelerated test methods (under 3% CO₂ concentration for example).
- The environmental parameter k_e overestimates the carbonation front for relative humidity lower than the “optimal” RH, which is usually around 60%.
- The model is highly sensible to the k_c parameter and the structural component orientation (p_{dr}).

III. Chapter III: Test protocols and materials

In this section, the main experimental techniques used in this thesis work are summarized. The gas diffusion and CO₂-binding capacity test methods developed during this thesis work are presented in the Chapter IV.

3.1 Microstructure characterization

3.1.1 Water porosity

The water porosity corresponds to the porosity accessible to water, up to pores with a diameter of 0.5 nm [121]. During this work, the water porosity of the tested concrete and hardened cement pastes is determined by hydrostatic weighting following the standard NF P18-459 [122]. The specimens are first placed under vacuum for 4 hours (pressure lower than 25 mbar). Then water is gradually added until the specimens are covered with about 20 mm of water, and the vacuum is kept for 44±1 hour. The specimens are afterwards subjected to hydrostatic weighing then weighed in air, in order to determine their volume and saturated mass. The dry mass of the samples is obtained by oven-drying at 105°C until the mass variation within a week is lower than 0.05%. The test can be applied to specimens of different sizes and shapes. However, the test is not valid for specimens with a volume higher than 1.6 L.

3.1.2 Mercury Intrusion Porosimetry (MIP)

The pore structure of the tested hardened cement pastes, before and after carbonation, and after hydration at different durations is characterized by means of Mercury Intrusion Porosimetry (MIP) using a porosimeter AutoPore IV. MIP provides information about the pore size distribution [123]. This technique is based on Laplace's (Washburn) equation [124], [125], which relates the pressure applied to the pore entry diameter through the surface tension of mercury and the contact angle with mercury. Despite its limits, such as the "ink bottle" effect [126], MIP is still considered as a method which provides valuable information about the pore structure. Very often, researchers refer to these results in a qualitative manner [55].

3.1.3 Scanning Electron Microscopy (SEM)

Scanning electron microscopy (SEM) [127] is used for two main aims : i) to estimate the degree of hydration of Slag hardened cement pastes (Paper I) and ii) to observe the

morphological changes upon carbonation of synthetic cement phases powders (CH, AFt, and C₃S) (Paper III).

Regarding the determination of the degree of hydration, SEM method was found to be more reliable than other methods [128]. The observed sample comes from a thin disc (3mm in thickness and 40mm in diameter) of a hardened cement paste crushed to obtain a piece of about 1 to 4 cm² of surface. This sample is dried under vacuum in an oven at 40°C, impregnated with degassed epoxy resin and hardener (PACK301) in a mold of 30 mm diameter and placed under vacuum for 20 min at 20°C. The resin is hardened after 48 hours, and then the surface of specimen is lapped, polished, cleaned using ethanol and placed under vacuum for 1 hour at 20°C before SEM observations. The observations are made with a MEB-FEG FEI Quanta 400 at an accelerated voltage of 15KeV.

Regarding the powders tested to observe morphological changes due to carbonation, they are placed on a carbon adhesive sample holder and coated using gold-palladium as a conductive material. The observations are made in the secondary electrons' mode. The number of secondary electrons that can be detected, and thus the signal intensity, depends, among other things, on the specimen topography. SEM can achieve a resolution better than 1 nanometer. Specimens are observed in high vacuum in conventional SEM. Further details about the SEM method used in this work are given in [127] and [129].

3.2 Physical properties

3.2.1 Degree of water saturation

During this work, the influence of the preconditioning relative humidity of HCP and concrete on the gas diffusion coefficient is investigated. Therefore, the degree of water saturation S_1 , which is of high relevance regarding the transport properties of cementitious materials, is determined for all tested specimens.

$$S_1 = \frac{m - m_0}{m_{\text{sat}} - m_0} \quad \text{Equation 28}$$

The degree of water saturation is calculated using Equation 28, where m [g] is the mass of the sample at moisture equilibrium, m_0 [g] the dry mass, and m_{sat} [g] is the saturated mass. The saturated mass of the samples is determined via water soaking under the vacuum for 48h. The dry mass is obtained after oven-drying at 105°C until mass variation of the specimen is lower

than 0.05% within a week.

3.2.2 BET surface area

Brunauer-Emmett-Teller (BET) is a technique used to investigate the influence of natural carbonation on the specific surface area of powdered synthetic anhydrous and hydrates (Paper III). This technique is based on calculating the amount of adsorbate gas (Nitrogen in our case) corresponding to a monomolecular layer on the surface of the solid. The physical adsorption results from relatively weak forces (van der Waals forces). This amount is correlated to the total surface area of the particles including pores in the surface. Therefore, the surface developed by the grains and their inner porosity are determined.

Assumptions of the BET technique are: i) gas molecules behave ideally; ii) only one monolayer forms; iii) all sites on the surface are equal; iv) no adsorbate-adsorbate interaction and v) adsorbate molecule is immobile. The apparatus used is Tristar II 3020 micrometrics.

3.2.3 Helium pycnometry

Helium pycnometry is a technique used in order to determine the apparent density of particles in synthetic anhydrous and hydrates before and after exposure to carbonation (Paper III). This technique is based on gas displacement and the volume pressure relationship known as Boyle's Law [130].

The tested specimens are stabilized at ambient temperature prior testing $20 \pm 1^\circ\text{C}$. Closed pores (i.e. those that do not communicate with the surface of the solid) are included in the measured volume. The apparatus is the pycnometer ACCUPYC 2 1340 MICROMERITICS. The measurement sequence is repeated until the results for the volume of the sample agree to within 0.2%.

3.2.4 Apparent oxygen permeability

Gaseous oxygen permeability K_{O_2} [m^2] is a general durability indicator [131] that depends on the porous network connectivity and the material micro-cracks [56]. This property is also required in some applications such as internal lining of underground geo-reservoirs for gas storage purposes. The apparent permeability is determined based on the Darcy law. Major limits of this test method are:

- Gas permeability is highly influenced by drying-induced microcracks [56].
- Concrete gas permeability reflects the degree of its accessibility to gases under a

pressure gradient only, which is unsuitable for diffusion-based phenomena (such as carbonation) [132].

- It is challenging to determine the influence of different degrees of water saturation on the gas permeability of the specimens because of the difficulty to obtain readings on the gas flow meter under the conditions of pressure difference employed in this test, and the impossibility to pre-condition the 50 mm thickness concrete specimen at different relative humidity levels in a reasonable time.

During this thesis work, the apparent oxygen permeability of different concrete mixtures is determined following the XP P18-463 standard [133] which is based on the CEMBUREAU apparatus [134][135]. Three replicates of the concrete are tested. After covering the specimen sides with epoxy resin, they are oven dried in a well-ventilated oven at $(80 \pm 5)^\circ\text{C}$ for 6 days and placed in a desiccator for 24h. The first measurement is made at 7 days. The specimens are then replaced in the oven at 105°C until constant mass and placed in desiccators 24h prior testing. The gas permeability measurements are determined at an absolute pressure of 2 bars.

3.3 Chemical composition

3.3.1 Thermogravimetric analysis (TGA)

Thermogravimetric analysis (TGA) [106] is conducted on the powdered samples in order to determine the amount of bound CO_2 (B_{CO_2}) in the specimens (Paper II and III). TGA measurements are made under nitrogen flow at a heating rate of $10^\circ\text{C}/\text{min}$ using a powdered sample of around 30 mg sieved at $63 \mu\text{m}$. The heating temperature varies from 30°C to 1000°C .

$$B_{\text{CO}_2} = \frac{m_{\text{CO}_2}}{m_{\text{oxydes}} + m_{\text{CO}_2}^0 + m_{\text{H}_2\text{O}}^0} \quad \text{Equation 29}$$

The amount of bound CO_2 [$\text{g}_{\text{CO}_2} \cdot \text{g}^{-1}_{\text{cement}}$] is calculated based on Equation 29, where m_{CO_2} [g] is the mass of CO_2 present in the sample and given by the TGA (Temperature between 550°C and 950°C [108]), m_{oxydes} [g] corresponds to the mass of the sample at 1000°C , $m_{\text{CO}_2}^0$ [g] and $m_{\text{H}_2\text{O}}^0$ [g] are the masses of the CO_2 and water initially present in the raw materials respectively. TGA results give the temperature ranges attributable to the relevant decomposition processes of the phases present in the tested specimen. TGA is carried out using TG SETARAM 92-16 apparatus and the raw data are analyzed using SETSOFT 2000

software.

3.3.2 X-ray diffraction (XRD)

X-ray diffraction technique is used for the following aims: i) the determination of the degree of hydration of Portland cement hardened cement pastes (by analyzing the XRD results using Rietveld method [109] (Paper I) and ii) the investigation of the carbonates crystal polymorphs formed upon carbonation (Paper II and paper III).

Around 1g of the powdered material (sieved at 63 μm) is introduced in a Philips/PANalytical X'Pert Pro-MPD diffractometer with an X'Celerator detector of an incident $\text{CuK}\alpha$ radiation beam by 40 kV and 40 mA to a rotation sample. The specimens are scanned for 40 minutes from $2\theta = 5$ to 65° by a step of 0.25° without protection from CO_2 but in a relatively dry environment (RH~40%). Despite the fact that X-ray diffraction (XRD) is a powerful technique, it can only be used to study crystalline materials and should be coupled to TGA technique that allows for the determination of the dry mass of the specimen.

3.4 Carbonation tests

3.4.1 Natural carbonation

The carbonation depth of concrete and hardened cement paste specimens is determined under natural carbonation at $55\% \pm 5\%$ RH and the ambient CO_2 concentration of the laboratory. The concrete specimens are cast in cylinder molds of 110 mm diameter and 220 mm height. The molds are then stored for 24 hours in a room regulated at 100% relative humidity ($20 \pm 1^\circ\text{C}$ temperature) and demolded afterwards to be immersed in water of ambient temperature (21°C) for a period of 90 days.

The protocol for natural carbonation test is as follows:

- The specimen sections (cylinders of 110 * 220 mm) are sealed with aluminum adhesive to obtain radial carbonation.
- The samples are placed in a relative humidity-controlled room ($55 \pm 5\%$) at a temperature of $20 \pm 2^\circ\text{C}$. The CO_2 concentration is the atmospheric concentration which is around 500 ppm.
- The carbonation depth of these specimens is determined after 1 and 2 years of exposure. At these two periods, the concrete cylinders are sawed to discs of 50 mm height,

split into two parts and phenolphthalein solution is sprayed on the freshly split faces.

- The carbonation depth is given as the average of 16 readings (8 on each face of the specimen).

The carbonation depth of six hardened cement pastes is determined under 55%RH and ambient laboratory CO₂ concentration. After a preconditioning period of 5 weeks in a climate chamber with low CO₂ concentration (soda lime was added inside the climate chamber). The HCPs are exposed to natural carbonation for 5 months. The carbonation depths are determined by phenolphthalein solution once a month. Note that 55% RH is chosen since it is suggested that the most rapid carbonation of concrete occurs at a relative humidity near 50% to 65% (as required also by the accelerated carbonates tests listed in Table 4).

3.4.2 Accelerated carbonation

The carbonation depth of concrete mixes is also determined under accelerated conditions (3% CO₂) over different exposure periods by means of phenolphthalein solution. The concrete specimens subjected to accelerated carbonation, are tested following the protocol described below:

- The cylinders are sawed to discs of 110 mm diameter and 105 mm height.
- The discs are then oven-dried at 45°C for 14 days. The relative humidity inside the oven is lower than 10%.
- After the oven-drying, the discs are cooled at 65±5% RH and 20±2°C for 7 days. The relative humidity is regulated by means of a saturated salt solution of ammonium nitrate.
- The carbonation depth is determined on one sample in order to evaluate the initial carbonation depth after the 21-day long preconditioning period.
- The specimens are stored in a carbonation chamber at 65±5% RH, 20±2°C and 3±0.5% CO₂ concentration by volume.
- Carbonation depths are determined after 28, 56 and 70 days for the concrete C_LS, and 7, 14 and 28 days for concrete C_FA and C_SL (section 3.7). After each carbonation period, three concrete cylinders are taken out of the carbonation chamber and split into two parts. Phenolphthalein solution is sprayed on the freshly obtained faces. The carbonation depth is an average of 10 values measured on the two split faces.

The influence of carbonation on the gas diffusivity and the microstructural properties of the tested materials is investigated after carbonating the materials at 1 vol.% CO₂ and 55% RH (see Paper II). 1 vol.% CO₂ by volume is chosen in order to avoid cracking [52] of the materials and carbonate the samples in a relatively fast time comparing to natural carbonation exposure. The accelerated carbonation is carried out until the pH-indicator is colorless on the specimen surface.

3.5 Synthetic anhydrous and hydrates

In order to enhance the understanding of the carbonation kinetics of anhydrous phases, triclinic tricalcium silicate (C₃S), dicalcium silicate (β -C₂S), and cubic tricalcium aluminate (C₃A), which are the three main non-hydrated phases present in the clinker are prepared. The synthesis of these pure materials is carried out following a modified Pechini process as described in [136]. The advantage of this method is that pure β -C₂S can be formed with no stabilizing impurities.

Table 9 shows the stoichiometric proportions of the synthesized materials used to prepare the anhydrous phases and the heating temperature of each. These materials are first mixed by a wet process in a rotary kiln; oven dried at 150°C, pressed in a cylinder press by 50 g portions and heated gradually for 2 hours until the heating temperature is reached. C₃S phase is metastable at temperature lower than 1100°C and decomposes into dicalcium silicate and lime [136].

The mix is slowly cooled until 1100°C, then rapidly cooled to ambient temperature at 10°C per minute to prevent C₃S decomposition [136]. Finally, these materials are grinded in a planetary crusher and sieved using a 63 μ m sieve. Pure triclinic alite, β -belite and cubic C₃A are thus produced.

	CaO	SiO ₂	Al ₂ O ₃	Heating Temperature
C ₃ S	73.7	26.3	-	1600°C
C ₂ S	65.1	34.9	-	1550°C
C ₃ A	62.2	-	37.8	1350°C

Table 9: Firing temperature and composition of the anhydrous minerals

The main hydrates present in a Portland cement are also prepared: Portlandite (CH), calcium silica hydrates (C-S-H) (C/S ~ 0.9) and ettringite (AFt). The synthesis of ettringite is achieved by mixing 27g of tricalcium aluminate and 51.6 g of gypsum for 4 hours using a wet process, and then the mix is dried at a temperature of 50°C. Pure portlandite is prepared by means of a decarbonation of Calcite at 1000°C, cooling it down to ambient temperature and adding water.

Calcium silicate hydrate with a C/S = 0.9 is synthesized with respect to the proportions shown in Table 10. CaO is obtained from the calcination of Ca(OH)₂ for 4h at 1100°C, SiO₂ comes from hydrophilic silica fume Aerosil 90 ®.

First, the mix is agitated for a month using a magnetic agitator, and then the solid phases are separated from the solution by centrifugation for 2 min at 12000 tours per minute, to be finally oven dried at 45°C under vacuum, slightly grinded and sieved to 63 µm.

C/S	Formula	CaO Mass	SiO ₂ Mass	Water volume
		g	g	mL
0.9	C _{0.9} SH _{1.7}	3.7	4.3	391.5

Table 10 : Amount of reagents to prepare 10 g of C-S-H

The preparation of the materials is carried out using boiled water cooled down at ambient temperature, and all the synthesized minerals are stored in closed bottles inside a chamber under vacuum with soda lime to avoid carbonation during the storage period. Qualitative XRD test is carried out on these phases directly after their synthesis (Table 40 in the appendix), furthermore the initial degree of carbonation of these materials is determined by means of TGA analysis (Paper III). More information about the preparation of these materials can be found in Paper III.

3.6 Hardened cement pastes (HCP)

During this work, nine hardened cement pastes are tested for oxygen-effective diffusion coefficient under different environmental conditions and after different hydration durations. These materials are also characterized using different methods stated previously. Details about the mix design of these materials and the investigations carried out are summarized in Table 11. The oxide composition of the raw materials used to cast the HCP is given in Paper I and Paper II. Note that the replacement of the cement by supplementary cementitious materials is given in mass percentage for all mixes. The W/B ratio is a volumetric ratio for the pastes HD_OPC_W/B, HD_OPC_SF_W/B and HD_OPC_Slag_W/B while it is a mass ratio for the other mixes.

Paste name	Cement type	Addition type and % mass	W/B	Investigations
HD*_OPC_W/B	CEM I	-	1.6 and 1.9 (%vol)	The influence of hydration duration, degree of water saturation, and W/B ratio on D_{e,O_2} .
HD*_OPC_SF_W/B		10% silica fume		The degree of hydration, the degree of water saturation, the pore size distribution and water porosity are determined in the non-carbonated state.
HD*_OPC_Slag_W/B		50% Slag		
PC6	CEM I 52.5 N	-	0.60	The influence of the degree of water saturation and the accelerated carbonation (1 %vol of CO_2) on D_{e,O_2} . Determination of the CO_2 -binding capacity at three RH levels. Determination of the degree of water saturation, the total porosity and the pore size distribution before and after accelerated carbonation.
FA6		30% fly ash	0.60	
SL6		60% slag	0.60	
LS6		40% Limestone	0.60	
SL35	CEM I 52.5 N PM	50% Slag	0.35	
MK45	CEM I 52.5 N	20% Metakaolin	0.45	

Table 11: Tested hardened cement pastes (*HD: hydration duration)

3.7 Concrete

A total of 44 different concrete mixtures are tested to oxygen permeability and diffusivity (Table 13) after drying at 105°C, only 10 concrete mixtures diffusivity is determined at different RH levels.

32 concrete mixtures come from the French project PerfDub (approche **PER**Formantielle de la **DU**rabilité des ouvrages en **B**éton). This project aims at designing on a national scale a methodology for specifying the durability of concrete structures based on performance-based approach specifications to bring together all relevant stakeholders and to make the performance based specifications operational, which is not yet the case today [137]. During

PerfDub project, the durability properties are investigated on concrete mixtures made with several standardized and non-standardized binders, various aggregates (rounded, crushed) with different mineralogy and porosities (Table 12), and considering different compactness (water to binder ratio varying from 0.35 to 0.60) to assess the evolution of the concrete performance with changes in composition. The main objectives of this project can be summarized as:

- Updating existing test procedures (standards, tests under standardization or development), taking into account the influence of materials composition (SCMs, aggregates, etc.).
- Developing new test procedures relevant to the investigations carried out.
- Investigating ageing effect and designing procedures to determine corresponding input parameters.
- Providing a comprehensive database of experimental results on concrete mixtures that comply or not with deemed-to-satisfy provisions.

Table 12 gives information about the different aggregate types used to cast the tested concrete mixtures. It is worth noting that the aggregate mineralogy, shape and porosity are different. The most porous aggregates are G2 and G4 with water absorption of around 2% and 4% respectively.

	G1	G2	G3	G4	G5	G6	G7
Mineralogy	Silica-limestone Alluvial	Silica-limestone Alluvial	Dense limestone	Limestone	Fine : marine Coarse: gneiss	Limestone	Limestone
Shape	Mixed rounded-crushed	Mixed rounded-crushed	Crushed	Crushed	Fine : rounded Coarse: crushed	Crushed	Crushed
Water adsorption	~ 1%	~ 2%	~ 0.6%	~ 4%	~ 0.6%	~ 0.6%	~0.8%

Table 12: Aggregate types of the concrete mixtures from PerfDub project (G1 to G5) and LafargeHolcim concrete (G6 and G7)

Concrete	Total W/B	cement type	cement content (kg/m ³)	Aggregate type	Air (%)	Compressive strength at 28 days (MPa)
1 (C_PC)	0.7	CEM I	280	G2	1.3	43.3
2 (C_FA)	0.7	CEM I + 30% FA	223	G2	1.9	33.3
3	0.6	CEM II/A-LL	280	G2	1	40.0
4	0.6	CEM III/A	280	G2	1.4	36.6
5 (C_SL)	0.8	CEMI + 60%slag	119	G2	1.5	26.4
6	0.5	CEM I + 30% LS	253	G2	2.4	34.4
7 (C_LS)	0.5	CEMI + 41% LS	270	G2	1.5	41.9
8	0.5	CEM II/A-LL	223	G2	1.3	30.6
9	0.6	CEM II/A-LL	161	G2	1.8	31.0
10	0.6	CEM II/A-LL	280	G2	1.5	32.1
11	0.5	CEM I	140	G1	0	49.6
12	0.5	CEM I	347	G1	1.4	57.8
13	0.5	CEM III/A	350	G1	1.8	51.2
14	0.5	CEM II/A-S	347	G3	1.1	56.1
15	0.4	CEM I	316	G1	2	60.0
16	0.5	CEM II/A-LL	363	G1	1	58.8
17	0.5	CEM II/B-S	350	G2	1.2	53.3
18	0.5	CEM II/B-S	342	G5	2.3	45.8
19	0.5	CEM I	386	G1	1.7	44.4
20	0.4	CEM I	189	G1	-	38.8
21	0.5	CEM II/A-LL	363	G1	1.6	39.4
22	0.4	CEM II/A-LL	154	G1	1.3	-
23 (C_SL4)	0.4	CEM I 52.5 N PM	200	G1	-	-
24	0.4	CEM III/A	380	G1	-	-
25	0.4	CEM III/A	370	G1	1.5	-
26	0.5	CEM III/A	371	G1	1.2	65.5
27	0.5	CEM V	369	G4	0.8	49.2
28	0.5	CEM V	369	G3	1	55.8
29	0.4	CEM I	357	G1	1.5	93.5
30 (C_MK)	0.5	CEM I + 20%MK	304	G2	2.5	62.3
31	0.4	CEM I + 20%MK	304	G3	1.9	66.5
32	0.5	CEM I +30% AS	253	G2	1.6	28.3

Table 13: the Perfdub concrete mixtures tested during this thesis project (- : missing information)

The other 12 concretes tested come from internal projects in LafargeHolcim research center (see Table 14 from 33 to 44).

Concrete	Total W/B	cement type	cement content (kg/m ³)	Aggregate type	Air (%)	Compression at 28 days (MPa)
33 (C1)	0.7	CEM I	280	G6	2	37.3
34 (C2)	0.4	CEM III/A	380	G6	2	63.4
35 (C3)	0.65	CEM III/A	280	G6	2	31.6
36 (C4)	0.4	CEM IV/A	380	G6	2	54.5
37	0.4	CEMI + 36% Slag	360	G7	2	92.0
38	0.4	CEMI + 19% Slag	360	G7	2	86.3
39	0.55	CEM I	340	G6	2	34.1
40	0.4	CEM I	380	G6	2	67.2
41	0.4	CEM II/B-LL	380	G6	2	44.9
42	0.65	CEM IV/A	280	G6	2	21.0
43	0.65	CEM I	280	G7	2	31.5
44	0.6	CEM III/A	280	G6	2	28.6

Table 14: The LafargeHolcim concrete mixtures tested during this thesis project

The different investigations carried out on the concrete mixtures shown in Table 13 and Table 14 are explained hereafter.

3.7.1 Concrete mixtures tested to O₂ permeability and O₂ diffusivity

The gas transport property commonly determined and for which the experimental method is standardized is oxygen permeability (K_{O_2}) [133]. Therefore, the oxygen-effective diffusion coefficient and oxygen permeability of a large set of concrete mixtures are compared in order to investigate the correlation between these two transport properties.

Oxygen permeability is determined for 44 concrete mixes cured for 90 days following the French Standards XP P18-463 [133], 32 concretes from Perfdub project, (see Table 13 concrete 1 to 32), and 12 concretes from LafargeHolcim (see Table 14 concrete 33 to 44).

For each concrete mix, three replicates of 50 mm thickness and 15 cm diameter are tested to oxygen permeability after a drying at 105°C. Concrete specimens (33 to 44 in Table 14) are cored into discs of 11 cm diameter to be tested to oxygen diffusivity. The specimens from concrete 1 to 32 are sawed from 11 cm diameter and 22 cm height concrete cylinders. These specimens are gradually dried: first at 50% RH, 50°C, 80°C and finally 105°C, until water

equilibrium criteria is reached: the mass variation of the specimens within a week is lower than 0.05%. 24 hours prior to the oxygen-effective diffusion and oxygen permeability tests, the concrete specimens are placed inside a desiccator under vacuum for 24h to 48h in order to cool down to room temperature without mass gain. Note that the specimens are gradually dried in order to minimize drying-induced microcracking.

3.7.2 Concrete mixtures used to investigate the influence of the specimen thickness on D_{e,O_2}

An experimental campaign is carried out on four concretes in order to study the influence of concrete specimen thickness on gas diffusivity (concretes C1, C2, C3 and C4). The concrete specimens are sawed to different thicknesses and tested to oxygen diffusivity. 2% air content is measured for these four concretes. The specimens' diameter is sawed from 220 mm height and 110 mm diameter cylinder. In order to collect statistical representative data, for each concrete mix, nine discs of 5 mm and 10 mm thickness are sawed and tested to oxygen diffusivity after preconditioning at 93% RH, and at the dry state (after oven-drying at 105°C). Three discs of 50 mm thickness that respect the criteria of a thickness of two times the minimum cover thickness [138] are also tested to oxygen diffusivity but only at the dry state. Moisture equilibrium of these specimens is supposed to be reached when the mass variation within a week is lower than 0.05%.

3.7.3 Concrete mixtures tested to the influence of accelerated carbonation on D_{e,O_2}

Six concrete mixes are chosen from PerfDub project in order to investigate the influence of the degree of water saturation on the oxygen-effective diffusion coefficient under both non-carbonated and carbonated states (accelerated carbonation 1 vol.% of CO₂). These concretes are sawed to 1 cm thickness (in order to test and precondition the specimens at different RH levels in a reasonable time) from cylinders of 110 mm diameter and 220 mm height. The tested concretes are:

- C_PC (concrete 1 in Table 13), C_FA (concrete 2 in Table 13), and C_SL (concrete 5 in Table 13) are cast using the same CEM I, at the same water-per-binder ratio but with different additions types. Therefore, the influence supplementary cementitious materials on the oxygen-effective diffusion coefficient can be investigated. C_PC and C_FA are in accordance with the standards NF EN 206-1 [139], while C_SL is not in accordance with the standards [139] since it contains a high proportion of Slag (60%, i.e. higher than standard limit of 50% slag [19]).

- C_LS (concrete 7 in Table 13) is chosen to investigate the influence of a higher limestone replacement (than recommended by the standards NF EN 206-1 [139]) on the oxygen-effective diffusion coefficient.
- C_SL4 (concrete 23 in Table 13), and C_MK (concrete 30 in Table 13) are mixes of interest to investigate the carbonation performance of a low water-per-binder ratio concretes.

IV. Chapter IV: Main results

In the following chapter, we present in details the gas diffusivity and CO₂ binding capacity test methods developed during the framework of this thesis work and analyze the reliability and detection limit of these experimental techniques. Results on the influence of different parameters such as the relative humidity of preconditioning, the material composition, hydration duration, carbonation... on the D_{e,O_2} are presented. The CO₂ binding capacity of the synthetic anhydrous and hydrates and HCP is determined at different RH levels.

4.1 Gas diffusivity of cementitious materials

4.1.1 Test method

i) The design of the diffusion cell

Gaseous carbon dioxide-effective diffusion coefficient is a property of high interest regarding the carbonation performance study of cementitious materials. Since so far, there is no standardized test method to determine this property, we designed and developed a new equipment to determine the gas diffusion coefficient of hardened cement pastes and concrete specimens. The main specifications set to design the diffusion test equipment are as follows:

- The diffusing gas must be safe and inert with most of the hydration products in order to avoid alteration of the microstructure during the test itself.

Therefore, atmospheric oxygen is chosen as the diffusing gas mainly because it is non-reactive with the hydration products. Moreover, the use of an oxygen bottle is avoided, which is convenient for practical reasons and helps avoiding safety problems. The CO₂-effective diffusion coefficient can be deduced from that of oxygen using a simple model developed originally by Thomas Graham [140]. This model validity has been confirmed several times [98].

- The test method must be easy to perform with minimum equipment.

Instead of using two diffusion cells as stated in the literature (see Table 5 and 6), a half diffusion cell is designed and used as a “downstream chamber”. The “upstream chamber” in our case is the climate chamber inside which the diffusion tests are carried out.

- The test method must allow for the determination of the gas diffusion coefficient under different environments.

The inside volume of the diffusion cells is minimized in order to avoid drying of the samples during the diffusion tests. Indeed, the mass variation of the tested specimens is determined after each diffusion test and found to vary by no more than 0.02%. The climate chambers inside which the diffusion tests are carried out are regulated at the same relative humidity level under which the tested specimens are preconditioned.

- The analysis of the experimental results must take into consideration the transient regime.

The raw data are accumulation curves of the gaseous oxygen that diffuses from the atmosphere through the tested specimen inside the cell. These curves are analyzed using an automatic tool that fits the data to Fick's second law of diffusion taking into account both the transient and steady states (see paper I).

- The test must be cost-effective and timesaving.

Regarding the tested specimens, thin specimens are tested which allows for preconditioning and testing the diffusivity in a reasonable time. The tested method is developed using low-cost but efficient equipment.

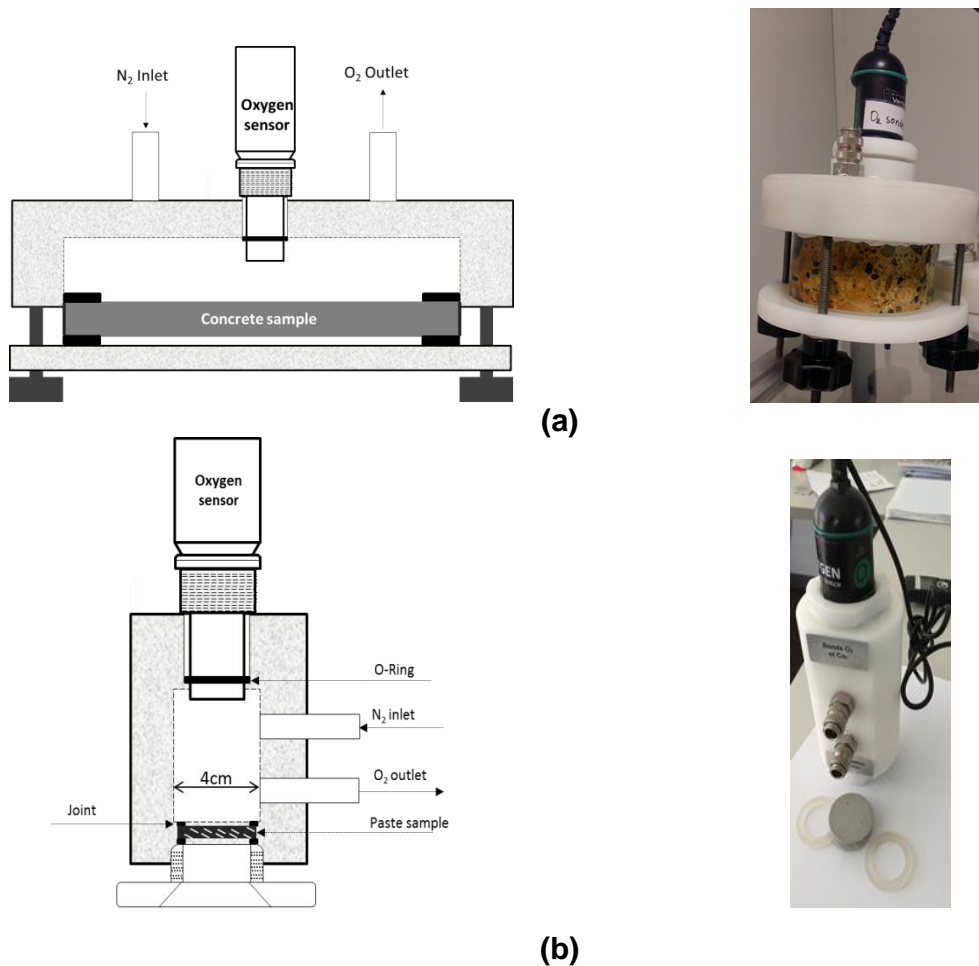


Figure 12: Diffusion cells sketches and photos (a) concrete diffusion cell and (b) hardened cement pastes diffusion cell

Figure 12 shows the diffusion cells designed in order to satisfy all the specifications stated above. More details about the test method can be found in Paper I and [141]. Table 15 gives information about the diffusion cells geometry. This geometry is determined to minimize the internal volume because a large diffusion volume may cause drying of the sample during the test. Moreover, the volume of the upstream chamber inside which the diffusion cell is placed is 200 to 571 times bigger than the inside volume of the diffusion cells, therefore the oxygen concentration variation inside the climate chamber is negligible.

	Internal diameter (mm)	Internal length (mm)	Total volume (ml)
Cement paste cell	44	45	68
Concrete cell	110	22	209

Table 15: Geometry of the diffusion cells

Note that during this work, the tested hardened cement pastes diameter is 40 mm and thickness is 3 ± 0.5 mm, while the tested concrete specimens have a diameter of 110 mm and a thickness that varies between 5 mm and 50 mm (the influence of the concrete thickness on the

determined diffusivity is discussed in the following section 4.1.3 i).

ii) Test method protocol and validation

The tested sample (concrete or hardened cement paste) is placed between two rubber joints and placed in the down part of the diffusion cell (see Figure 12). In the case of cement pastes, the sample is tight against joints by screwing. In the case of concrete sample, clamping is done by threaded rods. At the beginning of each test, the diffusion cell is flushed with nitrogen for a short period of 30 seconds with a slow rate and placed inside a relative humidity-controlled chamber. One face of the sample is then exposed to the internal volume of the cell filled with nitrogen and the other face to the relative humidity-controlled air of the upstream chamber which creates the concentration gradient of oxygen. Therefore, oxygen diffuses successively through the sample into the cell where O₂ concentration is monitored by a gas sensor (Vernier ©). When the steady state is reached (i.e. when O₂ concentration reaches 20%), the experiment is stopped and an accumulation curve (O₂ concentration vs. time) is collected.

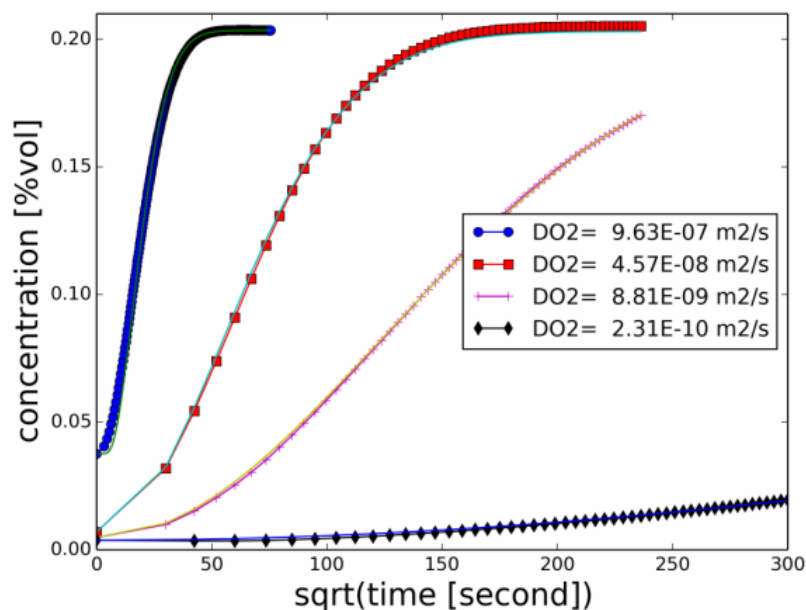


Figure 13: The fit of the raw experimental data of the oxygen-effective diffusion coefficient test method

As seen in Figure 13, O₂-effective diffusion coefficient (D_{e,O_2}) is determined by fitting Fick's second law of diffusion to the data of the accumulation curve by least square method (see Paper I). The tests are performed at a temperature of $20 \pm 1^\circ\text{C}$ under atmospheric pressure. Table 16 gives information about the reliability, measurement range, time, and conditions of the test method. The repeatability coefficient shows to what extent the absolute difference between two measurements on the same sample would differ in 90% of the occasions. The coefficient of variation varies between 15% for hardened cement pastes to 26% for concrete

(average value).

	Hardened cement paste cell (Figure 12 (b))	Concrete diffusion cell (Figure 12 (a))
Repeatability coefficient	7% to 10%	Not investigated
Coefficient of variation	15%	26%
Testing time	30 min to 4 weeks	30 min to 3 days
Preconditioning time	2 days to 5 weeks	3 days to 6 months
Measurements conditions	Ambient temperature and pressure, relative humidity level lower than 93% (O ₂ sensor working conditions)	
Measurement range	10 ⁻¹¹ to 10 ⁻⁶ m ² /s	

Table 16: Summary of the main information about the O₂ diffusion test method

It is worth noting that the long test period of 4 week was only reached for one HCP made with 10% silica fume replacement, hydrated for two months and preconditioned at 93% RH. Note that the coefficient of variation is higher for concrete specimen mainly because of the effects of heterogeneity of this material which results in a non-homogenous water distribution in the concrete porous network which directly affects the oxygen diffusivity. Another way is used to describe the data of the variation coefficient of D_{e,O_2} using the box plot (or whisker diagram) as shown in Figure 14. This way, we can display the full range of variation (from min to max), the likely range of variation (the inside of the box), and a typical value (the median) [142] at each preconditioning state (from dry to 93% RH).

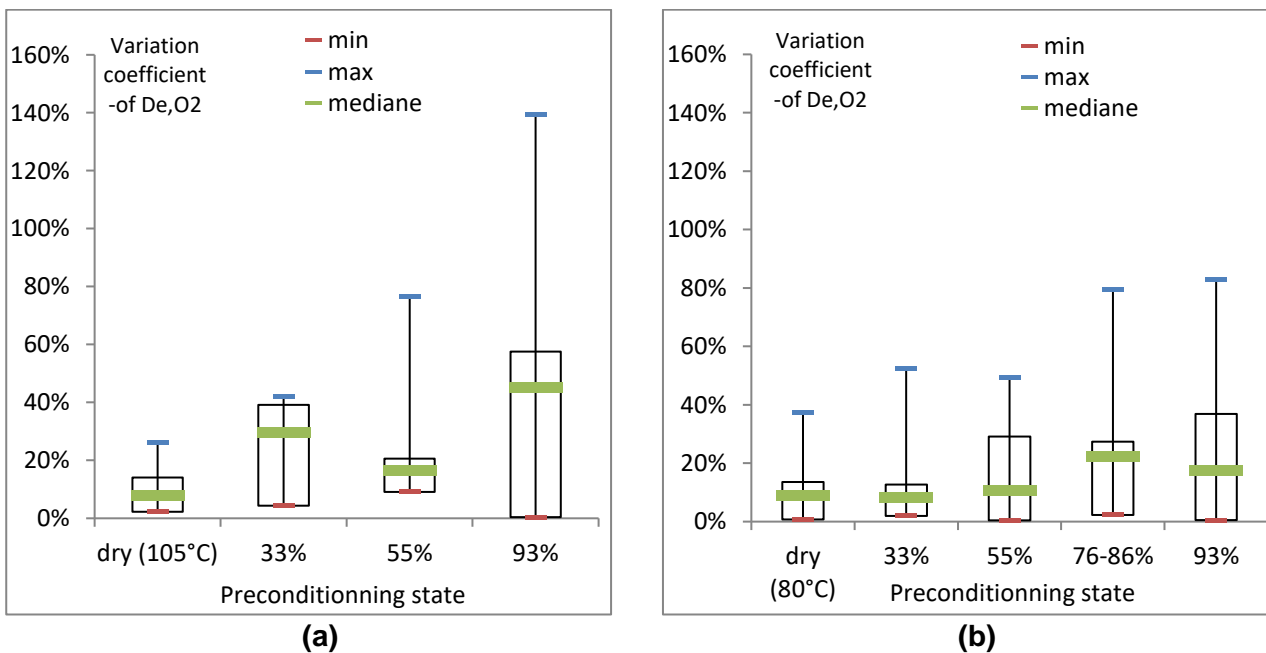


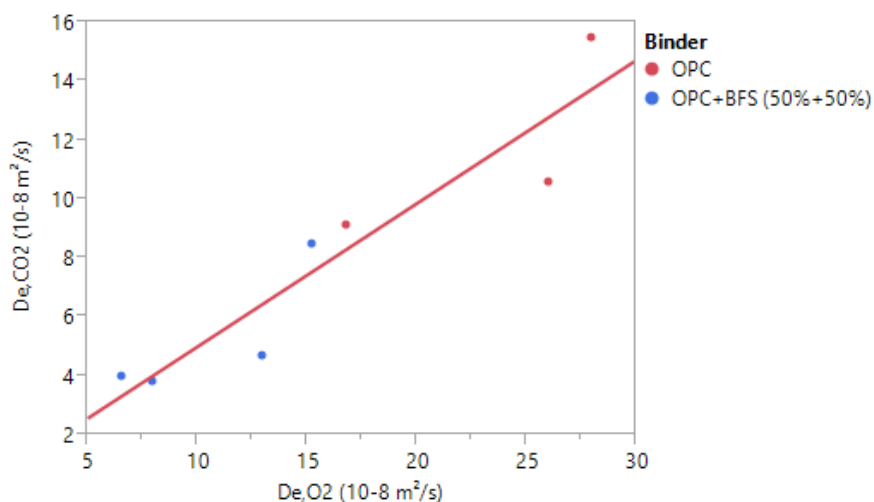
Figure 14: Box plots of the coefficient of variation corresponding to concrete specimens (a) oxygen-effective diffusion coefficient determined for different preconditioning environments for HCPs (b)

Figure 14 (b) shows box plots, each corresponds to datasets of the variation coefficient of experimentally determined diffusion coefficients after preconditioning the specimens at 5 states: oven-dried (105°C), 33%RH, and 55% RH, between 76% and 86% and 93% RH. For each respective category, we have the following amounts of data for concrete (Figure 14 (a)): 32, 11, 9 and 26, and for HCP (Figure 14 (b)): 18, 30, 26, 24 and 21.

The spacing inside each box indicates the degree of dispersion of the variation coefficient, which clearly depends on the preconditioning state. The average value of the coefficient of variation varies from 9% at the dry state to 48% when the concrete specimen is preconditioned at 93% RH. Note that the preconditioning period (due to the mass equilibrium criteria < 0.05% within a week) could also result in a higher scatter of the data.

iii) CO₂ diffusion coefficient vs. O₂ diffusion coefficient

In the framework of this thesis work and Gendron's thesis [89], an inter-laboratory comparison was carried out on the same hardened cement pastes. These materials are first tested to oxygen diffusivity using the experimental setup developed during this thesis work, and then the CO₂-effective diffusion coefficient of the same specimens is determined using the experimental setup developed in La Rochelle University by Namoulniara first [88], and improved later by Gendron [89]. The HCP tested are: 8M_OPC_1.9, 8M_OPC_1.6, 8M_OPC_Slag_1.6 and 8M_OPC_Slag_1.9 (see Table 11). The discs are gradually dried in the oven at 80°C until constant mass, tested to oxygen diffusion using our experimental setup, and then they are sent by post to La Rochelle University to be tested to CO₂ diffusivity. Before CO₂ diffusion tests, the specimens are re-dried at 80°C to obtain as much as possible the same hydric state than before O₂ diffusion tests.



$$D_{e,CO_2} = 0,14 + 0,5 * D_{e,O_2} , R^2 = 0.9$$

Figure 15: CO₂-effective diffusion coefficient vs. O₂-effective diffusion coefficient [90]

Figure 15 compares the O₂ and CO₂-effective diffusion coefficients. These coefficients display a linear relationship, with D_{e,CO_2} lower by a factor of 2 than D_{e,O_2} . This linear relationship is of high importance. It proves that the CO₂-effective diffusion coefficient can be deduced from that of oxygen. Therefore, the direct determination of O₂ diffusivity of partially water-saturated materials allows the calculation of the CO₂ diffusivity, which cannot be measured directly on these materials.

However, the correlation factor which corresponds to the ratio D_{O_2}/D_{CO_2} is higher than the expected ratio of 1.17, i.e. the squared ratio of molar masses $(M_{CO_2}/M_{O_2})^{1/2}$. Note that this ratio is only valid when the Knudsen regime is predominant. Regardless of the fact that the experimental setups are different, and a possible damage may occur during the transport of the specimens and their re-drying at 80°C, one explanation of this difference could be the possible and slight carbonation of the specimen during the CO₂ diffusion test itself which is performed using 10% CO₂ in upstream (although specimens are dried at 80°C). As seen from the results in (Paper II and section 4.1.2 iii)), the accelerated carbonation of CEM I hardened cement pastes at 1% CO₂ causes a decrease in the oxygen diffusivity for relative humidity levels lower than 55%. Note that Gendron's [89] experimental setup is equipped with a manometer in both compartment to avoid pressure variation between both chambers, while our half diffusion cell is not equipped with a manometer (although the inlet and outlet of the diffusion cell are designed to avoid overpressure in the cell). A pressure gradient could result in the higher D_{e,O_2} values. Still, the correlation between the two test methods results is promising.

In this context, we cite the previous works of Leemann et al. [91] who compared the non-steady state diffusivity of O₂ and CO₂ of carbonated CEM I mortars and found that the CO₂ diffusion coefficient is 1.37 lower (instead of 1.17).

The effective diffusion coefficient of oxygen is greater than that of CO₂ [143]. Similarly, the effective diffusion coefficient of H₂ is higher than that of xenon Xe [9]. The explanation lies in the difference in size of the atomic radius. A larger radius limits the diffusion of gas into the porous network of cementitious materials.

Before any definite conclusion can be made, new inter-laboratory tests must be carried out for a large set of materials (cement pastes, mortars, concretes...).

4.1.2 Hardened cement pastes diffusivity

i) Influence of the hydration duration and degree of water saturation on D_{e,O_2}

Figure 16 shows the influence of the degree of water saturation on the oxygen-effective diffusion coefficient of three hardened cement pastes hydrated at 100% RH for three periods (S = 1 day for OPC and S = 7 days for other HCPs, 2M = two months and 8M = eight months for all HCPs). All hardened cement pastes are cast at a constant volumetric W/B ratio of 1.6. Details about the specimens' preparation and mix design can be found Table 11 and in paper I. Note that each data point shown in Figure 16 is an average of the oxygen-effective diffusion coefficient of three replicates.

At 7 days of hydration, samples with silica fume are found to be 9 times less diffusive than Portland cement pastes and 4 times less diffusive than slag pastes. This could be due to the extreme fineness of silica fume that densifies the microstructure, which increases the water retention capacity, leading to a slower transport of oxygen through the sample [141] (Paper I).

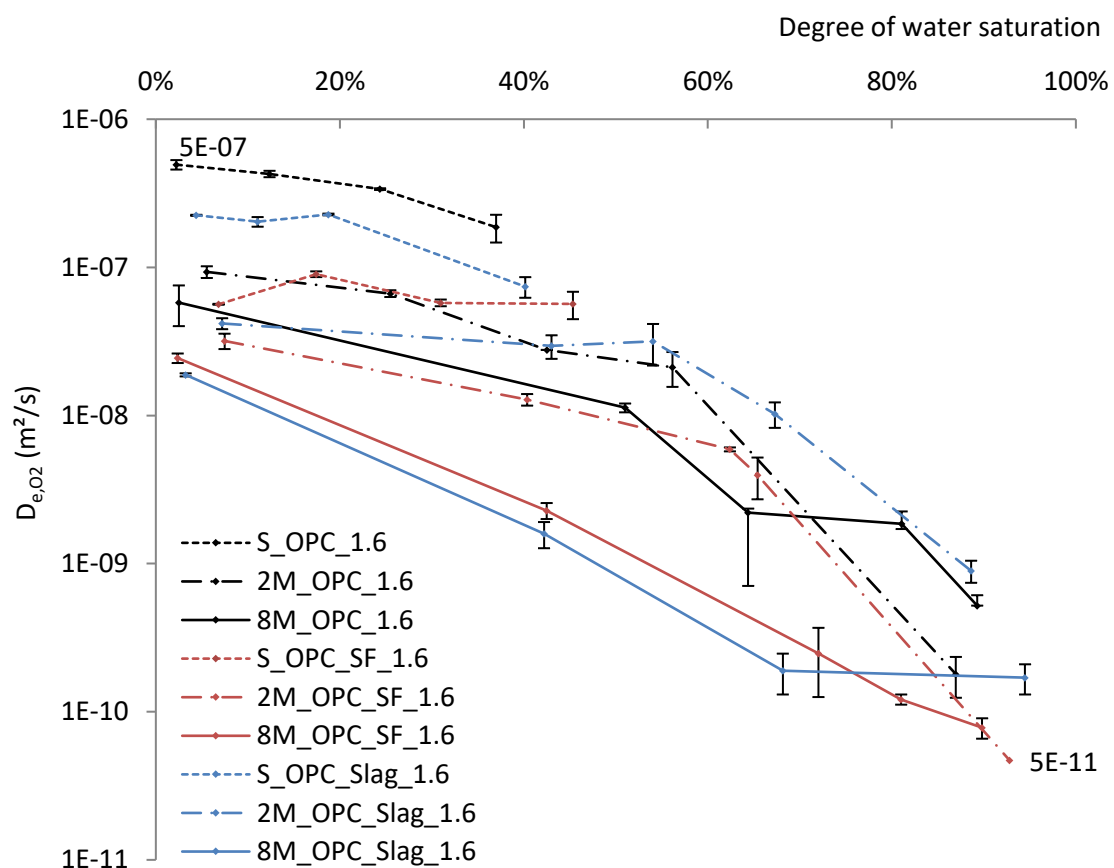


Figure 16: Influence of hydration duration and degree of water saturation on the hardened cement pastes' oxygen-effective diffusion coefficient (100% RH storage durations: S=1 day for OPC and S=7 days for the two others HCP, 2M = two months and 8M = eight months for all HCP)

The results in Figure 16 state that the hydration duration is a property that highly impacts the oxygen-effective diffusion coefficient.

D_{e,O_2} of HCP hydrated only for 1 day (OPC) and 7 days (OPC_SF and OPC_Slag) is only slightly dependent on the degree of water saturation and varies only by a factor of 3.5 at the most in the degree of water saturation range from 0% to 40%. However, once the same HCPs are hydrated for 2 months D_{e,O_2} is found to vary over three orders of magnitude with the degree of water saturation of the tested specimens. Even after 8 months of hydration D_{e,O_2} continues decreasing with the degree of water saturation. This is mainly observed for samples with slag and silica fume, as the reaction of SCMs is generally slower than the hydration reaction of Portland cement and requires longer periods of hydration. It is also worth noting that the three tested HCP behave differently regarding the oxygen-diffusivity even when hydrated at the same duration.

ii) Influence of the water-per-binder ratio on D_{e,O_2}

The influence of the water-per-binder ratio on the oxygen-effective diffusion coefficient is investigated on three HCP mixes by varying the volumetric W/B from 1.6 to 1.9 (see Table 11). The diffusion coefficient increases with the increase of the W/B by half to one order of magnitude, depending on the binder type (Paper I). This result is expected as an increase in the W/B results in an increase in the total porosity by around 3% at three hydration durations (Paper I).

iii) Influence of accelerated carbonation on D_{e,O_2}

The influence of accelerated carbonation (tests carried out at 55 %RH and 1 vol.% CO_2 concentration) is investigated on six HCP (Table 11). Figure 17 shows that accelerated carbonation has a different impact on each HCP and at each relative humidity of preconditioning. When the tested specimens are preconditioned at 33% and 55% RH, the D_{e,O_2} decreased after carbonation of PC6 and SL35 by a factor of 4.5 at the most, while for the other HCP D_{e,O_2} increased by a factor of 1.1 for LS6 and 10 for SL6 previously conditioned at the same relative humidity levels.

At the highest relative humidity level (93%), it is noticed that carbonation induced a high increase in the oxygen-effective diffusion coefficient of the all specimens. D_{e,O_2} increased by a factor of 2.5 for SL35 to three orders of magnitudes for FA6.

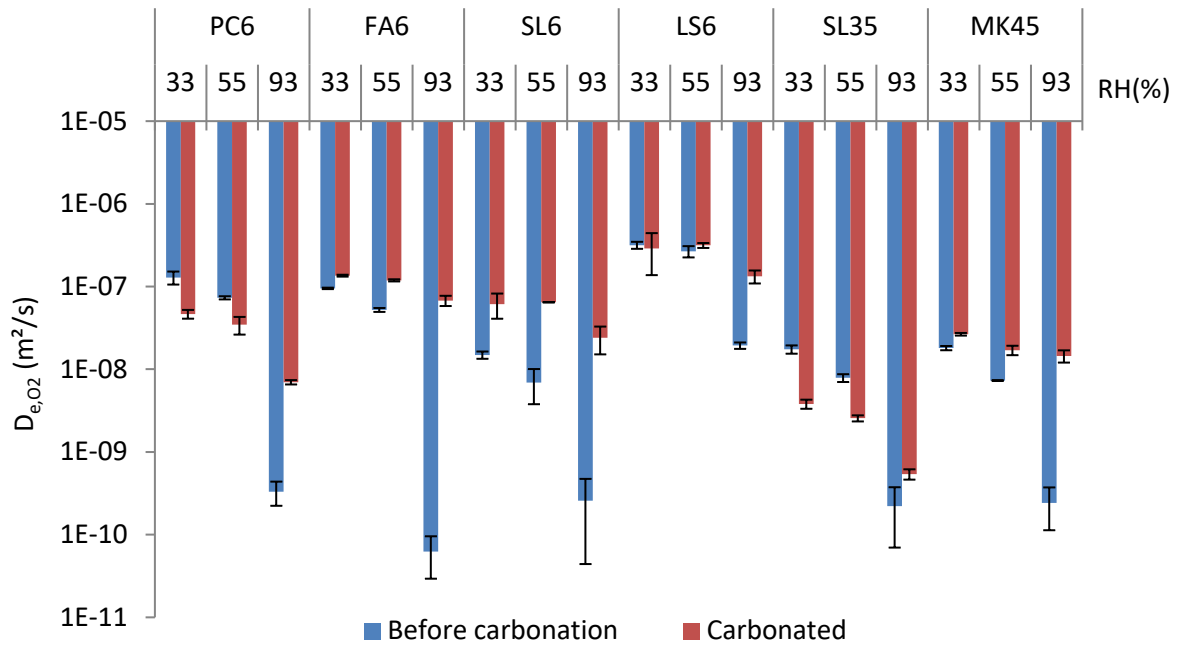


Figure 17: Influence of accelerated carbonation (1% CO₂) on the oxygen-effective diffusion coefficient of six HCPs after preconditioning at three relative humidity levels: 33%, 55%, and 93% RH

In order to deepen the understanding of the influence of accelerated carbonation on the oxygen-effective diffusion coefficient, the degree of water saturation after preconditioning at the three relative humidity levels is determined before and after carbonation of all the HCP using the protocol described in the section 3.2. Note that these values are determined in the desorption way for all the specimens. Figure 18 shows that carbonation caused a significant decrease in the water retention capacity especially at 93%RH, this result is in line with the decrease of D_{e,O_2} upon carbonation, since a high degree of water saturation hinders the transport of gases through the cementitious materials porous network (Paper I)[52][9].

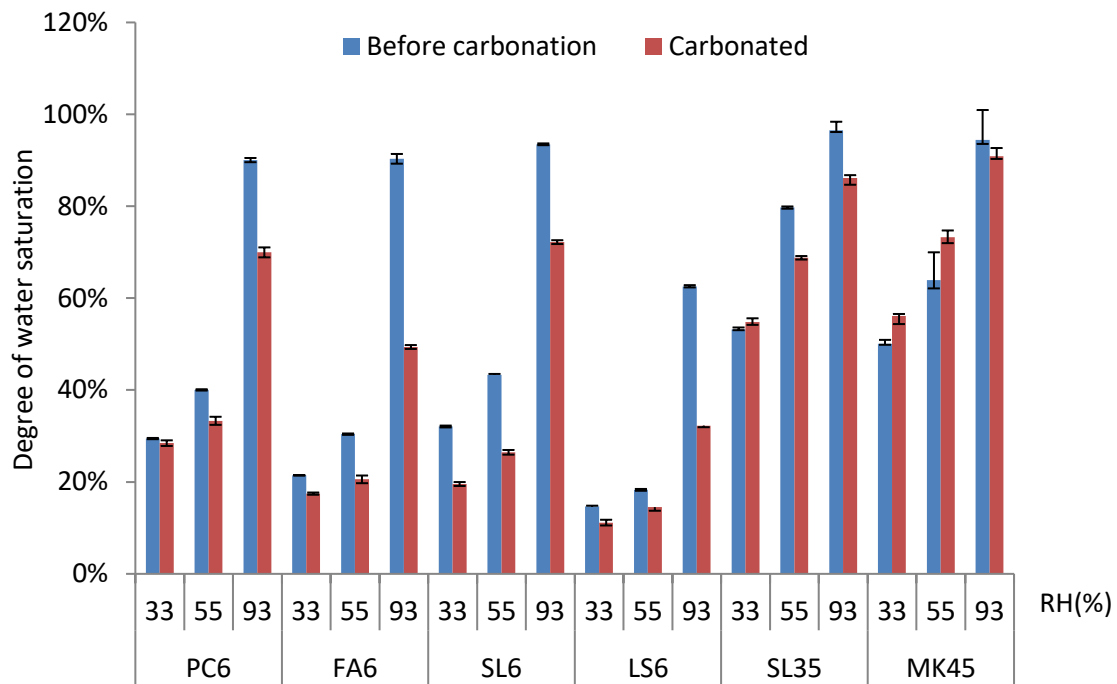


Figure 18: Influence of accelerated carbonation (1% CO₂) on the water saturation degree of six HCP

The degree of water saturation only slightly decreased upon carbonation for PC6 and SL35 when preconditioned at 33% and 55% RH, while it decreased by 13% for SL6 at these RH levels which explains partially the higher diffusivity of these materials at these RH. However, MK45 diffusion performance after carbonation is not completely in line with the S_i change upon carbonation: at 33% and 55% relative humidity the degree of water saturation of MK45 increased by 6% and 9% respectively, while the oxygen-effective diffusion coefficient increased by a factor of 1.4 and 2.3. At 93%RH, carbonated MK45 samples are only 3% less water saturated than non-carbonated specimens, but the diffusion coefficient of carbonated samples is almost two orders of magnitude higher. The latter could be due to cracking induced by accelerated carbonation.

The total porosity is also determined before and after carbonation of the HCP following the test protocol described in section 3.2, the results are given in Paper II. Accelerated carbonation caused a decrease in the total porosity for all HCP by a factor that varies from 6% to 12% depending on the binder type. The pore size distribution of these HCP and their composition variation upon carbonation are also investigated (Paper II).

iv) Influence of the pore size distribution on D_{e,O_2}

During this thesis work, the pore size distribution of all HCP specimens tested to oxygen-diffusion (124 specimens) is investigated using mercury intrusion porosimetry. MIP results are analyzed using an automatic tool that allows for the fitting of the data assuming that each

mode is of a normal distribution (Figure 19). This tool gives the mean pore diameter of each mode and its corresponding volumetric fraction. From these two values, we calculated a weighted average of the pore entry diameter for each HCP (denoted d_m). Note that the number of modes of each MIP data is chosen in order to optimize the fit. Table 39 gives the values of the pore entry diameters and their volumetric fractions for all HCP.

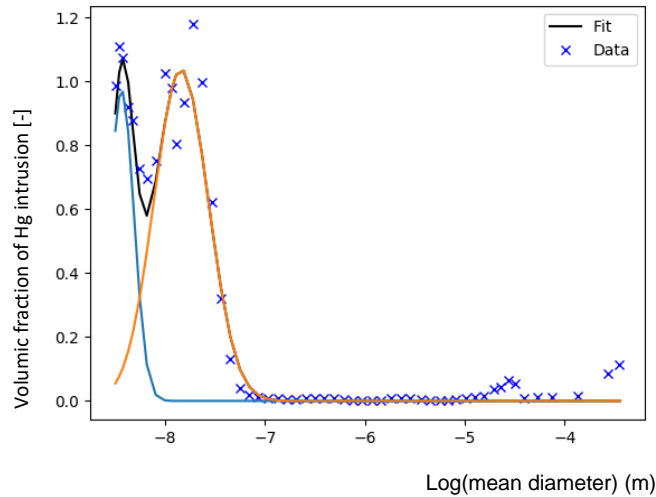


Figure 19: An example of MIP data automatically fitted

The mean pore entry diameter d_m is compared to the effective-diffusion coefficients determined experimentally on the HCP at different degrees of water saturation. The oxygen-effective diffusion coefficient is corrected by the total porosity (ϕ) and the degree of water saturation (S_l) of the tested samples. This correction is made in order to consider that the transport process is made only through the gas filled pores. The so-corrected diffusivity, i.e. $D = D_{e,O_2} / (\phi(1-S_l))$, is usually calculated using the so called “form factor” ($\phi(1-S_l)$) depending on parameters such as the tortuosity (see section 2.2.1). As seen in Figure 20, a good correlation between this diffusion coefficient and d_m of the hardened cement pastes is observed when the degree of water saturation S_l is lower than 30%. The data are much more scattered when the degree of water saturation is higher.

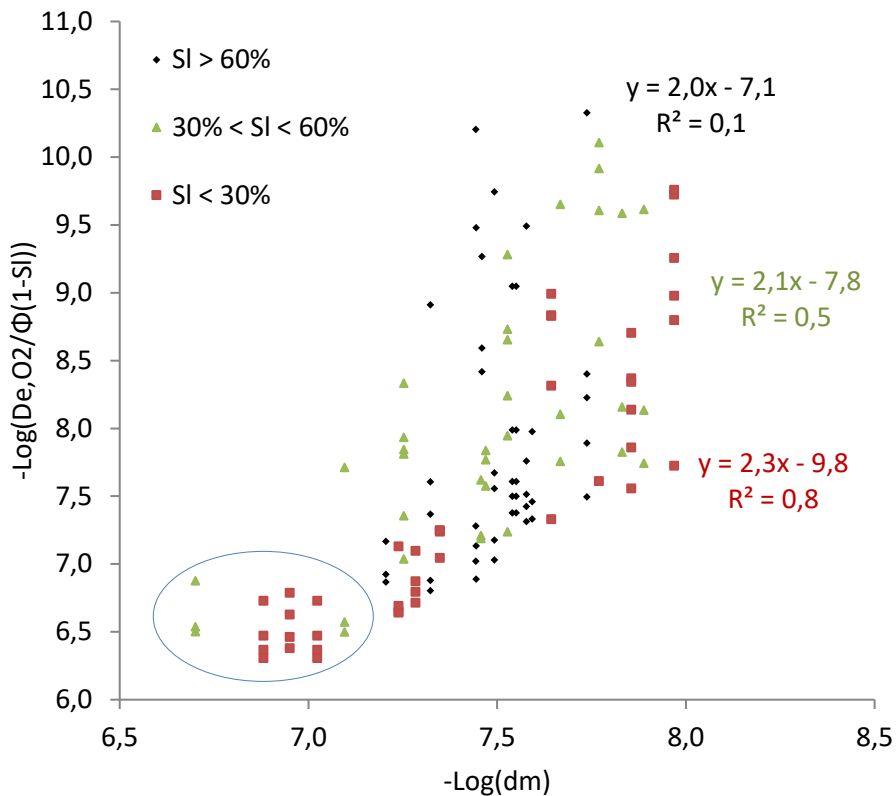


Figure 20: Oxygen-effective diffusion coefficient vs. the mean weighted pore diameter of the HCP in log scale

This result could present a first step towards an investigation that allows relating the gas-diffusivity of cementitious materials to their microstructure. The water content of the cement paste and its pore size distribution are key properties to predicting gas-diffusion coefficients. As seen in the section 1.1.1, under Knudsen diffusion (i.e. when the $K_n > 10$) the gas diffusion coefficient is proportional to the mean pore diameter, which indicates that the gaseous oxygen diffusion is under Knudsen regime when the degree of water saturation is lower than 30%. It is also worth noting that the linear correlation between D_{e,O_2} and d_m in log-scale is more pronounced when d_m is lower than 72 nm (which corresponds to the means free path of the gaseous oxygen), i.e. when $-\log(dm)$ is lower than 7 (see blue circle in Figure 20).

It has to be noted that all diffusion coefficients data were obtained on partially saturated and dried samples, whereas the MIP data were performed on the samples dried at 45°C. That is why the correlation of the diffusion coefficient with porosity parameters can be distorted especially at higher degrees of water saturation.

4.1.3 Concrete diffusivity

i) Influence of concrete specimen thickness on D_{e,O_2}

Usually, when concrete transport properties are experimentally determined, common practice

is to test specimens with a thickness three times higher than the maximum aggregates size present in the concrete, or two times the minimum cover thickness (50 mm) [138]. These specimens are assumed to be representative of the structure's property of interest. Nevertheless, some researchers even suggest that a thickness of at least ten times the maximum aggregate size is required to measure a reliable value of the transport property [144] (according to [138]). A major limit of testing this kind of concrete specimens is the fact that it requires very long periods of time to reach water equilibrium [145]. Indeed, as seen in Figure 21, the diffusion time is proportional to the square of the thickness of the tested specimen: testing specimen with 50 mm thickness is 100 times more time-consuming than specimens with 5 mm thickness.

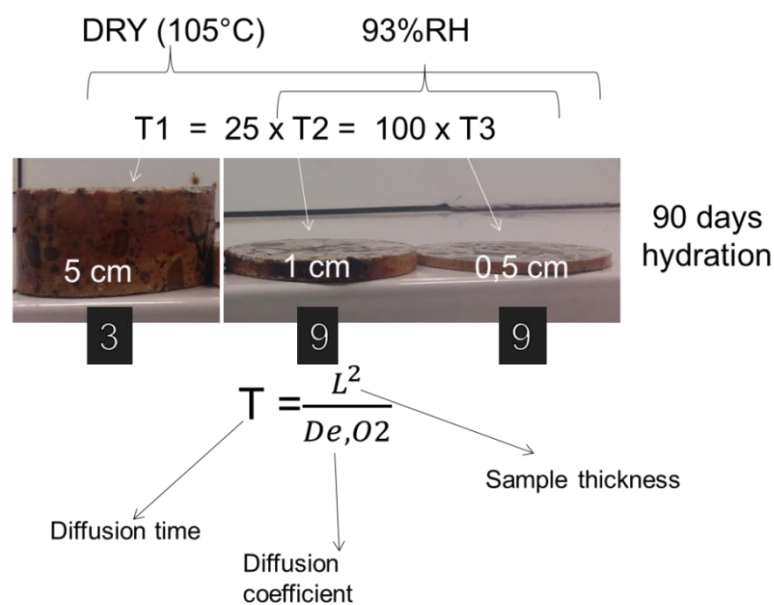


Figure 21: Sketch of the experimental program carried out to investigate the influence on concrete specimen thickness (T1, T2, T3 are the diffusion times required for concrete specimens with a thickness of 50mm, 10mm and 5mm respectively)

Figure 22 displays how the oxygen-effective diffusion coefficient varies with the concrete specimen thickness for four different concrete types dried at 105°C and preconditioned at 93% RH. The vertical error bars present one standard error of the nine measured $D_{e,O2}$ for 5 mm and 10 mm thick samples and for three $D_{e,O2}$ values of 50 mm discs. It can be seen from these results that oxygen diffusivity increases slightly with the specimen thickness for different concrete mixes (by a factor of 2.6 at the most). These results indicate an opposite trend as to that which was expected. Note that $D_{e,O2}$ decreases by up to three orders of magnitude (concrete C4) when the concrete specimens are preconditioned at 95% RH.

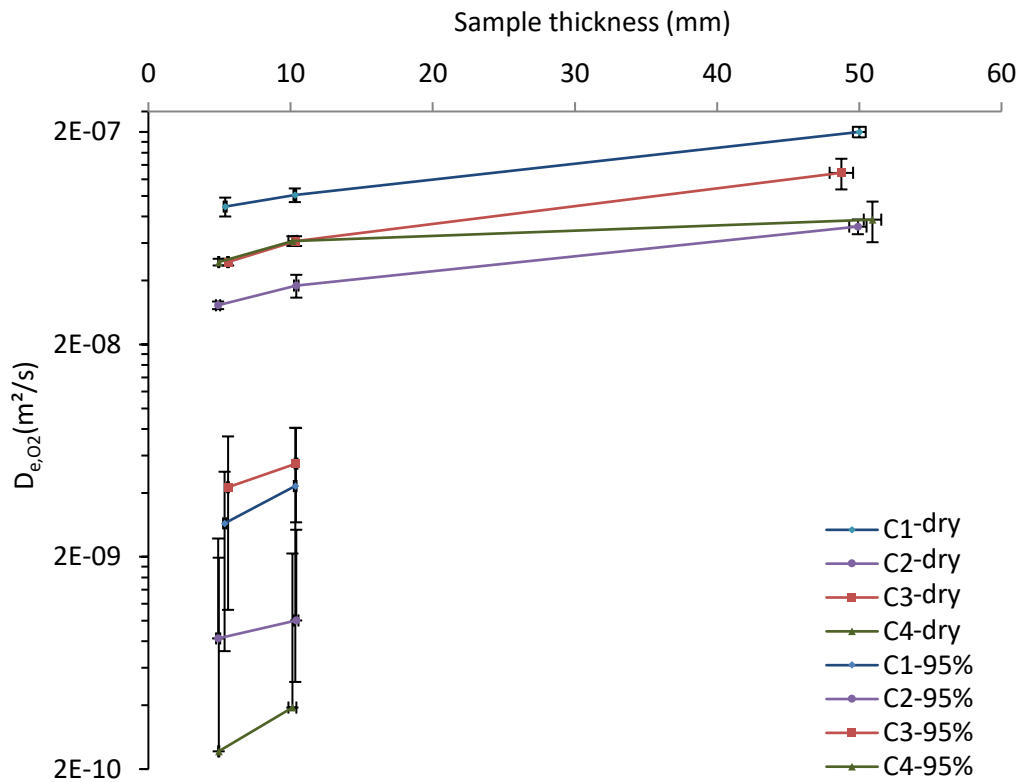


Figure 22: The effect of concrete specimen thickness on oxygen-effective diffusion coefficient

For dry specimens, the gas diffusivity variation with the concrete thickness could be a result of drying-induced microcracks at 105°C. Indeed, the thermal gradient during oven-drying is lower for thin samples, which could lead to a lower thermal stress in these samples hence less damage/cracks would appear on thin samples. In order to verify the assumption of cracking induced by thermal gradient, specimens of the concrete C₂ are impregnated under vacuum at 200 mbars for 24 hours with a fluorescent resin and their cross section illuminated with an ultra-violet lamp (Figure 23). The obtained images contradict the possible explanation of thermal cracks. Thin samples appear to be more damaged than 50 mm thickness samples, although no clear cracks are seen. It should be noted that this technique is usually used to investigate materials more porous than concrete.

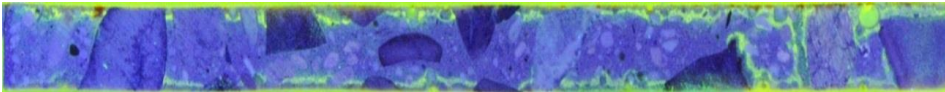
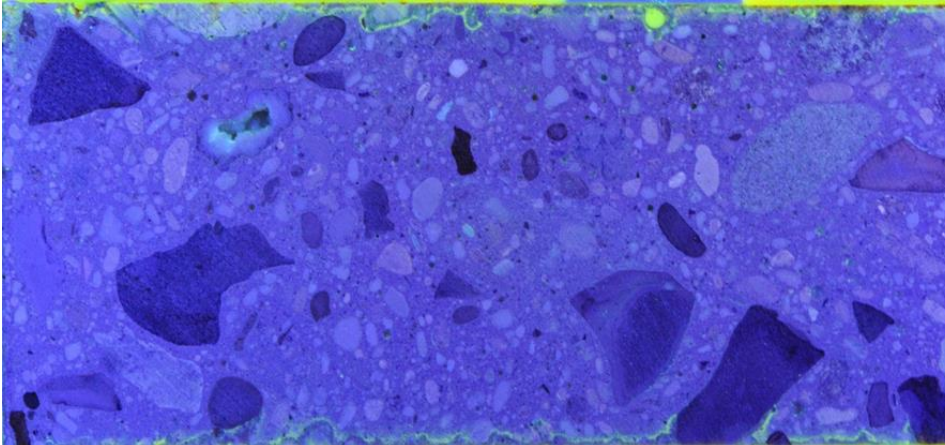
Thickness	D_{e,O_2} (m^2/s) at the dry state	Cross-section image
8 mm	$3 \cdot 10^{-8}$	
50 mm	$7 \cdot 10^{-8}$	

Figure 23: Cross-section of the impregnated concrete sample imaged with a microscope under UV lighting

As seen in Table 17, the total porosity of concretes C2, C3 and C4 slightly increases with the specimen's thickness. This could be due to the binder content in each disc. This content is higher for 50 mm thickness samples. Higher binder content not only leads to a higher total porosity but could also lead to a higher connectivity of the porous network, hence higher gas diffusivity. This could be an explanation to the results observed in Figure 22. Indeed Winslow et al. [146] found a sudden increase in the total porosity when the volumetric fraction of sand in mortars goes from 44.8% to 48.6%. They explained these results by the interconnectivity of the interfacial transition zones around the aggregates which varies from 15 to 20 μm . The aggregate volume fraction of the four tested concrete mixtures is 70%, however the aggregate volume fractions in thin specimens (5 mm and 10 mm) and 50 mm thickness specimens may be different.

Concrete number	Thickness (mm)	Water porosity (%)	Average Diffusion coefficient at dry state (m ² /s)	Average Diffusion coefficient after preconditioning at 93% RH (m ² /s)
C1	5.4	14.4	9.5·10 ⁻⁰⁸ (CV = 14%)	6.0·10 ⁻⁰⁹ (CV = 30%)
	10.3	13.7		
	50.0	14.1		
C2	4.9	11.0	3.9·10 ⁻⁰⁸ (CV = 5%)	2.8·10 ⁻⁰⁹ (CV = 55%)
	10.4	11.2		
	49.9	11.4		
C3	5.6	13.3	5.5·10 ⁻⁰⁸ (CV = 13%)	5.3·10 ⁻⁰⁹ (CV = 15%)
	10.4	14.4		
	48.7	14.6		
C4	4.9	11.1	4.0·10 ⁻⁰⁸ (CV = 12%)	2.1·10 ⁻⁰⁹ (CV = 57%)
	10.1	11.8		
	50.9	12.3		

Table 17: Concrete gas diffusivity, water porosity and coefficient of variation (CV) under two environmental conditions

As seen in Figure 22 and Table 17, the averaging error for specimens preconditioned at 93% RH is high and it includes the diffusion coefficient values for 10 mm thickness samples. This is mainly due to the inhomogeneous distribution of water inside the specimen's porous network. D_{e,O_2} varied by a maximum factor of 2. Note that results from Table 17 show that the coefficient of variation (CV) depends on the concrete type and the hydric state of the tested samples. CV for dry samples is found to be lower than the CV for the samples conditioned at 93% RH. Note that the water saturation degree of these samples is found to vary between 65% and 70% [141].

In this context, we cite the previous work of Chan [138] who found that oxygen diffusivity increases slightly with the ratio of the concrete specimen thickness to the maximum size of the aggregate present in the concrete. His results show that the standard error bars were much larger than the slope (diffusivity vs thickness); he then assumed that the increment was originated from an averaging error. However, in our case results from Figure 22 show a slight, but out of the error bars range increase of the effective diffusion coefficient of the four concrete tested at the dry state. These results are in agreement with previous works of Gardner [147] who found a slight increase of chloride diffusivity when varying the concrete specimens thickness (5 mm, 10 mm, 15 mm and 25 mm). It is also worth noting that Tuutti [13] tested the influence of different concrete specimen thickness on gaseous oxygen diffusion coefficient (10, 20, 30 and 50mm, fixe diameter of 150mm), and found results that contradict ours; the effective diffusion coefficient of oxygen increased by a factor of almost 50 for thin specimens

(10 mm). He then explained these results by the fact that the degree of hydration in thick specimens (50 mm) could be higher which results in lower porosity thus lower diffusivity. He also suggests that thinner specimens are more inclined to crack which results in high diffusivity. Besides the fact that our experimental technique and Tuutti's are different, our concrete specimens were cut after hydration of the concrete cylinder (11cm diameter 22cm height) for 90 days therefore the concrete specimens have more or less the same hydration degree [138].

To sum up, the dependence of D_{e,O_2} on the tested concrete specimens thickness must be further investigated on different concrete mixtures before any definite conclusions can be made.

ii) Influence of accelerated carbonation on D_{e,O_2} of concrete

Similarly to the investigations carried out on HCP, the influence of accelerated carbonation (1 vol.% CO_2) on the oxygen-effective diffusion coefficient and the water saturation degree is investigated on the concrete specimens described in section 3.7. Figure 24 shows that D_{e,O_2} increased by a factor that varies from 1.2 (C_FA) to 10 (C_MK and C_PC) for carbonated concretes preconditioned at 93% RH. This result is observed for all concrete mixtures except C_SL4 for which D_{e,O_2} slightly decreased by a factor of 1.6 but this could be due to an error of averaging since the results are within the error bars. At intermediate relative humidity 55%RH, carbonation caused a decrease of D_{e,O_2} by 1.4 and 3 for C_FA and C_PC respectively, while the latter increased for other concrete mixtures by a factor of 9 (for C_SL) at the most. At low relative humidity level (33%) D_{e,O_2} decreased for C_PC, C_FA, C_LS and C_SL4 by a factor that varies from 1.33 (C_LS) to 10 (C_FA), while D_{e,O_2} increased only for C_SL and C_MK by a factor of around 2. Note that although the influence of carbonation on the D_{e,O_2} is different for each concrete mixture and each relative humidity level, the total porosity of all concrete mixtures decreased upon carbonation (Figure 26).

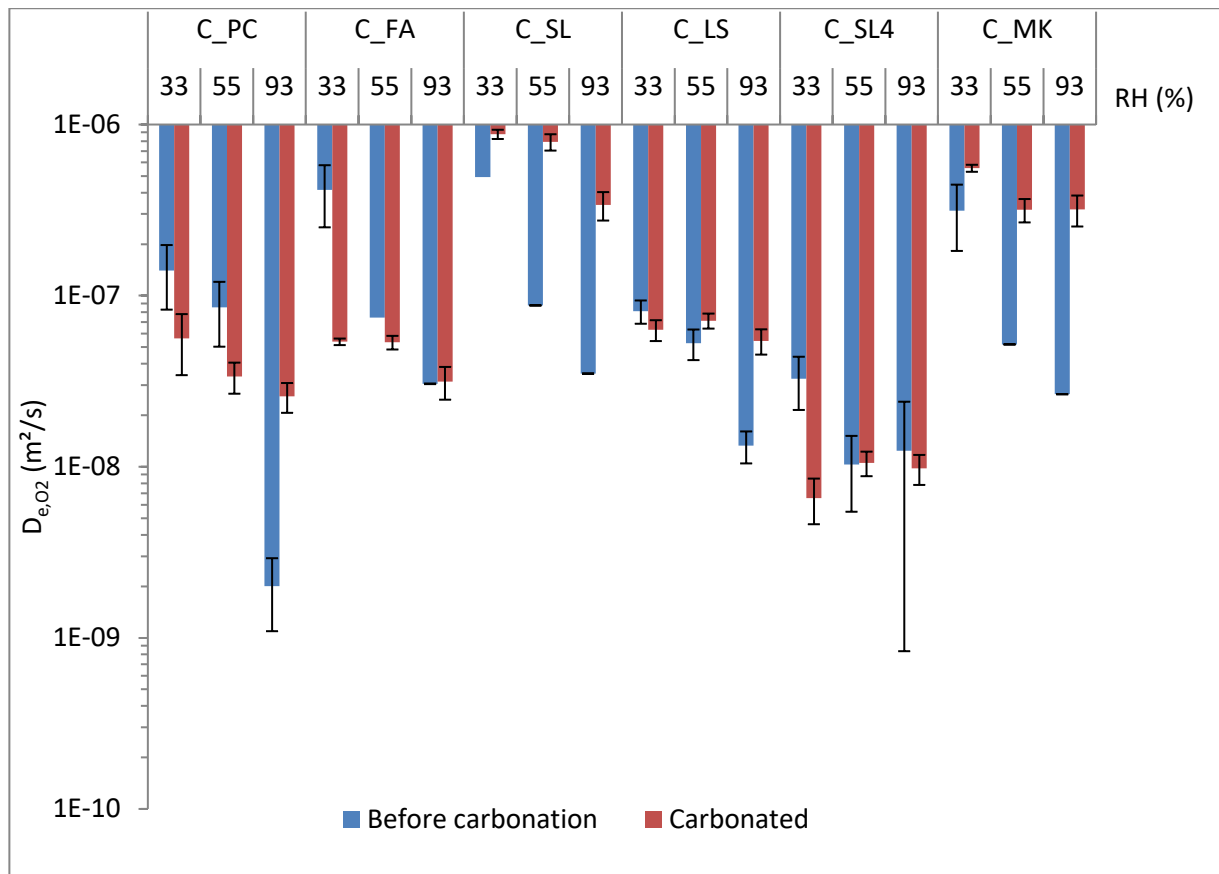


Figure 24: Influence of accelerated carbonation (1% CO₂) on the oxygen-effective diffusion coefficient of concrete

Figure 25 shows that the degree of water saturation of all tested concretes decreased upon carbonation for the three relative humidity levels of preconditioning. An exception is seen for C_MK. However, it is believed that for this mixture the degrees of water saturation obtained at 33% and 55% RH before and after carbonation could be erroneous (S_i at 55%RH is lower than S_i at 33%RH) because of the inhomogeneous water distribution inside the material which did not reach the equilibrium yet mainly because of the mass equilibrium criteria adopted in this study (mass variation within a week < 0.05%). We would like to note that the criteria of water equilibrium followed in this thesis work (mass variation < 0.05% within a week) could result in a non-homogenous water distribution inside the HCP and concrete specimens.

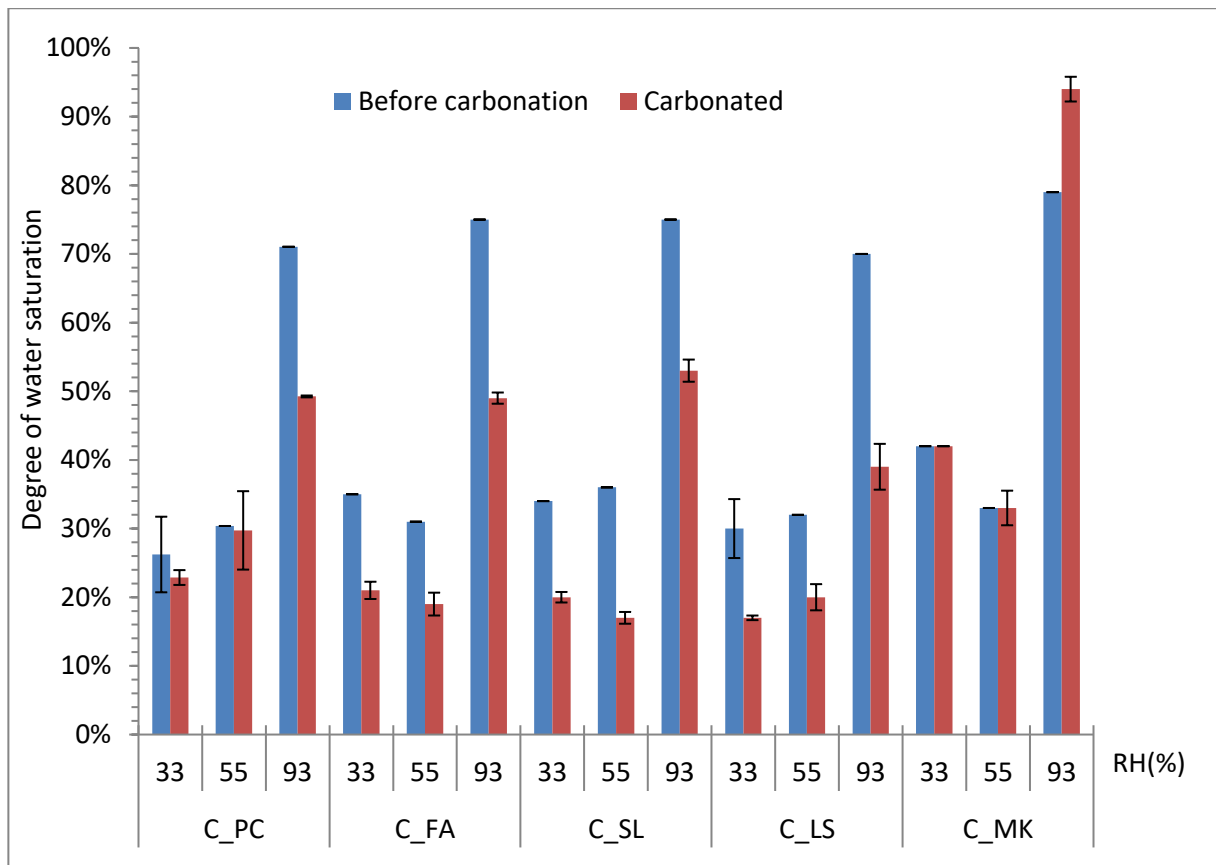


Figure 25: Influence of accelerated carbonation (1% CO₂) on the degree of water saturation of concrete previously conditioned at 33%, 55%, and 93% RH

Figure 26 shows that the total porosity decreased for all six concrete mixtures by 1% to 5%. This result is expected, since carbonation is known to decrease the total porosity of the cementitious materials and this result is also seen for hardened cement pastes HCP (by up to 12%) (Paper II).

Papadakis et al. [6] reported a decrease by 6% to 9% in the total porosity of mortar specimens upon carbonation. It is also reported that the variation in porosity is greater on cement pastes compared to mortars and concretes [148] (Paper II). A high content of portlandite and C-S-H tends to maximize the drop in porosity. Indeed, the decrease in the total porosity upon carbonation is mainly due to the filling effect of calcium carbonate [55], since the molar volumes of calcium carbonate polymorphs is higher than the molar volume of the hydration products. For example, the carbonation of one mole of Portlandite is expected to result in the reduction of the porous space by $2 \text{ cm}^3 \cdot \text{mol}^{-1}$ when calcite is formed [20].

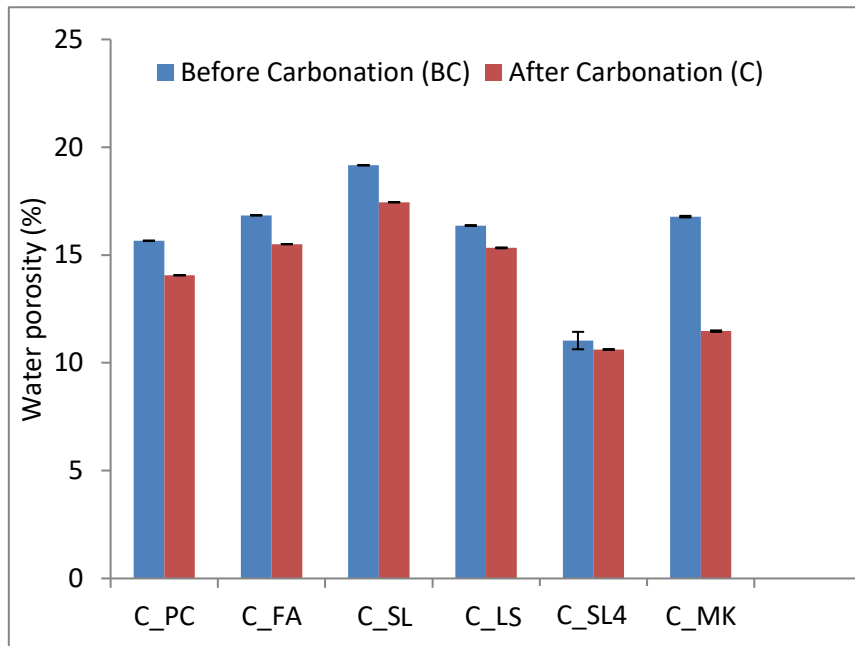
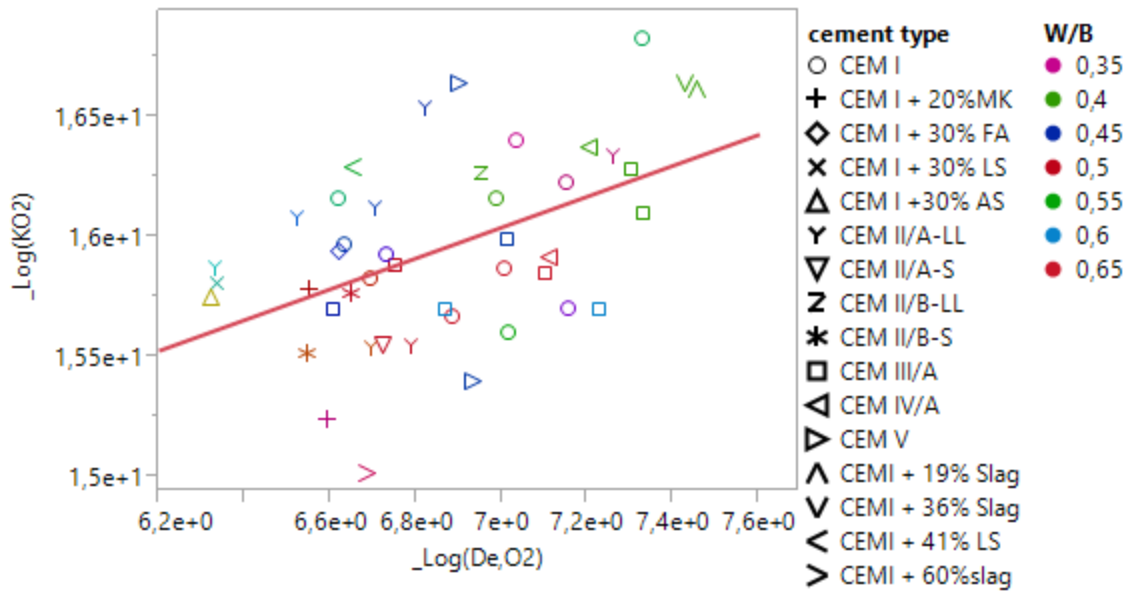


Figure 26 : effect of carbonation on the total porosity of the concrete specimen

iii) Oxygen permeability vs oxygen diffusivity

Currently, in performance based approach, the oxygen permeability is the transport property of interest [133]. This measurement procedure is still preferred to gas diffusivity mainly due to its ease of manipulation. Furthermore, the performance of a diffusivity test requires specific attention to pressure variation which could be challenging. The oxygen permeability test suitability to investigate the carbonation performance of concrete can be evaluated through a comparison with the oxygen diffusivity.

Figure 27 compares the oxygen permeability with the oxygen diffusivity of 44 concretes dried at 105°C in log-scale. For each mix, values of D_{e,O_2} and K_{O_2} are computed as the average value of three replicates. Markers on Figure 27 present the cement type used for the tested concrete and colors indicate the W/B ratio. For example, a light red circle is a CEM I concrete of a W/B = 0.65. The results show a very poor correlation between the two transport properties. Therefore, the relevance of the gas permeability results to investigate the carbonation performance of cementitious materials is questionable.



(a)

$$-\text{Log}(K_{O_2}) = 11.5 - 0,64 * \text{Log}(D_{e,O_2})$$

$$R^2 = 0.24$$

Figure 27: O₂-effective diffusion coefficient (-Log(D_{e, o₂})) vs O₂ gas permeability (-Log(K_{O₂}))

These results could be explained by the fact that permeability and diffusion are two different processes with two different driving mechanisms; pressure gradient and concentration gradient respectively. Furthermore, the oxygen permeability and diffusivity may be influenced differently by different factors including drying temperature, moisture distribution, gas pressure, gas flow, and specimens' geometry.

It is also worth noting that this comparison is carried out by determining the apparent permeability and not the intrinsic K_{O₂}, and the drying protocol for the specimens tested to oxygen-diffusivity is different than the drying protocol required by the French standard XP P18-463 [133] for oxygen permeability although the determination of both transport properties was carried out after drying at 105°C.

Drying induced microcracks (at 105°C), influences highly the oxygen permeability (a factor up to 100), while they only vary D_{e,O₂} by a factor of 2 at the most [56].

Some researchers [99], [8], [149], [107] suggest that there is a good correlation between these two properties. However, these results are only determined for a limited number of concrete mixtures. Moreover, these results are established using different experimental setups than ours and different drying protocol. Villani et al. [99] tested mortar samples prepared with OPC cement with a water-per-cement of 0.30, 0.40, 0.42 and 0.50, and an aggregate volume fraction of 55%. Oxygen diffusivity was determined using an equipment based on Lawrence

setup [8], and the oxygen permeability was determined following the procedure used in south Africa [149]. The correlation between D_{e,O_2} and K_{O_2} was established on 6 concretes.

Salvodi et al. [149] established a good correlation between D_{e,O_2} and K_{O_2} of four concrete mixtures made with OPC, Fly ash, Slag and silica fume. Oxygen Permeability was measured using the South African Oxygen Permeability Index (OPI) test (after 7 days drying at 50°C) the effective dry diffusion coefficient was calculated from results of accelerated carbonation test and corrected by an environmental parameter.

4.2 CO₂-binding capacity

4.2.1 Test method

i) Equipment

The second objective of this thesis work is to develop a new test method to determine the second property of interest regarding carbonation: the CO₂ binding capacity and reaction rate. The main idea of this test method is to determine the carbonation kinetics and the amount of carbonatable products based on the measurement of the instantaneous CO₂ binding rate. Therefore, an experimental setup is designed in order to meet the following specifications:

- The diffusion process must be neglected:

The tested samples are powdered materials sieved using a 63 μm sieve and of a mean diameter of 43 μm. Using this grain size allows for neglecting the mass diffusion between the grains according to Thiele modulus ϕ_n^2 (Paper III).

$$\phi_n^2 = \frac{T_{\text{diffusion}}}{T_{\text{reaction}}} = \frac{d^2 * k_0 * \rho}{D_{e,CO_2} * [CO_2]_0} \quad \text{Equation 30}$$

The Thiele modulus is defined as the ratio of the diffusion time ($T_{\text{diffusion}}$) to the reaction time (T_{reaction}). D_{e,CO_2} is the CO₂-effective diffusion coefficient in air [1.6×10^{-5} m²/s], $[CO_2]_0$ [g_{CO2}/m³] is the CO₂ concentration at the surface of the specimen, d [m] is the specimen thickness, k_0 [g_{CO2}·g⁻¹_{powder}·s⁻¹] is the reaction kinetic constant and ρ [g_{powder}/m³] is the material density. Low values of the Thiele modulus indicate the surface reaction control and a significant amount of the CO₂ diffusing well into the grains' interior without reacting. High values of the Thiele modulus indicate that the surface reaction is rapid and that the reactant is consumed very close to the external surface so only very little penetrates into the interior of the grain [150].

Testing a powdered material allows for neglecting the mass diffusion according to the calculation of this modulus (Further details about the computation of this number can be found in Paper III).

- The ageing process / exposure to carbonation must be under controlled relative humidity and ambient CO₂ concentration.

The carbonation chambers, inside which the powdered specimens are exposed to carbonation, are equipped with saturated salt solutions and a ventilation system to ensure stable relative humidity and settled CO₂ concentration at room concentration (Figure 28 (a)). The air pump draws in the ambient air, passes it through the bubbler to regulate it at the RH of the test by means of a saturated salt solution. Therefore, the pump circulates the air at the room CO₂ concentration and the desired RH inside the climate chamber. The flow rate of the air pump is 300L/h. The volume of the chamber is of 40L and is well aerated thanks to an axial fan.

- The total measurement time must be negligible with regards to the overall carbonation period of the sample

The measurement time is set to 5 min to 15 min and the overall carbonation time is 28 days at the most.

- Carbonation cells used to measure the CO₂ uptake must be of variable volume since the CO₂ depletion time is proportional to the gas volume. The equipment must be easy to handle and equipped with a CO₂ sensor.

The measurement cell is designed in a cylindrical shape with an adjustable volume (from 10 to 285 ml thanks to a piston), and the upper side of the cell is equipped with a CO₂ sensor (Figure 28 (b)). For powders that are highly reactive with CO₂, the cell volume is set at its maximum value and vice versa.

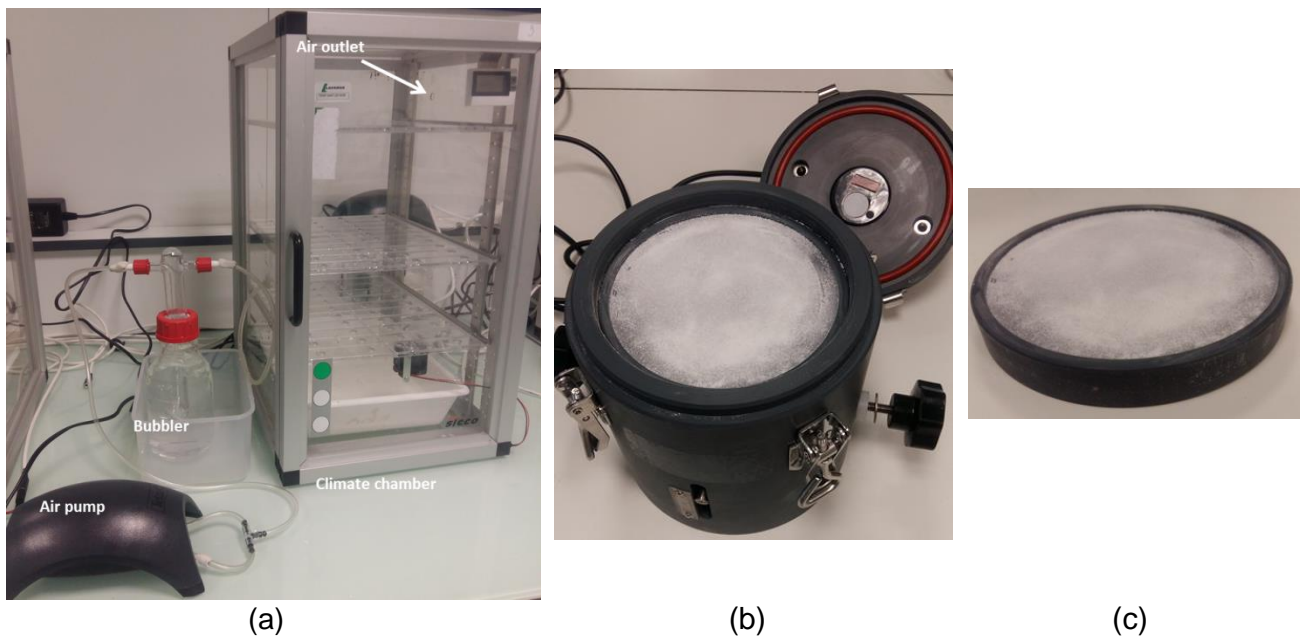


Figure 28: CO₂ binding capacity test method equipment: (a) climate chamber, (b) closed cell for carbonation, (c) sample holder [151]

The infrared CO₂ sensor determines the CO₂ uptake by the tested powder inside the cell once the measurement starts (cell closed). The sensor is provided by CO2Meter. Its response time is of 30 sec and its measurement range is of 0 – 10.000 ppm with an accuracy of 50 ppm. Data logging is made using GasLab software which allows real-time data analysis.

ii) Test protocol

The tested materials are first grinded and sieved to 63 μm , then 1g of the powder is evenly and thinly distributed on a sample holder (a disc of 110 mm diameter as shown in Figure 28 (c)) and placed inside a climate chamber regulated at a certain RH by means of saturated salt solutions. Soda lime is added inside the climate chamber in order to avoid carbonation during this preconditioning period of 15 days (CO₂ concentration 10 ppm at the beginning of the preconditioning period, this concentration was not monitored continuously).

The sample holders are then placed in the carbonation cell which is exposure to natural carbonation (around 450 ppm) under a specific relative humidity in the open system that consists of the equipment shown in Figure 28 (a).

The CO₂ uptake by the tested specimen is determined in the closed cell shown in Figure 28 (b) once a day the first week for a period of 15 min. Then, the frequency of CO₂ uptake measurement is adapted as a function of time evolution of the reaction rate. During the period of 15 min, the CO₂ sensor measures the decrease of CO₂ concentration inside the closed cell, where the reaction of carbonation took place. The test is stopped if the amount of carbonatable products vs. the carbonation time reaches a plateau or when the CO₂ depletion

rate is below the detection limit of the experimental setup or when the test is time-consuming: longer than 28 days. This lower limit is determined by running a leakage test on the carbonation cell for 24h after flushing it with gaseous nitrogen. The variation of CO₂ concentration during the blank test corresponds to an equivalent CO₂ instantaneous binding rate of $6.10^{-10} \text{ g}_{\text{CO}_2} \cdot \text{g}_{\text{cement}}^{-1} \cdot \text{s}^{-1}$. This value is computed using Equation 31, for which the slope is the leakage rate. More details about the test method can be found in (Paper III). Six carbonation cells are designed and used in this thesis work.

iii) Experimental data analysis

The collected raw data consist in the variation of CO₂ concentration as a function of time measured by a CO₂ gas sensor over the carbonation exposure period (see Figure 29).

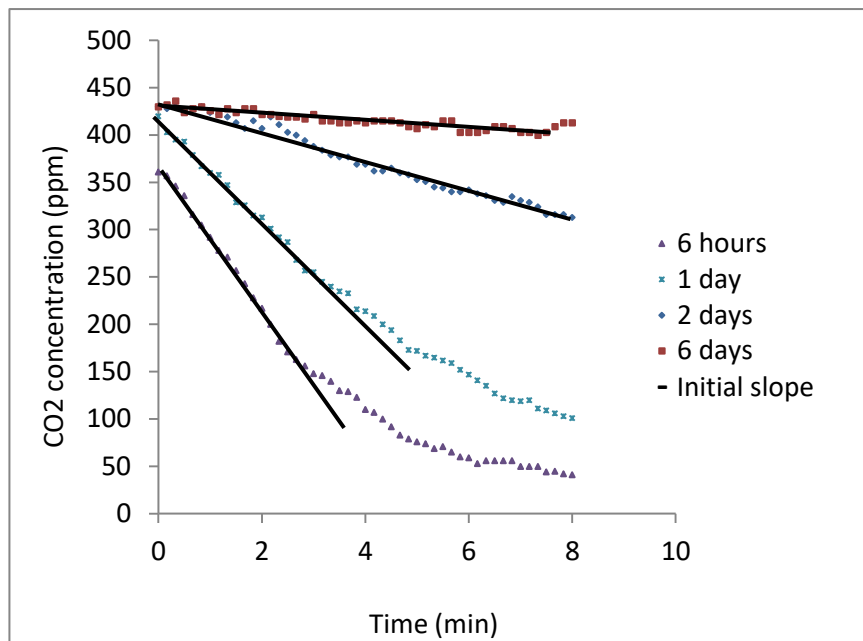


Figure 29: Raw experimental data of the CO₂-uptake curves of Portlandite powder carbonated at 55% RH at different carbonation periods: 6 hours, 1, 2 days (gas volume = 200 mL), and 6 days (gas volume = 10 mL)

The initial CO₂-consumption slope is determined from each CO₂-uptake curve using a data analysis software. The measured slope [$\text{ppm} \cdot \text{s}^{-1}$] is converted into an instantaneous CO₂ binding rate IBR [$\text{g}_{\text{CO}_2} \cdot \text{g}_{\text{cement}}^{-1} \cdot \text{s}^{-1}$] according to Equation 31. P [Pa], M_{CO_2} [$\text{g} \cdot \text{mol}^{-1}$], V_g [m^3], R [$\text{m}^3 \cdot \text{Pa} \cdot \text{K}^{-1} \cdot \text{mol}^{-1}$], and T [K] are the ambient pressure, the molar mass of carbon dioxide, the inside volume of the closed cell, the ideal gas constant and the ambient temperature respectively. m_0 [g] is the mass of the tested specimen with no bound CO₂ or water; it is corrected by the TGA results (at 1000°C) performed after preconditioning of the powders.

$$IBR = \frac{\text{Slope} * P * M_{CO_2} * Vg}{R * T * m_0} \quad \text{Equation 31}$$

$$B_{-CO_2}(t) = \int_{t=0}^t IBR d\tau \quad \text{Equation 32}$$

$$\text{carbonatable products} = \frac{CBC * \text{cement dosage}}{M_{CO_2}} \quad \text{Equation 33}$$

$$DoC = \frac{CBC}{MBC} \quad \text{Equation 34}$$

$$MBC = \sum \%CaO * \frac{M_{CO_2}}{M_{CaO}} - \%SO_3 * \frac{M_{CO_2}}{M_{SO_3}} \quad \text{Equation 35}$$

The amount of CO₂ bound at different exposure periods to carbonation (t) is determined by trapezoidal integrating the curve of the instantaneous binding rate as a function of time (Equation 32). The CO₂ binding capacity (CBC) of the tested material after the overall exposure period to carbonation is the amount of bound CO₂ at the last CO₂-uptake measurement (CBC = B_{-CO₂} (t = T_f)). The amount of carbonatable products (per m³ of the material) [mol.m⁻³] is then deduced from the CO₂-binding capacity [g_{CO₂}.g_{cement}.s⁻¹], the cement dosage [kg.m⁻³] and the molar mass of carbon dioxide [g.mol⁻¹] as shown in Equation 33. The degree of carbonation (DoC) is calculated following Equation 34, where the maximum binding capacity (MBC) is calculated from the chemical composition of the tested material assuming that all CaO will be transformed into CaCO₃ except the one that reacts with SO₃ to form CaSO₄ (Equation 35). M_{SO₃} [g.mol⁻¹], M_{CO₂} [g.mol⁻¹], M_{CaO} [g.mol⁻¹], are the molar masses of trioxide sulfur, carbon dioxide and calcium oxide respectively. Further information about the test method can be found in Paper III.

4.2.2 CO₂ binding capacity of the synthetic cement phases

In order to enhance the understanding of the carbonation behavior of the main cement phases present in hydrated and non-hydrated cement pastes, portlandite, ettringite, calcium-silicate-hydrate (Ca/Si = 0.9), triclinic alite, β-belite and cubic Tricalcium aluminate are synthesized and tested to natural carbonation using the method we developed (section above).

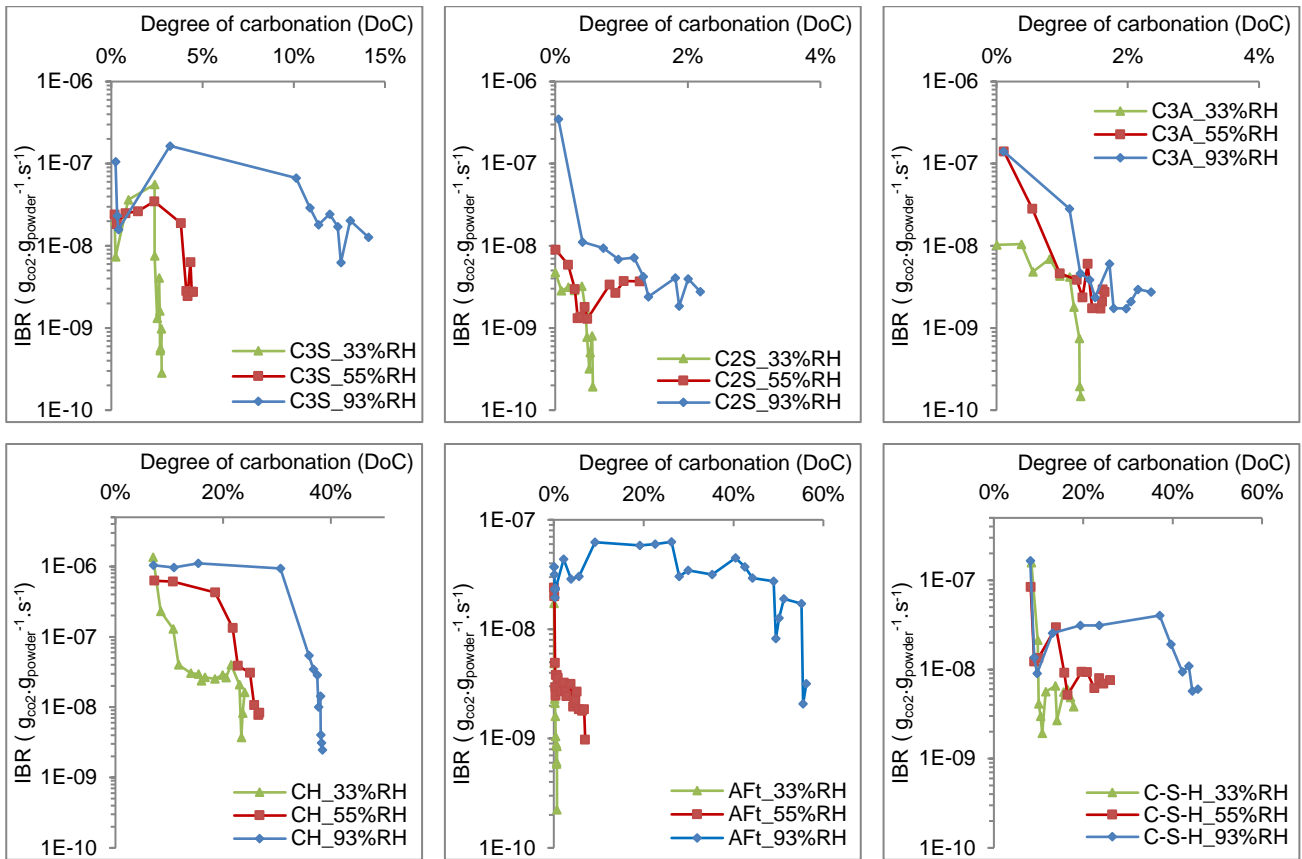


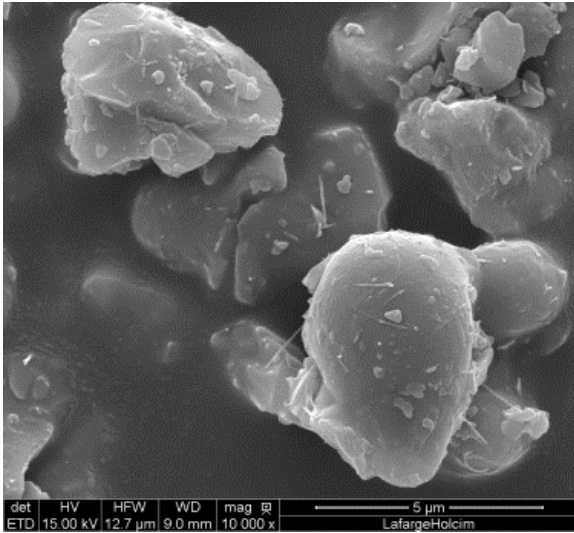
Figure 30: Variation of the Instantaneous binding rate (IBR) as a function of the degree of carbonation (DoC) at three relative humidity levels for synthetic anhydrous and hydrates

Figure 30 presents the evolution of the carbonation rate (IBR) with the degree of carbonation (DoC) at three relative humidity levels for the carbonation periods shown in Table 18.

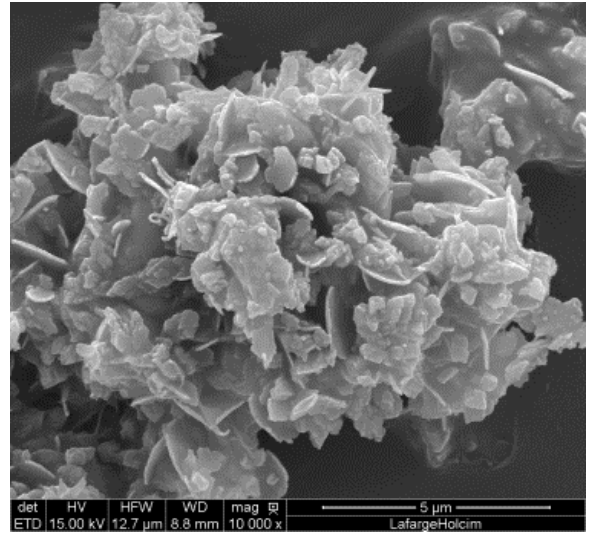
Material	CH			C-S-H			Ettringite			C ₂ S			C ₃ S			C ₃ A		
	93	55	33	93	55	33	93	55	33	93	55	33	93	55	33	93	55	33
Ageing period (days)	14	15	25	27	27	27	35	11	29	13	13	13	14	14	15	13	13	13

Table 18: Carbonation exposure period of synthetic materials at different RH

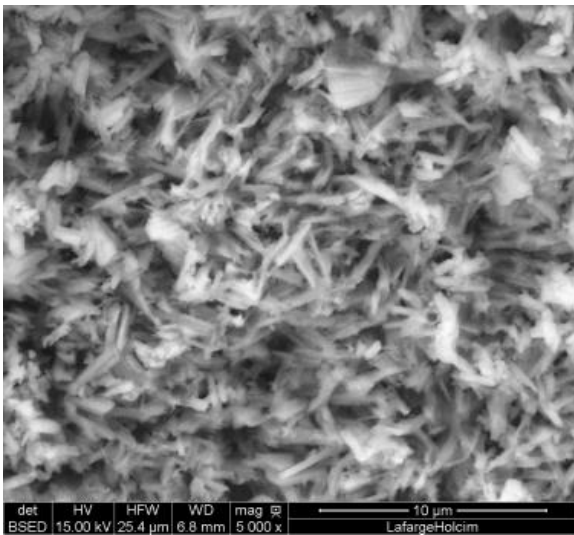
The results show that the carbonation rate decreases remarkably with the increase of the degree of carbonation except for ettringite powder carbonated at 93% RH. This result could be due to the formation of carbonates layer on the surface of the tested grains, which hinders further dissolution of the calcium oxide and transport of CO₂. Figure 31 shows the morphological changes on C₃S and ettringite powder after carbonation at 93%RH. The carbonate products cover the C₃S surface while they precipitate between the ettringite needles, which could explain the IBR variation of ettringite powder.



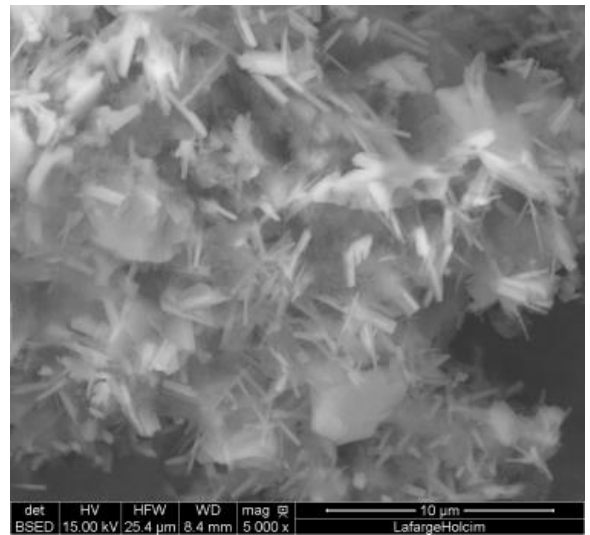
(a) C₃S before carbonation



(b) C₃S carbonated at 93%



(c) Non-carbonated Ettringite



(d) Ettringite carbonated at 93% RH

Figure 31 : Morphological evolution of C₃S, and AFt powders after exposure to carbonation at 93% RH (Paper III)

Figure 30 shows that the degree of carbonation increases with the relative humidity under which the carbonation experiments are carried out. This result is expected as the carbonation reaction kinetics are controlled by the dissolution of gaseous CO₂ and CaO. Portlandite and C-S-H degree of carbonation reached around 26% even when carbonation at 33% and 55% relative humidity due to their relatively higher solubility. For other materials, no significant carbonation is observed at these relative humidity levels. Regarding anhydrous materials, only C₃S carbonated at 93%RH (DoC ≈ 14%). This result could be due to the formation of a C-S-H layer on the grain surface as suggested SEM image in Figure 31 (b) (see Paper III).

The powders did not reach the theoretical maximum degree of carbonation (MBC). In fact, the decrease of the rate of carbonation reaction can be related to the decrease of the reactive

surface area. During carbonation, calcite precipitates which results in the reduction of porosity. Calcite creates also a layer which covers the non-carbonated materials and as a consequence, carbonation reaction stops before the complete carbonation of materials (Paper III).

Note that the BET surface area and density of these materials are determined before carbonation and after carbonation at 93%RH. Results (Paper III) show that the surface area increased for all powders except for portlandite and C-S-H powders, while the apparent density decreased for anhydrous mineral and increased for portlandite and ettringite to values close to the density of calcium carbonates (2.7 g/cm^3) [152].

Fluctuations of the instantaneous binding rate are noticed in Figure 30 what can be explained by the variability of the CO_2 concentration at the beginning of each measurement because of the presence of different operators inside the room. Figure 32 shows a distribution of the initial CO_2 concentration of the measurements and the number of the data in each range of the CO_2 concentration. The mean value of the initial concentration is 474.5 ppm with a standard deviation of 114.3 ppm. This result confirms that the initial CO_2 concentration is mostly around 450 ppm.

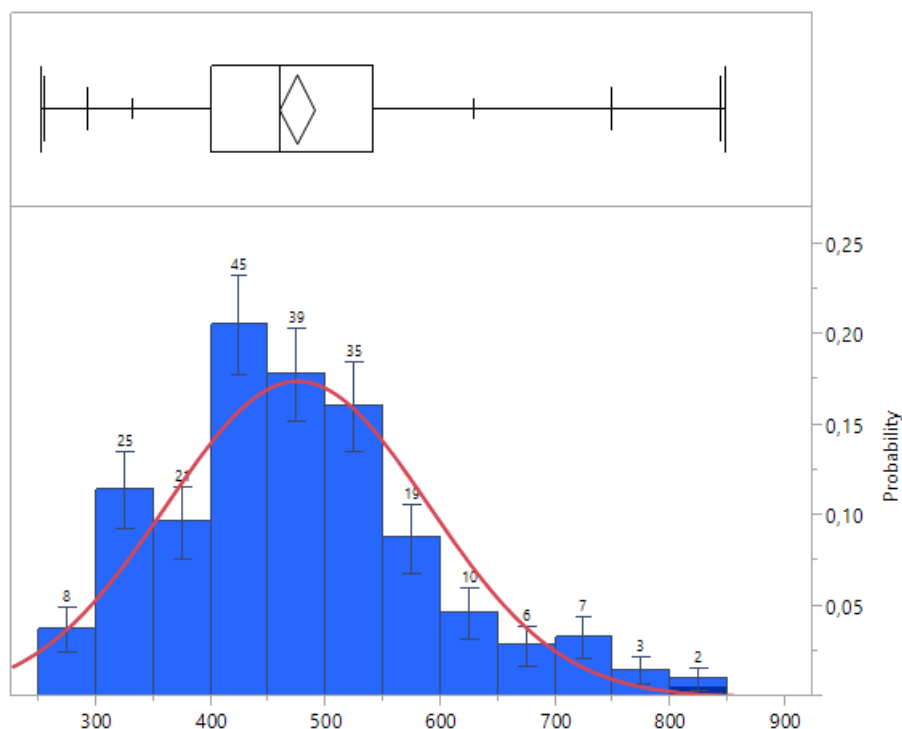


Figure 32: Initial CO_2 concentration distribution

Note that regulating the CO_2 concentration inside a concrete laboratory is a challenging task because of the depletion of atmospheric CO_2 in the presence of cementitious materials and the operators' presence inside the room [3].

4.2.3 CO₂ binding capacity of hydrated cement pastes

The hardened cement pastes shown in Table 11 are hydrated for 90 days, sawed to thin discs of 3 mm thickness, dried under vacuum for 48 hours, grinded and sieved to 63 μm. The powders are then preconditioned at three relative humidity levels (33%, 55% and 93% RH) for 15 days with soda lime before starting the atmospheric carbonation test. After this preconditioning period, the initial degree of carbonation is determined by means of TGA analysis (Equation 29). As seen in Figure 33, the HCP carbonated significantly during the preconditioning period even though soda lime was added inside the climate chambers and the CO₂ concentration did not exceed 10 ppm. This carbonation could be due to a leakage problem inside the climate chambers. The initial degree of carbonation varied from 9% (PC6 at 33%RH) to 44% (LS6 at 55% RH).

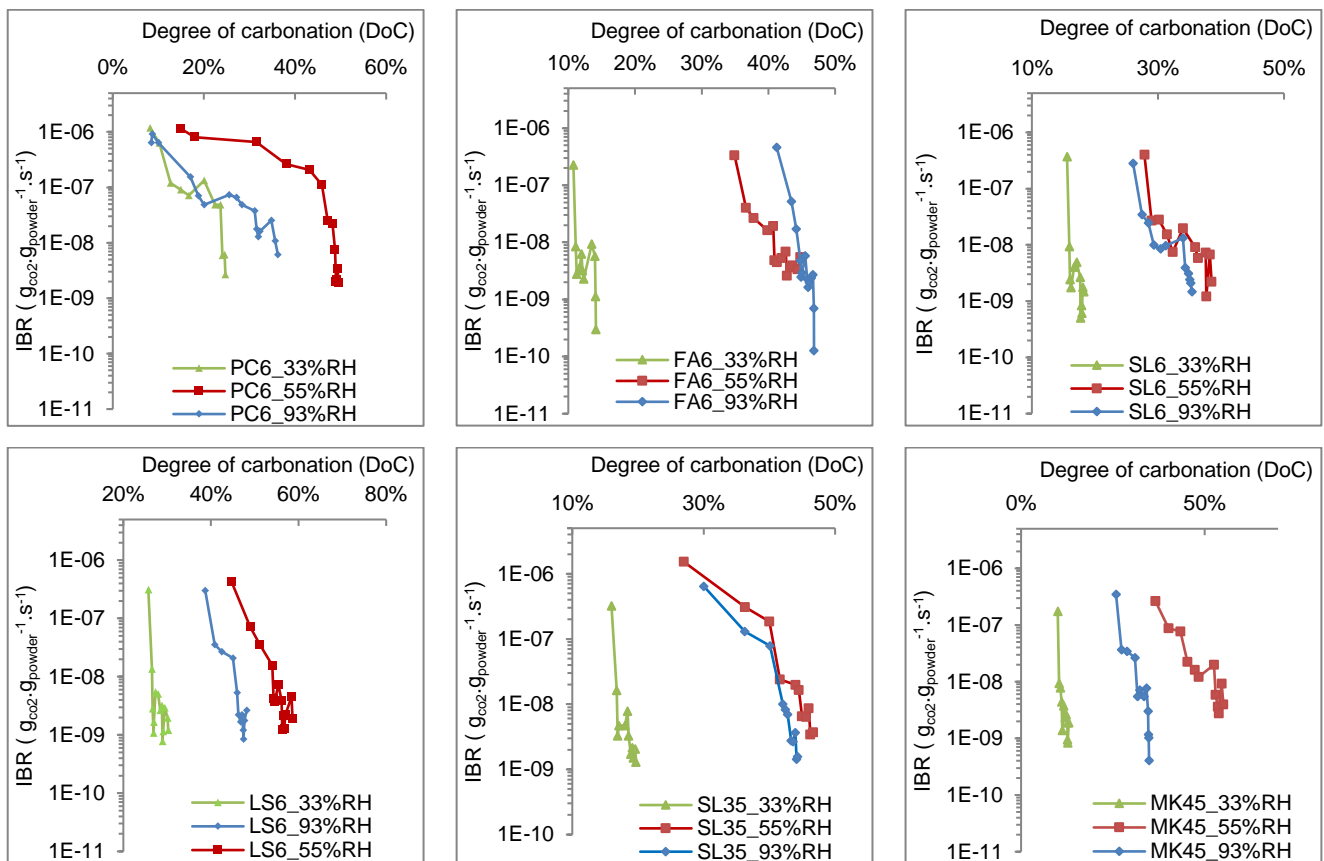


Figure 33: Variation of the Instantaneous binding rate (IBR) as a function of the degree of carbonation (DoC) at three relative humidity levels for the tested HCP

Figure 33 shows the evolution of the IBR with the DoC after 28 days of carbonation at 33%, 55% and 93% RH. Unlike pure synthetic phases (Figure 30), the maximum degree of carbonation is reached when the carbonation test is carried out at 55%RH for PC6, LS6 and MK45. The DoC values after 28 days of carbonation at 55% and 93% RH are close for FA6, SL6 and SL35. At low relative humidity (33%RH), the degree of carbonation varied from 14%

to 30%, while it reached up to 53% and 46% when the HCP are carbonated at 55%RH and 93%RH respectively.

4.2.4 Comparison with TGA results

The degree of carbonation (DoC) determined using the new test method is compared with the DoC obtained from TGA analysis. Figure 34 (a) shows that the results are in agreement (the average percent error is 24%), which highlight the accuracy of the measurements with the IBR method, since TGA results are hard evidence on the carbonation reaction.

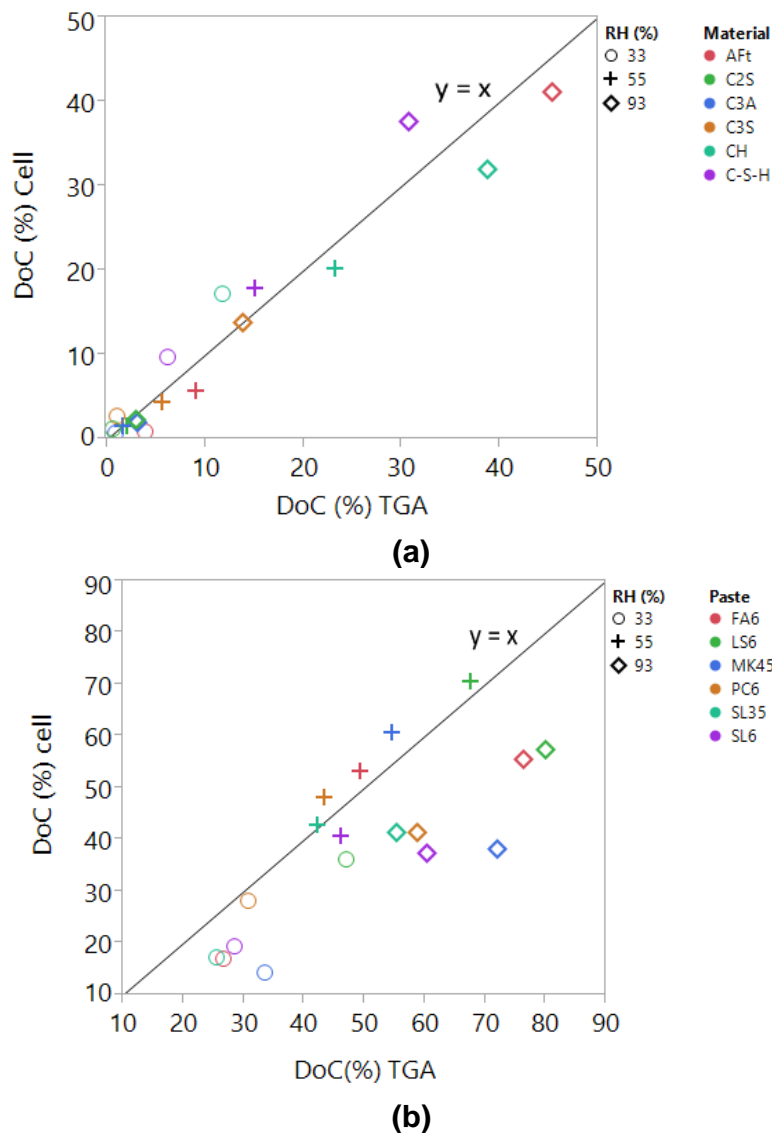


Figure 34: DoC (degree of carbonation) results from TGA vs DoC results from carbonation cell (a) synthetic minerals (b) HCP

The DoC reached by the six hydrated cement pastes after 28 days of carbonation calculated based on the CO₂ IBR method are also compared with TGA results (Figure 34 (b)). The degrees of carbonation from the new method are in a less favorable agreement with TGA results in the case of HCP (average percent error of 35%). This result could be mainly due to

the high carbonation of the HCP during the preconditioning period and to the representativeness of sample used for TGA analysis, which represents only 1/20th of the powder tested to CO₂ binding capacity CBC. In the case of HCP, the carbonation is more complex since many reactions occur simultaneously. Still, the obtained results are encouraging, giving that TGA is based on direct solid analysis and our test method consists in instantaneous non-continuous measurements of the CO₂ uptake.

V. Chapter V: Discussion

5.1 Limits and advantages of the developed test methods

This thesis project proposes two simple, timesaving, reliable and cost-effective test methods to determine the carbonation properties required for carbonation depth prediction models. The following chapter gives a summary of the main advantages and limits of the developed test methods. The experimental data obtained using these techniques are discussed and compared to literature findings and used as direct input parameters for two carbonation depth prediction models. The results are compared to the carbonation depths given by a pH-indicator under natural and accelerated exposures for HCPs and concrete specimens.

5.1.1 Gas diffusion coefficient test method

Oxygen-effective diffusion coefficient test method is interesting due to its ease and safe manipulation, its non-destructive and time-saving nature, its potential to give an indication of the material's performance, and its ability to test all types of cementitious materials under different degrees of water saturation in the range from 10^{-11} to 10^{-6} m²/s. The existing test methods in the literature (section 2.2) are all based on the use of two half diffusion cells which could raise leakage problems and increases the detection limit of the test method. Furthermore the reproducibility and detection limit of these setups are scarcely reported [13][87]. The test methods based on the determination of the CO₂ diffusion coefficient [89][94] limit the condition of the tested material to the dry state only. On the other hand, the test methods based on the diffusivity of pure gaseous oxygen are neither practical nor safe because of the need to use an oxygen bottle [100][13].

The coefficient of variation of our test method varies between 4% (at dry state) and 48% (at 93% RH) depending on the hydric state which controls the water distribution inside the material. This result is promising comparing to the coefficient of variation of oxygen permeability that varied between 10% and 94% at the dry state (from our results presented in Figure 27). Nevertheless, the decision as to whether these results are to be judged 'sufficiently precise' depends on how they are to be used.

Since the oxygen-effective diffusion coefficient test method measurement range is [10^{-11} , 10^{-6}] m²/s, the diffusion coefficient of cementitious materials with high gas tightness cannot be determined with sufficient precision. Furthermore, according to the previous works of Soukup et al. [97] a small pressure difference (around 8 Pa) between the Wick Kallenbach and

Graham's diffusion cells compartments (based on the flux principle), leads to a deviation of the net volumetric diffusion flux by more than 5% specially for materials with a mean pore diameter above 6 μ m. Moreover, the condition of application of the Graham's law is the pressure equality in both compartments [98]. Therefore, the influence of the pressure gradient in our half diffusion cell must be investigated, even though care was taken to flush the inside of the cell with a very slow flow rate.

Moreover, regarding the impact of the tested concrete specimen thickness, an increase in D_{e,O_2} by a factor of 2.6 at the most is observed when the concrete thickness varies from 5 mm to 50 mm. This variation could cause an underestimation of the carbonation depth by a factor of 1.6 when testing only thin samples (which is more convenient). This variation is still very low compared to drying induced microcracks effect on other transport properties such as gaseous oxygen permeability [56][153]. Still the dependence of the oxygen diffusivity on the specimen thickness is established for 4 concrete mixes only and further tests are necessary.

Note that the test method is already being used (Soja et al. [154][36], Bertin [46]) and a round robin test to further validate the method is planned in the framework of the TC Rilem GDP [155]. The main objective of the latter is building a consensus on gas diffusion test methods by comparing testing principles.

5.1.2 CO₂-binding capacity test method

The method developed to determine the CO₂ binding capacity and rate is simple, safe, reliable and cost-effective compared to thermogravimetric analysis. Results from this test method allow for the determination of the amount of bound CO₂ under different relative humidity levels, rather than predicting this value from C-S-H and CH content in the paste or CaO content in the cement. Moreover, the carbonation reaction kinetics can be determined at different periods of carbonation which is of high interest in the modeling of the carbonation front progress.

The test method results are in a satisfactory agreement with the TGA results: the average percent error is 24% and 35% for synthetic materials and HCP respectively. Note that there are few test methods based on the determination of the CO₂-binding capacity of powdered HCP in a non-continuous manner [113][156], and the existing ones are based on the TGA analysis [14] or the weight monitoring [157]. The first one is expensive and destructive while the latter induces errors as the carbonation reaction is accompanied by water release also.

The developed method is rather time-consuming taking 7 to 28 days to complete. This is also valid if the test method used is thermogravimetric analysis, as the carbonation exposure period is the same. Nevertheless, one TGA result requires approximately 2 hours depending on the

heating rate, while a single CO₂-uptake measurement doesn't exceed 20 min. Still, the CO₂-binding capacity technique requires preconditioning in a CO₂-free environment, which is rather challenging from a practical point of view. Furthermore, the preconditioning period of the tested powdered cementitious materials must be determined precisely prior preconditioning at different relative humidity levels.

5.2 Materials properties

5.2.1 Influence of different parameters on D_{e,O_2}

The diffusion coefficient increases with the increase of the volumetric W/B ratio (by half to one order of magnitude), which can be explained by the formation of higher porous volume that allows for an easier and faster ingress of gaseous oxygen. These results are in agreement with several studies in the literature [143][9][55]. Bentz et al. [158] explains that, for a lower W/B, the capillary porosity consists of a network of pores finer and more discontinuous. Furthermore, Baroghel-Bouny [159] explains that when the W/C decreases, the capillary porosity is reduced and the pore network becomes finer, which increases the water content at a given RH. This result explains the increase in D_{e,O_2} with the volumetric W/B especially at high relative humidity levels as a higher water content would hinder the gas transport. Note that gas transport through water filled pores is 10^4 to 10^5 slower than gas transport through air filled pore.

The diffusion coefficient decreased with the hydration duration. Prolonged hydration results in the formation of more hydrates, finer porosity and a more tortuous network. Therefore, the water retention capacity of the material increased highly which substantially reduces the diffusion coefficient (by up to three orders of magnitudes), especially for samples with slag and silica fume, as the reaction of SCM is generally slower than the hydration reaction of Portland cement. Silica fume and Slag mixes diffusivity is around 10 times lower than OPC's after 8 months of hydration. This could be explained by the fine pore structure of these mixes (see Paper I). In this context we cite the previous work of De Belie et al. [160] that revealed the high amount of gel pores in a HCP with 10% silica fume, related to the high amount of C-S-H. The latter would increase the water retention capacity of the HCP which would result in a D_{e,O_2} 10 times lower than D_{e,O_2} of OPC pastes.

The D_{e,O_2} highly decreases when the degree of water saturation is higher than 40% for HCP hydrated for 2 and 8 months. D_{e,O_2} varied by up to three orders of magnitude from the dry state to high degrees of water saturation (>80%). The higher degree of water saturation is seen on

well hydrated pastes as a prolonged hydration causes the formation of a greater amount of hydrates that fill the capillary porosity and help retain higher amounts of water which hinders the gas diffusivity. This result is consistent with other studies carried out on similar cement pastes well hydrated using a different test method that also showed a great decrease in gas diffusivity for $RH > 55\%$ [161][56]. It is of high importance to note that even though the hydration stopped samples were previously preconditioned at high relative humidity level (93% RH), their degree of water saturation S_i is lower than 45% and the D_{e,O_2} only slightly depends on the preconditioning RH. Therefore, it is more consistent to relate the carbonation performance of the cementitious materials to their degree of water saturation rather than the relative humidity of preconditioning.

Table 19 gives a summary of the influence of accelerated carbonation (1% CO_2 at 55%RH) on D_{e,O_2} and S_i of HCP and concrete (the results previously presented in Figure 24 and Figure 25). It is noted from these results that accelerated carbonation induced comparable effects on the water retention capacity of all tested concretes and their corresponding HCP. However, an opposite trend is observed regarding the oxygen diffusivity of fly ash materials: while the D_{e,O_2} decreased upon carbonation of concrete specimen, it increased highly upon carbonation of the HCP at the three relative humidity levels. In agreement with our results on HCP, Dutzer et al. [52] states that after accelerated carbonation (3% CO_2) cracking dominates for blended cements leading to significant increase in transport properties (gas diffusivity of helium and nitrogen), while pore clogging is observed for OPC pastes which lower their gas diffusivity. In agreement with our results on concrete specimens, Bertin [46] noted that the oxygen diffusivity decreased by a factor of about 2 for fly ash concrete at the dry state while it increased by almost a factor of 2 for slag concrete. The increase in the oxygen diffusivity could be explained by the fact that the pore structure connectivity increases after carbonation due to the decalcification of C-S-H.

		$D_{e,O_2} (BC) / D_{e,O_2} (C)$			$S_i (BC) / S_i (C)$		
RH (%)		33	55	93	33	55	93
Hardened cement pastes	PC6	2.8	2.1	0.1	1.0	1.2	1.3
	FA6	0.7	0.4	$\sim 10^{-4}$	1.2	1.5	1.8
	SL6	0.2	0.1	0.0	1.6	1.6	1.3
	LS6	1.1	0.9	0.2	1.3	1.3	1.9
	SL35	4.6	3.1	0.4	1.0	1.2	1.1
	MK45	0.7	0.4	0.0	0.9	0.9	1.0
Concrete	C_PC	2.5	2.5	0.1	1.2	1.0	1.4
	C_FA	7.7	1.4	1.0	1.7	1.6	1.5
	C_SL	0.6	0.1	0.1	1.7	2.1	1.4
	C_LS	1.3	0.7	0.2	1.8	1.6	1.8
	C_SL4	5.0	0.6	2.6	-	-	-
	C_MK	0.6	0.2	0.1	1.0	1.0	0.8

Table 19 : Summary of the influence of accelerated carbonation (1% CO₂) on S_i and D_{e,o2} of concrete and their corresponding HCP. BC: before carbonation, C: carbonated

Regarding the direct link between the pore size distribution and the oxygen-effective diffusion coefficient, our results reveal a good correlation between the pore diffusion coefficient (corrected by $\Phi(1-S_i)$: apparent diffusivity) and the mean pore diameter of the hardened cement pastes (in log-scale) when the degree of water saturation S_i is lower than 30% which could be due to the predominance of Knudsen diffusion regime. In this context we cite the previous works of Peretti et al. [85] who suggest that oxygen diffusivity is related to the moisture-free porosity volume fraction with an exponential correlation, and Peng et al. [100] who investigated the correlation between oxygen diffusivity and pore size distribution of rock samples, repacked sand and sediment and found a linear regression coefficient that describes the exponent in Archie's law and the volumetric mean pore diameter. The correlation between the critical pore radius obtained from MIP and the oxygen-effective diffusion coefficient (obtained using our experimental setup) was also highlighted in the work of Soja [154].

5.2.2 CO₂-binding capacity and rate at different RH

The CO₂ binding capacity (CBC) and rate of the synthetic anhydrous, hydrates, and powdered HCP is determined at three relative humidity levels (33%, 55% and 93%). The bound CO₂ and instantaneous binding rate increase with the relative humidity under which the carbonation of synthetic materials test is carried out, while the maximum binding capacity of the hardened cement pastes is observed at 55% RH. The amount of bound CO₂ increases highly during the first week of exposure to carbonation and only slightly varies afterwards (Paper III), which is of high interest in a practical point of view since it could shorten the measurement time to 7 days instead of 28 days.

Table 20 gives a summary of the CO₂ binding capacity and the instantaneous binding rate of

the HCP and synthetic phases (detailed results are shown in sections 4.2.2 and 4.2.3). The maximum CO₂ binding capacity is observed for portlandite powders, followed by PC6 and the other hydrated cement pastes. This result highlights the role of portlandite to fix CO₂ in cementitious materials. Furthermore, among synthesized phases, CH and C-S-H are the only phases that carbonated also at 33% and 55% RH. These phases presence in the tested HCP (see Paper II) could explain their carbonation at 33% and 55% RH, since no carbonation of the other synthesized phases is noticed at these RH. The highest CBC is observed for the non-blended HCP which contains the highest amount of CH (paper II). Since portlandite is produced only by clinker, it is expected that the portlandite proportion decreases with the proportion of clinker as already observed in previous works [162] [163] and in Paper II.

Regarding the CO₂ binding capacity of hydrated cement pastes, an increase is noticed in the CBC when the carbonation is carried out at 55% and 93% RH. However, the maximum CBC is reached at 55% RH for most HCP except FA6. This result could be explained by the important carbonation of these HCP during the preconditioning period.

		MBC (10 ⁻² g _{co2} g _{cement} ⁻¹)	CBC (10 ⁻² g _{co2} g _{cement} ⁻¹)			IBR (g _{co2} g _{cement} ⁻¹ s ⁻¹)		
			33% RH	55% RH	93% RH	33% RH	55% RH	93% RH
Synthetic phases	C ₃ S	58	1.6	2.6	8.2	10 ⁻⁸ to 10 ⁻¹⁰	10 ⁻⁸ to 10 ⁻⁹	10 ⁻⁷ to 10 ⁻⁸
	C ₂ S	51	0.3	0.6	1.1	10 ⁻⁹ to 10 ⁻¹⁰	10 ⁻⁸ to 10 ⁻⁹	10 ⁻⁷ to 10 ⁻⁹
	C ₃ A	49	0.6	0.8	1.1	10 ⁻⁸ to 10 ⁻¹⁰	10 ⁻⁷ to 10 ⁻⁹	
	CH	60	14.3	16.0	23.0	10 ⁻⁶ to 10 ⁻⁹	10 ⁻⁷ to 10 ⁻⁸	10 ⁻⁶ to 10 ⁻⁹
	AFt	39	0.3	2.7	16.4	10 ⁻⁸ to 10 ⁻¹⁰		10 ⁻⁸ to 10 ⁻⁹
	C-S-H	36	6.4	9.3	22.0	10 ⁻⁸ to 10 ⁻⁹	10 ⁻⁸ to 10 ⁻⁹	10 ⁻⁷ to 10 ⁻⁹
Hardened cement pastes	PC6	60	14.6	25.0	21.4	10 ⁻⁶ to 10 ⁻⁹		10 ⁻⁶ to 10 ⁻⁹
	FA6	44	6.3	20.0	21.0	10 ⁻⁷ to 10 ⁻¹⁰	10 ⁻⁷ to 10 ⁻⁹	10 ⁻⁷ to 10 ⁻¹⁰
	SL6	45	8.3	17.5	16.1	10 ⁻⁶ to 10 ⁻⁹	10 ⁻⁶ to 10 ⁻⁹	10 ⁻⁷ to 10 ⁻⁹
	LS6	38	11.1	21.5	17.8	10 ⁻⁶ to 10 ⁻⁹		
	SL35	42	8.2	19.7	18.6	10 ⁻⁷ to 10 ⁻⁹	10 ⁻⁶ to 10 ⁻⁹	10 ⁻⁷ to 10 ⁻⁹
	MK45	45	6.0	25.0	16.0	10 ⁻⁷ to 10 ⁻⁹	10 ⁻⁷ to 10 ⁻⁹	10 ⁻⁷ to 10 ⁻¹⁰

Table 20: Summary of the CO₂-binding capacity and rate of the HCP and synthetic minerals. MBC: maximum theoretical CO₂ binding capacity (from mineral composition), CBC: maximum measured CO₂ binding capacity, IBR: instantaneous binding rate.

Table 20 shows that the IBR of the tested materials varied over four orders of magnitudes and depends on the material composition and the relative humidity under which the carbonation tests are carried out. The highest IBR are observed for CH and PC6 powders.

5.3 Comparison of experimental results to Millington's model

As explained in section 2.2.1, the CO₂-effective diffusion coefficient can be estimated using models developed to predict D_{e,CO₂}. Based on Millington model [102], Thiéry et al. [39] proposed an expression (Equation 11) giving D_{e,CO₂} as a function of the water saturation degree S_l, total porosity φ, and the CO₂ diffusion coefficient in air (D_{0,CO₂} = 1.6x10⁻⁵ m²/s). Empirical parameters of this model (a = 2.74, b = 5.17) were obtained by fitting experimental data of tests performed on carbonated mortars at different RH [11].

The oxygen-effective diffusion coefficient (D_{e,O₂}) can be estimated from the CO₂ diffusion coefficient (D_{e,CO₂}) using Graham's law. Equation 36 gives D_{e,O₂} (from Millington's model Equation 11) and Graham's law. M_{CO₂} and M_{O₂} are the molar mass of carbon dioxide and oxygen respectively.

$$D_{e,O_2} = \left(\frac{M_{CO_2}}{M_{O_2}}\right)^{\frac{1}{2}} D_{0,CO_2} \phi^a (1 - S_l)^b \quad \text{Equation 36}$$

Table 21 gives the total porosity Φ and the degree of water saturation S_l regression parameters a and b of the HCP tested during this thesis work (Table 11). These parameters are calculated by least square fitting of all the experimental data for each binder type (section 3.6).

Note that the good quality of the least square fit is achieved by minimizing value of the sum of squared residuals r. In our case, r is in the range of 10⁻¹² to 10⁻¹⁰ m²/s, which is lower than the average measured diffusion coefficients.

	OPC	Silica fume	Slag	Fly ash	Metakaolin	Limestone
a	5.5	4.8	5.5	5.6	2.6	5.2
b	2.7	3.7	8.9	2.6	2.8	1.2
Residual (r)	8.9·10 ⁻¹¹	9.8·10 ⁻¹²	7·10 ⁻¹¹	5.8·10 ⁻¹²	2.7·10 ⁻¹¹	2.8·10 ⁻¹⁰
Number of fitted data	94	71	114	18	21	21

Table 21: Calculation of Millington's model parameters based on our experimental data obtained on HCP

The obtained parameters a and b are specific of each binder type. The total porosity regression parameter a is around 5 for all binders except for metakaolin binder for which a is equal to 2.6. The degree of water saturation S_l parameter b varies between 1.2 (limestone HCP) to 8.9 (for Slag pastes). These results are obtained for non-carbonated specimens. Note

that Thiéry et al. [39] determined a and b parameters based on nitrogen diffusion tests performed on carbonated, non-blended cement pastes and concretes [18], and obtained the empirical parameters values ($a = 2.74$, $b = 5.17$).

Recently, Gendron [89] found also that the exponent a depends on the binder type ($a = 6.0$ and 5.3 for slag and OPC non-carbonated mortars, respectively). These values are closed to the ones found in the present work.

The major limitation of this kind of model is that the diffusion coefficient is related to averaged descriptors of the pore structure, which are the total water porosity and the water saturation, while neglecting actual pore-size distribution, binder type and pore connectivity.

5.4 Comparison of experimental results to literature models

In order to further analyze the experimental results obtained from the developed test methods, the gas diffusivity and CO_2 binding capacity results are used as input parameters in two carbonation depth prediction models and the results are compared to the pH-indicator under natural and accelerated carbonation

5.4.1 Prediction of the HCP carbonation depth

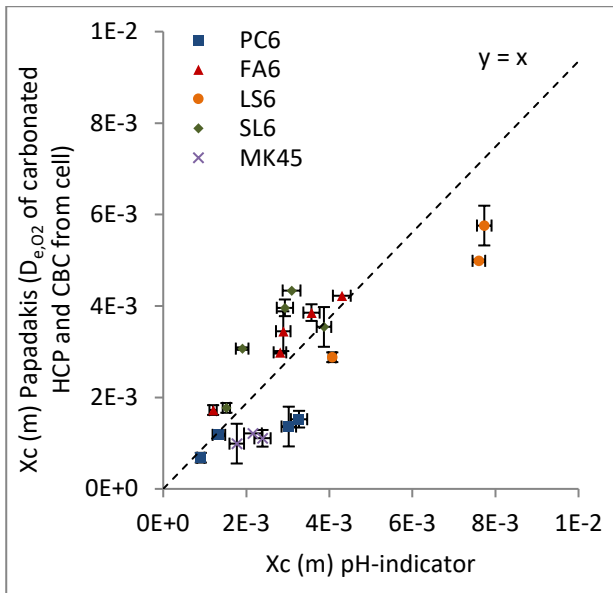
Based on the results shown in Chapter IV, the amount of carbonatable products of the tested HCP and concrete are determined using Equation 33 (section 4.2.1). Table 22 gives the amount of carbonatable products, the oxygen-effective diffusion coefficients determined before and after carbonation. These results are obtained after preconditioning at 55%RH.

HCP	Amount of carbonatable products [mol.m ⁻³]	D_{e,O_2} [10 ⁻⁷ m ² .s ⁻¹] of the HCP before carbonation	D_{e,O_2} [10 ⁻⁷ m ² .s ⁻¹] of the HCP after carbonation	Carbonation rate (mm/year ^{0.5}) HCP after carbonation
PC6	6152	0.7	0.3	2.3
FA6	3306	0.5	1.2	5.9
SL6	1699	0.1	0.6	6.0
LS6	3129	2.6	3.1	9.8
MK45	5737	0.1	0.1	1.3

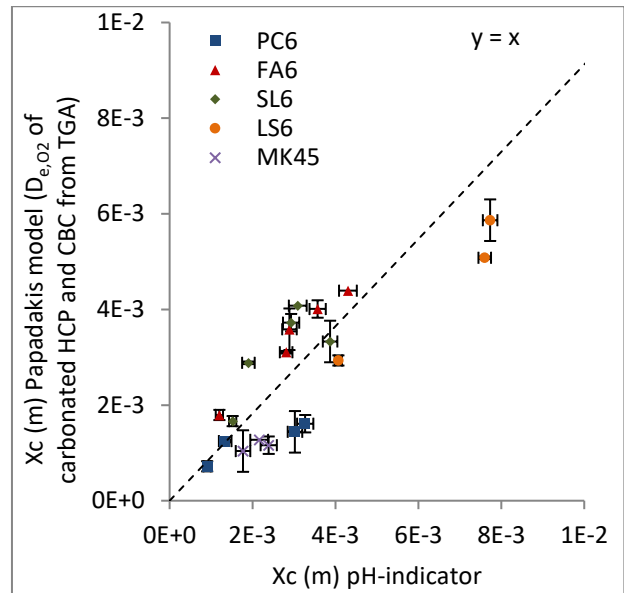
Table 22: Amount of carbonatable products, the oxygen-effective diffusion coefficient of HCPs at 55% RH before and after carbonation

In order to investigate the reliability of our test methods results, the five HCP (Table 21) are exposed to natural carbonation at 55% RH for 5 months. The carbonation depths are determined by phenolphthalein solution once a month. These depths are compared to the

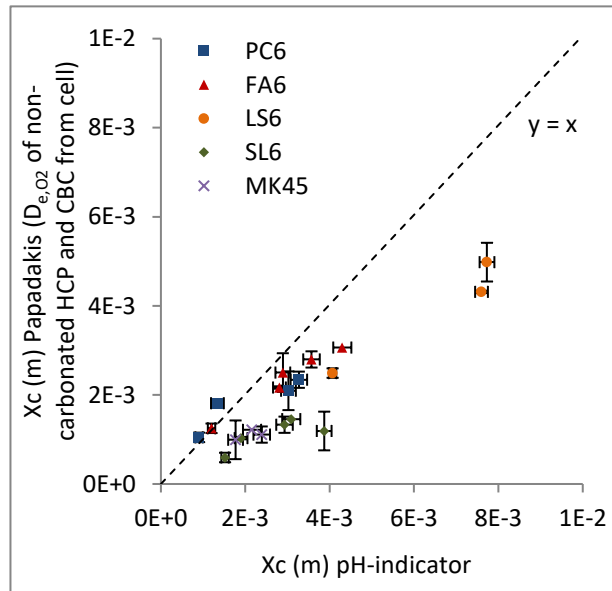
carbonation depths calculated from our experimental results using the coefficient of diffusion and the amount of carbonatable products shown in Table 22 and using Papadakis' model (Equation 20). Note that the amount of carbonatable products used in the our calculations are obtained from our experimental results while Papadakis' model relies on the phase assemblage of the material (Chapter II section 2.3.2). Carbonation at 55% RH is chosen since it is suggested that the most rapid carbonation of concrete occurs at a relative humidity near 50% to 65% (the RH required by the standards as shown in section 2.1). Note that the carbonation depth calculations are carried out using the diffusion coefficient of carbonated and non-carbonated HCP (Table 22) as input parameter in Papadakis' model[164].



(a)



(b)



(c)

Figure 35: HCP carbonation depths determined with pH-indicator vs. the carbonation depths predicted using our experimental results

Figure 35 shows that the carbonation depths obtained from Papadakis' model are well correlated to the carbonation depths measured experimentally using phenolphthalein solution. The vertical error bars are due to oxygen-effective diffusion coefficient variation within replicates, and the horizontal errors bars are a result of averaging 5 carbonation depth readings. A slightly better agreement is observed when the carbonation depth predictions are made using the carbonatable products determined from TGA results (Figure 35 (b)). Still, Figure 35 (a) and Figure 35 (b) results are very comparable which could indicate that the diffusion coefficient controls the carbonation depth more than the amount of carbonatable

products. Indeed, for the tested HCPs, D_{e,O_2} varies over two orders of magnitude at 55% RH, while the amount of carbonatable compounds varies only by a factor of 4 at the most. This result was also confirmed by the previous works of Dutzer et al. [52] who indicate that the change in mineralogy of HCP almost had any influence on the estimated carbonation rate, while the increase in diffusivity is the major cause of the increase in carbonation rate.

Figure 35 (c) compares the carbonation depths obtained from the diffusion coefficient results of non-carbonated HCP to the pH-indicator results and reveals that a better agreement is observed when the carbonation depth predictions are carried out using the diffusion coefficient of carbonated HCP. The pH-indicator results are slightly higher than Papadakis' model. This overestimation could be due to errors of averaging or microcracks within the samples (that Papadakis model does not take into consideration).

The average percent error (the difference between the model results and the pH-indicator divided by the pH-indicator results) between the results shown in Figure 35 (a), (b), and (c) is 31%, 29% and 37% respectively.

5.4.2 Prediction of the concrete carbonation depth

Table 23 shows the amount of carbonatable products (deduced from the CBC results of the HCP), the D_{e,O_2} , and the inverse carbonation resistance of the three concrete mixtures at 55% RH. The lowest value of R^{-1}_{NAC} (see section 2.3.3) is obtained for C_PC, and C_LS in the carbonated, and non-carbonated states respectively. This result is mainly due to the decrease of D_{e,O_2} upon carbonation for C_PC and its increase for carbonated C_LS (in addition to the lower amount of carbonatable products of this concrete mixture).

Concrete	Amount of carbonatable products (mol/m ³)	D_{e,O_2} [10 ⁻⁷ m ² .s ⁻¹] before carbonation	D_{e,O_2} [10 ⁻⁷ m ² .s ⁻¹] after carbonation	R^{-1}_{NAC} (m ² .s ⁻¹ .kg _{CO2} .m ⁻³)	
				Carbonated specimens	Non-carbonated specimens
C_PC	1584.5	0.9	0.3	4.1·10 ⁻¹⁰	1.1·10 ⁻⁰⁹
C_FA	1013.6	0.7	0.5	1.0·10 ⁻⁰⁹	1.3·10 ⁻⁰⁹
C_LS	1350.0	0.5	0.7	1.0·10 ⁻⁰⁹	7.2·10 ⁻¹⁰

Table 23 : Amount of carbonatable products, oxygen-effective diffusion coefficient and the inverse carbonation resistance of concrete at 55% RH before and after carbonation

i) Papadakis' model

Figure 36 shows the results of the carbonation depth given by Papadakis' model (Equation 20) using our experimental results and the carbonation depths given by the phenolphthalein solution up to two years under natural carbonation exposure for concrete mixtures showed in Table 23. Figure 36 (a) and (b) present the carbonation depths obtained using the diffusion

coefficient of non-carbonated and carbonated concretes respectively.

The pH-indicator predictions shown in Figure 36 computed using our experimental results and Papadakis' model lead to an overestimation of the latter by a factor of around 4.5 under natural carbonation exposure.

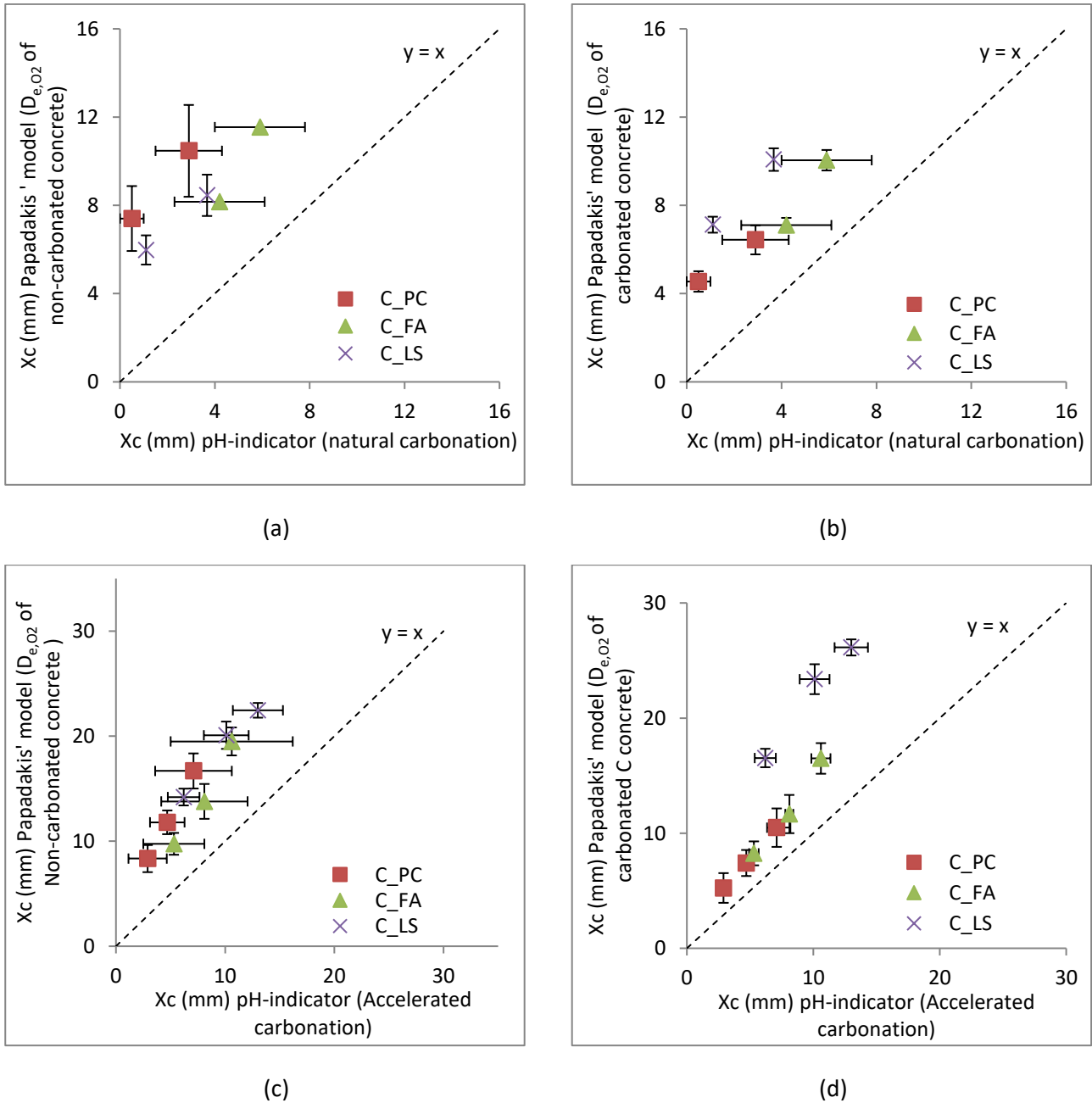


Figure 36: Comparison of carbonation depth calculated from Papadakis model using our experimental data of gas diffusivity and CO₂-binding capacity ($Xc_{papadakis}$) and carbonation depth determined directly concrete specimen ($Xc_{pH_indicator}$) under accelerated conditions

Figure 36 (c) and (d) show results of the carbonation depth determined under accelerated exposure (3% CO₂) using Papadakis' model and the gas diffusivity of carbonated and non-carbonated specimens respectively. In comparison with the results obtained under natural

carbonation, a better agreement is observed in this case. Still, the model results overestimate the pH-indicator results by a factor of around 2 (Figure 36 (c) and (d)). It is worth noting that the a pH-indicator is a chemical compound that changes its color depending on the pH of the solution or surface with which it is in contact, while the carbonation depth models are based on the physicochemical description of the carbonation process.

ii) Gehlen's model

Since the carbonation depths are determined under natural sheltered exposure, the weather function $W(t)$ is taken equal to 1. The curing parameter k_c is taken equal to 1 is the following, since the tested concrete specimens are cured for 90 days (curing reference in our case). (See section 2.3.3)

According to [15], the environmental parameter k_e , which expresses the influence of RH on the gas diffusion coefficient, can be determined directly from the relative humidity of reference and the relative humidity of carbonation only (Equation 24) regardless the concrete type.

In an attempt to determine this parameter from our experimental results, the k_e parameter can be determined using Equation 37 [15]. $X_{c,NAT,component}$ [mm] is the carbonation depth of stored specimens protected from rain that have carbonated under natural carbonation conditions at time t , and $X_{c,NAT,Lab}(t)$ [mm] is the carbonation depth at time t determined on specimens that have carbonated naturally under laboratory conditions (identical curing to component). The ratio of these parameters can be rewritten as a function of our experimental data of diffusion coefficient and carbonatable products using Papadakis' model. Taking 55% as the relative humidity of reference and using Equation 37 [15] D_{RH} and CP_{RH} are the diffusion coefficient and the amount of carbonatable products (mol/m^3) determined at a certain RH level respectively.

$$k_e = \left(\frac{X_{c,NAT,component}(t)}{X_{c,NAT,Lab}(t)} \right)^2 = \frac{\frac{D_{RH}}{CP_{RH}}}{\frac{D_{55\% RH}}{CP_{55\% RH}}} \quad \text{Equation 37}$$

Figure 37 shows that the k_e parameter value calculated for the tested concrete using results of gas diffusivity at the non-carbonated and carbonated states. k_e depends on the concrete mixture and carbonation state. It is lower than 1 (from 0.03 to 0.9) when the relative humidity is 93% for concrete C_PC, C_FA, and C_LS, while it is higher than 1 for 33% RH which highlights the fact that at this relative humidity level, the carbonation depth would progress faster than at the relative humidity of reference (55% RH) for all tested concrete.

Since the natural carbonation tests are carried out at 65%RH, the k_e parameter value used in the calculation of the carbonation depths is determined by linear interpolation between the k_e parameter at 55% and 93% RH. The k_e used in this study are 0.29, 0.71 and 0.49 for concretes C_PC, C_FA, and C_LS respectively using the diffusion coefficient of non-carbonated specimens, and 0.97, 0.89 and 0.98 for the same respective concretes in the carbonated state.

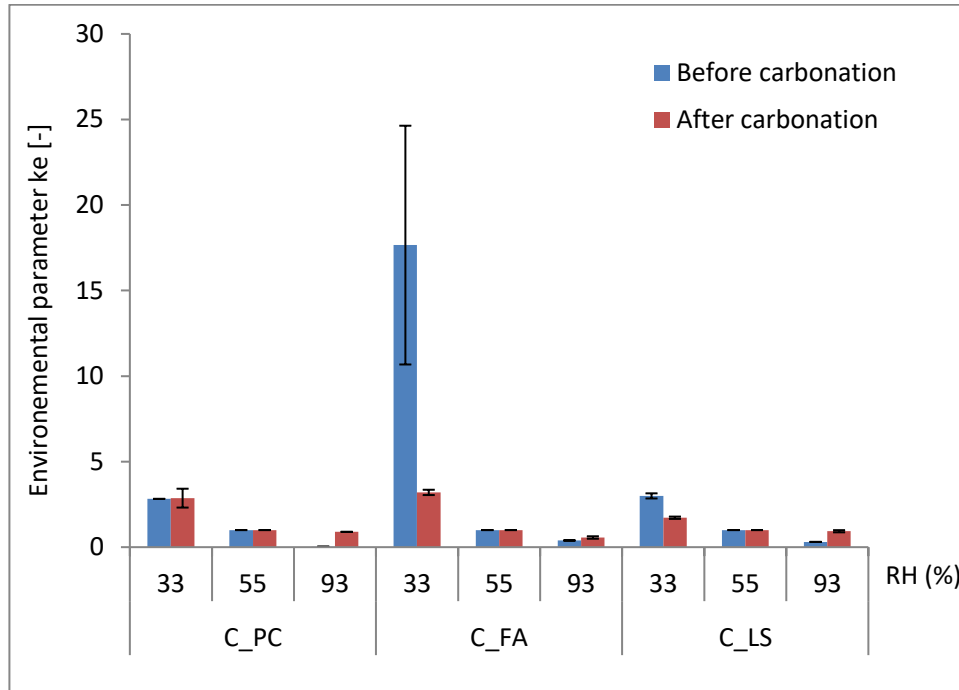
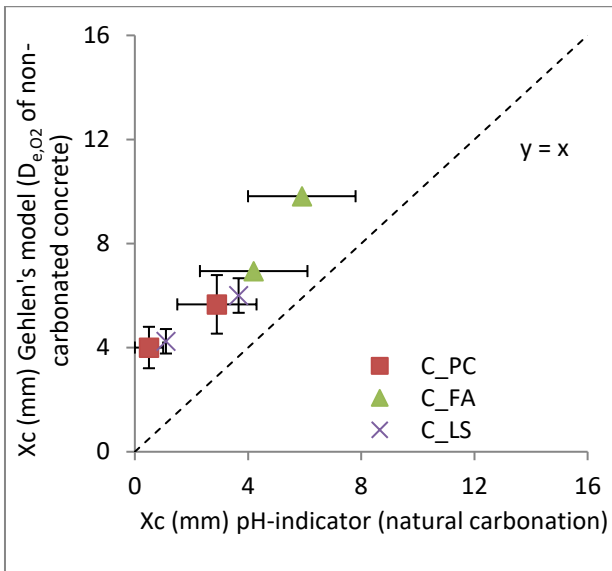


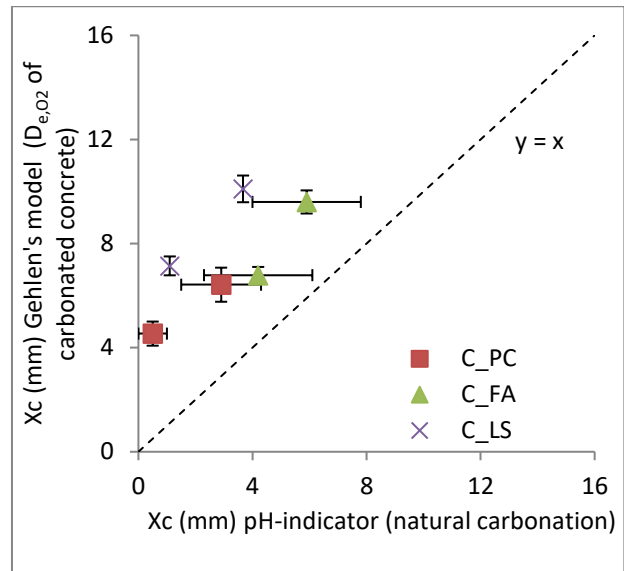
Figure 37: k_e parameter calculation determined using our experimental results

The high k_e value for C_FA is due to the 10 times higher value of D_{e,O_2} at 33%RH than 55% RH.

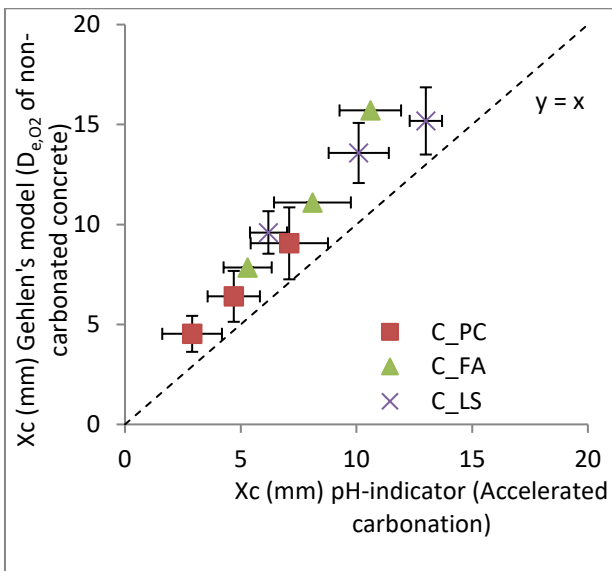
Figure 38 (a) and (b) compares the carbonation depths calculated using results of gas diffusion coefficient of concrete previously preconditioned at 55% RH and the pH-indicator results obtained under natural carbonation exposure. The inverse carbonation resistance of the tested concretes is shown in Table 23. The model overestimates the carbonation depths determined by means of the pH-indicator by a factor of 3.1 and 4 using the results of the diffusion coefficient of non-carbonated and carbonated concrete specimens respectively.



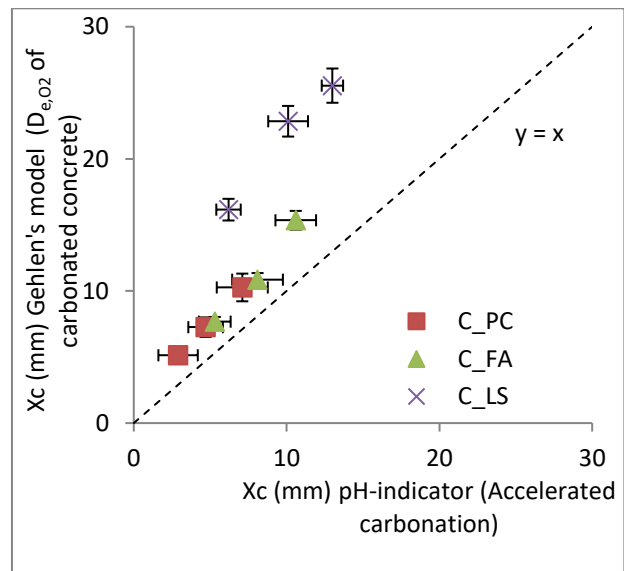
(a)



(b)



(c)



(d)

Figure 38: Comparison between the carbonation depths determined under natural carbonation using phenolphthalein and the carbonation depths obtained from Gehlen's model. (a) X_c predicted using the diffusivity of non-carbonated concretes and (b) X_c results from the gas diffusion of carbonated concretes

The carbonation depth predictions shown in Figure 38 (c) and (d) compare the pH-indicator results obtained under accelerated carbonation (section 3.4.2) using D_{e,O_2} results of non-carbonated and carbonated concretes respectively. In comparison with the previous results (Figure 38 (a) and (b)), the model results are in a better agreement with the pH indicator. In this case, the model overestimates the carbonation depth by a factor of 1.4 and 1.8 using the diffusivity results of non-carbonated and carbonated concretes respectively.

iii) Differences in the carbonation tests protocols

Differences between the carbonation depths obtained from the pH-indicator results and the models results can be attributed to one or a combination of the following factors:

- It should be kept in mind that the carbonation depth prediction models are determined using our experimental data, which are physical properties of the tested materials, whereas the phenolphthalein solution results are a pH-indicator ($\text{pH} < 9$). The overestimation obtained by the model results could be explained by the non-sharp carbonation front leading to a higher ingress of CO_2 (given by the models) than what is indicated by the phenolphthalein solution.
- The concrete specimens exposed to accelerated carbonation tests were oven-dried at 45°C for 14 days before the exposure to accelerated carbonation tests, whereas the specimens exposed to natural carbonation did not undergo this pretreatment. Therefore, the specimens tested to accelerated carbonation are much less water saturated than the specimens exposed to natural carbonation. This could explain the better correlation observed between the models and the pH-indicator results obtained under accelerated conditions. At the beginning of natural carbonation tests, specimens are water-saturated and not at moist-equilibrium with the environment.
- The diffusion coefficient of carbonated specimens is determined after carbonation of concrete specimens at 1% CO_2 while the accelerated carbonation depths determined by means of phenolphthalein solution are obtained from carbonation tests carried out at 3% CO_2 . Although Morandeu [24] states that the carbonation behavior of cementitious materials is comparable if the CO_2 concentration is lower than 3% .vol, the microstructure of the concrete, which controls directly the diffusivity, could be affected differently [69].
- For acceleration carbonation tests, the amount of carbonatable products is determined under natural CO_2 concentration while the carbonation depth of the concretes is determined under 3% CO_2 concentration.
- The models used to predict the carbonation depths using our experimental data are based on the assumption of a constant water content of the material, while the carbonation reaction is usually accompanied by water release.

5.5 Comparison between the carbonation test methods

Table 24 gives a summary of the main information about the pH-indicator test methods and the developed test methods in this thesis work. The main advantages of the developed test methods is their cost-efficiency, relatively time-saving nature (comparing to natural carbonation tests), their fair repeatability and reproducibly (depending on the hydric state of the tested material), and mainly the fact that these test method allow for the determination of the cementitious materials physical properties that control the carbonation progress while the pH-indicator tests give only information about the pH drop (<9). Still, the accuracy of the tests methods results is to be investigated on a large set of materials before any definite conclusions are made.

	pH-indicator test methods		Properties of the material	
	Natural carbonation (mm)	Accelerated carbonation (mm)	Gas diffusivity (m ² /s)	CO ₂ -binding capacity (g _{co2} g _{cement} ⁻¹)
Output	x _c	x _c	D _{e,O2}	Carbonatable products
Accuracy	Accurate	Above 3% CO ₂ by volume, the results accuracy is questionable. There is no international agreement on the test protocol	The models' results overestimate the pH-indicators results by a factor of around 4 and 2 for concrete exposed to natural and accelerated carbonation respectively The error percent for the prediction of the HCP carbonation depth is around 35%. The average percent error between the CO ₂ -binding capacity and TGA results is 24% and 35% for synthetic and HCP respectively.	
Repeatability (%) [165]	10	3.6 to 9.1	7 to 10	-
Reproducibility (%) [165]	25	5.8 to 10.3	4 to 48	<30
Cost-efficiency	Reasonable	Quite expensive depending on safety regulations	Cost-effective	
Test Duration	> 365 days	> 28 days	3 days to 4 weeks of preconditioning g. 30 min to 6 days measurement	48 hours to 15 days of preconditioning (still to be determined precisely) 8 to 28 days of exposure to carbonation 5 min to 20 min CO ₂ -uptake measurement
Detection limit	-	-	10 ⁻¹¹	IBR = 10 ⁻¹⁰ g _{co2} g _{cement} ⁻¹ s ⁻¹
Main advantages	Innovative materials can be tested and reliably compared to a reference material Standardized test method	Very simple Standardized test method	Simple Rapid Affordable Results are required for service life prediction models	
Main inconvenience	Time consuming	Expensive	Requires automatic resolution of Fick's second law of diffusion. Not commercially available at the moment. More investigations about the results accuracy are required. Non-standardized test methods	

Table 24: Comparison between the carbonation tests

Conclusions

Existing tests to determine the carbonation resistance either take more than 365 days (natural carbonation) or, if test duration is shortened by acceleration, results are criticized for lacking in transferability to field behavior. In view of this, new tests have been developed during this thesis work. The approach adopted in the study of carbonation is based on decoupling the main mechanisms that control this physicochemical process, i.e. gas diffusion and CO₂-binding capacity. The main results from this work allow drawing the following conclusions.

By using the newly developed methods, oxygen diffusivity and the amount of carbonatable products can be determined in a reliably short term comparing to natural carbonation tests (8 weeks at the latest instead of 1 year or more). Moreover, the developed test methods are capable of reproducing expected results: the decrease of the oxygen diffusivity with the degree of water saturation and hydration duration, and the dependence of the amount of carbonatable products on the relative humidity of carbonation.

For all tested materials, the oxygen-effective diffusion coefficient of carbonated samples is less dependent on the relative humidity of preconditioning comparing to the same materials before carbonation. The oxygen-effective diffusion coefficient shows a good correlation with the mean pore diameter of the tested HCPs (in log scale) when the degree of water saturation is lower than 30%. This result proves the dependence of the gas diffusivity on the pore size distribution and degree of water saturation of cementitious materials.

Although a decrease in the total porosity is observed after carbonation of all tested concrete mixtures and HCP specimens, the D_{e,O_2} can either increase or decrease after carbonation. Its variation depends on the material composition and degree of water saturation. Carbonation is found to lower the water retention capacity of concrete and HCP.

The CO₂ binding capacity and rate depend highly on the RH and material composition. The highest CO₂-binding capacity is noticed for portlandite, C-S-H, and OPC cement pastes exposed to carbonation at 93%. Still, the maximum theoretical binding capacity of all tested materials was not reached in the time scale of our experiments (28 days). The carbonation process was extremely slowed before all calcium oxide is carbonated. An agreement is found between TGA and the developed test method results.

Effective diffusion coefficient and CO₂ binding capacities determined for HCP and concrete were used as entry data of two literature analytical models. The results these models overestimate the pH-indicators results by a factor of around 4 and 2 for concrete exposed to

natural and accelerated carbonation respectively. A better agreement is observed for the HCP as the error percent for the prediction of their carbonation depths is around 35%, which could be explained by more homogenous nature of the HCP in comparison to concrete that results in more reliable D_{e,O_2} determination. The carbonation depth predictions made using the diffusion coefficient of non-carbonated or carbonated concrete specimens are comparable as carbonation affects the oxygen-diffusion coefficient especially at high relative humidity level. Still, a large set of concretes should be tested to obtain statistically representative data before definite conclusions can be made regarding the accuracy of the developed test methods results.

The assessment of the gas diffusivity and amount of carbonatable products of Portland cement pastes and blended pastes showed a comparable carbonation performance of the blended cement pastes cast at low water-per-binder ratio to Portland pastes. This provides a promising opportunity to decrease the clinker content in concretes without impacting negatively the durability performance related to carbonation.

Although the experimental methods were developed to study the carbonation performance, other applications could be considered.

The oxygen-effective diffusion coefficient test method can be also be used to control the quality of innovative binders and study the diffusion-based phenomena of these materials, as the gas diffusion coefficient is a specific durability indicator of cement based materials.

Oxygen diffusion coefficient could be used as an indicator for corrosion initiation, for the assessment of corrosion propagation period in wet environment, and for the design of cathodic protection.

The CO_2 binding capacity test method could also be used to study the CO_2 footprint of concrete. Cement industry is known for being a massive CO_2 emitter. Through carbonation, concrete has a CO_2 uptake potential and can take part in CO_2 capture and storage technologies. The effective carbonatable products of cement need to be experimentally assessed as well as the rate of CO_2 uptake.

The experimental data obtained from the developed test methods could be of high interest in the study and validation of existing models based on reactive transport in porous media.

Perspectives

The oxygen-effective diffusion coefficient test method can be improved by adding a relative humidity sensor (wireless) and a manometer inside the half-diffusion cell, while avoiding leakage problems. This would permit to monitor the RH level inside the cell and any possible pressure variation during the flushing period with nitrogen. It is also of importance to study the effect of pressure gradient that could result from multi-species diffusion, temperature and physical sorption of diffusing species on the oxygen-effective diffusion coefficient as the latter is highly dependent on these parameters. The experimental data fit could be carried out following Stefan Maxwell model that describes diffusion on multicomponent systems, which is the case in our study (air – nitrogen).

Although no clear correlation was found between the oxygen diffusion coefficient and the apparent permeability, it is of interest to further investigate the relation between these two properties (for concrete specimens dried at 40°C for example) before any definite conclusions.

The experimental data collected from this thesis work of oxygen-diffusion coefficient, degree of water saturation, pore size distribution and total porosity are of high importance in the development of a microstructural model allowing for the prediction of oxygen-effective diffusion coefficient from these parameters, in addition to the degree of hydration, and phase assemblage of the tested materials.

The CO₂-binding capacity test method can be further improved by increasing the measurement frequency during the first week of carbonation and avoiding carbonation of the tested materials during the preconditioning period, in order to minimize the integration errors. The experimental data of IBR and CBC obtained from the synthetic materials can be completed by further investigations (C-S-H phase with different C/S for instance) in an attempt to investigate a possible prediction of the carbonation kinetics of a hydrated cement paste from the kinetics of its constitutive phases.

The results obtained in this work and the following works would help to better understand the process of carbonation and to advance the carbonation modeling by providing new set of data for reactive transport models built by combining chemistry, microstructure and diffusivity. In a global perspective, this will contribute to a more accurate prediction of the service life of real concrete structures.

Appended documents

This thesis includes the following four appended documents, composed by three papers and the appendices.

Paper I	M. Boumaaza, B. Huet, G. Pham, P. Turcry, A. Aït-Mokhtar, C. Gehlen, A new test method to determine the gaseous oxygen diffusion coefficient of cement pastes as a function of hydration duration, microstructure, and relative humidity, Mater. Struct. 51 (2018).
Paper II	M. Boumaaza, P. Turcry, B. Huet, A. Aït-Mokhtar, Influence of carbonation on the microstructure and the gas diffusivity of hardened cement pastes, Constr. Build. Mater. 253 (2020) 119227.
Paper III	M. Boumaaza, B. Huet, P. Turcry, A. Aït-Mokhtar, The CO ₂ -binding capacity of synthetic anhydrous and hydrates: validation of a test method based on the instantaneous reaction rate. Cem. Concr. Res. 135 (2020) 106113

1 Paper I: A new test method to determine the gaseous oxygen diffusion coefficient of cement pastes as a function of hydration duration, microstructure, and relative humidity

1.1 Abstract

A new test method is developed to determine the gaseous oxygen-effective diffusion coefficient through hardened cement pastes conditioned at different relative humidity. The method relies on the measurement of gaseous oxygen accumulation in the downstream compartment of a diffusion cell and on the numerical fitting of a classical diffusion equation (Fick's second law) on experimental results. Oxygen-effective diffusion coefficients in the range of 10^{-6} m²/s to 10^{-11} m²/s can be determined using this test method. The present paper gives a detailed description of the experimental setup, the numerical procedure and presents results obtained on different Portland-based cement pastes. Cement pastes containing silica fume (SF) and slag are also tested. Samples are cast at two different volumetric water-cement ratios (1.6 and 1.9 m³/m³), tested at three different ages (from 1 day to 8 months) and preconditioned at different relative humidity (3% to 93%). Hence, the influence of cement composition, hydration duration, relative humidity and the water-per-binder ratio on the oxygen-effective diffusion coefficient D_{e,O_2} is investigated. Four microstructural properties: total porosity, pore-size distribution, hydration degree and the degree of water saturation of the tested samples are assessed as intermediate parameters to model oxygen diffusivity as a function of the mix design. Results show that well hydrated blended cement pastes have lower diffusivity than Portland pastes (over one order of magnitude for RH within [33-76] %), even though their total porosity was higher than Portland pastes. For all cement pastes diffusivity is found to be well correlated to the mean pore diameter of samples, at different degrees of water saturation.

1.2 Introduction

Cement-based materials are composite of a binding matrix primarily containing hydrated Portland cement paste, which is a porous medium with a continuous range of pore sizes from nanometers to micrometers. This porous network makes the concrete structure exposed to chemical reactions caused by the ingress of aggressive species from the environment. These species may lead to the decrease of its mechanical and durability performance, thus to a

reduction of its expected service life.

The target service life of a concrete in a real environment is often estimated using a performance approach based on so-called durability indicators, which are key material properties with regard to durability [84][166]. Depending on the damage mechanism of the material, adequate durability indicators should be chosen. For deterioration mechanisms that involve the transport of aggressive species in the gas phase, gas diffusion coefficient which describes a movement under a concentration gradient is the material property of interest in this regard.

In a porous media, the gaseous-effective diffusion coefficient is the key parameter to describe diffusion-based phenomena such as carbonation (diffusion of CO_2 [39]), drying (diffusion of water vapor [167]), and corrosion (diffusion of O_2 [168]). Usually, the effective diffusion coefficient $D_{e,g}$ is correlated to the corresponding diffusion coefficient of the gaseous specie through air $D_{0,g}$ by a correction term that accounts for the effects of the porous network connection, the material hydrothermal condition, and microstructure [74]. The effective diffusion coefficient for transport through the pores is macroscopic in nature since the entire pore space needs to be considered [9].

Additionally, as gas molecules travel through the porous media, three different diffusivity mechanisms can occur independently or simultaneously, depending on the characteristic of the diffusing gas species and the microstructure of the porous media. These mechanisms are : molecular diffusion, surface diffusion and Knudsen diffusion [99].

Note that usually the concrete penetrability property standardized and determined by most laboratories is the gas permeability [169]. However, it is the gas diffusion coefficient that is a particularly relevant input parameter for the service life prediction models [18][84]. We can state the example of Papadakis model for concrete carbonation [83] that requires a CO_2 diffusion coefficient and the amount of carbonatable products as input parameters to predict the carbonation depth. Indeed, carbonation is a result of the diffusion of gaseous CO_2 in the material and its reaction with calcium from the cementitious material. Consequently, it is relevant to experimentally determine the gaseous diffusion coefficient of cementitious materials.

In this context, we may cite the work of Namouniara [95] which involves the development of an experimental setup to measure the CO_2 effective diffusion coefficient on oven-dried, non-carbonated cement pastes. The CO_2 diffusion coefficient was investigated only at the dry state to avoid the carbonation of the sample during the test itself. Measurements are performed with pure CO_2 gas using a two-chamber cell at atmospheric pressure and ambient temperature

(20°C). Portland cement pastes, limestone pastes and pastes containing slag were tested. CO₂ effective diffusion coefficients determined in this study are ranked between 10⁻⁸ m²/s and 10⁻⁷ m²/s.

Another example of studies involving the development of test methods to measure the gas diffusion coefficient on cementitious materials is the experimental setup developed initially by Lawrence(1984) [8] and used by Villani [99] and Wong [86]. The diffusion test consists of exposing each side of a disc-shaped concrete sample to a stream of pure nitrogen and pure oxygen, respectively at the same pressure and temperature, and measuring the concentration of oxygen incorporated in the nitrogen stream after it has passed over the concrete specimen. The diffusion coefficient is then computed using the equation introduced by Lawrence [8]. Values of oxygen diffusivity in the study carried out by Villani [99] are in the range of 10⁻⁸ m²/s to 10⁻⁷ m²/s for mortar samples and between 10⁻⁹ m²/s to 10⁻⁷ m²/s for concrete samples. These values correspond to a W/B between 0.3 and 0.7 and to preconditioning relative humidity between 50% and 65%.

We also cite Houst's experimental setup that allows for the simultaneous determination of effective diffusion coefficients of two gases (CO₂ and O₂) as a function of the relative humidity. The measuring cell is divided into two chambers by a porous disc of hydrated cement paste at a temperature range from 20°C to 25°C. Oxygen and carbon dioxide diffuse from the upper chamber through the sample into the lower chamber, where the two gases are monitored as a function of time by gas analyzers. O₂ and CO₂ effective diffusion coefficients are calculated by fitting the experimental data to an empirical function proposed by Papadakis [170]. Oxygen and carbon dioxide diffusion coefficients are found to vary between 10⁻⁹ m²/s and 10⁻⁷ m²/s for carbonated cement pastes and mortars at two W/B (0.4 and 0.5) and different relative humidity (from 48% to 95%) [10]. The diffusion coefficient of other gases like hydrogen and xenon was experimentally determined by Sercombe [9] on non-carbonated pastes pre-conditioned in specific atmospheric conditions (from dry state to 100% RH). Results obtained for CEMI and CEMV samples ranked between 10⁻⁷ m²/s to 10⁻¹² m²/s.

In this contribution, we attempt to develop and validate a simple test method that allows for the measuring of the gas diffusion coefficient through cement pastes. Since this material property is highly dependent on mix design parameters, the degree of hydration, and environmental parameters [9], measurements are made at different hydration durations and degrees of water saturation (or alternatively relative humidity) and with two different water-per-cement ratios. For an investigation of this kind, it is necessary that the pore microstructure of the specimen to be tested does not change during the test itself; for this reason, it is relevant to perform the test using an inert gas with respect to most hydration products. Therefore, the most convenient

gas specie for this experimental investigation is atmospheric oxygen. Carbon dioxide and other gases, effective-diffusion coefficients can be deduced from that of oxygen using a simple model developed by Thomas Graham[140]. Note that this law is found to be valid only in the case of Knudsen diffusion [171][172].

The two main objectives of this study are summarized as follows: first, developing and checking the reliability and range of validity of a simple technique to determine the oxygen diffusion coefficient using gaseous oxygen from the atmosphere. Second, investigating the influence of material composition, degree of water saturation, and hydration duration on D_{e,O_2} of Portland-based cement pastes.

Finally, it is worth noting that, to our knowledge, there is currently no standardized diffusion test for cement pastes or concrete, which is another reason why this paper investigates the effect of different material properties on the oxygen-effective diffusion coefficient.

1.3 Materials and methods

1.3.1 Tested materials

The present research focuses on investigating the diffusivity of thin, hardened cement pastes rather than concrete or mortars for the following reasons: cement paste fraction of mortar or concrete usually contributes for the greatest part of the porosity and thus determines their transport properties to a great extent [9][173]. Conditioning thin cement paste samples at different relative humidity and testing their oxygen diffusivity can be carried out in limited time, while testing concrete or mortars requires experimental validation of the choice of the tested specimen thickness in relation to the size of the grains of cement or aggregates of concretes. Although they contain more porosities in the aggregate-paste interfacial zone [174], which leads to the assumption that their transport properties are going to be higher, a study made by Wong [56] has shown that their contribution is small on the overall transport properties.

The cement used to prepare the samples is an ordinary Portland cement for which the chemical composition is shown in Table 25.

	OPC	Slag
SiO ₂	20.4	36.1
Al ₂ O ₃	5.5	11.4
Fe ₂ O ₃	2.5	0.2
CaO	64.8	42.1
MgO	1.16	7.6
K ₂ O	0.23	0.4
Na ₂ O	0.20	0.3
SO ₃	3.34	0.9
TiO ₂	0.15	0.5
Mn ₂ O ₃	0.09	0.6
P ₂ O ₅	0.27	-
ZrO ₂	-	0.02
Cr ₂ O ₃	0.02	-
SrO	0.06	0.04
LOI	1.09	-
CO ₂		0.17

Table 25: Chemical composition of ordinary Portland cement and slag

Three cement pastes were tested: pastes with OPC only and two paste mixtures prepared by replacing OPC with 50% slag and 10% silica fume by mass.

These additions grain size distribution, fineness and specific surface, are given in Table 26.

	D10 μm	D50 μm	D90 μm	D(4,3) μm	Density g/cm ³	Specific surface [BET] cm ² /g
Slag	2.87	15.06	36.27	17.63	2.91	3656.0
Silica Fume	>45 μm = 1.5%				2.28	>1.5x10 ⁵
OPC	2.68	16.94	51.2	22.48	3.14	3630.0

Table 26: Tested materials grain size distribution density and specific surface

All pastes are cast at two constant volumetric water-to-cement ratios: 1.6 and 1.9 (which corresponds to 0.5 and 0.6 by weight for OPC pastes). Pastes are cast with respect to a volumetric W/B so that the initial porosity of all the samples is similar (62% and 65% theoretical initial porosity, respectively, assuming that the samples have no air content) and to study samples with a wide range of pore structure characteristics [175].

The pastes are cast in cylindrical molds (4*11 cm), rotated for 24h to avoid any sedimentation and stored at a relative humidity of 100% before being sawed under water. To investigate the

influence of maturity, specimens were left in the mold at 100% RH and tested after different hydration durations, namely: 1 day, two months and eight months for OPC samples, and 7 days, two months and eight months for OPC_SF and OPC_Slag mixes.

In the case of 1 or 7 days hydration duration, hydration is stopped by immersing the samples in an organic solvent (isopropanol) to drive off the free water, and then samples are placed under vacuum for 24 hours to drive out the solvent. Hydration stopping of other samples was achieved by drying the samples at different relative humidity (RH) in well-aerated chambers at two and eight months. We assume that hydration stops when the relative humidity drops below 80% [176].

Samples are preconditioned at the following relative humidity by means of saline solutions at a temperature of 20°C : 33%(MgCl₂), 55%(Mg(NO₃)₂), 76%(NaCl), 86%(KCl), 93%(KNO₃). Samples that are conditioned at 65% RH were stored in a relative humidity controlled room. Dry samples were oven dried at 80°C, which corresponds to a relative humidity of 3%, assuming a dew-point of 12°C since laboratory relative humidity is 70% at 20°C. The moisture equilibrium state is assumed to be reached at a given preconditioning relative humidity when the mass variation within a week is no more than 0.05% [86]. This equilibrium is usually reached after four or five weeks.

For this test method, it is recommended to prepare samples thin enough to reduce moisture equilibrium time and to allow oxygen to diffuse through them in a relatively short time. Therefore, discs of 3 mm thickness and 4 cm diameter are sawed. These samples are cut from the center of the specimens, and the outer surfaces were not tested. Since these samples are to be tested for a transport property, water content should not increase during the diffusion test itself. Therefore, samples' weight is checked after each diffusion test, and the mass variation is found to be negligible (0.02% < 0.05%). The oven-dried samples were placed under a vacuum for 24h to cool down at laboratory temperature (20°C) before each diffusion test.

Sample treatment before and during testing may cause microcracks. However, according to Wong [56], oxygen diffusivity was found to vary only by a factor of 2 at most for samples with microcracks dried at 105°C.

On the other hand, concrete in real structures is almost always micro-cracked. Testing only laboratory materials that did not undergo severe environmental stress may be unrepresentative.

In the following parts of this paper, samples will be named using the following convention:

1.3.2 Diffusion test protocol

The testing method gives an accumulation of O₂ concentration from ambient air in the downstream compartment called the “diffusion cell” until the steady state is reached. The main element of this experimental setup is the diffusion cell shown in Figure 39. It consists of a high-density polyethylene cell, separated from the ambient air by the sample, which is placed between two silicon joints compressed by firmly tightening the screw on them to ensure air tightness and unidirectional diffusion flux. The oxygen sensor is also surrounded by an O-ring to minimize leakage of the setup.

The volume of the diffusion cell is flushed at the beginning of the test with pure nitrogen. This gas is chosen because it is inert and safe. The N₂ inlet and O₂ outlet (plug and play system) are designed to avoid any residual overpressure in the cell and to ensure gas tightness and ease of handling during the flush.

The cell geometry is determined to enable the diffusion coefficient to be obtained with sufficient reliability: minimizing the internal cell volume (113 cm³) helps to avoid hydric changes of the sample during the test and to position the sensor as close as possible to the sample. Plus, minimizing the cell volume allows for a reduction of the duration to reach the steady state, hence, the diffusion test duration. This cell design also allows a range of specimen sizes to be examined: from 2 mm to 16 mm.

A diffusion test consists of placing the sample and the oxygen sensor in the cell and flushing the inside volume of the cell with nitrogen (this step usually takes 15 to 20 seconds to reach a value of 0.3% of oxygen inside the cell, which avoids drying the sample during the flush). The cell is then placed inside a climate chamber pre-equilibrated at the same relative humidity used for the sample preconditioning. Oven-dried samples are placed in a chamber with silica gel during the diffusion test. The relative humidity inside is 26%. These samples' diffusion test lasts from 30 min to 2h at the longest. Mass gain is checked after each diffusion test and found to be negligible <0.02%.

The climate chamber atmosphere in contact with one face of the sample also acts as a steady-state concentration of oxygen (20%). All diffusion tests are performed under constant temperature (20°C) and pressure (1atm).

In the inside volume of the cell, the concentration of oxygen diffusing from the ambient air of the climate chamber through the sample is measured continuously by the sensor.

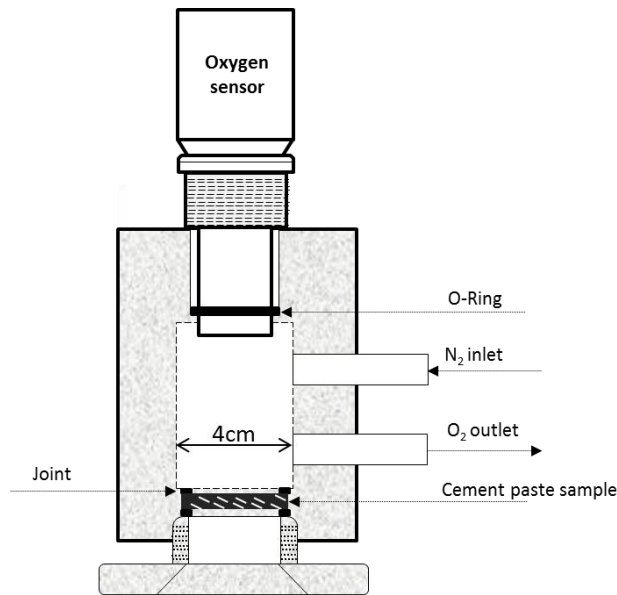


Figure 39: Oxygen diffusion cell sketch

This sensor continuously measures the oxygen gas concentration using an electrochemical cell with an accuracy of 1%, which is an acceptable level in the range of our measurements 0% to 21% volume O₂ as no noise was observed on the collected data. Note that several diffusion cells are used in order to perform diffusion tests in parallel.

1.3.3 Determination of the effective diffusion coefficient

Fick's second law is the governing differential equation that evaluates gaseous diffusion through a porous media. Neglecting the absorption process and gas solubility in water confined in the media pores, considering one dimensional gas diffusion, and given the assumption that there is no crack in the material, Fick's second law can be written as follows [39].

$$\phi(1 - S_l) \frac{\partial C}{\partial t} = \frac{\partial}{\partial x} (D_{e,O_2} \frac{\partial C}{\partial x}) \quad \text{Equation 38}$$

Where D_{e,O_2} is the oxygen-effective diffusion coefficient, C the oxygen concentration, ϕ the total porosity and S_l the water saturation degree of the sample. Note that Equation 38 is also solved in the inside volume of the cell to account for transient diffusion; for this volume we have porosity = 1, water saturation = 0 and $D_{O_2-N_2} = 10^{-5} \text{ m}^2/\text{s}$.

The test method output is an accumulation curve of oxygen concentration as a function of time. The oxygen diffusion coefficient is calculated from the automatic analysis of this curve, using a Python program (Scipy.optimize.curve_fit [177]) that minimizes the difference between experimental data and Fick's second law model results by means of non-linear least squares

fitting.

The resolution of Fick's second law is done using a Python finite volume package for solving partial differential equations called FiPy [178].

The program outputs are the effective diffusion coefficient D_{e,O_2} and the uncertainty on the calculation of D_{e,O_2} . An example of the results of the calculation of oxygen-effective diffusion coefficients from experimental data is given in Figure 40. This program allows for the calculation of oxygen-effective diffusion coefficients over five orders of magnitude and computes the relative standard error of the fitting, which is found to be negligible (0.1% to 1%).

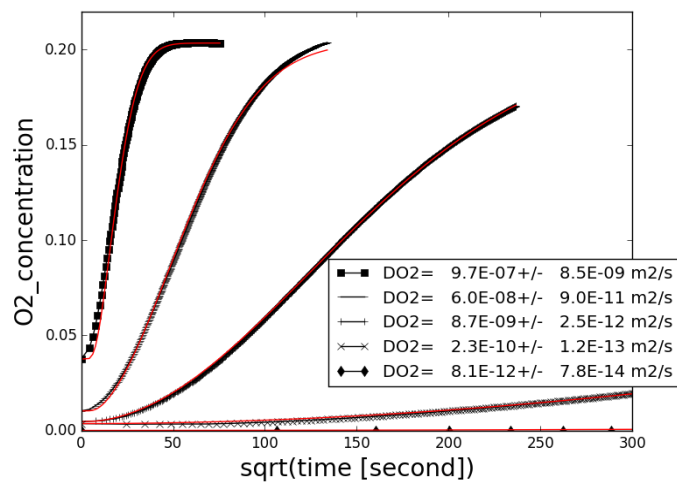


Figure 40: Example of fitting result over five orders of magnitude D_{e,O_2} . The bottom curve presents a leakage curve ($D_{e,O_2}= 8.1 \times 10^{-12} \text{ m}^2/\text{s}$)

1.3.4 Other test procedures

Total porosity (i.e. the volumetric proportion of voids) is determined by water soaking under the vacuum following the French standard NF P18-459. The dry mass of the samples is given by oven-drying at 105°C. The following weights were recorded:

- m_{RH} : mass of the sample when equilibrated at its corresponding RH.
- m_{dry} : dry mass of the sample (dried in the oven at 105°C).
- m_{air} : mass in the open air of the water-saturated sample.
- m_{hydro} : hydrostatic weight, mass of the water-saturated sample by immersion in water under a vacuum for 48h.

The total porosity and water saturation are then obtained from the following equations:

$$\phi = \frac{m_{\text{air}} - m_{\text{dry}}}{m_{\text{air}} - m_{\text{hydro}}} \quad \text{Equation 39}$$

$$S_l = \frac{m_{\text{RH}} - m_{\text{dry}}}{m_{\text{air}} - m_{\text{dry}}} \quad \text{Equation 40}$$

Since the oxygen diffusion coefficient depends highly on the microstructural properties, it is also of interest to get information about the pore-size distribution, a property that affects pores' degree of water saturation. Therefore, mercury intrusion porosimetry [179] is performed on one sample of each mix composition for the three different hydration durations. MIP samples are cored out from the hardened cement paste and their diameter is 1cm. These samples are pre-dried at 45°C for 24H.

The influence of these materials' hydration degree on the oxygen-effective diffusion coefficient is also of great relevance. Therefore, OPC and OPC_Slag hydration degrees at early age (1 day for OPC and 7 days for OPC_Slag), two months, and eight months of hydration are assessed using the XRD/TGA technique (for OPC samples) and scanning electron microscopy SEM (for OPC_Slag samples).

For Portland cement pastes, combining XRD with TGA analysis allows for quantitative measurement of the degree of dissolution of un-hydrated cement phases [109].

For slag cement pastes, the SEM method can estimate the degrees of hydration of both cement and slag in the mix and was found to be more reliable than other methods [128]. The strategy used in this work is detailed in [127] and [129].

However, a reliable determination of the degree of hydration for SF samples becomes difficult using SEM or XRD, as SF is a very amorphous product. Therefore, their degree of hydration was taken from the literature from the work of Muller [180], who quantified the reaction degree of 10% silica fume cement pastes with a ratio of W/B=0.5 using the ²⁹Si MAS NMR technique.

1.4 Results

1.4.1 Test method validation

The experimental setup gas tightness is evaluated by performing a blank test. The test consists of measuring a leak rate by filling the cell with nitrogen, replacing the sample by a gastight disc and measuring the variation of oxygen concentration inside the cell. 11 cell leakage rates are measured for 20 days, providing an average leakage rate of 3.6% in oxygen concentration per month.

For each leakage test of a diffusion cell, we calculated the equivalent oxygen-effective diffusion coefficient. The average value of this coefficient calculated on six cells is $1.74 \times 10^{-11} \text{m}^2/\text{s} \pm 9 \times 10^{-12}$. The leakage tests set the lower limits for the oxygen-effective diffusion coefficient to be determined, which corresponds, in our case to oxygen diffusion coefficients of values three or four times less than $8 \times 10^{-12} \text{m}^2/\text{s}$ to determine a value of D_{e,O_2} with sufficient reliability.

In order to assess the uncertainty of the method, repeatability and reproducibility are studied. First, for repeatability to be established, the following conditions were respected: tests were performed in the same location using the same diffusion setup by the same operator, under the same conditions, and over a short period of time [181]. Diffusion coefficient measurements are repeated 5 times on each of the three samples. The objective is to then quantify the agreement and reliability of measurements. This agreement is described by reporting a repeatability coefficient that can be estimated using the within-subject standard deviation, which is the standard deviation of the measurement errors [181]. For our cells, this coefficient is found to vary between 7% and 10%, which denotes that the absolute difference between two measurements on the same sample is expected to differ no more than the repeatability coefficient on 90% of occasions. Variability in measurements made on the same subject in a repeatability study can then be ascribed only to errors due to the measurement process itself.

As for reproducibility, we investigated the closeness of agreement between the results of diffusion tests conducted in different climate chambers equilibrated at the same relative humidity of the samples to be tested, with three different diffusion cells on three replicates. Reproducibility is then qualified with a standard deviation of the three measurements. An example of a diffusion coefficient value determined on three replicates is $D_{e,O_2} = 2 \times 10^{-7} \pm 1 \times 10^{-9} \text{m}^2/\text{s}$. The low standard deviation ($1 \times 10^{-9} \text{m}^2/\text{s}$) indicates that the three diffusion coefficients tend to be close to the average value.

A further way to report the reproducibility is to report the coefficient of variation (ratio of the standard deviation to the mean). During this work, 270 diffusion tests are performed, and an average value of the coefficient of variation is found to be 15%. Note that the decision as to whether these results are to be judged 'sufficiently precise' depends on how the measurements' results are to be used.

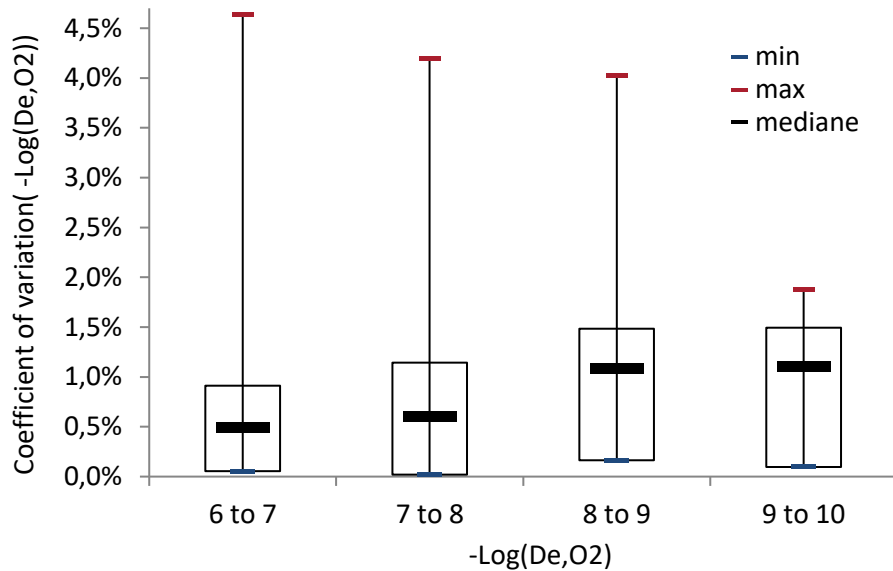


Figure 41: Box plots of the coefficient of variation corresponding to four orders of magnitude of the diffusion coefficient experimentally determined

Another way to describe the data of the variation coefficient calculated from the measurement of the three replicates is the box plot (or whisker diagram). It is a standardized way of displaying the distribution of data based on the five number summaries: minimum, first quartile, median, third quartile, and maximum. This way we can display the full range of variation (from min to max), the likely range of variation (the inside of the box), and a typical value (the median) [142].

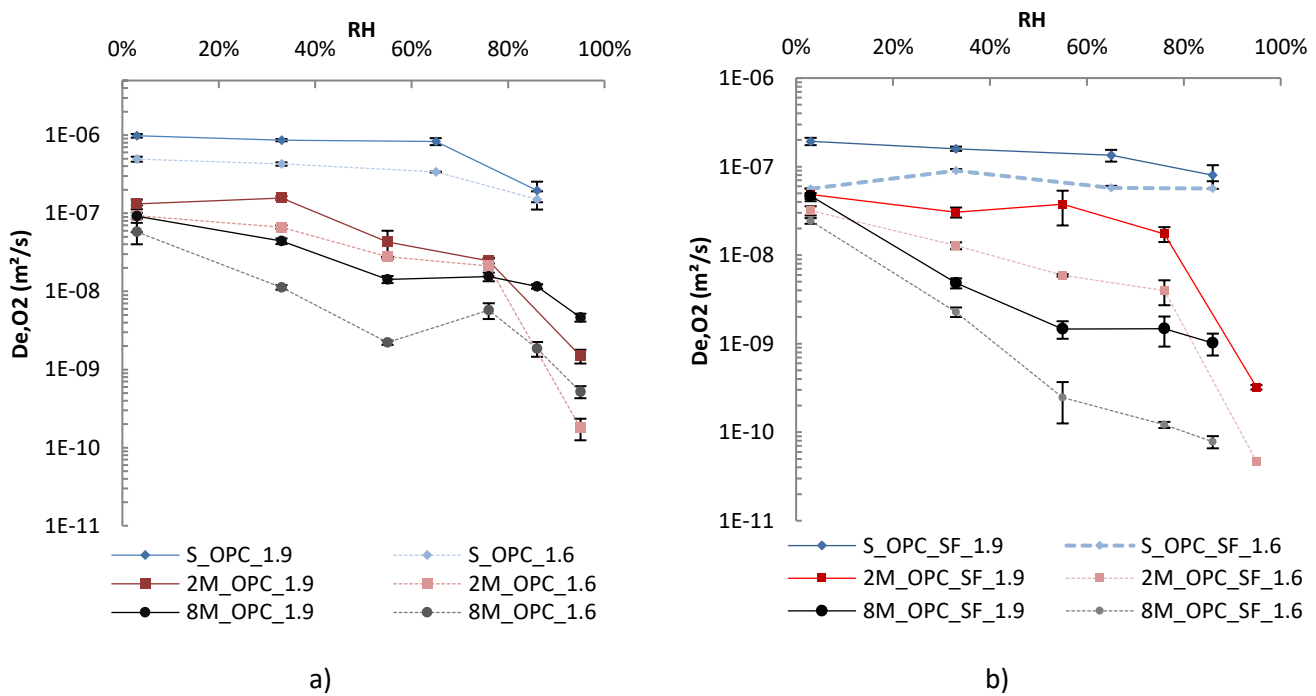
Figure 41 shows four box plots, each corresponds to datasets of the variation coefficient of experimentally determined diffusion coefficients in Log-Scale. The spacing inside each box indicates the degree of dispersion of the variation coefficient. The mean value of the diffusion coefficient of these four box plots is in order: $3.4 \times 10^{-07} \text{ m}^2/\text{s}$, $4.2 \times 10^{-08} \text{ m}^2/\text{s}$, $3.3 \times 10^{-09} \text{ m}^2/\text{s}$ and $4.5 \times 10^{-10} \text{ m}^2/\text{s}$. For each respective category we have the following amounts of data: 20, 35, 18 and 12.

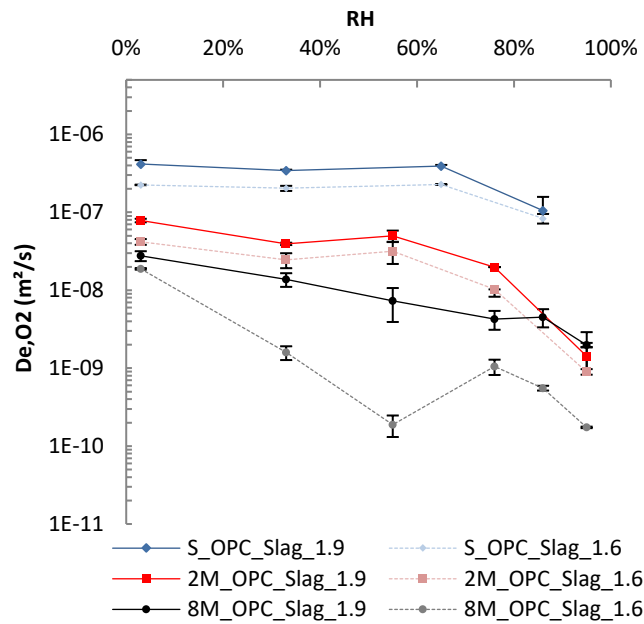
1.4.2 Results of diffusion tests

Results of oxygen-effective diffusion coefficients obtained on OPC, OPC_SF and OPC_Slag pastes as a function of relative humidity are presented in Figure 42. Each oxygen-effective diffusion coefficient value is an average of three replicates, and precision is expressed as the standard deviation. The measured diffusion coefficient ranged from 10^{-7} and $10^{-6} \text{ m}^2/\text{s}$ for hydration-stopped samples (denoted S) and from $10^{-11} \text{ m}^2/\text{s}$ and $10^{-7} \text{ m}^2/\text{s}$ for two-month (2M) and eight-month (8M) hydrated samples. The figure shows that the oxygen diffusion coefficient slightly decreases with the increase of relative humidity for hydration-stopped samples,

whereas it decreases significantly with relative humidity for fully hydrated samples. For all samples, the diffusion of oxygen through dry pores is much faster than through wet pores: the oxygen diffusion coefficient is half an order of magnitude higher for dry and hydration-stopped samples and three orders of magnitude higher for dry hydrated samples. These results are consistent with other studies carried out on similar cement pastes using a different test method that also showed a great decrease in gas diffusivity for $RH > 55\%$ [161][56].

It is also seen that lowering the volumetric W/B ratio can substantially decrease the oxygen diffusion coefficient by half to one order of magnitude, depending on the binder type. Note that OPC_SF samples hydrated for eight months are not tested at $RH = 93\%$, as measurements were below the detection limit: the calculated oxygen diffusion coefficient is below the order of magnitude of the leakage-equivalent diffusion coefficient ($1.7 \times 10^{-11} \text{ m}^2/\text{s}$).





c)

Figure 42: Experimentally determined oxygen-effective diffusion coefficients for (a) OPC samples, (b) OPC_SF samples and (c) OPC_Slag samples

1.4.3 Other microstructural properties' measurements

i) Total porosity and pore-size distribution

For hardened cementitious materials, two types of porosity are usually distinguished: gel porosity (i.e. internal porosity of the C-S-H gel phase) and capillary porosity[182]. The latter is a residue of the space between the anhydrous grains that has not been filled by hydration products [183]. This space is a function of the water-per-binder (W/B) volumetric ratio and hydration duration. Therefore, in this study, water porosity is measured at three different ages for all tested samples. Results are shown in Table 27. As expected, total porosity slightly decreases with hydration duration between two months and eight months. By increasing the volumetric W/B from 1.6 to 1.9, total porosity is increased by around 3% at three hydration durations, which corresponds to the initial effect (62% and 65%).

Paste sample \ Hydration duration	T=0	T= 1day(OPC) or 7 days (others)	T= Two months	T= eight months
OPC_1.6	62	49.2	45.5	41.7
OPC_1.9	65	53.5	48.3	45.4
OPC_SF_1.6	62	48.3	47.0	44.9
OPC_SF_1.9	65	52.5	50.8	51.0
OPC_Slag_1.6	62	51.5	45.8	45.4
OPC_Slag_1.9	65	54.4	50.6	47.7

Table 27: Water porosity (%) at different hydration durations for all tested materials

However, total porosity is seen to significantly decrease with hydration duration at early age (1 and 7 days), which can be explained by the fact that the development of the microstructure is highly controlled by the critical first few days after mixing [183]. The porosity of SF and slag cement pastes is slightly higher (1% to 6%) than that of Portland cement paste, even at eight months hydration. These results are in agreement with the work of Yu [124] who found that total porosity of cement pastes blended with fly ash (30% and 50% replacement at W/B=0.4) was higher than Portland pastes at ages up to 3 years.

For all other samples, we can see that the total porosity varies slightly as the hydration proceeds from 1 day to eight months. Therefore, in order to provide important insights about the microstructure and the porous system of our materials, changes in pore-size distribution with hydration duration are obtained by mercury intrusion porosimetry (MIP). Results are shown in the Appendix Fig 72. Capillary pores that are closely related to mass transport are reported be within the size of 0.01 μ m to 10 μ m [182], this range of pore size is covered by the results from MIP.

Observation of these results reveals that most of the pastes measured here have a pore-size distribution with a mean pore diameter of less than 10 μ m, except for samples with silica fume for which the pore-size distribution is less than 1 μ m. These results also show that hydration causes the main porous mode to decrease this may be due to the progress of cement hydration, which gradually decreases the volume fraction of large pores. It is also seen that an increase in the volumetric water-per-binder ratio causes a shift from the main porous mode to larger diameters.

ii) Water vapor sorption/desorption isotherm

Water vapor sorption/desorption isotherms, expressed in terms of water saturation degrees,

are graphically presented in Figure 43. These results are obtained only by sorption for hydration-stopped samples and only by desorption for other samples. At 3% RH, all pastes with different volumetric W/B ratios and at different hydration durations are in the same range of water saturation: [0%, 10%]. From a relative humidity of 33%, the degree of water saturation present in the samples increases substantially with hydration duration due to a change in the pore structure as hydration proceeds. The water retention capacity at both early ages and 2 months is not significantly reduced when the volumetric W/B ratio is reduced from 1.9 to 1.6 m³/m³. However, at the hydration age of 8 months, a slight increase in water saturation is observed when this ratio is reduced.

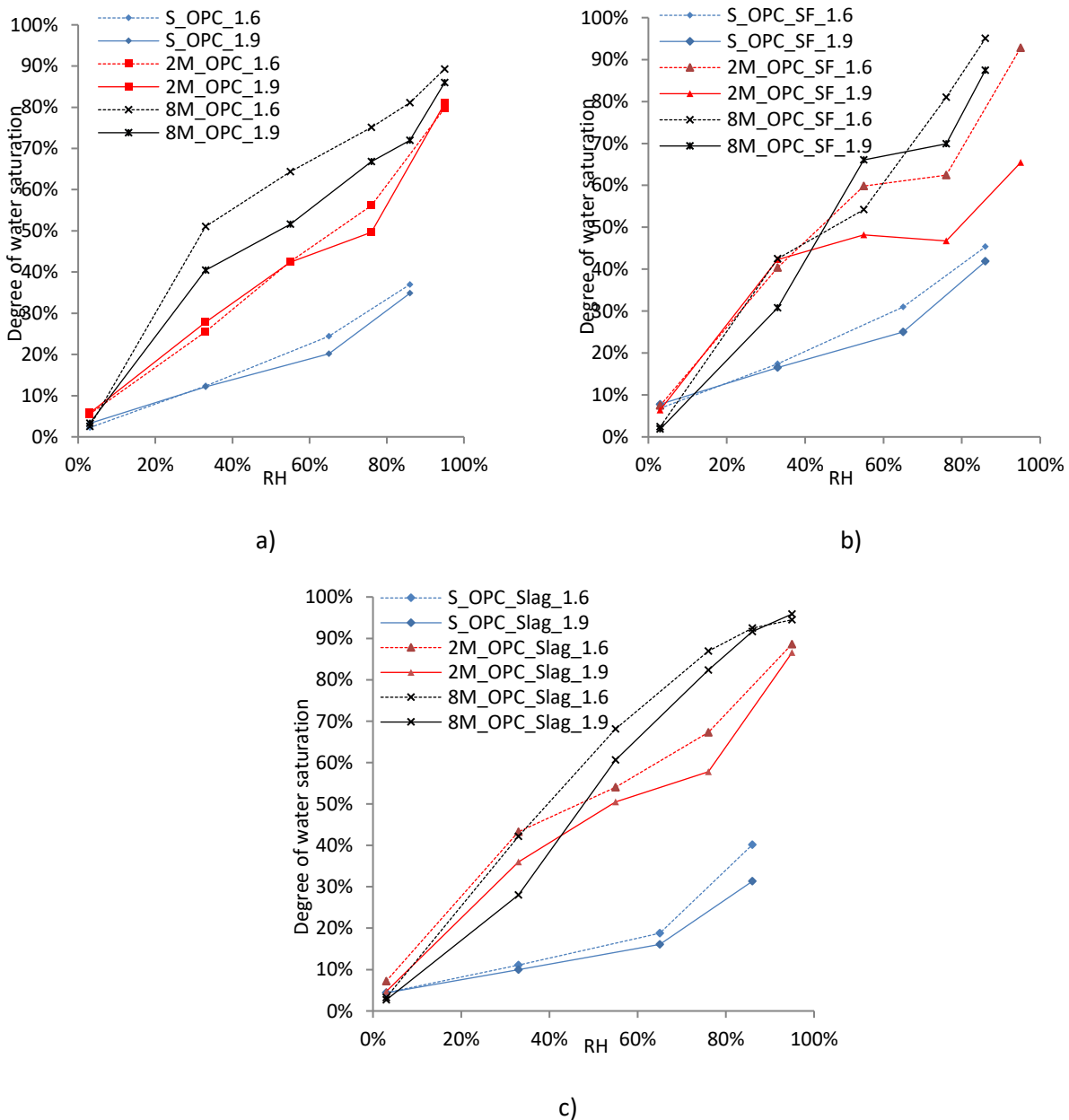


Figure 43: Water saturation degree at different relative humidity for: (a) OPC samples, (b) OPC_SF samples and (c) OPC_Slag samples

iii) Degree of hydration of the tested samples

The degree of hydration of the sample is also critical information required for the full understanding of the material transport behavior, thus samples' degree of hydration is determined through the X-ray diffraction (XRD) technique and thermogravimetric analysis (TGA) for OPC samples [28], after all diffusion tests are concluded. For that, samples are dried in the oven at 105°C until constant mass, crushed/milled, and sieved through a 63µm sieve. OPC_Slag samples' degree of hydration was estimated by scanning electron microscopy [184][179]. OPC_SF pastes degree of hydration was taken from previous works in literature [175][180]. Results are shown in Table 28.

Hydration duration	mix	Additions' degree of hydration	OPC degree of hydration	Determination method
1 day and 7 days	S_OPC_1.6	-	62.0%	TGA/XRD
	S_OPC_1.9		65.0%	
	S_OPC+SF_1.6	43.0%	80.0%	Literature
	S_OPC+SF_1.9			
	S_OPC+Slag_1.6	0.0%	89.8%	SEM
	S_OPC+Slag_1.9			
2 months	2M_OPC_1.6	-	91.0%	TGA/XRD
	2M_OPC_1.9		93.0%	
	2M_OPC+SF_1.6	70.0%	91.0%	Literature
	2M_OPC+SF_1.9			
	2M_OPC+Slag_1.6	46.1%	94.1%	SEM
	2M_OPC+Slag_1.9			
8 months	8M_OPC_1.6	-	95.5%	TGA/XRD
	8M_OPC_1.9		95.9%	
	8M_OPC+SF_1.6	80.0%	97.0%	Literature
	8M_OPC+SF_1.9			
	8M_OPC+Slag_1.6	77.8%	98.8%	SEM
	8M_OPC+Slag_1.9			

Table 28: Degree of hydration of tested pastes at different hydration durations

1.5 Discussion

1.5.1 Test procedure

The diffusion test developed during this work allows for the determination of the oxygen-effective diffusion coefficient of paste samples under well-controlled laboratory conditions. This experimental setup provides reproducible and repeatable diffusion coefficients over 4 orders of magnitude [10^{-6} , 10^{-11} m²/s]. Furthermore, the test method has a short time of measurement at dry state: 30 to 45min. It takes less than 5 weeks to stabilize the 3 mm thickness samples at a

certain relative humidity (for a water equilibrium criteria: less than 0.05% mass variation in a week) and from 30min to four weeks to make most measurements, depending on the water saturation degree of the sample and its composition. Two additional big advantages of this experimental set-up are, first, it does not require an oxygen bottle, thus no safety problems could arise, and, second, it contains low-priced equipment that is affordable for most laboratories.

However, while the basic concept of the test method is relatively straightforward, handling the experimental results involves a numerical resolution of Fick's second law of diffusion, taking into consideration the transient conditions. In addition to that, the determination requires knowledge of the total porosity and degree of water saturation of the sample.

Note that the leakage test of the experimental setup sets the detection limit of oxygen-effective diffusion coefficients: values below 10^{-12} m²/s cannot be determined with good precision. In this context, we refer to the previous works of Peng on the development of a diffusion chamber to measure oxygen gas diffusivity for different rocks and construction materials. These chambers' leakage rate corresponded to a diffusion coefficient of 4.8×10^{-9} m²/s, which is due mainly to the contact between the sample and its holder [100].

1.5.2 Effect of the water saturation degree on the diffusion coefficient

Results on oxygen diffusion coefficient as a function of relative humidity show that the diffusivity of gaseous oxygen through cement pastes is quite sensitive to hygroscopic conditions. Relative humidity of preconditioning determines the degree of saturation of the pores that is directly related to the percentage of pores available to gas transport. The oxygen-effective diffusion coefficient is found to vary between 10^{-6} m²/s for dry samples and 4×10^{-11} m²/s for samples at high relative humidity.

At intermediate relative humidity (<55%), samples appear to be available to gas transport mainly due to the increase of the pore space available to gases and due to the increase of connectivity and to the reduced tortuosity of the gas path [99]. These results are in agreement with some literature findings that suggest that at a relative humidity lower than 60%, the variation in transport properties is negligible because most of the pores relevant to transport (capillary pores and microcracks) have already been emptied [185][9].

On the other hand, samples conditioned at high relative humidity contain many saturated pores that are effectively blocked and do not contribute to gaseous oxygen transport. Gaseous oxygen can diffuse through water-filled space or through air-filled space but, in the former case, the process is 10^4 to 10^5 times slower than in the latter [186], because oxygen has a low

solubility in water (10^{-4} mol/l). In addition to that, at high relative humidity ($RH > 60\%$), mobility of oxygen in the gas phase is limited by the comparatively high-water content in the pores. These results are in agreement with some previous works that suggest that the influence of pore saturation on the transport properties of cement-based materials is only significant when the preconditioning relative humidity (RH) is greater than about 60% [167][145].

1.5.3 Influence of the degree of hydration

Regarding the impact of hydration duration on the oxygen-effective diffusion coefficient, results show that this coefficient is greatly affected by the degree of hydration: good and prolonged hydration reduces the oxygen diffusion coefficient by up to four orders of magnitude at high relative humidity, and a constant degree of hydration. Note that if the hydration is stopped at early age by drying at low relative humidity, it could restart at high relative humidity or exposure to water during the water porosity measurements [176].

The oxygen diffusion coefficient's variation with relative humidity is more pronounced for fully hydrated samples. At high relative humidity, the oxygen diffusion coefficient for samples at two months hydration is one order of magnitude lower than hydration-stopped samples and two to three orders of magnitude lower at eight months hydration. This may be explained by the fact that a longer hydration promotes the formation of a greater amount of hydrates that fill the capillary porosity and help retain higher water content for samples at the same RH as seen in Figure 43.

1.5.4 Influence of paste composition

Another important factor that influences D_{e,O_2} is the volumetric W/B ratio because it directly affects the pore structure and diffusivity of the concrete. The lowering of the volumetric W/B ratio slightly decreases the oxygen diffusion coefficient for hydration-stopped samples and samples that were hydrated for two months, whereas it causes a higher decrease of D_{e,O_2} for samples that were hydrated for eight months, especially OPC_SF samples.

Although the effect of SCMs is not appreciated in the early age (before 7 days), samples with 10% silica fume gave the most remarkable positive effect on transport properties and pore refinement, as it can also serve as a pore filler that provides additional nucleation due to small particle size. It is established that for the two tested supplementary cementing materials at a volumetric W/B = 1.6 (silica fume and slag), oxygen diffusivity decreases by at least one order of magnitude at two and eight months at all levels of relative humidity. The lowest oxygen-effective diffusion coefficient is observed for mixes with silica fume at volumetric W/B = 1.6 ; this is the case mainly because of two reasons: (a) SF is extremely finer than slag and is thus

more effective in densifying the microstructure of the cement paste matrix and (b) SF has a higher reactivity [187], and OPC have a higher degree of hydration degree in the mix with 10% SF replacement [175] . After only seven days of hydration, Figure 43 shows that silica fume samples retain slightly more water than slag samples, which can be explained by the fact that relatively fine pores are formed in pastes of silica fume.

1.5.5 Pore-size distribution effect

Using an automatic analysis that allows for the fitting of the data from the MIP analysis (Appendix 1), the porous structure of these pastes is found to be of unequal trimodal type. For each mode, we calculated the mean pore diameter and its corresponding volumetric fraction and standard deviation (Figure 74). Using these results, a weighted arithmetic mean of the mean pore diameter of each mode is calculated and compared with the diffusion coefficients determined experimentally on samples with different saturation degrees. Figure 44 shows the relation between the oxygen-effective diffusion coefficients from our experimental data at three different saturation degree ranges: 1.83% to 20%, 40% to 60% and 80% to 95.8%, and the mean pore diameter of the tested samples in Log-scale. An analysis of this figure reveals that oxygen-effective diffusion coefficients display a somewhat linear trend with respect to the mean pore diameter with a slope of 1.4 and 1.6 and 2.9 for the three degrees of water saturation ranges 1.83% - 20%, 20% - 40% and 80% - 95.8% respectively, with the following regression coefficients: 0.92, 0.60, and 0.63. Dispersion in experimental data is more pronounced for samples with high degrees of water saturation.

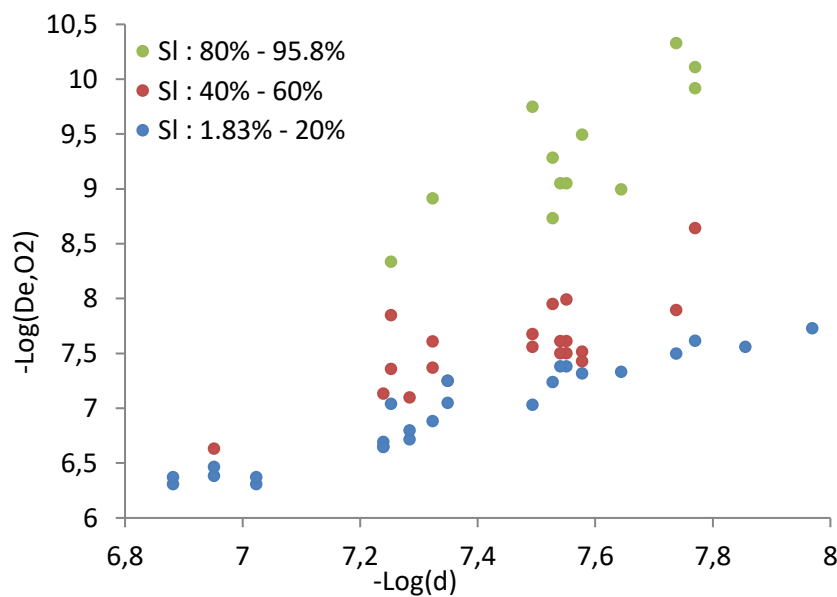


Figure 44: Oxygen-effective diffusion coefficient versus weighted mean pore diameter in Log-scale at three different saturation degree ranges

The dependence of the effective diffusion coefficient experimentally measured on the mean pore diameter of the samples is consistent with the theoretical estimation of the gas diffusion coefficient under Knudsen diffusivity. Indeed, the Knudsen diffusion coefficient D_K is directly proportional to the mean pore diameter d , as seen in Equation 41 [92], where ϕ is the porosity available for the transport, τ is the tortuosity, T [°K] is the temperature, and M_{gas} is the molar mass of the diffusing gas. Note that this equation is valid under the assumption that the pores in which diffusion can take place are cylindrical and interconnected [10].

$$D_K = \frac{\phi}{\tau} \frac{d}{3} \left(\frac{8RT}{\pi M_{\text{gas}}} \right)^{\frac{1}{2}} \quad \text{Equation 41}$$

Knudsen flow is known to occur in the gaseous phase of the pores when gas molecules collide much more frequently with the pore walls than with each other. This diffusion mechanism generally occurs when the mean pore diameter is much lower than the mean free path of oxygen molecules at atmospheric pressure and 20°C ie: $d < 50 \text{ nm}$ [19] ($-\log(d) \gg 7.3$), which is the case of most of the data shown in Figure 44. However, for high degrees of water saturation ($S_l > 20\%$), the big dispersion of the data does not allow for the definite conclusion of Knudsen regime predominance. It is also of relevance to note that Equation 41 is developed for materials that are entirely inert with regards to the gas-diffusing species. In our case, pastes containing slag are expected to react with oxygen due to the oxidation of the sulfur content species [188].

Pore size does contribute to the effective diffusion coefficient as much as the degree of water saturation. For the same range of water degree of saturation, the oxygen diffusion coefficient varies over one to three orders of magnitude when the mean pore diameter varies within one order of magnitude.

1.5.6 Comparison with literature model

The oxygen-effective diffusion coefficient may also be estimated using models developed to predict the carbon-dioxide-effective diffusion coefficient and Graham's law. The most commonly used model for D_{e,CO_2} prediction is Papadakis model [83], giving the diffusion coefficient as a function of the ambient RH. Based on these experimental data, Thiéry [39] proposed a derived expression giving the coefficient as a function of the water saturation degree S_l , total porosity ϕ , and the carbon-dioxide-diffusion coefficient in air ($D_{\text{air},\text{CO}_2} = 1.6 \times 10^{-5} \text{ m}^2/\text{s}$).

$$D_{e,\text{CO}_2} = D_{\text{air},\text{CO}_2} \phi^a (1 - S_l)^b$$

Empirical parameters in this model ($a = 2.74$, $b = 5.17$) were obtained by fitting experimental data of tests performed on carbonated mortars at different RH [11]. The oxygen-effective diffusion coefficient can be estimated from the carbon-dioxide diffusion coefficient using Graham's law, where M_{CO_2} and M_{O_2} are the molar mass of carbon dioxide and oxygen respectively.

$$D_{e,O_2} = \left(\frac{M_{CO_2}}{M_{O_2}}\right)^{\frac{1}{2}} D_{air,CO_2} \phi^a (1 - S_1)^b \quad \text{Equation 43}$$

Using Equation 43, regression parameters a and b are recalculated by least square fitting of all the experimental data of this work for each mix. Note that the good quality of the least square fit is achieved by minimizing value of the sum of squared residuals r . In our case r is in the range of 10^{-7} m²/s, which is in the same order of magnitude as the measured diffusion coefficients. These large residuals could give a large uncertainty on the prediction of the regression coefficients a and b .

- For OPC samples : $a = 5.5$; $b = 2.2$; $r = 7,2 \times 10^{-7}$
- For OPC_SF samples : $a = 7.5$; $b = 4.9$; $r = 3.5 \times 10^{-7}$
- For OPC_Slag samples : $a=6.8$; $b=2.4$; $r = 3.9 \times 10^{-7}$

These results show that the total porosity regression coefficients (a in equation Equation 43): 5.5, 7.5, and 6.8) are more than two times higher compared with the Thiéry model ($a = 2.74$), whereas the water saturation degree parameter b is found not to vary so much for silica fume ($a=4.9$, compared to 5.17 for Thiéry model). However, it is two times lower for OPC pastes. Note that these model parameters were developed based on nitrogen diffusion tests performed on carbonated, non-blended cement pastes and concretes [18].

The major limitation of this model is that the diffusion coefficient is related to an averaged descriptor of the pore structure, which is the total porosity and the water saturation, while neglecting actual pore-size distribution and topology. These kinds of models do not take into consideration the binder type or the effects of hydration that affect the microstructure, unless regression coefficients become specific of each mix design.

1.6 Conclusions

In this work, a new test method is developed to determine the oxygen-effective diffusion coefficient of cement pastes. It is used to measure diffusion coefficients of cement pastes made with different binders and volumetric W/B ratios at different water saturation degrees and hydration durations.

The test method is interesting due to its ease of manipulation, its non-destructive nature, its potential to give a reasonable indication of the material quality, and its ability to more closely monitor site conditions by testing the samples at different RH. This method is proven capable of rapidly measuring the diffusion coefficient for hardened cement paste of 3 mm thickness in a reasonable duration (30 minutes to 4 weeks) and with a good accuracy for oxygen-effective diffusion coefficients between 10^{-10} m²/s and 10^{-6} m²/s.

According to the results obtained from this work, the hydration duration is found to be a property that highly impacts the oxygen diffusion coefficient. Prolonged hydration substantially reduces the diffusion coefficient, especially for samples with slag and silica fume, as the reaction of SCM is generally slower than the hydration reaction of Portland cement and requires longer periods of hydration. The diffusion coefficient and total porosity increase with the decrease of hydration duration and the increase of the volumetric W/B ratio. This can be explained by the formation of higher connectivity and porous volume that allows for an easier and faster ingress of gaseous oxygen.

Hydration duration, volumetric W/B ratio, and the material composition control the pore-size distribution of the cement paste, which influences the liquid saturation of the pores at different preconditioning relative humidity. Thus, knowledge of the water content of the cement paste and its pore-size distribution are key properties to predicting gas-diffusion coefficients. It is expected that the collected data can thus be extrapolated to other gases like carbon dioxide and therefore used in the service life models of carbonation induced corrosion.

2 Paper II: Influence of carbonation on the microstructure and the gas diffusivity of hardened cement pastes

2.1 Abstract

The influence of carbonation on the oxygen-effective diffusion coefficient (D_{e,O_2}) of hardened cement pastes (HCP) is investigated in the scope of durability. Experiments are carried out on HCP made with different binders (Portland cement, fly ash, slag, metakaolin binders) and water-to-binder ratios at three relative humidity levels. At a given RH, the change in D_{e,O_2} due to carbonation depends on the mix composition. However, in most of cases, D_{e,O_2} increases after carbonation, despite the porosity clogging. This is explained by both the decrease in the water saturation degree, especially at high RH, and the change in the pore size distribution. A good correlation is found between the mean pore diameter and gas diffusivity before and after carbonation at low water saturation degree ($R^2 > 0.84$ on a log-log scale). D_{e,O_2} is significantly less dependent on the water saturation degree after carbonation.

2.2 Introduction

Carbonation is recognized as a significant cause of corrosion in concrete reinforcement [189][190]. This physicochemical process causes diverse chemo-mechanical changes in the cement paste, especially changes in the microstructure and chemistry of the cementitious matrix [48][31].

The first mechanism controlling concrete carbonation is the gaseous CO_2 diffusion process by which CO_2 moves through the gas-filled pores. This phenomena is governed by an effective-diffusion coefficient, which is a durability indicator of concrete, a quality parameter indicating the level of gas tightness of cementitious materials, and a relevant input parameter for service life prediction models of concrete in a real environment [6][84][191]. Previous works [86][192] show that transport properties of cementitious materials are highly dependent on the degree of water saturation. Hence, the determination of transport properties at various hydric states is of high importance. On the other hand, carbonation causes numerous changes in the cement paste microstructure [31][35]. It should be noted that, in the literature, experimental data on the effect of carbonation on gas diffusivity are lacking compared to investigations on other transport phenomena such as chloride diffusion and water transfer [51][193][194]. The microstructure of the hardened cement paste (HCP) determines the transport properties of

concrete to a high extent, since HCP is the component that contributes for the greatest part of the concrete porosity [9][195]. Therefore, in the present work, diffusion tests are carried out on HCP samples, employing an experimental setup from our previous works [192]. The latter uses atmospheric oxygen as the diffusing gas and allows for the determination of oxygen diffusivity under different hygrometric conditions. Admittedly, major differences exist between O₂ and CO₂ gases: their solubility in fluids, their molecular size, etc. Nevertheless, it is possible to obtain a good prediction of CO₂ diffusivity by means of values of O₂ diffusivity [100][91]. Plus, the CO₂-effective diffusion coefficient of partially water saturated cementitious materials cannot be measured using gaseous CO₂ since it chemically reacts with the calcium-bearing phases of the materials and changes their microstructure.

The second mechanism controlling the carbonation progress of concrete is the CO₂-binding capacity of its hardened cement paste. This property is directly related to the amount of the calcium-bearing phases that could dissolve and react to result in the formation of calcite. The amount of carbonatable compounds influences the rate of carbonation: a higher amount of carbonatable compounds hinders the carbonation depth progress [6]. Note that the amount of bound CO₂ varies with the different humidity levels in each exposure site: the pastes exposed to the higher humidity (unsheltered from rain) are those fixing a higher amount of CO₂ [196].

The partial replacement of cement with alternative powders entails a considerable environmental impact. However, the use of these additions, also called Supplementary Cementitious Materials (SCMs) should not adversely affect the behavior of the material. SCMs can be classified into pozzolanic, hydraulic or inert substances. There are great differences in the respective contribution of each SCM's type to the hydration reaction of the cement and, consequently, to the HCP microstructure. Therefore, it is important for the carbonation resistance of cementitious materials to know what role an optional additive play in the microstructure of the material.

In the present work, the oxygen-effective diffusion coefficient of six different HCPs blended with fly ash, slag, limestone and metakaolin additions is determined after full hydration (90 days) in the non-carbonated state and after full carbonation under 1% CO₂ concentration by volume. The influence of the degree of water saturation is assessed at both states after a preconditioning at three relative humidity levels: 55%, 95% and 33%. The microstructural changes, phase assemblage and CO₂-binding capacity of the tested HCPs are investigated using water porosity, mercury intrusion porosimetry (MIP), and XRD and TGA techniques, respectively. The carbonation resistance is deduced from this work's results using a deterministic model from the literature. The carbonation performance of the six HCPs is compared to experimental results after exposing the HCPs to carbonation in a room regulated

at 50%RH.

2.3 Materials and methods

2.3.1 Cement pastes mixtures

With the aim of testing the most widely used binders, six types of cement pastes, including blended cements, are tested. Two cement types are used to prepare the samples. The oxide composition of the raw materials is given in Table 29. The cement pastes mix compositions are shown in Table 30. Note that the water-per-binder ratio W/B is expressed in mass and the replacement percentage of the additions is expressed in relation to the total amount of additions plus ordinary Portland cement (i.e. CEMI according to European nomination). Only binary systems are investigated. Note that in the case of limestone, the EN 197-1 standard accepts 35% of replacement at the most [197]. Therefore, it was decided to increase the limestone content to 40% to evaluate the consequences of such a high value.

Material	Constituent (%)									
	CaO	SiO ₂	Al ₂ O ₃	Fe ₂ O ₃	MgO	K ₂ O	Na ₂ O	SO ₃	TiO ₂	LOI
CEMI 52.5 N	64.1	20.1	5.2	3.3	0.8	0.76	0.28	3.0		1.8
CEMI 52.5 N PM	60.8	19.27	4.59	3.25	2.01	0.97	0.19	2.88		1.99
Fly ash	5.08	83.45				1.66	1.4	0.58		<5
Slag	43.7	37.4	10.8	0.5	6.5	0.36	0.49	0.1	0.6	<1.5
Metakaolin	0.2	55	40	1.4	0.1	0.4	0.4	-	1.5	1

Table 29: Oxide composition of the raw materials

Mix name	W/B	Cement type	Addition type	Addition content (wt%)	Air content (vol%)
PC6	0.60	CEM I 52.5 N	-	0	0.2
FA6	0.60	CEM I 52.5 N	FA	30	0.1
SL6	0.60	CEM I 52.5 N	Slag	60	0.7
LS6	0.60	CEM I 52.5 N	Limestone	40	1.0
SL35	0.35	CEM I 52.5 N PM	Slag	50	0.1
MK45	0.45	CEM I 52.5 N	MK	20	0.1

Table 30: Mix design of the tested cement pastes

2.3.2 Preparation of the HCPs samples

The cement pastes are prepared using a waring blender until homogenization of the fresh mix. The pastes are poured in cylindrical molds (diameter 4 cm; height 10 cm) and vibrated to remove entrapped air bubbles. The molds are rotated for 24h in order to avoid the sedimentation of solid particles. The mixes are then demolded and stored in a 100% RH room at ambient temperature for 90 days. Note that the hydration duration is a very important parameter when studying pastes containing pozzolanic additions such as fly ash. After 90 days, it is supposed that the portlandite content of such a paste will only slightly change over a further hydration duration, since most of the pozzolanic hydration reactions have already taken place [198][199][200]. For each mix, 6 molds are prepared. The air content of each mold is determined through the density measurements of the fresh paste. Cylinders with the lowest air content are used for the diffusion tests (Table 30).

For each HCP mix, two cylinders are used for the diffusion tests before carbonation and two in the carbonated state. From these cylinders, thin samples of 2.5 mm are sawed using a precision saw. Testing thin samples is convenient since they carbonate and reach water equilibrium in a reasonable amount of time (3 to 5 weeks). First, 60 discs are used to be tested in the non-carbonated state. These discs are placed directly in climate chambers equilibrated at three different relative humidity levels (33% 55% and 93%). The hygrometry is maintained at a constant level by means of saturated salt solutions, and soda lime was added in the climate chambers in order to avoid the carbonation of the samples during preconditioning. The CO₂ concentration inside these chambers did not exceed 10 ppm (using a sensor with a detection limit of 75 ppm). In parallel, 60 discs from the six paste mixtures are tested in the carbonated state. Full carbonation of the tested samples is achieved using accelerated

carbonation in an environment-controlled climate chamber equipped with a system that allows for an accurate regulation of the CO₂ partial pressure and temperature. Prior to carbonation, the 60 discs are kept in a room regulated at 55% relative humidity for a month in order to reach a constant degree of water saturation that promotes carbonation. Afterwards, they are placed in the carbonation chamber with a CO₂ content of $1 \pm 0.2\%$ for six weeks and 55%RH. This value is chosen to ensure the representativeness of the mineralogical evolution compared to atmospheric carbonation [201], to avoid the cracking of the cement paste after carbonation, and to carbonate the samples in a reasonable amount of time. The temperature at each conditioning step is 20°C. The carbonation progress is monitored in a simple way through a phenolphthalein solution: the colorlessness of the phenolphthalein indicator test was the termination criterion. This procedure is chosen to examine samples with the same or comparable progress of carbonation. The oxygen-effective diffusion coefficient is also determined for carbonated samples at three relative humidity levels. Note that in order to test the carbonated HCP at 93% RH, all the discs are first water saturated under vacuum for 48h and placed in a climate chamber at 93%RH until mass equilibrium is reached. The reason behind water saturating these samples is to test all the HCPs in the desorption state only. After all diffusion tests are performed, the samples are dried in the oven at 105°C to reach their dry mass, which allows for the determination of their degree of water saturation at the three relative humidities chosen.

2.3.3 Oxygen-effective diffusion coefficient

The oxygen-effective diffusion coefficient is measured using an experimental setup developed during our previous works [192]. The test method relies on the accumulation of gaseous oxygen inside a diffusion cell called a “downstream chamber”. The tested specimens are discs with a diameter of 4 cm and a thickness of 2.5 mm. This experimental setup contains no upstream chamber: one face of the tested specimen is in contact with the ambient air of the climate chamber (volume of 40 L), i.e. at an O₂ concentration of around 20% by volume, and the other face is in contact with the inside volume of the cell (68ml). The absence of the O₂ bottle is of relevance from a practical point of view. The volume of the climatic chamber is much larger than the volume of the downstream cell, so the oxygen concentration in the climatic chamber is constant over the test duration. At the beginning of the test, the downstream chamber is flushed with nitrogen for 20s to reach an O₂ concentration lower than 0.3%. The experimental setup (Figure 45) is then placed inside a temperature and relative humidity-controlled climate chamber (also called an “upstream chamber”).

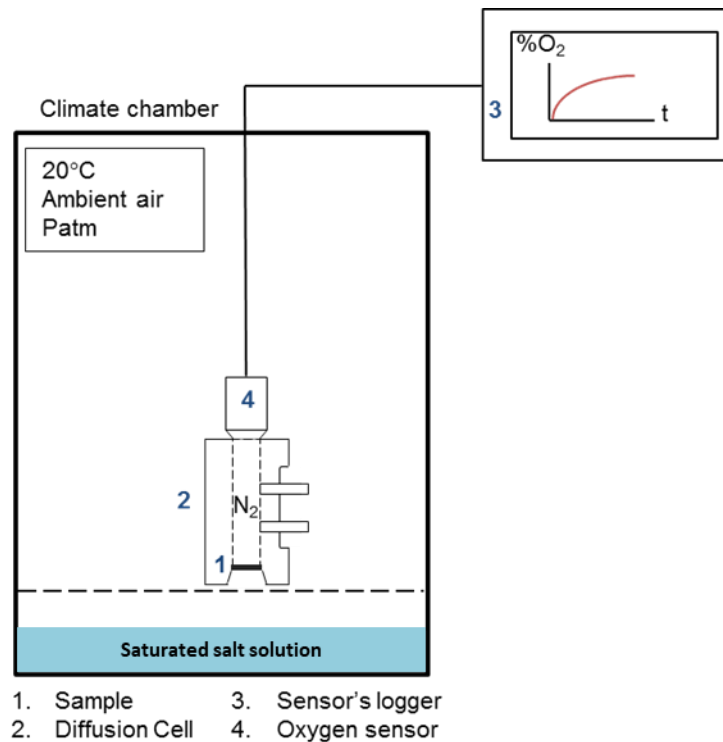


Figure 45: Schematic description of the setup of the determination of the oxygen-effective diffusion coefficient

By means of saturated salt solutions, the relative humidity inside the climate chamber is set at the same relative humidity as the one used for the pre-conditioning of the tested samples during the diffusion test. The relative humidity level is monitored inside the climate chamber by means of a sensor during the test period and found to vary slightly (2% to 5% at the most).

Oxygen diffuses successively from the ambient air through the sample into the cell initially filled with nitrogen. Oxygen concentration is monitored inside the cell by an oxygen gas sensor. This sensor allows for continuous readings of the oxygen concentration. All measurements are carried out at 20°C and 1 atm. The oxygen-effective diffusion coefficient is determined by minimizing the residue between the experimental and numerical accumulation curve. The numerical accumulation curve is obtained by solving Fick's second law of diffusion with a finite volume solver in python called fipy, version 3.1.3 [178]. More details about the experimental setup and data analysis are given in [192].

2.3.4 Microstructure characterization techniques

Water porosity (ϕ) is obtained using hydrostatic weighting and oven-drying the HCP samples at 105°C. The specimens are preliminarily water-saturated under vacuum for 48h following the current standard used in France [202]. The pore size distribution of the samples is determined using mercury intrusion porosimetry (MIP). The degree of water saturation of the tested

samples at 33%, 55% and 93% RH is calculated using Equation 44, where m is the mass of the sample at moisture equilibrium, m_0 the dried mass, and m_{sat} the saturated mass. The saturated mass of the 2.5 mm thick samples is determined via water soaking under the vacuum for 48h. The dry mass is obtained after drying the samples in the oven at 105°C for 3 days.

$$S_r = \frac{m - m_0}{m_{sat} - m_0} \quad \text{Equation 44}$$

Changes in the pore structure characteristics of the paste samples after exposure to 1% CO₂ are assessed using mercury intrusion porosimetry. MIP provides information about the connectivity of the pores and reveals information about pore geometry [123]. This technique is based on the Laplace equation [125], which relates the pressure applied to the pore diameter. This diameter actually corresponds to the entry diameter of the pore. The tested samples are small blocks of a typical size of a few mm to 1 cm. These samples are cored out from the hardened cement paste discs and pre-dried at 45°C for 24h. Note that the smallest pores (gel pores) are only partly measured by this technique. Thus, the water porosity is certainly higher [179].

Note that these tests are carried out right after sawing the thin cement pastes under water (and pre-drying at 45°C for MIP test) in order to avoid carbonation of the discs. After carbonation, when the pH-indicator becomes colorless over the 3mm thickness samples, water porosity, pore size distribution and degree of water saturation are determined on the carbonated discs. MIP test is run on one specimen only while the other tests are carried out on three replicates.

2.3.5 Mineralogical changes

Before and after carbonation of the HCP, one complete disc of each mix at both states is grinded and sieved completely using a sieve of 63 µm, and then 30 mg of this powder is used for the TGA and XRD tests. Only one test is run for each mix.

The mineralogical changes induced by carbonation are identified using TGA and XRD techniques. The degree of carbonation (DoC) is determined using TGA. DoC is defined as the CO₂-bound with respect to the total theoretical maximum binding capacity MBC (equation 4). The six cement paste mixtures are finely powdered and sieved using a sieve of 63 µm for these analyses. TGA (Mettler TGA-DSC 3+) is used to quantify all carbonates polymorphs. Around 30 mg of the powder sample is placed in the device and heated from 30 to 1000°C at

10°C/min under a small nitrogen flow (20 mL/min). The temperature of the carbonates' decomposition is assumed to range from 550 to 1000°C [108]. Previous work of Radha et al. [27] shows that the decomposition temperature of all carbonates polymorphs is around 800°C. The samples' degree of carbonation DoC is determined based on the amount of anhydrous cement using equations 3 and 2:

$$D_oC = \frac{BC}{MBC} \quad \text{Equation 45}$$

$$B_{-CO_2} = \frac{m_{CO_2}^{550-1000^\circ}}{m_{Oxyde}^{1000^\circ C} + m_{CO_2}^0 + m_{H_2O}^0} \quad \text{Equation 46}$$

$$MBC = \sum \frac{\text{carbonatable cationic oxide}}{M(\text{carbonatable cationic oxide})} * M_{CO_2} - SO_3 * \frac{M_{CO_2}}{M_{SO_3}} \quad \text{Equation 47}$$

Where B_{-CO_2} is the bound CO_2 , $m_{CO_2}^{550-1000^\circ}$ is the mass loss that corresponds to the decarbonation of $CaCO_3$, $m_{CO_2}^0$, and $m_{H_2O}^0$ are, respectively, the CO_2 and water amount present in the raw materials (cement and mineral additions used). MBC is the maximum amount of CO_2 that could be present in the sample if all CaO (except the one coming from $CaCO_3$ present in the raw materials, and the one introduced in the mix LS6 as an additive) was carbonated. This value could be approximately inferred by the quantity of its main carbonatable cationic oxides such as CaO, MgO, SO_3 , etc.

The amount of SO_3 is deduced in the calculation of the maximum degree of carbonation because in the presence of an excess of sulfate anions, calcium cations react with sulfate anions to form gypsum at room temperature even when the system is buffered by atmospheric CO_2 .

The X-ray diffraction (XRD) is used to identify the nature and amount of the different calcium carbonate polymorphs. XRD tests were carried out with a Philips/PANalytical X'Pert Pro-MPD Powder Diffractometer with an X'Celerator detector of an incident $CuK\alpha$ radiation beam by 40 kV and 40 mA to a rotation sample. The specimens are scanned for 40 minutes from $2\theta = 5$ to 65° by a step of 0.25° without protection from CO_2 and in a dry environment (RH~40%).

The carbonation depths of the six HCPs are measured directly by means of phenolphthalein solution after exposing side-sealed discs of 3 cm thickness and 4 cm diameter to natural carbonation in a relative humidity-controlled room at 50%. The carbonation depth is measured

once a month for six months. Note that the samples were preconditioned for one week in a climate chamber with soda lime prior exposure to carbonation.

2.4 Results

2.4.1 Changes in the chemical composition

The amount of portlandite, calcite and other hydration products such as C-S-H and ettringite is estimated before and after the carbonation test. The recorded mass losses during TGA are expressed in the percentage relative to the residual mass of the sample at 1000°C.

	Before carbonation (g /100g)			After carbonation (g /100g)		
	30-350	350-550	550-950	30-350	350-550	550-950
Temperature range (°C)	30-350	350-550	550-950	30-350	350-550	550-950
Released component	H ₂ O	H ₂ O	CO ₂	H ₂ O	H ₂ O	CO ₂
Main cement phases [108]	C-S-H, AFt & other hydrates	CH	C \bar{c}	C-S-H, AFt & other hydrates	CH	C \bar{c}
PC6	18.4	9.2	4.4	10.8	7.6	36.6
FA6	16.0	5.7	4.7	5.1	0.7	33.4
SL6	15.3	4.0	3.5	5.4	0.6	30.5
LS6	12.3	6.0	21.3	4.9	1.2	51.2
SL35	14.4	5.0	4.5	5.0	0.6	27.7
MK45	19.9	4.7	4.4	5.9	0.5	24.9

Table 31: TGA results before and after carbonation of the six HCP

Table 31 presents the TGA results on the evolution of the content of bound water and CO₂ to portlandite (CH), (C-S-H), and calcium carbonate, respectively. The six HCP are tested before and after accelerated carbonation at 1%. The high content of calcium carbonate before the carbonation of the paste's LS6 corresponds to the unreacted limestone present in the initial mix, while the small amounts of calcium carbonate present in the other HCPs before carbonation are due to the initial CO₂ amount in cement (up to 2%) and to a slight carbonation of the paste during the preparation and conditioning in a CO₂-low concentration environment (10ppm). Results from Table 31 reveal that portlandite is still present only in the PC6 after carbonation, while it is consumed for blended systems. Even though the highest amount of calcium carbonate formed after carbonation is observed for PC6, the lowest consumptions of hydration products upon carbonation are observed for this HCP. Before carbonation (BC), results from Table 32 also reveal that a slight amount of calcite was formed during the

preparation of the samples. The portlandite content of the blended cement pastes is remarkably lower than the portlandite content of PC6 because they contain less OPC that can hydrate to form portlandite. Moreover, the reduced amount of portlandite formed is consumed by the pozzolanic reaction of fly ash, slag, and metakaolin.

	PC6		FA6		SL6		LS6		SL35		MK45	
	BC	C	BC	C	BC	C	BC	C	BC	C	BC	C
Calcite%	<2	9.2	<2	10.8	2.3	30	39.8	66.6	5.2	13.4	3.5	8.3
Portlandite%	18.0		7.8	4.8	5.4		8.5		4.0		6.0	
Ettringite%	<2		<2		<2		<2		<2		<2	
Vaterite%		77		57.3		57.8		13.7		56.7		78.1
Aragonite%		7.7		9		6.4				22.5		6.7

Table 32: Estimation of the content of some crystal minerals before (BC) and after carbonation (C) based on the raw data from XRD analysis

Results from Table 32 show that for all HCPs the CaCO_3 polymorph predominantly formed after carbonation is the metastable vaterite (vaterite is the second most metastable CaCO_3 polymorph after amorphous calcium carbonate [27]). Calcite and aragonite formation also took place but to a much lesser extent. Only the samples with limestone powder showed an exception, containing mainly calcite after carbonation. The presence of limestone seems to favor the further precipitation of calcite. According to [30], calcite precipitates preferentially on limestone particles as the latter acts as a nucleation surface for calcite.

2.4.2 Degree of carbonation

The amount of bound- CO_2 during the preparation and the conditioning of the six HCPs ($\text{B-CO}_2^{\text{ini}}$), and the bound CO_2 after the carbonation test (B-CO_2^{f}) are investigated using TGA analysis (cf Table 5). These values are used to calculate the carbonation degree, expressed as the bound CO_2 per maximum bound CO_2 (MBC). Note that the amount of limestone introduced initially during the preparation of the LS6 is deducted in the calculation of the initial and final degrees of carbonation in table 5 and not deducted in the results of table 3.

Table 33 shows results of the amount of CO_2 that disappeared due to the carbonation of portlandite in the HCPs. This value (CO_2^{CH}) is calculated according to Equation 48.

$$\text{CO}_2^{\text{CH}} = \left(\frac{\Delta\% \text{CH}}{M_{\text{H}_2\text{O}}} M_{\text{CO}_2} \right) * \frac{1}{B_{-\text{CO}_2}^f} \quad \text{Equation 48}$$

$\Delta\% \text{CH}$ (results taken from Table 31) corresponds to the variation of the amount of water in portlandite per unit mass of anhydrous cement before and after carbonation. $B_{-\text{CO}_2}^f$ is the total amount of bound- CO_2 after carbonation of the HCPs (results shown in Table 31) M_{CO_2} and $M_{\text{H}_2\text{O}}$ are the molar masses of carbon dioxide and water respectively. Note that the small amount of CO_2 present in the raw materials (<2%) is taken into consideration in these calculations.

The highest degree of carbonation is observed for PC6, even though the amount of bound CO_2 by portlandite is the lowest comparing to other systems, which highlights the important carbonation of other phases (C-S-H, ettringite... c.f Table 31). Meanwhile the lowest degree of carbonation is observed for SL35 (Table 33). This could be explained by the low diffusivity of the SL35 (due to the low water-binder-ratio 0.35) and their high C-S-H content. Previous works in the literature show that the carbonation of C-S-H leads to the formation of calcium-enriched silica gel. Part of the calcium would remain trapped in this gel and would not participate in the formation of CaCO_3 [203].

Although the phenolphthalein solution was colorless for all the six HCP after the accelerated carbonation period, the degree of carbonation of these materials varies between 34.1% and 68.4%. This result highlights the questionable reliability of the pH-indicator method to study the carbonation performance of cementitious materials. In agreement with this results, Omikrine-Metalssi et al. [204] show that the carbonation continues even 1cm beyond the carbonation depth indicated by the phenolphthalein indicator. Andrade [205] also states that the DoC in the carbonated zone is not a direct function of the carbonation depth.

	MBC	B-co ₂ ⁱⁿⁱ	DoC ⁱⁿⁱ	B-co ₂ ^f	DoC ^f	CO ₂ fixed by portlandite / Total CO ₂	Carbonatable compounds
	g _{co2} /100g anhydrous	g _{co2} /100g anhydrous	%	g _{co2} /100g anhydrous	%	%	mol/m ³
PC6	51.2	3.1	6.1	35.3	68.4	10.7	8686.1
FA6	37.6	2	5.3	24.3	64.7	36.6	4017.4
SL6	43.1	2	4.5	21.5	49.9	27.2	2087.4
LS6	30.5	0.4	1.3	17.1	56.1	22.9	2432.1
SL35	43.4	2.4	5.5	14.8	34.1	38.8	2465.4
MK45	41.5	3.2	7.6	20.8	50.2	41.2	4773.6

Table 33: Bound CO₂ values before (B-co₂ⁱⁿⁱ) and after carbonation (B-co₂^f); carbonation degrees of the tested material before (DoCⁱⁿⁱ) and after carbonation (DoC^f); maximum CO₂-binding capacity (MBC), and the amount of carbonatable compounds of the six HCPs

Note that the amount of carbonatable compounds is deduced from the final bound-CO₂ by multiplying this value with the cement dosage and dividing by the molar mass of carbon dioxide. This property is a direct input parameter required by service life prediction models (Equation 49).

2.4.3 Porosity changes upon carbonation

Figure 46 gives the porosities of the six HCPs before and after full carbonation. The total water porosity of the carbonated cement pastes is 6 to 12% smaller than the total porosity of HCPs before carbonation. The carbonation of the hydrates phases in cement is known to cause an increase in the solid phase volume.

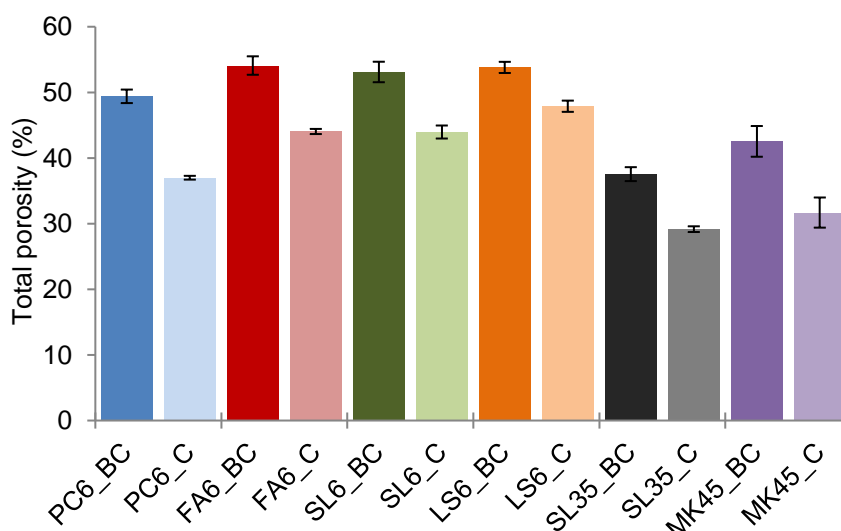


Figure 46 : Influence of carbonation on the water porosity of the six HCPs. BC: before carbonation C: carbonated

Although FA6, SL6, and MK45 contain a large amount of C-S-H, their total porosity decrease was lower than PC6. This could be due to the smaller molar volume (change due to carbonation) of low Ca/Si C-S-H in HCPs with pozzolanic additions, which generally causes a slight decrease in the porosity [206]. The effect of carbonation on the six HCPs' pore size distribution (PSD) is investigated by means of MIP (Figure 47). It is noted that for PC6 carbonation resulted in a reduction of the amount of small pores ($d < 8$ nm) and a formation of a large amount of pores with a bigger diameter than 20 nm. The carbonation of the paste FA6 even induced the disappearance of pores with a small diameter < 10 nm and the formation of pores with a diameter of 200 nm. Note that this paste pore size distribution goes from a bimodal distribution to a trimodal distribution upon carbonation. This result is also observed for the pastes' SL6; the pore size distribution goes from a monomodal distribution centered on pores with a diameter of 10 nm to a bimodal distribution of higher pore diameter: 60 and 30 nm. A coarsening in the pore size distribution of LS6 is observed: carbonated LS6 contains a lower number of small pores and a shift of the main mode to a bigger pore diameter is observed. As for SL35, carbonation caused the formation of small pores with a diameter of around 3 nm, the clogging of pores with a diameter of around 7 nm, and an increase in the pores entry diameter. This result is also observed on MK45, where carbonation caused a clogging of pores with a diameter of 20 nm and an appearance of a small amount of pores with a bigger diameter of 40 nm after carbonation.

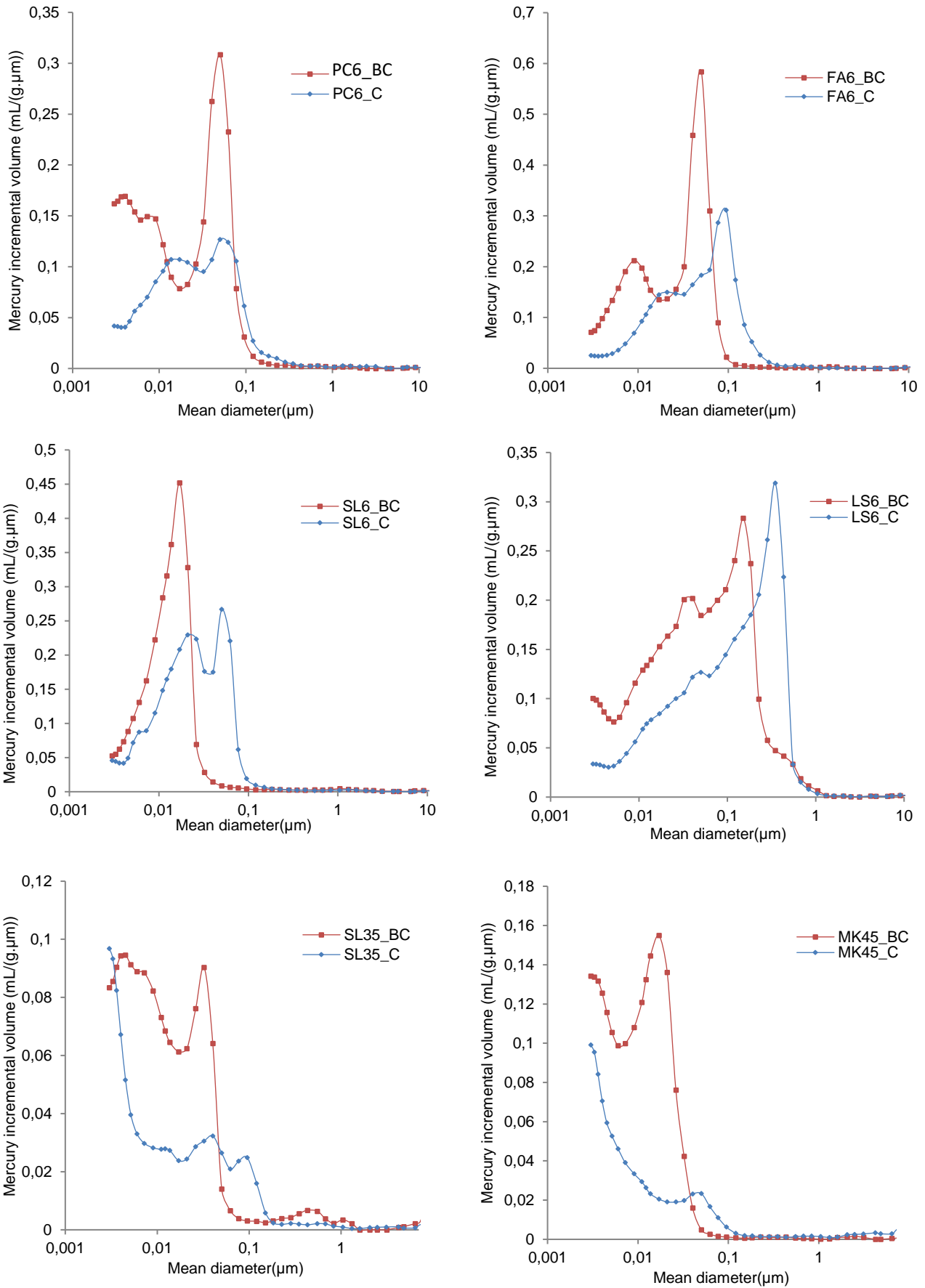
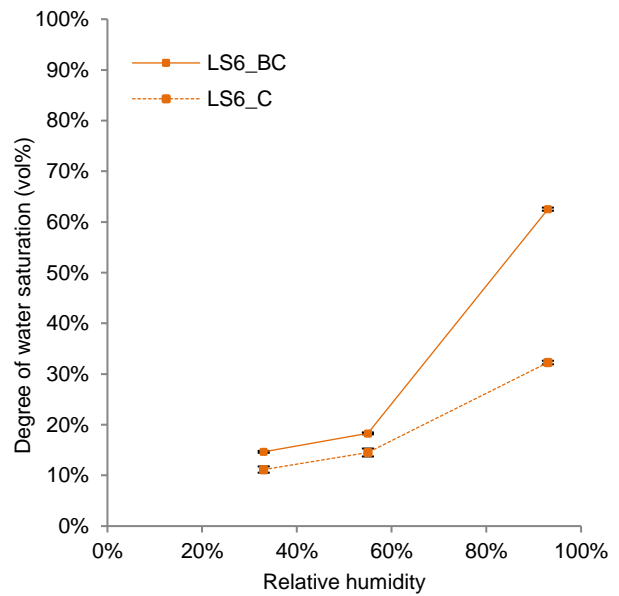
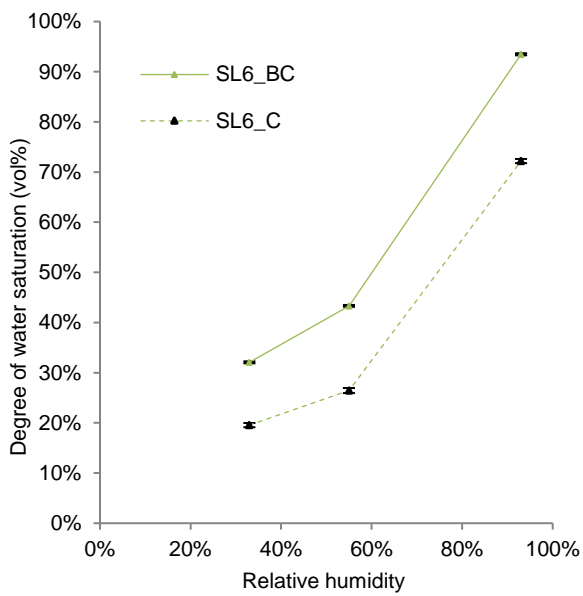
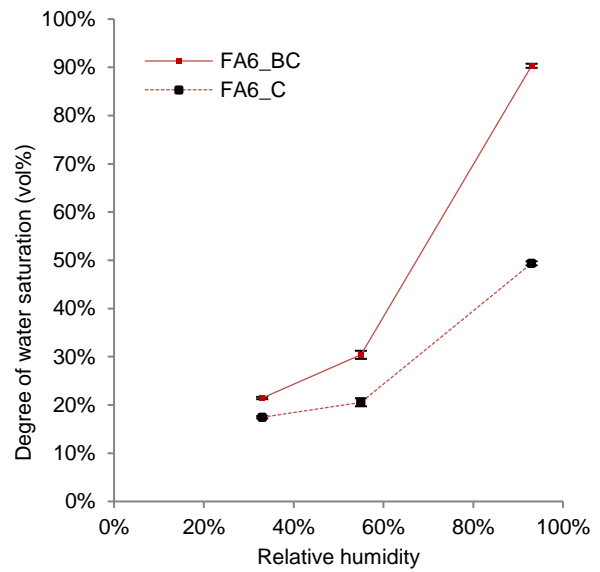
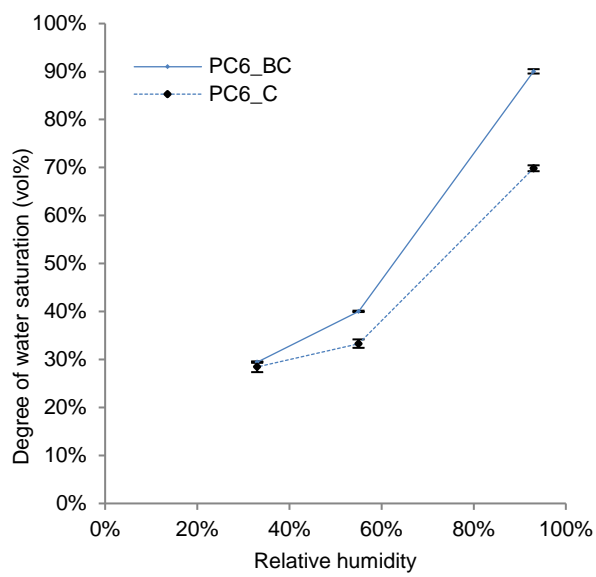


Figure 47 : MIP results on the PSD of the six HCPs before carbonation (BC) and after carbonation (C)

2.4.4 Effect of carbonation on the water retention capacity



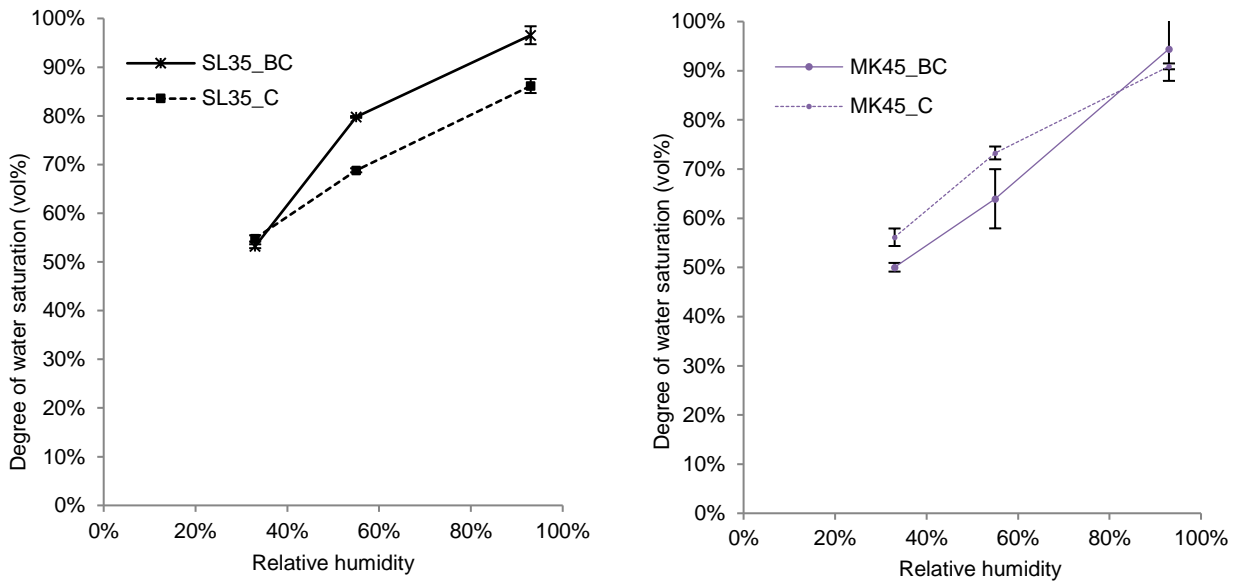


Figure 48: The degree of water saturation (vol%) of the tested HCPs before carbonation (BC) and after carbonation (C) at three relative humidity levels

Results shown in Figure 48 indicate that carbonation exerts a different effect on the water retention capacity of the hardened cement pastes. For pastes PC6, FA6, LS6 and SL35, the degree of water saturation at 33%RH only slightly changed; however, at 55% RH, carbonated samples are 3% to 17% less water saturated and at 93% RH, carbonated samples are 11% to 41% less water saturated. As for SL6, carbonated samples are 20% less water saturated at almost all relative humidity levels; however, carbonated MK45s are 6% to 9% more water saturated than the non-carbonated samples at 33% and 55% RH, and only 3% less water saturated at 93% relative humidity. Note that the decrease in the water retention capacity upon carbonation is investigated in the first desorption isotherm (from water saturated condition) and is more significant for blended cement pastes and appears to be all the more significant as the amount of additions and the water-per-binder ratio are high (SL6).

2.4.5 Effect of carbonation on oxygen-effective diffusion coefficient

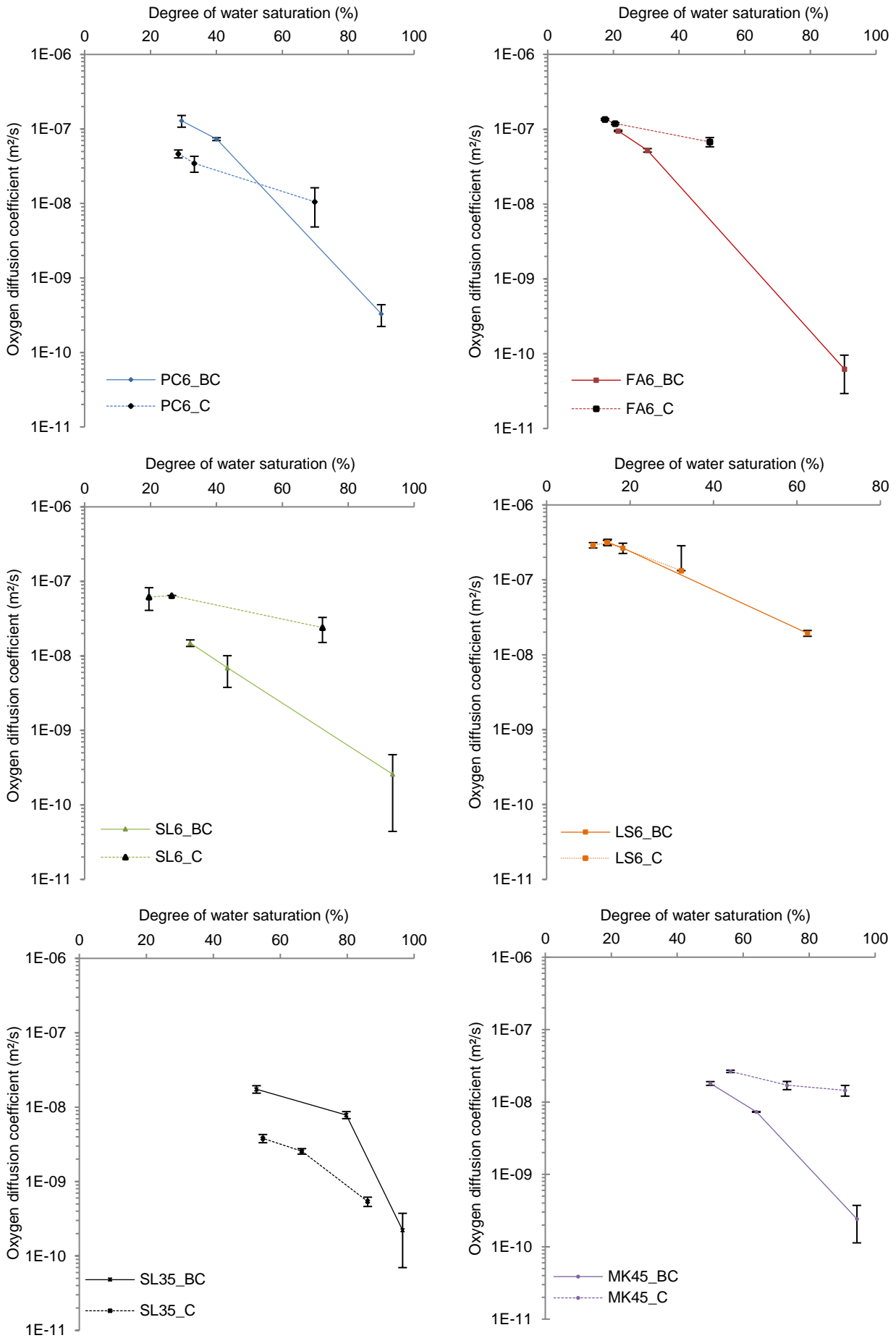


Figure 49: Oxygen-effective diffusion coefficient of the tested HCPs before and after carbonation at three degrees of water saturation

The oxygen-effective diffusion coefficient depends both on the degrees of water saturation corresponding to the relative humidity of preconditioning and on the state of carbonation (Figure 49). PC6 pastes exhibit a decrease in the oxygen-effective diffusion coefficient by a factor of 3 at low and intermediate relative humidity upon carbonation, whereas an increase in D_{e,O_2} by a factor of 21 at 93% RH is observed upon carbonation. The same is observed for SL35; D_{e,O_2} decreased by a factor of 5 and 3 at 33% and 55% RH, respectively, and increased by a factor of 2.5 at 93% RH.

As for FA6 pastes, carbonation caused an increase in the D_{e,O_2} at all relative humidity levels by a factor of 1.5, 2.3 and 1000 at 33%, 55% and 93% RH, respectively. D_{e,O_2} also increased for SL6 by a factor of 4, 9 and 93 at 33%, 55% and 93% RH, respectively, while for LS6, D_{e,O_2} is hardly influenced by carbonation at 33% and 55% RH while it increased by a factor of 7 at a high RH of 93%. Note that LS6 diffusivity before carbonation is the highest. Carbonated MK45 exhibits higher oxygen diffusivity at all RHs. D_{e,O_2} increases by a factor of 1.5, 2.3 and 60 at 33%, 55% and 93% RH, respectively. Note that the oxygen-effective diffusion coefficient is highly dependent on the relative humidity of preconditioning for non-carbonated HCPs and only slightly dependent on the RH of carbonated HCPs.

2.5 Discussion

2.5.1 Microstructural changes upon carbonation

The decrease in the total porosity given in the results (Figure 46) is also noticed by several authors in the literature [36][20], either on-site [207][208] or under accelerated exposure conditions [18][43]. Pihlajavaara et al. [143] and Tri et al. [43] measured a decrease in the total porosity (clogging) ranging from 10% to 15% on CEMI-based carbonate cement pastes ($0.3 < W/C < 0.8$). Figure 46 shows that the nature of the binder is involved in the variation of porosity; the highest porosity change is found for PC6 (12%). In agreement with our findings, Hyvert [53] also found that the total porosity variation is more important for CEMI (9.4%) materials than CEMIII (6%) materials. This result could be directly linked to the nature and relative amount of the hydrates formed by pozzolanic reactions that lower the amount of portlandite and that lower the Ca to Si ratio in C-S-H phases, as the high content of C-S-H tends to maximize this drop in porosity [20]. Note that FA6 total porosity is 5 to 7% higher than the total porosity of PC6. This result was also obtained by Papadakis et al [172] when testing mortar samples prepared with 30% fly ash, an increase in porosity of 13% is found.

The pore size distribution is also strongly impacted by carbonation (cf. Figure 47). When the W/B is high, which is the case of the HCPs PC6, SL6, and LS6, the carbonation caused a coarsening of the PSD. However, for SL35 and MK45, carbonation resulted in the formation of

both finer and coarser pores. Johannesson and Utgenannt [209] also reported a redistribution of pore sizes upon carbonation in Portland cement mortar samples. The authors predicted that well-carbonated mortar has a significantly higher volume of pores in the pore size range of 2 to 7 nm. Those MIP results are also consistent with the observations of Shah et al. [35].

As a consequence of the variation in the pore size distribution and porosity of the HCPs upon carbonation, the water retention capacity decreased notably (Figure 48). These results are explained, together with the overall evolution of pore size distribution, by the consumption of the C-S-H phase after carbonation and the increase of pore entry diameter. In agreement with our results, it has been reported by Johannesson and Utgenannt [209] that the degree of water saturation (obtained by desorption) for the non-carbonated mortars is higher (by 15%) when compared with a well-carbonated sample, especially at 95% relative humidity. The reduction of liquid saturation (SI) is observed in spite of the reduction of total porosity (ϕ), which means that the average volume content of water per unit volume of paste decreases but the pore entry diameter tends to increase upon carbonation.

2.5.2 Mineralogical changes

Table 31, 32, and 33 results show that after carbonation, portlandite is still present in carbonated PC6 (only 10% of bound- CO_2 was due to carbonation of portlandite) while it is highly consumed for blended cement pastes. In agreement with our findings, Soja et al. [36] determined a higher portlandite consumption for blended cements with limestone with regards to OPC pastes after exposure to natural carbonation, which is a rather encouraging result for predicting the natural carbonation mechanisms from accelerated carbonation tests at 1% CO_2 . MK45, which contains 20% metakaolin, also showed an almost complete depletion of portlandite (41% of the total bound- CO_2 is due to portlandite carbonation Table 33) and a high consumption of C-S-H after carbonation at 1% CO_2 (cf Table 31: TGA results). The same conclusion is drawn by Machner et al. [210], who noted that carbonation caused an almost complete decomposition of the C-S-H phase and the consumption of the portlandite after carbonation at 1% CO_2 of HCPs with 20% metakaolin. XRD results (Table 32) show the formation of the three CaCO_3 polymorphs for all HCPs with a high amount of calcite for LS6 and a predominant formation of vaterite for other HCP. The high formation of vaterite could be explained by the carbonation of CSH phases. Indeed, Black et al. [211][212] studied the carbonation of synthetic C-S-H in which the initial Ca/Si ratio appeared to influence the crystalline carbonate species formed. For Ca/Si ratios greater than 0.67, principally calcite and vaterite were observed and for ratios below 0.50, aragonite was most prevalent. Thiéry et al. [39] attributed the more poorly crystallized and the more thermodynamically unstable forms of CaCO_3 to the carbonation of the CSH phases.

2.5.3 Oxygen-effective diffusion coefficient

The pronounced reduction in the total porosity as a result of carbonation (precipitation of calcium carbonates causes clogging of total porosity) of the six HCPs is expected to positively affect the durability performance of the materials, thus reducing the oxygen-effective diffusion coefficient. This is indeed observed for PC6, LS6 and SL35 at 33%, at 55% RH. This reduction could be explained by the fact that carbonation only slightly varied the degree of water saturation at these two RH levels (3 to 8%). However, at a high relative humidity of 93%, the O₂-effective diffusion coefficient for carbonated samples decreased notably by a factor that varies from 2.4 (SL35) to 10 (LS6). This result is a consequence of the decrease of the water retention capacity of these HCPs after carbonation (cf. Figure 48). An increase in the diffusion coefficient is obtained after the carbonation of FA6 and SL6 because of the low degree of water saturation of these samples upon carbonation (cf. Figure 48). In agreement with our results, Dutzer et al. [52] show an increase in the gaseous helium diffusivity upon accelerated carbonation (3% CO₂ vol.) for blended cement pastes, a result they attributed to the cracking induced carbonation.

However, D_{e,O_2} results of MK45 are inconsistent: Although the degree of water saturation slightly increased upon carbonation (Figure 48) and MIP results showed the formation of small porosity for carbonated samples (Figure 47), the oxygen-effective diffusion coefficient increased at all RH levels (factor up to 60 at 93% RH). This result could be explained by the slight increase of the largest pore diameter, even if its volume fraction is lowered (Figure 47). Note that the oxygen-effective diffusion coefficient of the six HCPs after carbonation is less dependent on the RH of preconditioning compared to the non-carbonated state diffusivity. Soja et al. [36] investigated the influence of natural carbonation on the oxygen-effective diffusion coefficient on CEMI and limestone blended cement pastes. Results show a lower oxygen-effective diffusion coefficient even for limestone blended samples equilibrated at 70% RH. Houst et al. [143] noted that the carbonation of Portland cement paste samples caused a decrease in the diffusivity of CO₂ and O₂ at intermediate RH. These microstructural modifications strongly modify the transfer properties in cementitious materials, especially in terms of diffusion and permeability. However, we noticed that this conclusion is only valid for PC6, LS6 and SL35 at low and intermediate relative humidity levels. Our results on the variation of D_{e,O_2} upon carbonation for the six HCPs can be summarized as follows: (i) for blended cement pastes with a W/B 0.45 and 0.6, an increase of the gas diffusivity is observed at all RH levels, (ii) PC6 and SL35 show a decrease in the diffusion coefficient at 33% and 55% RH and an increase in the D_{e,O_2} at 93% RH, (iii) for all HCP (but LS6), D_{e,O_2} is less dependent on the RH in the carbonated state.

2.5.4 Gas-diffusivity vs mean pore diameter

Using an automatic tool that allows for the fitting of the data from the MIP analysis (Figure 47), the mean pore diameter and its corresponding volumetric fraction is computed assuming that each mode is of a normal distribution (Figure 50). This analysis is carried out for all HCPs before and after carbonation. The number of modes of each MIP result is chosen in order to optimize the fit.

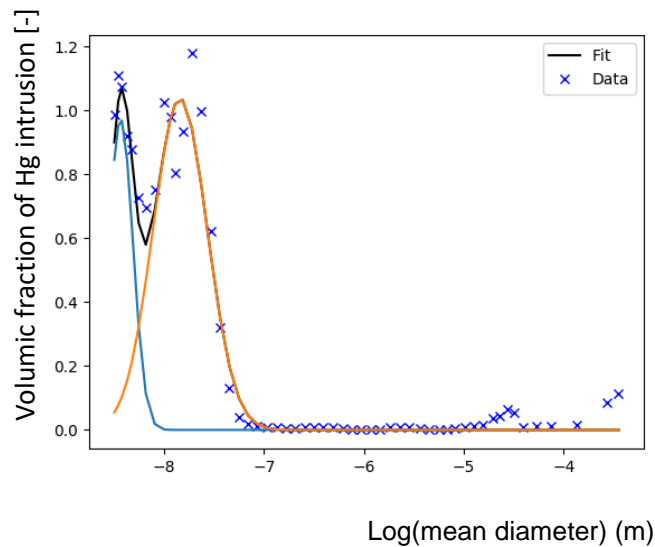


Figure 50: An example of MIP data automatically fitted

Using these results, a weighted arithmetic mean (the weight in the volumetric fraction of each mode) diameter of each paste's MIP data (Figure 47) is calculated and compared with the effective-diffusion coefficients determined experimentally on samples with a saturation degree lower than 50%. The oxygen-effective diffusion coefficient is corrected by the total porosity (ϕ) and the degree of water saturation (S_l) of the tested samples. This correction is made in order to consider that the transport process is made only through the gas filled pores.

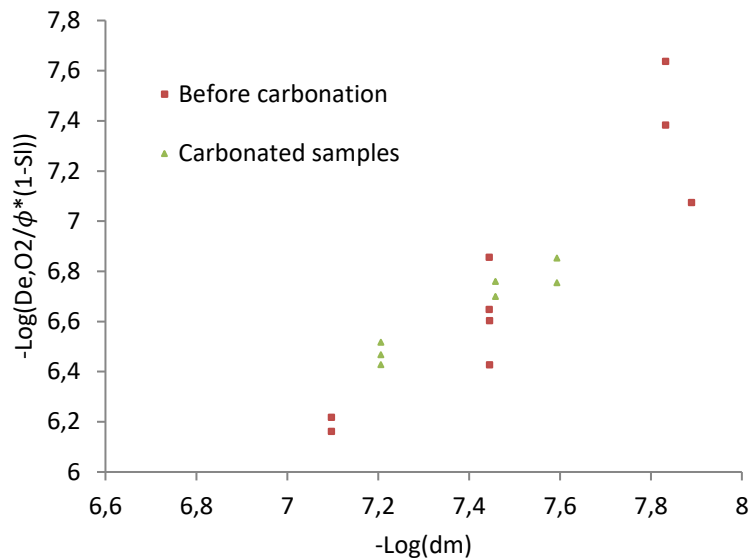


Figure 51: Oxygen-effective diffusion coefficient versus weighted mean pore diameter at different of saturation degrees

Under the Knudsen diffusion assumption, the effective diffusion coefficient is directly proportional to the mean pore diameter of the cementitious material when the mean pore diameter is lower than the mean free path of oxygen molecules at atmospheric pressure and 200C (i.e. $-\log(dm) > 7$) [19][10]. Indeed, Figure 51 shows that the oxygen-effective diffusion coefficient displays a somewhat linear trend (in log-scale) with respect to the weighted mean pore diameter ($-\log(dm) > 7$). For carbonated and non-carbonated samples, the slope equals 0.9 ± 0.05 ($R^2 = 0.92$) and 1.6 ± 0.2 ($R^2 = 0.84$), respectively. These results show that the pore size distribution and the degree of water saturation are appropriate material properties to consider in the modeling of the gas-diffusivity of cementitious materials. Note that this result is consistent with previous findings in the literature [192] carried out on HCPs hydrated at different durations.

2.5.5 Carbonation performance of different HCPs

The carbonation rate ($\text{mm/year}^{0.5}$) of the tested HCPs is calculated at 55% RH from the results of oxygen gas diffusivity at the carbonated state and TGA results of the amount of carbonatable compounds (Table 33). Note that the carbonatable compounds are the product of the cement dosage in the paste by the CO_2 -binding capacity. This 55% relative humidity is chosen since it is suggested that the most rapid carbonation of concrete occurs at a relative humidity near 50% to 65%, which is also the recommended RH for natural carbonation tests by the EN 12390-10 standard [197]. The carbonation depth (X_c) of these HCPs are calculated based on the Papadakis deterministic model [6] (Equation 49), where $[\text{CO}_2]_0$ is the ambient CO_2 concentration ($400 \pm 25 \text{ppm}$) converted to mol.m^{-3} , t is the carbonation exposure duration

(s), D_{e,CO_2} the CO_2 -effective diffusion coefficient in the carbonated layer, and CM [$mol.m^{-3}$] is the carbonatable compounds of the paste. Note that D_{e,CO_2} is calculated using Graham's law, which allows it to be deduced from the O_2 -effective diffusion coefficient.

$$x_c = \sqrt{\frac{2 D_{e,CO_2} [CO_2]_0}{\text{carbonatable compounds}} t} \quad \text{Equation 49}$$

SL35 results are not shown on Figure 52 because no sharp carbonation depth could be seen on these samples even after 4 months of exposure.

HCP	Carbonation kinetics (mm/year ^{0.5})
PC6	1.7
FA6	4.6
SL6	4.7
LS6	9.6
SL35	1
MK45	1.6

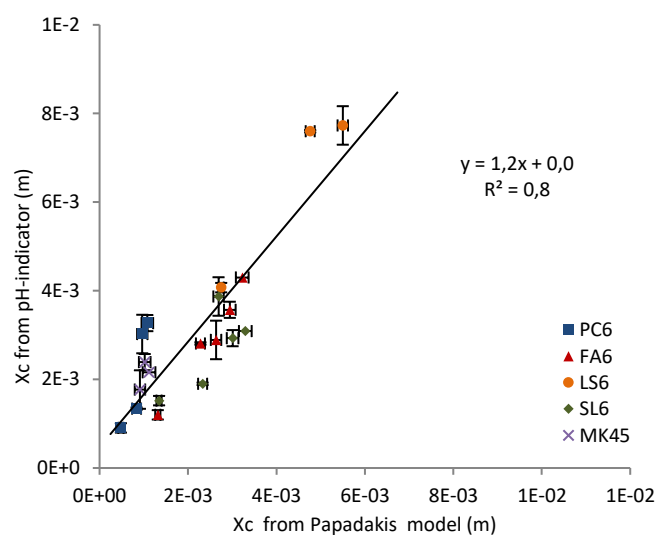


Table 34: Carbonation kinetics calculated under natural carbonation (400 ppm) carbonation at 55% RH

Figure 52: HCPs' X_c determined with pH-indicator vs X_c predicted using Papadakis' model

Figure 52 shows that the carbonation depths obtained from Papadakis' model are correlated to the carbonation depths measured experimentally using phenolphthalein solution. The horizontal error bars are due to oxygen-effective diffusion coefficient variation within replicates, and the vertical errors bars are a result of averaging 5 carbonation depth readings. The pH-indicator results are slightly higher than Papadakis' model; this overestimation could be due to errors of averaging or microcracks within the samples (that the model does not take into consideration).

As expected, PC6 and blended HCPs with low W/B ratios (SL35 and MK45 c.f Table 34) present the highest carbonation resistance. These results are explained by the very low gas diffusion coefficient of the SL35 and MK45 and PC6's high amount of carbonatable products. Although PC6 contains the highest carbonatable products, SL35 and MK45 have a higher

carbonation resistance (i.e. lower carbonation kinetics). These results show that the carbonation depth progression is mainly driven by the CO₂-effective diffusion coefficient of these pastes: the gas-diffusivity of SL35 and MK45 is 10 and 2 times lower than for PC6, respectively. Therefore, the low value of gas diffusivity can compensate for the low carbonatable compounds content. FA6, containing 30% fly ash, showed low carbonation resistance high carbonation kinetics of 4.6 mm/year^{0.5}). Fly ash is known to react with the calcium hydroxide CH formed during the hydration of the cement to form calcium silicate hydrate C-S-H with a lower C/S ratio [206] than the C-S-H phase in pure Portland cement. Indeed, various studies in the literature found increased carbonation depths of concrete when adding fly ash. Morandea et al. [213] reported that with increasing clinker by fly ash (0%, 30%), the carbonation depth under accelerated carbonation (10% CO₂, 63% RH) increases by a factor of 2. SL6 and SL35 with 60% and 50% slag replacement by mass, respectively, contain a comparable amount of carbonatable compounds because of the similar cement composition. In spite of that, SL6 carbonation resistance is almost 5 times higher than SL35 (cf. Table 34). This is due to the low W/B ratio of SL35, which caused the oxygen-effective diffusion coefficient of SL35 to be 26 times lower than SL6. In comparison to PC6, SL6, which is cast at the same W/B (0.6), has a carbonation kinetic that is 2.8 times higher. This is explained by the low carbonatable compound of SL6 compared to PC6 (cf. Table 32). Furthermore, HCPs containing slag have a C-S-H phase with a C/S ratio around 1.5 and below [214]. LS6 performed the worst concerning carbonation resistance. This is due to the high limestone substitution level (40%), low carbonatable products, and high oxygen-effective diffusion coefficient in both carbonated and non-carbonated states. The latter is due to the coarser pore structure compared to pure Portland cement (PC6) (cf. Figure 47), which is characterized by larger, interconnected pores. Such a pore structure promotes gaseous CO₂ transport. The high carbonation kinetics of limestone cement pastes is also justified with the fact that calcite forms preferentially on limestone particles, and less on portlandite and the C-S-H phases [30][215]. The latter would prevent their further carbonation or slow it down considerably. Lollini et al. [216] reported that with a limestone content of 15%, no influence on the carbonation behavior was observed, but at 30%, a remarkable worsening of the carbonation resistance is observed (by 60% to 80%). The MK45 carbonation rate is found to be comparable to that of PC6, although the latter is cast at a W/B ratio of 0.6 and the MK45 W/B ratio is 0.45, and MK45 carbonatable compounds is twice lower than PC6. Note that MK45 gas diffusivity is two times lower than PC6, which compensates for the lower amount of carbonatable compounds in MK45 pastes. Bucher et al. [217] investigated the natural and accelerated carbonation (4% CO₂) of concrete specimen with a cement replacement of 15 to 25% metakaolin cast at a water per binder ratio of 0.6. In this case, the carbonation depth of concrete with metakaolin is found to be 2 to 4 times higher than the carbonation depth of

concrete specimen with CEMI: the higher the metakaolin content, the greater the carbonation depth.

2.6 Conclusions

The results of this work allow drawing the following conclusions:

- Despite a porosity clogging, carbonation induces an increase in the oxygen-effective diffusion coefficient for most of the tested HCPs at all relative humidity levels. Only the Portland cement paste with $W/B=0.6$ and the slag paste with $W/B=0.35$ have a decreased gas diffusivity at 33% and 55% RH after carbonation.
- The oxygen-effective diffusion coefficient variation upon carbonation at a given RH is explained by changes in both the water retention capacity and the pore size distribution.
- For all HCPs, the oxygen-effective diffusion coefficient is less dependent on the relative humidity of preconditioning after carbonation than before.
- The gas diffusion coefficient shows a good correlation with the mean pore diameter of the tested HCPs (in log scale) when the degree of water saturation is lower than 50%. This result is established for both carbonated and non-carbonated HCPs, which proves the direct dependence of the gas diffusivity on the pore size distribution and degree of water saturation of cementitious materials.
- Regarding the durability performance, the theoretical carbonation rate should be dominated by the gas diffusivity, since, for the tested HCPs, the latter varies over two orders of magnitude, while the amount of carbonatable compounds varies only by a factor of 4.
- Materials made with a combination of OPC, slag or metakaolin could behave as well as material containing only OPC with respect to carbonation, providing a low gas diffusivity which can be obtained by a W/B ratio carefully optimized. This could provide a real opportunity to decrease the clinker content in concretes without impacting negatively the durability performance related to carbonation. Further studies on the reinforcement corrosion rate using this kind of mixtures must be carried out before definite conclusion can be made.

3 Paper III: The CO₂-binding capacity of synthetic anhydrous and hydrates: validation of a test method based on the instantaneous reaction rate

3.1 ABSTRACT

In the present work, a new experimental setup is designed and validated to characterize the CO₂-binding capacity of cementitious materials based on their instantaneous rate of CO₂ uptake. An experimental investigation is carried out on synthesized anhydrous (C₃S, C₂S, C₃A) and hydrates (CH, C-S-H, AFt) exposed to ambient CO₂ concentration at three different relative humidity (RH) levels. The BET surface area and the density are determined before and after exposure to natural carbonation. Results show that the CO₂- binding capacity and rate increases highly with the RH. The instantaneous binding rate of the materials ranges from 10⁻⁶ to 5.10⁻¹⁰ g_{co2}.g_{powder}⁻¹.s⁻¹. The highest degree of carbonation is found for ettringite powder (DoC=45%). C₂S and C₃A are only slightly carbonated (DoC=3%), while significant carbonation of C₃S is observed only at 93% RH (DoC=14%). A good (R²=0.94) agreement between the results determined using the new test method and thermogravimetric analysis (TGA) is noticed.

Key words: CO₂-binding capacity; instantaneous binding rate; test method; hydrates; anhydrous

3.2 INTRODUCTION

Steel bars in reinforced concrete are protected from corrosion by means of a passivation layer, which forms at high pH values (>12). This high pH environment is obtained from the surrounding hydrated cement paste. However, once the atmospheric CO₂ manages to move through the concrete porous network [192], it dissolves in the pores' water, forming carbonate ions (CO₃²⁻) [218] that reacts with the reactive calcium content from the calcium-bearing phases in the cement. This reaction converts Ca²⁺ ions into calcium carbonate (CaCO₃). Carbonation is the term used to describe this physicochemical process.

The carbonation front is usually determined using a colorimetric method based on a pH indicator solution, such as phenolphthalein [204]. This method provides only an approximate measurement of the real carbonation depth in terms of pH values and does not give an

estimation of the carbonation extent at any depth [190].

The carbonation depth and rate are controlled by the diffusion process of gaseous CO₂ and the CO₂-binding capacity [6], which is the quantity of CO₂ bound per mass of binder. Test methods that determine the gas diffusivity of cementitious materials can be found in the literature, e.g. [192][141][8][94]. Although gas diffusion is in many situations the slowest mechanism of the overall process [22], an accurate quantification of the CO₂-binding capacity is of critical importance for understanding and modeling the carbonation behavior of cementitious materials. So far, to the authors' knowledge, there is no standardized test method that allows determining these two properties. To address this issue, it is very important to develop reliable, accurate, cost-effective and time-saving test methods to determine the gas transport property of cementitious materials and their CO₂-binding capacity and rate separately.

One way to evaluate the CO₂-binding capacity is applying the thermogravimetric analysis technique (TGA) to measure the weight loss resulting from the thermal decomposition of different phases in the cementitious materials. The temperature of decarbonation is defined separately for each mineral. Usually, the weight loss peak between 530°C to 950°C is caused by the decomposition of CaCO₃ and the consequent release of CO₂ [108]. This technique is destructive, allows a rough quantification of the CO₂-binding capacity in an uncontinuous way and gives an average value of its cumulative rate. TGA is sometimes coupled with XRD-Rietveld that helps quantifying the amounts of CO₂ bound in the crystalline phases only. Major limitations of these techniques are that the CO₂ contained in the amorphous carbonated pastes is not considered by XRD and the CO₂ mass loss due to some carbonates (e.g. MgCO₃) has a temperature range that may overlap the portlandite's and the bound water in the C-S-H gel pores in TGA results [107].

Other techniques in the literature have been developed to examine the CO₂-binding capacity and rate. Van Balen et al. [113] developed an experimental setup to continuously measure the carbon dioxide uptake of lime samples. It consists of a closed loop in which a mixture of air and carbon dioxide (15-50% CO₂ concentration) is introduced at a certain RH (at 20°C). From the analysis of the CO₂ concentration vs. time, the uptake rate (derivative), maximum and average speed of carbon dioxide uptake is calculated. These authors found that the carbonation reaction is zeroth order within the CO₂ concentration range of their study (as also reported by Shih-Min Shih et al. [219]). A good reliability of the test method (10-20%) is reported, but the test method results do not agree with the TGA results.

El-Turki et al [157] developed a micro-balance technique to measure the mass variation of

samples of mortars, cement and lime pastes during carbonation at 100% CO₂ concentration by volume and a RH between 65% and 97%. Analysis of the mass-variation data provides direct determination of the carbonation rates. However, using this method, it is challenging to distinguish between the mass change due to water vapor absorption and the mass gain due to carbonation. The weight gain technique induces a lot of errors for evaluating the carbonation extent [156].

Little information on the carbonation kinetics and mechanisms of the anhydrous and hydrates can be found in the research involving carbonation of cementitious materials. The present work seeks to address this gap through an investigation of the carbonation kinetics and mechanisms of the main hydrates (CH, AFt, and C-S-H) and anhydrous phases (C₃S, C₂S, and C₃A) present in concrete. First, a simple and affordable test method is developed and validated. This method allows determining the CO₂-binding capacity and rate of cementitious materials by monitoring their CO₂ uptake during the exposure to ambient CO₂ concentration in a RH and temperature-controlled environment. Direct measurements of carbon dioxide uptake should avoid possible errors using weight gain as a measure for the carbonation process, as has been shown by Aono [220]. A range of complementary analytical techniques, including thermogravimetric analysis (TGA), Brunauer-Emmett-Teller (BET), density, and scanning electron microscopy (SEM) are used to help the further understanding of the carbonation behavior of the tested materials.

3.3 MATERIALS

3.3.1 Synthetic minerals preparation

In order to enhance the understanding of the carbonation kinetics of the anhydrous phases of cement paste, triclinic tricalcium silicate (C₃S), dicalcium silicate (β -C₂S) and cubic tricalcium aluminate (C₃A), which are the three main anhydrous phases present in the clinker, are prepared. The synthesis of these pure materials was carried out following a modified Pechini process, as described in [136]. The advantage of this method is that pure β -C₂S can be formed with no stabilizing impurities. Phases are produced, respecting the stoichiometric amounts of the oxide components of the anhydrous phases. The heating temperature for C₃S, C₂S and C₃A are: 1600°C, 1550°C, and 1350°C, respectively. These materials are grinded and sieved to 63 μ m.

The main hydrated phases present in Portland cement were also prepared: portlandite (CH), calcium silica hydrates (C-S-H), and ettringite (AFt). The synthesis of ettringite is achieved by mixing tricalcium aluminate and gypsum using a wet process and then dried at 50°C. Pure portlandite was prepared by calcite decarbonation at 1000°C, cooling it down to ambient

temperature and adding water. Calcium silicate hydrate with a Ca/Si = 0.9 was synthesized using CaO obtained from the calcination of Ca(OH)₂ for 4h at 1100°C, SiO₂ comes from hydrophilic silica fume Aerosil 90®. The water-per-solid ratio was 49. The mix was agitated for a month and then the solid phases were separated from the solution by centrifugation for 2 min at 12000 rpm, to be finally oven dried at 45°C under vacuum. The quality of the synthesis was controlled by means of a qualitative XRD test. Even though the preparation of the materials was done in a CO₂-free environment using boiled water cooled down to ambient temperature, and all the synthesized minerals were stored in closed bottles inside a chamber under vacuum with soda lime, traces of calcite were present in the XRD results and were quantified using the thermogravimetric analysis (TGA) technique. After preparation of the samples, their density was measured using the helium pycnometer technique. The initial densities were found to agree with the results found by Balonis et al. [152].

3.3.2 Solid analysis

A Brunauer–Emmett–Teller (BET) measurement was conducted on all the tested samples before and after the CO₂-binding capacity test. This technique uses an inert gas that does not react with the materials surfaces as an adsorbate to quantify the specific surface area [49]. In our case, the sample was first outgassed in a vacuum oven at 0.04 atm and 45°C.

The density of the tested samples is measured applying the helium pycnometer method [130] using the ACCUPYC 2 1340 MICROMERITICS pycnometer. A powdered specimen of about 5 g was compacted and placed inside a cell of a known volume pressurized with helium.

TGA tests were conducted in order to determine the bound CO₂ caused by the preparation of the samples before we began our tests, and the overall CO₂ binding capacity of the material afterwards [106]. The TGA measurements were made under nitrogen flow at a heating rate of 10°C/min until 1000°C using a powdered sample of around 30 mg sieved at 63 µm.

The amount of bound CO₂ is calculated based on Equation 50, where m_{CO2} is the mass of CO₂ present in the sample and given by the TGA results, m₀ corresponds to the mass of the sample at 1000°C, m_{H2O}⁰ is the mass of water initially present in the raw materials.

$$CBC = \frac{m_{CO2}}{m_0 + m_{H2O}^0} \quad \text{Equation 50}$$

The XRD technique was mainly used after the synthesis of the materials to evaluate their purity qualitatively and investigate the type of carbonates formed upon carbonation. Around

1 g of the powdered material (sieved at 63 μm), was introduced in a Philips/PANalytical X'Pert Pro-MPD diffractometer with an X'Celerator detector of an incident $\text{CuK}\alpha$ radiation beam by 40 kV and 40 mA to a rotation sample. The specimens were scanned for 40 minutes from $2\theta = 5$ to 65° by a step of 0.25° without protection from air CO_2 and in a dry environment (RH~40%).

Parallel to these experiments, scanning electron microscopy SEM [127] technique was used in order to observe the morphological changes in some powders upon carbonation. The powders were placed on a carbon adhesive sample holder and coated using gold-palladium as conductive material. The observations were made with a MEB-FEG FEI Quanta 400 device in the secondary electrons mode at an accelerated voltage of 15 KeV.

3.3.3 Carbonation exposure conditions and equipment

In order to perform a CO_2 -binding capacity test, 1 g of the tested powder was evenly and thinly distributed over a PVC sample holder (Figure 53 (a)) of 110 mm diameter for exposure in the carbonation chamber in a room at $20 \pm 2^\circ\text{C}$ (Figure 53 (b)). The RH inside the climate chamber was controlled by means of saturated salt solutions.

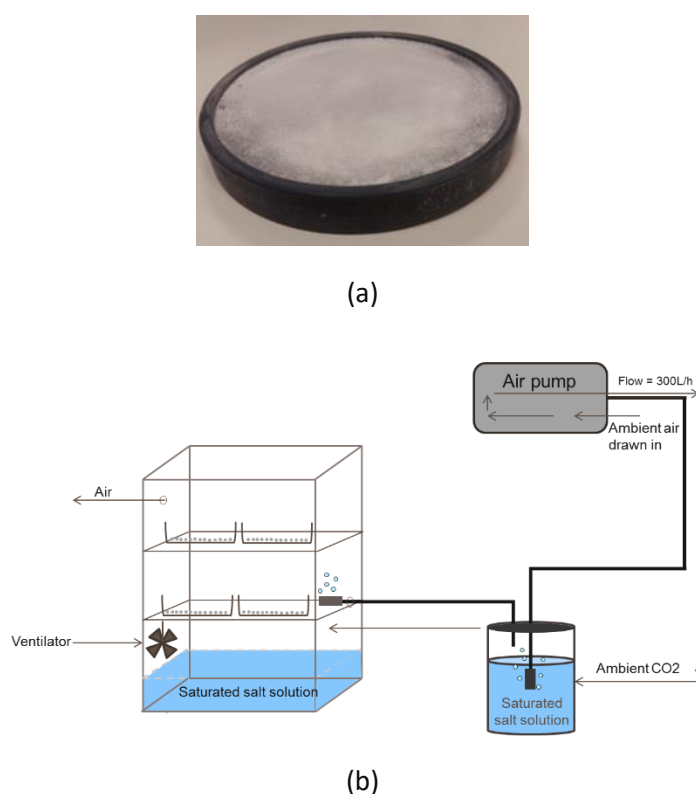


Figure 53: (a) A tested powder sample on the sample holder; (b) climate chamber during the natural carbonation of the powder specimen

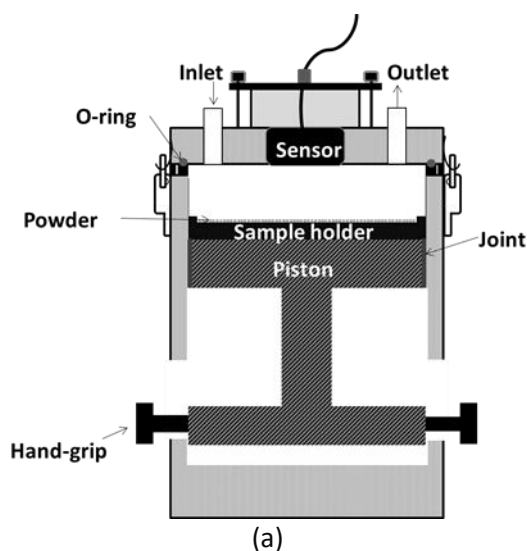
In order to maintain the CO_2 concentration constant inside the climate chamber, an air pump

of 300L/h flow rate was used to pass the ambient air through a bubbler filled with a saturated salt solution to regulate it at a certain RH and circulate it inside the climate chamber. This way, the RH, temperature and CO₂ concentration (450 ± 100 ppm) were kept constant inside the climate chamber. The volume of the chamber (40L) was well-ventilated thanks to a ventilator that ensured homogenization of the humid air at ambient CO₂ concentration.

3.3.4 Instantaneous rate measurements

3.3.4.1 Principle and apparatus

A new experimental device able to directly measure the CO₂-uptake of powdered samples was designed. The principle is to place a given mass of reactive powder in a closed gas volume of controlled initial composition. The measured CO₂ depletion in the gas phase over a short time interval (minutes) is then exactly compensated by the CO₂ uptake in the solid. During the carbonation period, the instantaneous CO₂ uptake of the powder was measured occasionally in a closed system (closed cell). The frequency of the CO₂ uptake measurements was twice a day for the first three days of carbonation and once a day afterwards. The experimental data collected from these experiments were CO₂ depletion curves in a closed cell over the carbonation exposure period. The carbonation cell (Figure 54) consists of a closed system in which the sample holder containing the powdered material is introduced during the CO₂-uptake measurements. The cell is a cylinder having an outside and inside diameter of 140 mm and 120 mm, respectively.





(b)

Figure 54 : (a) the carbonation cell sketch (b) photo of the carbonation cell

The cell cover incorporates the infrared IR CO₂ gas sensor. An O-ring with a round cross-section is placed around the cover in order to seal the interface between the cover and the cell body. The cell closure is done manually by means of four stainless steel lockable clips. The total measurement time of the CO₂ uptake by the sample must be negligible with regards to the overall carbonation period. Therefore, the cell body contains a 140 mm diameter piston of an adjustable height to vary the inside volume of the chamber. The latter can vary from 10 to 285 mL. The tests were carried out at ambient temperature (20°C) and pressure (1 atm).

3.3.4.2 Analysis of the rates (from experimental data)

The experimental setup allows for the direct measurements of the CO₂-uptake of the tested powders at different times of exposure to ambient CO₂ concentration. Figure 55 gives examples of CO₂ depletion in the gas phase over time in the case of ettringite powder after 1, 2, 5 and 30 days of exposure to ambient CO₂ concentration in a climate chamber regulated at 93% RH. CO₂ depletion in the gas correspond to CO₂ uptake by the solid: we refer only to CO₂ uptake curves later in the document. The measurement period was around 30 min long. Each curve allows defining a rate of carbon dioxide uptake, which is proportional to its initial slope. It is noticed from Figure 55 that ettringite's reaction rate decreases as the carbonation reaction proceeds to drop sharply after 30 days of carbonation when the detection limit is reached.

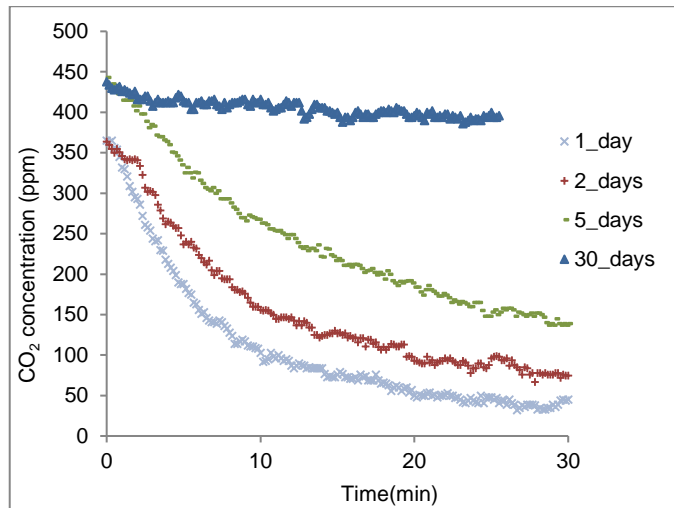


Figure 55: CO₂-uptake curves of ettringite powder at different carbonation periods: 1 and 2 days (gas volume = 123 mL), 5 and 30 days (gas volume = 10 mL)

By considering the CO₂-uptake curves, the instantaneous binding rate (IBR), the bound-CO₂ (B_{CO₂}), and the degree of carbonation (DoC) are determined.

First, the initial slope (S) of each CO₂-uptake curve was determined automatically by maximizing the R-squared and minimizing the mean squared error using statistical software (JMP). The instantaneous binding rate is then calculated according to Equation 51, where IBR (g_{CO₂} g⁻¹_{powder} s⁻¹) is the instantaneous CO₂-binding rate, S (s⁻¹) is the CO₂-uptake initial slope, P (Pa) the ambient pressure, R (m³·Pa·K⁻¹·mol⁻¹) the ideal gas constant, T (K) the ambient temperature, V_g (m³) the inside volume of the carbonation cell, M_{CO₂} (g) the molar mass of carbon dioxide, and m₀ (g) is the mass of the material with neither unbound CO₂ nor water. This mass was calculated from the mass of the tested powder corrected by the mass loss results from TGA before carbonation of the sample (at 1000°C).

$$IBR = \frac{S * P * M_{CO_2} * V_g}{R * T * m_0} \quad \text{Equation 51}$$

$$B_{CO_2} = \int_{t=0}^T IBR dt \quad \text{Equation 52}$$

$$DoC = \frac{CBC}{MBC} \quad \text{Equation 53}$$

$$MBC = \sum \%CaO * \frac{M_{CO_2}}{M_{CaO}} - \%SO_3 * \frac{M_{CO_2}}{M_{SO_3}} \quad \text{Equation 54}$$

The bound-CO₂ (B_{CO₂}) is deduced from the IBR by the trapezoidal integration of the IBR

values between two CO₂-uptake measurements (from t=0 to T the time of the CO₂ uptake measurement) (Equation 52). The total CO₂-binding capacity (CBC) of the tested powder is the maximum value of the B_{CO₂} at the end of the carbonation period.

Note that the B_{CO₂} is expressed as the mass of CO₂ bound per mass of the powder (m₀). The degree of carbonation is calculated following Equation 53, where the maximum binding capacity (MBC) is calculated from the chemical composition of the tested material assuming that all CaO will be transformed into CaCO₃ except the one that reacts with SO₃ to form CaSO₄. The oxides molar ratio is given from the stoichiometry of the chemical formulas of each synthesized material. M_{SO₃}, M_{CO₂}, M_{CaO} (g/mol) are the molar masses of trioxide sulfur, carbon dioxide and calcium oxide, respectively.

3.3.4.3 Analysis of the reaction order

The analysis of the CO₂-uptake curves determined using our experimental setup allows for the determination of the reaction order and the rate constant k_i (see Equation 55, 56 and 57). The analysis of the reaction order is of relevance regarding the measured instantaneous binding rates (see Equation 51) that are corrected according to the reaction rate.

The order of the reaction was determined by analyzing the slope of the linear graph obtained, whether with [CO₂], ln ([CO₂]) or 1/[CO₂], versus time and the linear fit quality (R-squared).

Zero order	$[\text{CO}_2](t) = -k_0 * t + [\text{CO}_2]_0$	Equation 55
------------	---	-------------

First order	$\ln ([\text{CO}_2](t)) = -k_1 * t + \ln ([\text{CO}_2]_0)$	Equation 56
-------------	---	-------------

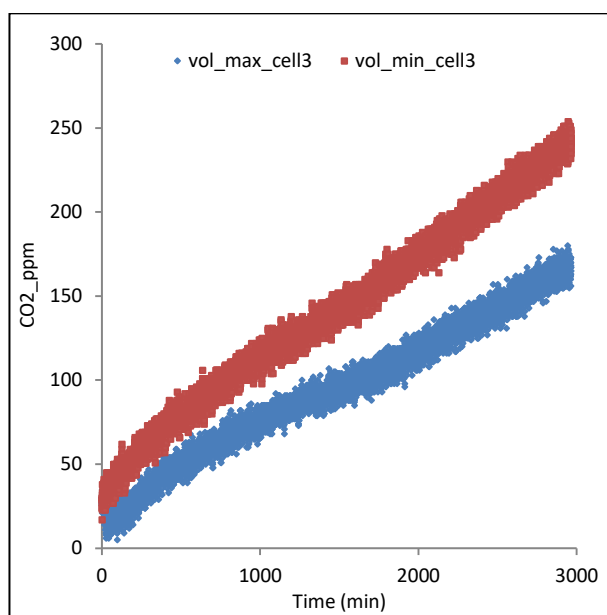
Second order	$\frac{1}{[\text{CO}_2](t)} = -k_2 * t + \frac{1}{[\text{CO}_2]_0}$	Equation 57
--------------	---	-------------

The order of reaction of a reactant indicates how much the rate of reaction changes if the concentration of the reactant is changed. The CO₂ concentration has no effect on the reaction rate of zeroth order reactions, while for first-order reactions, the rate of reaction changes directly with the concentration of the corresponding reactant. For second-order reactions, the rate of reaction changes as the square of the reactant concentration.

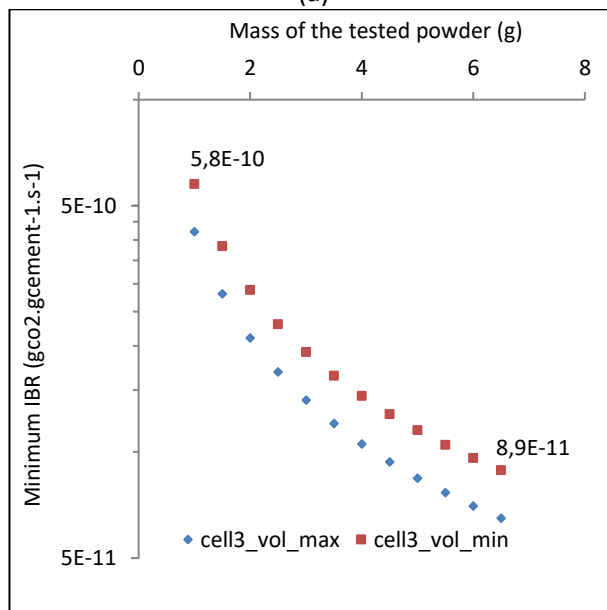
3.3.4.4 Test method and detection limit

In this work, six carbonation cells were used in parallel. Cells leakage rates were determined by performing blank tests: the cells were first flushed with nitrogen (from the inlet as shown on

Figure 53), then the CO₂ concentration inside the cell was measured for 48 hours. Note that the blank tests were performed on all the cells at their maximum (285 mL) and minimum (10 mL) volumes. The collected data (CO₂ concentration vs. over time) were analyzed to calculate an equivalent CO₂-binding rate that sets the lower detection limit of the test method. Figure 56 (a) gives an example of leakage tests on a given cell (cell3). The minimum IBR that can be measured using our experimental setup depends on the mass of the tested powder. Figure 56 (b) shows the decrease of the minimum IBR with the mass of the sample. However, experiments are conducted using 1 g of the powder in order to minimize the thickness of the grains layer and thus avoid mass diffusion during the carbonation exposure time. Therefore, the detection limit of the cell taken as an example is set at $5.8 \times 10^{-10} \text{ gCO}_2 \cdot \text{g}_{\text{powder}}^{-1} \cdot \text{s}^{-1}$.



(a)



(b)

Figure 56: (a) example of a leakage test performed on a closed cell (cell3), (b) the minimum IBR that can be detected as a function of the sample mass

Note that the highest IBR ($1.1 \times 10^{-6} \text{ g}_{\text{CO}_2} \cdot \text{g}_{\text{powder}}^{-1} \cdot \text{s}^{-1}$) determined with our test method corresponds to the value of the most reactive material (portlandite powder) tested during the first day of exposure to carbonation at the highest RH (93%).

3.4 Results

3.4.1 TGA and XRD results

3.4.1.1 TGA results of the materials after carbonation at 93% RH

Figure 57 shows the TGA results of the tested powders after carbonation at 93% RH. The TGA results are shown after carbonation at this RH only because the C_3S powder only carbonates at 93%RH. It is worth noting that a peak is observed from 550°C to 950°C after carbonation of the materials. This result corresponds well to the temperature range of the decomposition of calcium carbonate reported in the literature [108]. After carbonation of C_2S and C_3S at 93% RH, TGA results show a certain amount of bound water (temperature range $[150\text{-}250^\circ\text{C}]$), which could be due to the formation of C-S-H during the preconditioning.

The TGA results of carbonated ettringite and C_3A show a peak around $280\text{-}300^\circ\text{C}$, which corresponds to the decomposition of aluminum hydroxide. According to Collier [108], the thermal decomposition of aluminum hydroxide occurs within the same temperature range.

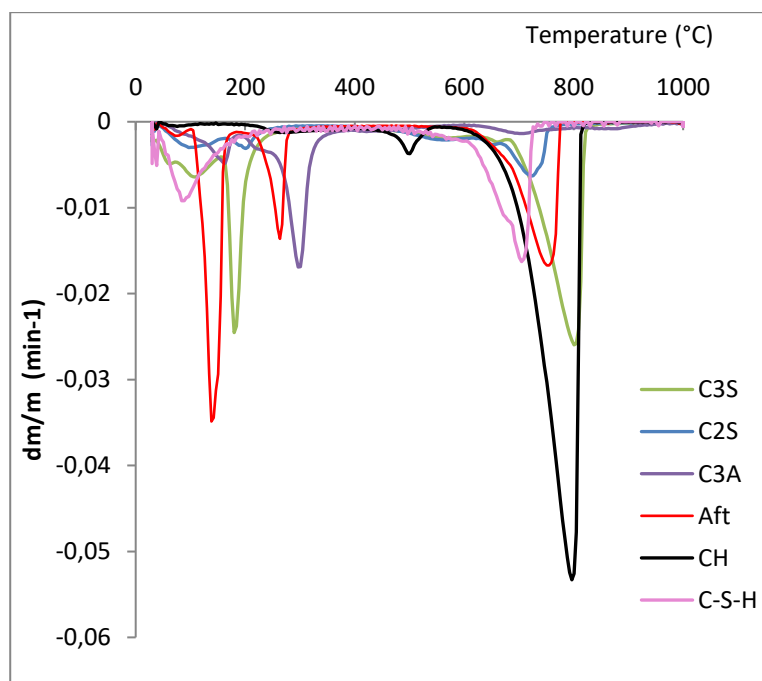


Figure 57: TGA results of C_3S , C_2S , C_3A , Aft, CH and C-S-H after carbonation at 93% RH

3.4.1.2 CO_2 -binding capacity of the tested materials

The bound-CO₂ of the synthetic materials was determined using TGA, just before the conditioning at different RH levels with soda lime. Table 35 (column TGA initial in 10⁻² g_{CO₂} g⁻¹_{powder}) shows that some carbonation of the powdered samples could not be avoided, even if great care was taken to fill the climate chamber with soda lime (the CO₂ concentration inside the chamber was found to be less than 10 ppm). The maximum initial bound CO₂ is reached for portlandite powder (4.1 * 10⁻² g_{CO₂} g⁻¹_{powder}, DoC = 6.8%).

The bound CO₂ was also determined by TGA at the end of the carbonation period corresponding to the durations given in Table 35. Note that the initial bound CO₂ is deduced from these results. The CO₂-binding capacity of all the systems under all conditions is determined using Equation 50. Table 35 shows that the CO₂-binding capacity of all materials increases with the RH of exposure. The degree of carbonation varies between 1% and 45%, which highlights the incomplete carbonation of the materials, inspite of the very low rate at the end of the ageing period.

Material	Theoretical maximum binding capacity 10 ⁻² g _{CO₂} g ⁻¹ _{powder}	B _{CO₂} in 10 ⁻² g _{CO₂} g ⁻¹ _{powder} before the carbonation test (degree of carbonation)	RH (%)	CO ₂ (ppm)	Ageing period (days)	B _{CO₂} in 10 ⁻² g _{CO₂} g ⁻¹ _{powder} after the carbonation test (degree of carbonation)
CH	59.5	4.1 (7%)	93	~450	14	23 (39%)
			55	~450	15	13.8 (23%)
			33	~450	25	7.0 (12%)
C-S-H	35.9	2.9 (8%)	93	~450	27	11.0 (31%)
			55	~450	27	5.4 (15%)
			33	~450	27	2.2 (6%)
Ettringite	38.9	2.1 (5%)	93	~450	35	17.6 (45%)
			55	~450	11	3.5 (9%)
			33	~450	29	1.5 (4%)
C ₂ S	51.2	0.1 (0.1%)	93	~10	32	0.5 (1%)
				~450	13	1.5 (3%)
			55	~450	13	0.8 (2%)
				33	~450	13
C ₃ S	57.9	0.1 (0.1%)	93	~10	32	2.1 (1.2%)
				~450	14	8.0 (14%)
			55	~450	14	3.2 (6%)
				33	~450	15
C ₃ A	48.9	0.6 (1.2%)	93	~10	32	1 (2.1%)
				~450	13	1.5 (3%)
			55	~450	13	1 (2%)
				33	~450	13

Table 35: B_{CO₂} before and after the carbonation test at three RH levels: TGA results

In order to investigate the possible carbonation and hydrate formation by anhydrous materials

during the preconditioning at 33%, 55% and 93% RH, the powders were stored inside climate chambers regulated at these RH for 32 days. Soda lime was added inside the climate chamber to avoid carbonation during this preconditioning period ($\text{CO}_2=10\text{ppm}$). The TGA raw data reveal only two peaks: [100-250°C] and [550-950°C]. The first corresponds to bound water, which could be a result of the formation of C-S-H for C_3S and C_2S , and the formation of aluminum hydroxide for C_3A powders [108]. Table 35 shows that the degree of carbonation after the preconditioning without soda lime of anhydrous minerals at 93% RH varies between 0.1% and 1.2%.

3.4.1.3 XRD results

XRD tests were carried out before the exposure of the materials to carbonation, after carbonation at 93% RH, and also after preconditioning of the anhydrous powders (C_3S , C_2S and C_3A) at 93%RH with soda lime for 32 days ($\text{CO}_2 = 10 \text{ ppm}$) in order to investigate any possible formation of hydrates. Note that only the 93% RH exposure was tested for anhydrous minerals preconditioned without CO_2 and all materials carbonated at 93% RH, since the amount of bound CO_2 was the highest at this RH level. Indeed, Flatt et al. [221] suggest that alite stops hydrating below 80% RH. Qualitative XRD results are summarized in Table 36. All the powders did not carbonate fully, since a trace of the pure mineral in the powder is confirmed by XRD results (Table 36).

Material	State	Calcite	Aragonite	Vaterite	Gypsum	C_3S	AFt	CH	C_2S	C_3A
CH	After carbonation at 93%RH	++	-	-	-	-	-	+	-	-
C-S-H		++	+	+	-	-	-	-	-	-
AFt		+	++	-	++	-	+	-	-	-
C_3S		++	-	+	-	++	-	-	-	-
C_2S		+	-	-	-	-	-	-	++	-
C_3A		+	-	-	-	-	-	-	-	++
C_2S	After conditioning at 93%RH with soda lime.	-	-	-	-	-	-	-	++	-
C_3S		-	-	-	-	++	-	-	-	-
C_3A		-	-	-	-	-	-	-	-	++

Table 36: results of qualitative XRD on synthetic materials after carbonation at 93% RH (++: phase highly present, +: phase present in lower quantity, -: phase not detected)

Results show that the only carbonate formed after the carbonation period of pure portlandite is calcite, which agrees with several findings in the literature [222][223]. Calcite is also the primary polymorph produced during the carbonation of C-S-H coexisting with small amounts of aragonite and vaterite, which could be linked to the Ca/Si ratio of the tested C-S-H (0.9). Indeed, Black et al. [211][212] studied the carbonation of synthetic C-S-H in which the initial Ca/Si ratio appeared to influence the crystalline carbonate species formed. For Ca/Si ratios greater than 0.67, principally calcite and vaterite were observed, whereas for ratios below 0.50, aragonite was most prevalent.

Ettringite carbonation is expected to form gypsum and amorphous aluminum hydroxide, which were not detected by XRD analysis (Table 36). However, the TGA results in Figure 57 for carbonated ettringite at 93% RH show a peak around 280-300°C, which corresponds to the decomposition of aluminum hydroxide according to Collier [108]. In agreement with our results, Nishikawa [224] and Zhou [225] reported that the carbonation of synthetic ettringite is accompanied by increasing formation of vaterite or aragonite, alumina gel and gypsum. However, Zhou and Glasser [225] observed only vaterite as the carbonate product formed, while Nishikawa et al. [224] described vaterite forming initially but aragonite being predominant at later stages.

The XRD analysis of the carbonated C₃S powder shows the formation of calcite as the main carbonation product with a trace of vaterite, while the analysis of the C₃A and β-C₂S powders after 14 days of natural carbonation at 93% RH only revealed small traces of calcite.

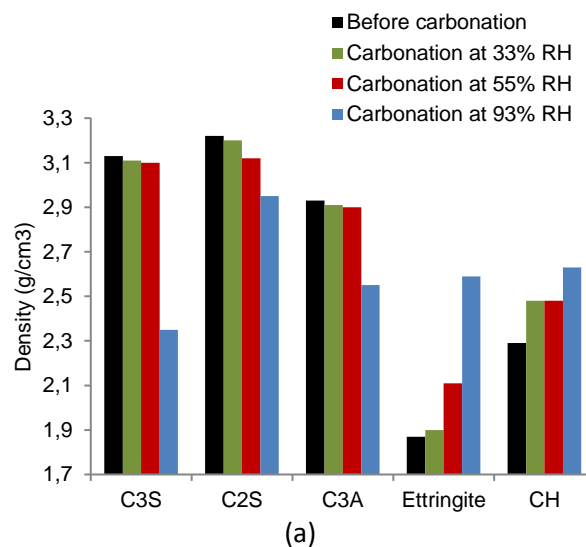
The XRD analysis of the C₃A and β-C₂S powders after 14 days of natural carbonation at 93% RH only revealed small traces of calcite. This result is due to the small B_{CO₂} of β-C₂S and C₃A and could be also a consequence of the formation of an amorphous calcium silicate hydrocarbonate phase that is also shown by several researchers [226][227][228]. It is worth noting that no calcium hydroxide is detected by the XRD analysis after carbonation of C₃S. XRD results show no trace of calcite even though the degree of carbonation of anhydrous materials reached up to 1.2% (cf. Table 35). This could be explained by the formation of amorphous calcium carbonate.

Research conducted by Seishi et al. [226] on the morphology of the carbonates formed after the reaction of pure C₃S with 5% CO₂ concentration under saturated humidity at room temperature revealed that calcite was the main product, coexisting with vaterite and aragonite. However, aragonite is recognized as the main carbonate for β-C₂S coexisting with traces of calcite and vaterite. Our differing results may be due to the fact that CO₂ concentrations differ. Han et al. [229] showed that C₃S and C₂S carbonation reaction results in the formation of

CaCO₃ and silica gel.

3.4.2 Microstructure results (BET, SEM)

The BET surface area and density of anhydrous minerals CH and ettringite were determined before the beginning of the carbonation test and after carbonation at the three levels of RH. Figure 58 (b) shows that the BET surface area increased by a maximum factor of 1.7 when the anhydrous minerals and ettringite are carbonated at 33% and 55% RH, while it increased significantly (by a factor of 7) when these materials are carbonated at 93% RH. Nevertheless, for portlandite powder, the BET surface area decreases with the RH under which the carbonation test was carried out (by a factor of 6 at 93% RH). Regarding the density variation upon carbonation (Figure 58 (a)), an opposite trend is noticed: the density of the anhydrous phases decreased with the RH (by almost 1g/cm³) and the density of portlandite and ettringite increased significantly with the RH of carbonation. The BET surface area of C-S-H powder was only tested after carbonation at 93% RH and the density was not determined for practical reasons. A high decrease in the BET surface area was noticed on this powder (from 190 m²/g to 88 m²/g), which could be due to the precipitation of carbonates on the surface of the grains.



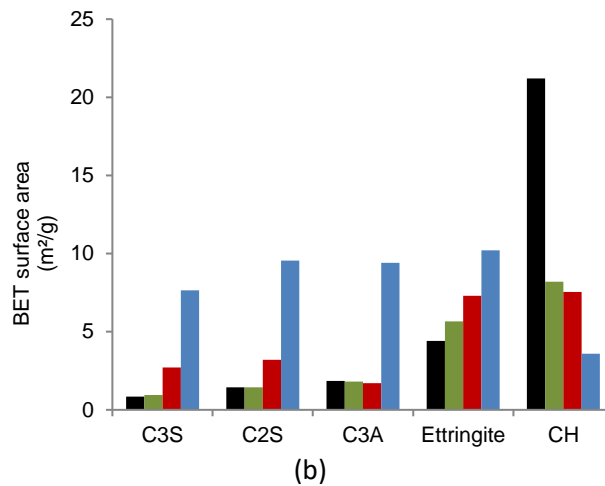
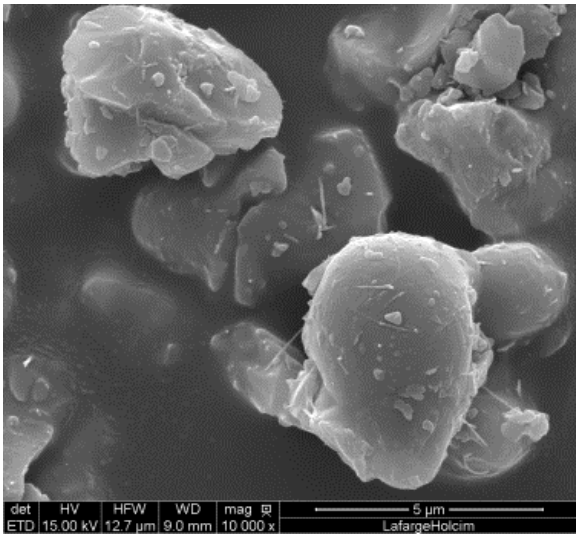
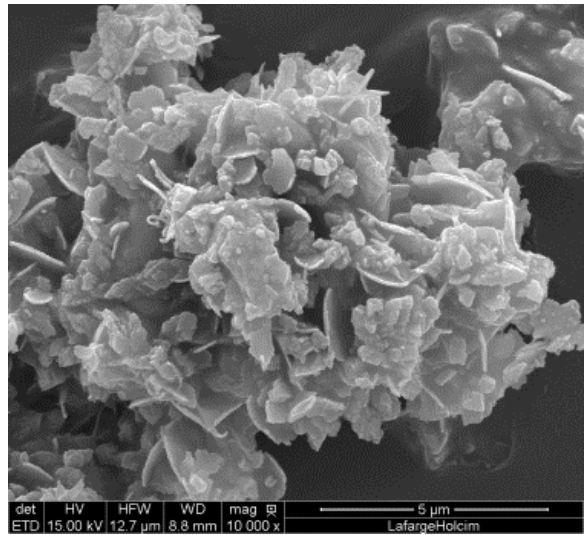


Figure 58 : The density (a) and BET surface area (b) of the materials before and after carbonation at different RH

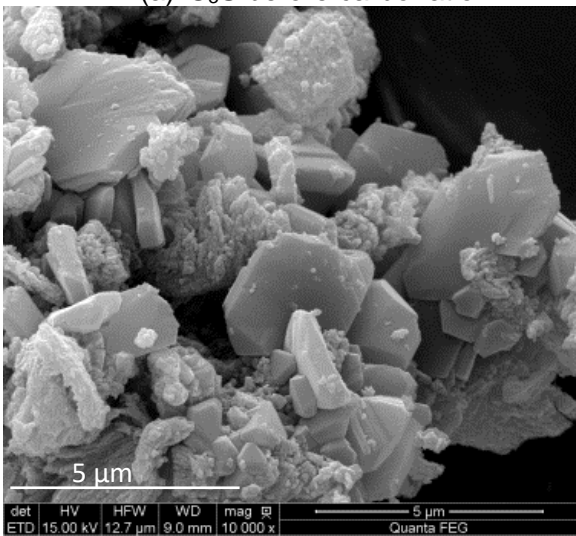
Figure 59 shows the SEM images of C₃S, CH and AFt before carbonation and after carbonation at 93% RH. These images allow for the observation of the morphological evolution of the grains upon carbonation. Figure 59 (b) and (c) show an increase in the amount of carbonation products on the surface of C₃S and CH after carbonation. As for ettringite powder, carbonation is known to result in the formation of carbonates (vaterite and aragonite), alumina gel and gibbsite [36]. Figure 59 (f) shows the formation of carbonate crystals between the needles of ettringite with a shape that resemble to vaterite (hexagonal) and calcite (trigonal) [29]. Indeed, XRD results (Table 36) confirm the formation of these two carbonates.



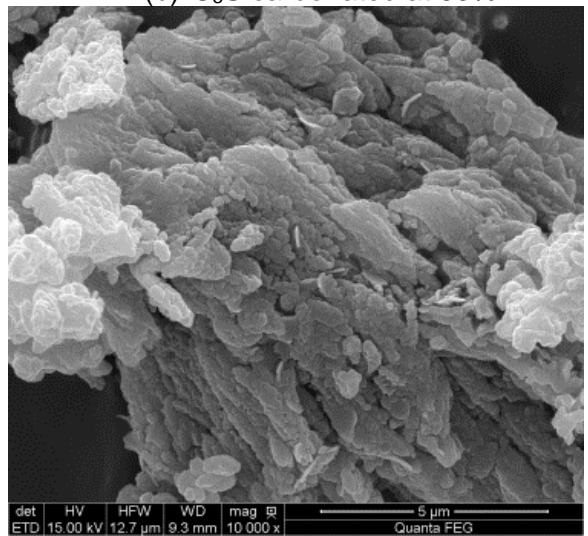
(a) C₃S before carbonation



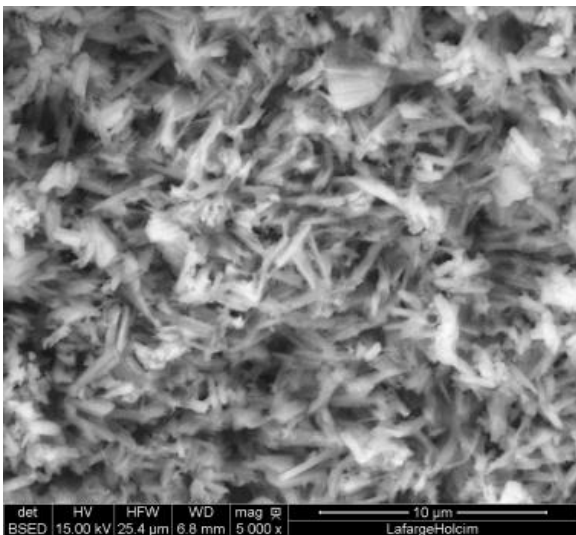
(b) C₃S carbonated at 93%



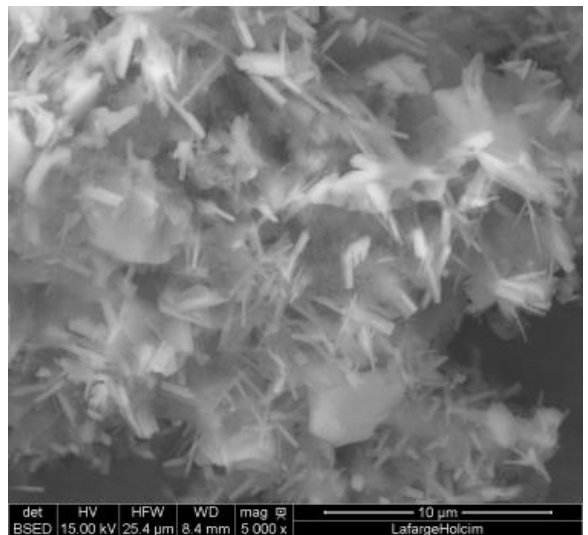
(c) CH before carbonation



(d) CH carbonated at 93%



(e) Non-carbonated ettringite



(f) Ettringite carbonated at 93% RH

Figure 59 : Morphological evolution of C₃S, CH and Af_t powders before carbonation and after exposure to carbonation at 93% RH

3.4.3 Reaction order analysis

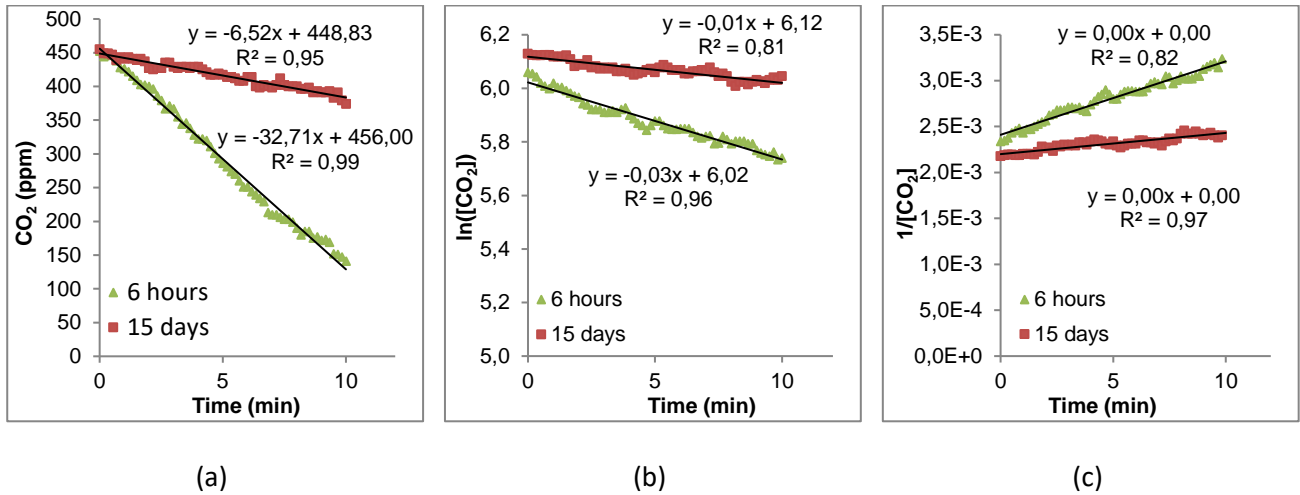


Figure 60: Reaction order analysis of portlandite after 6 hours and 15 days of exposure to carbonation. Order 0 (a), order 1 (b), order 2 (c)

Figure 60 shows an example of the reaction order analysis of portlandite powder carbonated at 33% RH. The analysis of Figure 60 reveals that the best linear fit for the considered timescale is obtained for the zeroth order (cf. Table 37). Consequently, the carbonation reaction kinetics (hence the CO₂ binding capacity) are independent of the CO₂ concentration within the concentration range of our experiments (450 ± 100 ppm). In agreement with these results, Van Balen et al. [230] and Shih et al. [219] suggest that the carbonation reaction of lime and portlandite powders at 7 - 17% CO₂ and 3.15-12.6% of CO₂, respectively, are of order 0.

Material	RH (%)	Exposure period (day)	order 0	order 1	order 2
CH	93	1	0.98	0.97	0.86
		8	0.69	0.62	0.68
	55	2	0.98	0.98	0.80
		13	0.88	0.80	0.81
	33	8 hours	0.99	0.96	0.96
15		0.85	0.81	0.82	
C-S-H	93	6 hours	0.99	0.99	0.98
		7	0.92	0.91	0.91
	55	5 hours	0.99	0.99	0.98
		22	0.82	0.81	0.82
	33	1	0.99	0.99	0.98
22		0.54	0.51	0.53	
AFt	93	1	0.99	0.97	0.96
		28	0.91	0.89	0.87
	55	8 hours	0.96	0.95	0.94
		17	0.91	0.92	0.89
	33	8 hours	0.97	0.83	0.83
10		0.67	0.29	0.29	
C ₃ S	93	4 hours	0.95	0.94	0.93
		9	0.99	0.99	0.97
	55	1	0.99	0.98	0.98
		12	0.78	0.78	0.79
	33	6 hours	0.96	0.95	0.94
6		0.42	0.41	0.36	
C ₂ S	93	1	0.96	0.96	0.96
		11	0.96	0.97	0.97
	55	0	0.96	0.96	0.97
		11	0.92	0.92	0.91
	33	2	0.92	0.92	0.92
10		0.84	0.83	0.84	
C ₃ A	93	2	0.97	0.97	0.91
		10	0.95	0.89	0.96
	55	0	0.97	0.96	0.97
		9	0.57	0.56	0.56
	33	0	0.85	0.85	0.85
10		0.19	0.20	0.21	

Table 37: R-square values for the reaction order analysis

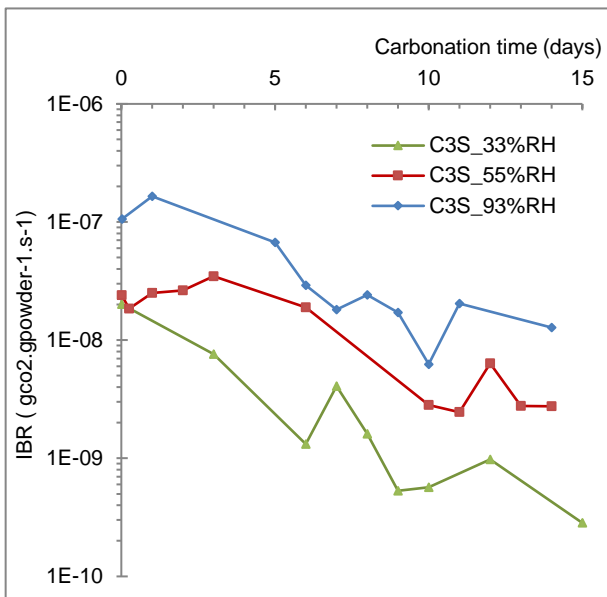
Table 37 gives a summary of the reaction order analysis of the tested materials at different RH levels, and the R-squared of the linear fit analysis of the reaction orders. From analyzing the CO₂-uptake curves, it is noticed that the carbonation reaction during the first week of exposure is zeroth order in most cases. However, for anhydrous powders, a good fit is obtained for all orders. This result could be due to the carbonation reaction of more than one reactant. Still, Table 37 shows very comparable results of the fit quality of the CO₂-uptake curves for order 0,

1 and 2.

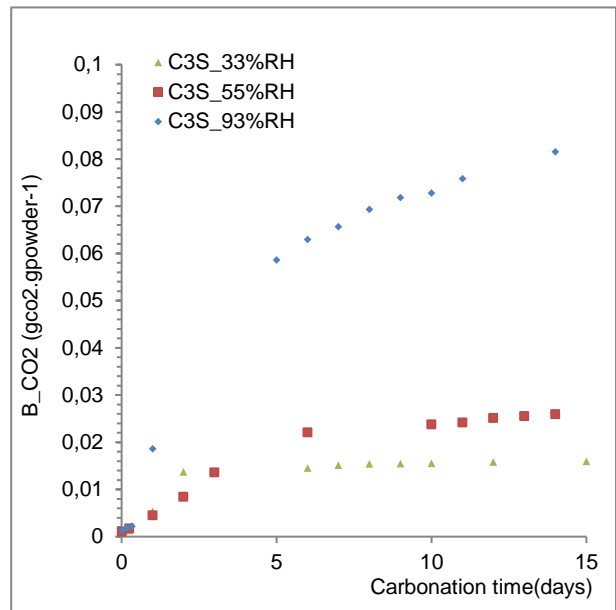
3.4.4 CO₂-binding capacity of anhydrous minerals from IBR

For each tested anhydrous material, Figure 61 and Figure 62 give the IBR and B_{CO_2} , respectively. The IBR of anhydrous materials decreases with the exposure time. Note that since the IBR values are higher than the detection limit of the setup (5.8×10^{-10} gCO₂.gpowder⁻¹.s⁻¹), these results refer to the properties of the materials rather than to any cell leakage. The IBR depends on the RH: the higher the RH, the higher the CO₂-binding rate. The IBR varies from $[10^{-8}$ to $10^{-10}]$, $[10^{-8}$ to $10^{-9}]$, and $[10^{-7}$ to $10^{-9}]$ gCO₂.gpowder⁻¹.s⁻¹ when the carbonation tests are carried out at 33% RH, 55% RH, and 93% RH, respectively. It is known that the controlling factor in the carbonation reaction rate is the dissolution of CaO and gaseous CO₂. At high RH, there is more water present to dissolve CaO and CO₂, which increases the rate of the reaction. After 14 days of exposure to ambient CO₂ in climate chambers with constant RH levels (33, 55 and 93%), no anhydrous material reached the maximum binding capacity MBC, which was theoretically calculated (Table 35).

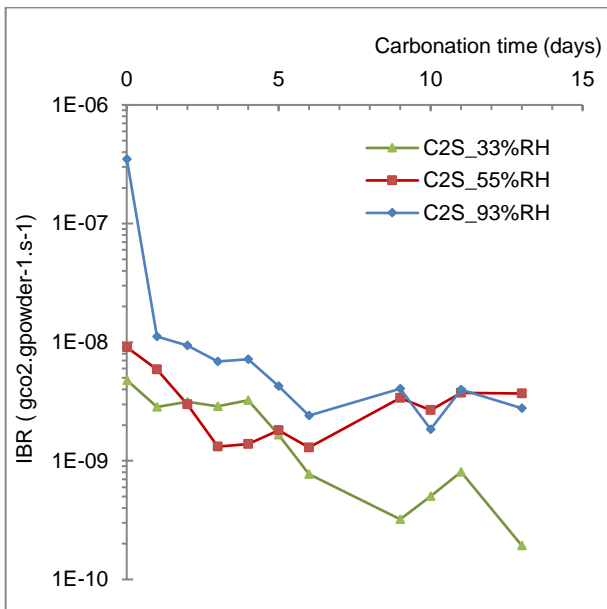
A slight carbonation of C₂S and C₃A powders was observed. The highest CBC was observed for C₃S powders carbonated at 93% RH. Furthermore, Figure 61.b shows that, after 14 days of exposure, the amount of bound CO₂ at 93% RH of the C₂S powder continued to increase but at a very slow rate (2×10^{-9} gCO₂.gpowder⁻¹.s⁻¹) while this rate was 10 times higher for C₃S powder.



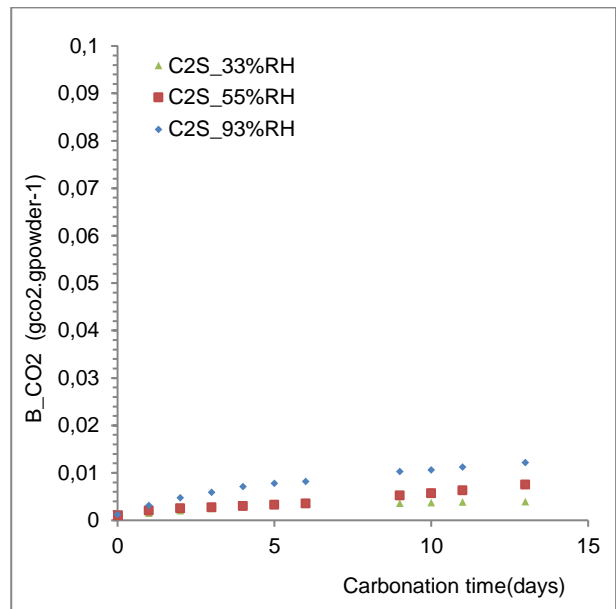
(a)



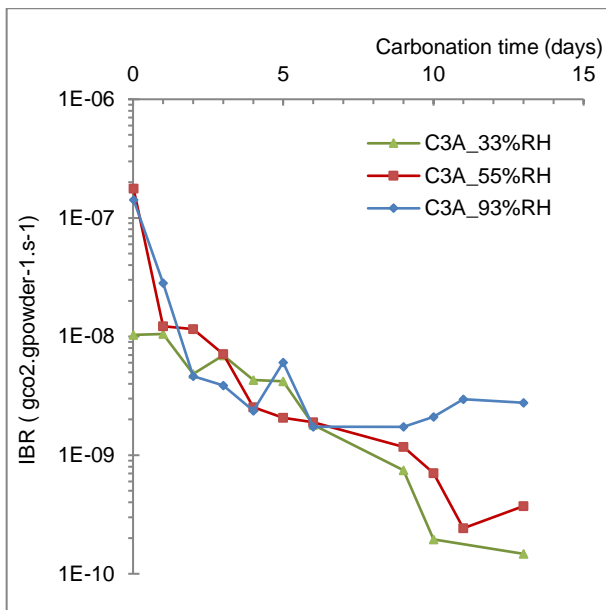
(a)



(b)

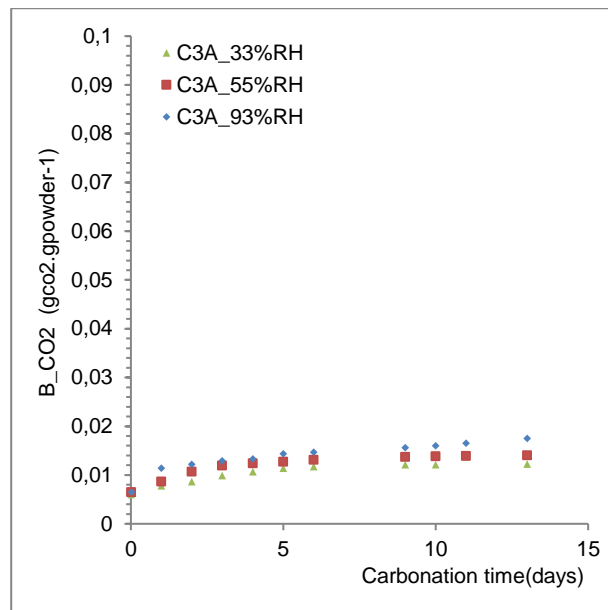


(b)



(c)

Figure 61: IBR of anhydrous phases



(c)

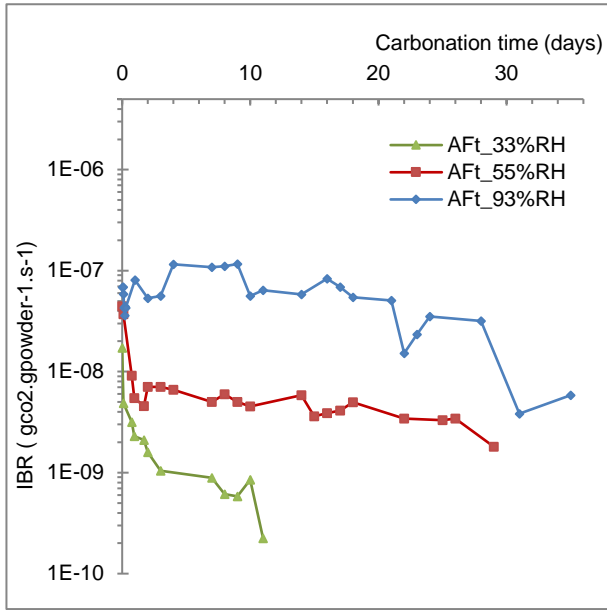
Figure 62: the amount of bound CO₂ at different carbonation periods of anhydrous phases

3.4.5 CO₂-binding capacity of hydrates from IBR

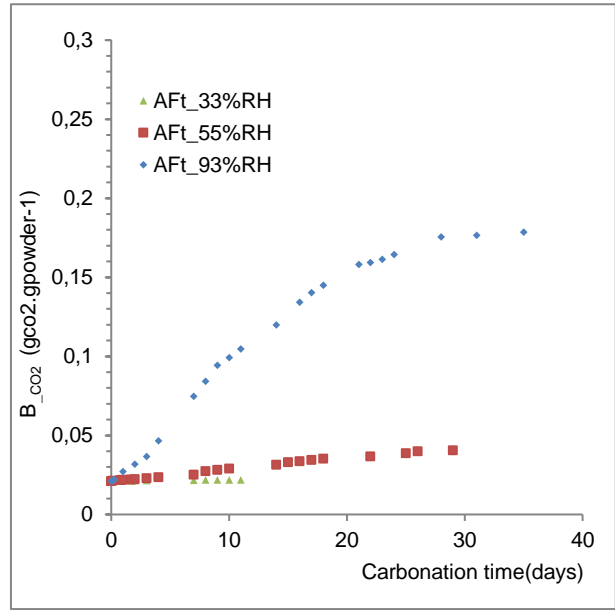
For each tested hydrate, Figure 63 and Figure 64 give the IBR and B_{CO_2} , respectively. Figure 63 (a) shows that the IBR of ettringite powder decreased by one order of magnitude only after 2 days of carbonation at 33% and 55% RH. At 55%, the IBR only slightly changed afterwards even after 29 days of carbonation, while the detection limit of the experimental setup was reached after 8 days of carbonation at 33% RH. Therefore, the experiments at these two RH levels were stopped after 11 and 28 days. Ettringite powder only slightly carbonates at 33% and 55% RH: CBC are $0.1 \cdot 10^{-2}$ and $2 \cdot 10^{-2} \text{ g}_{CO_2} \cdot \text{g}_{powder}^{-1}$, respectively. On the other hand, at 93% RH, ettringite carbonated with a high IBR until 28 days of exposure, to reach a B_{CO_2} of $16 \cdot 10^{-2} \text{ g}_{CO_2} \cdot \text{g}_{powder}^{-1}$ that slightly varied afterwards. The present results confirm that the role of water in the carbonation of ettringite is highly important. It was also reported by Robl et al. [231] that ettringite only carbonates at 400 ppm CO₂ when ambient RH is higher than 60%.

Figure 63(b) shows that the IBR of portlandite decreased by 3 orders of magnitudes after 10 days of exposure to ambient CO₂ concentration at 93% and 55% RH. Consequently, Figure 64(b) shows that the B_{CO_2} increased significantly during the first 10 days of exposure to carbonation to reach a plateau that corresponds to its CBC afterwards ($19 \cdot 10^{-2}$ and $16 \cdot 10^{-2} \text{ g}_{CO_2} \cdot \text{g}_{powder}^{-1}$ at 93 and 55% RH respectively). When carbonated at 33% RH, portlandite's IBR only decreased significantly after 16 days of carbonation to reach a CBC of $10 \cdot 10^{-2} \text{ g}_{CO_2} \cdot \text{g}_{powder}^{-1}$.

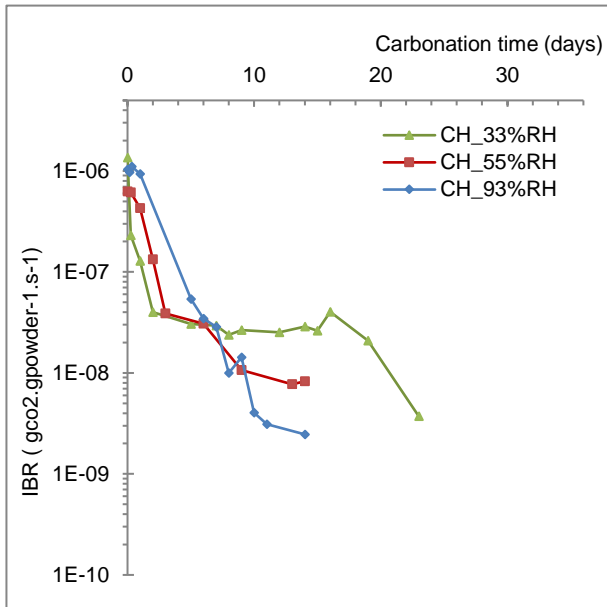
1.



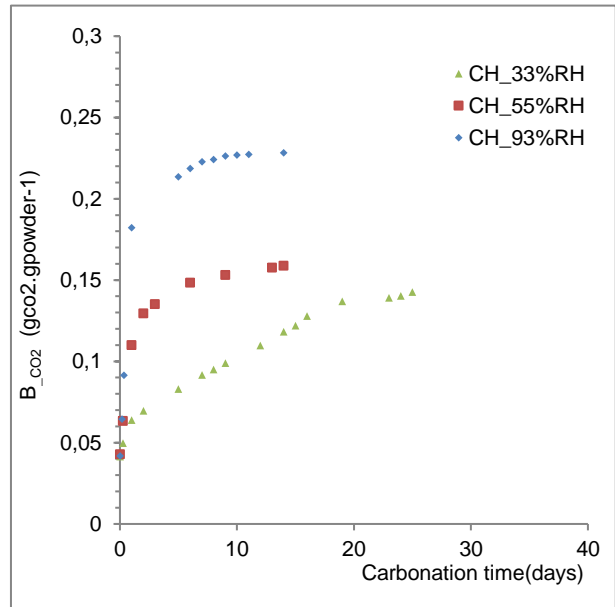
(a)



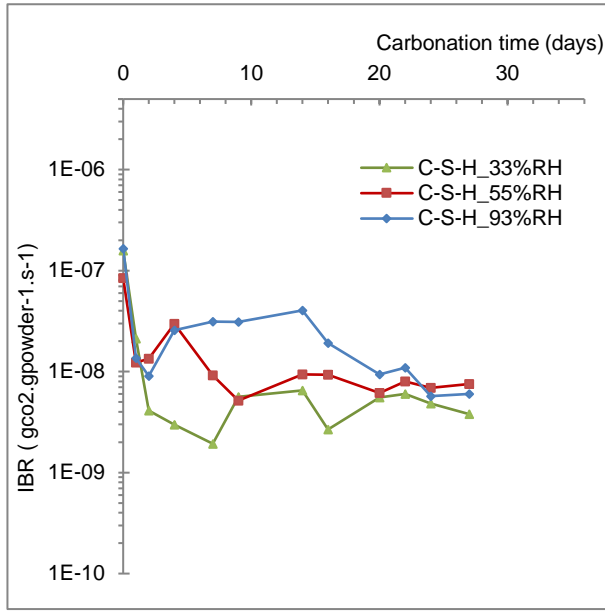
(a)



(b)

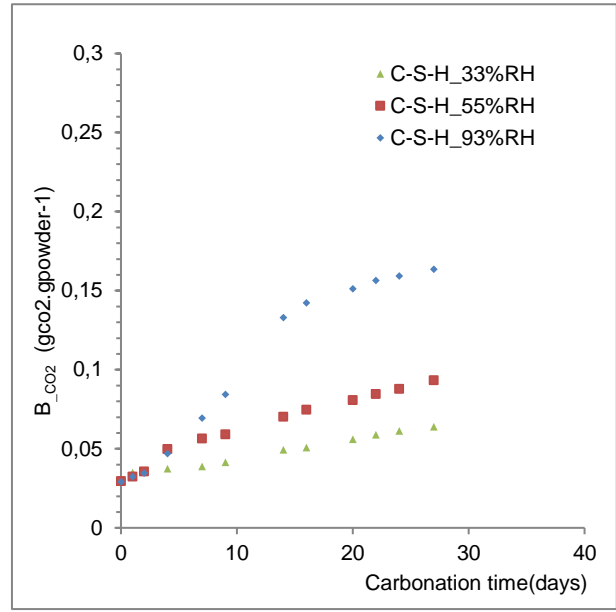


(b)



(c)

Figure 63: IBR of hydrates phases



(c)

Figure 64: the amount of bound CO₂ at different carbonation periods of hydrates

As shown in Figure 63 (c), the *IBR* of the C-S-H powder decreased by almost one order of magnitude after two days of carbonation at 93% and 55% RH, 2 orders of magnitude at 33% RH after 9 days and only slightly varied afterwards. At three RH levels, the CBC of C-S-H powder was not reached, as observed in Figure 64 (c): the B_{CO_2} continues increasing even after 28 days of exposure to ambient carbon dioxide.

3.5 Discussion

3.5.1 Reaction vs. mass diffusion

In an attempt to identify the mass transport effect and the reactivity of the tested powders on a powder layer scale, the dimensionless Thiele modulus (Φ_n^2) was used to compare the transport and the reaction timescales. ϕ_n^2 is an important dimensionless number within the dual lens approach reaction, it appears in the mass balance, after introducing the dimensionless spatial variable [150].

$$\phi_n^2 = \frac{T_{\text{diffusion}}}{T_{\text{reaction}}} = \frac{d^2 * k_0 * \rho}{D_{e,CO_2} * [CO_2]_0} \quad \text{Equation 58}$$

The Thiele modulus is defined as the ratio of the diffusion time ($T_{\text{diffusion}}$) to the reaction time (T_{reaction}). D_{e,CO_2} is the CO₂-effective diffusion coefficient in air (1.6×10^{-5} m²/s), $[CO_2]_0$ (gCO₂/m³) is the CO₂ concentration at the surface of the grain, d (m) is the powder layer thickness, k_0 is

the reaction kinetic constant ($g_{CO_2} \cdot g^{-1}_{powder} \cdot s^{-1}$) and ρ (g_{powder}/m^3) is the powder density. Low values of the Thiele modulus indicate surface reaction control and a significant amount of the CO_2 diffusing well into the grains' interior without reacting. High values of the Thiele modulus indicate that the surface reaction is rapid and that the reactant is consumed very close to the external surface so only very little penetrates into the interior of the grain [150].

	Highest reaction kinetic constant ($10^{-6} g_{CO_2} \cdot g^{-1}_{powder} \cdot s^{-1}$)	Lowest reaction kinetic constant ($10^{-10} g_{CO_2} \cdot g^{-1}_{powder} \cdot s^{-1}$)
Powder layer thickness (d in mm)	3	350

Table 38: The critical powder layer thickness at the lowest and highest values of the kinetic constant (Thiele modulus = 1)

The critical thickness of the powder layer is determined for a $\phi_n^2 = 1$ and the kinetic rate constant varies between 10^{-10} and $10^{-6} g_{CO_2} \cdot g^{-1}_{powder} \cdot s^{-1}$ (lowest and highest values determined from our experiments). For a powder layer of a thickness lower than 3 mm (which is the case in our study), the Thiele modulus is largely lower than 1. This result shows that the diffusion of CO_2 into the pores water is fast; so that the limiting factor is the CO_2 uptake by the solids.

3.5.2 From instantaneous rate to “cumulative” CO_2 uptake

The reliability of our test method results was investigated by comparing to the *CBC* values at the end of the carbonation period of each material obtained by both TGA and our method (cf. Table 35). Figure 65 shows that the *CBC* from TGA analysis and the *CBC* calculated based on our test method are in agreement. No evidence of an offset related with mineral type, relative humidity or range of *CBC* is noticed. These results are very promising regarding the accuracy and reliability of the new test method because they show that the analysis of the CO_2 -uptake curves corresponds well to the carbonation reaction, since TGA data are hard evidence that the uptake of carbon dioxide is due to carbonation [113].

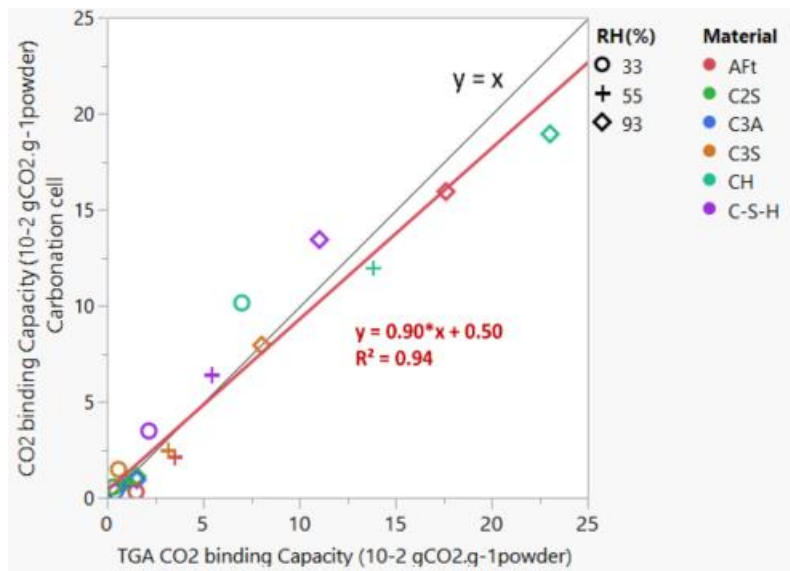


Figure 65: TGA CO₂-binding capacity vs. the carbonation cell CO₂-binding capacity (JMP)

The difference between TGA and the carbonation cell results could be a consequence of a slight carbonation during the preconditioning of the powders in the climate chamber even though soda lime was added. Moreover, the nature of these test methods is different: the *CBC* from TGA is determined purely on the basis of changes in the mass with respect to temperature and in correspondence with the amount of volatile matter and moisture content, and the carbonation cell test method is based on the measurement of the instantaneous CO₂ binding rate determined punctually during the carbonation period.

Note that the amount of bound CO₂ determined by the developed test method is dependent on the frequency of the CO₂-uptake measurements, especially during the first three days of exposure to ambient CO₂ concentration. The results reliability also depends on the response time and precision of the CO₂ gas sensor, especially for highly reactive phases.

The test method can be improved by using a CO₂ sensor with lower response time, performing more measurements, which results in the improvement of integration method accuracy, and controlling the CO₂ concentration inside the room, especially for first and second order reactions.

Nevertheless, the agreement between the results obtained from the two techniques is quite promising (Figure 65), since they differ by no more than 38% for the range of the conditions and materials tested.

3.5.3 Reaction mechanisms

3.5.3.1 Anhydrous carbonation

Regarding the carbonation of anhydrous materials, the CBC of C₂S and C₃A powders didn't exceed $2 \cdot 10^{-2} \text{ g}_{\text{CO}_2} \cdot \text{g}^{-1}_{\text{powder}}$. However, C₃S powder carbonated significantly at 93% RH only (DoC = 14%).

Figure 58 shows a decrease in the density and a significant increase in the BET surface area of C₃S and C₂S powders due to carbonation, which can be explained by the formation of a thin layer of C-S-H on the surface of the grains [232][233]. Indeed, Houst et al. [87] reported that the carbonation of β-C₂S and C₃S results in the formation of aragonite, silica gel and a small amount of C-S-H, no trace of calcium hydroxide is observed during the carbonation [87].

The same result is observed for C₃A powder, which could be due to the formation of aluminum hydroxide since Figure 57 shows that the TGA results of C₃A powder after exposure to carbonation reveal a peak around 280-300°C, which corresponds to the decomposition of aluminum hydroxide.

The fact that only C₃S powder reacted at 93% RH could be explained by the high reactivity of C₃S with water, giving rise to the formation of calcium hydroxide and a number of different amorphous or poorly crystalline calcium silicate hydrates phases that would carbonate rapidly. These results are generally consistent with previous studies, which show that even though C₃A is much more water reactive than C₃S and C₂S [22], it only carbonates slowly.

3.5.3.2 Hydrates carbonation

The amount of bound CO₂ of both anhydrous and hydrates increased with the RH level where water is more available for the dissolution of CO₂ and CaO.

Although portlandite powder carbonated significantly at the three RH levels, the CBC is reached only after 7 days of carbonation. Images of portlandite powder shown in Figure 59 could explain the rapid decrease of the IBR, which would be due to the fact that the carbonation takes place on the surface of the grains, and its rate of proceeding inwards is very slow. Hence, when the surface is covered with CaCO₃, the carbonation is practically ceased. This is also facilitated by the relatively small surface areas of portlandite crystals in comparison with calcium silicate hydrates. This phenomenon is similar to the one addressed by Sohn and Szekeley [234] for porous solid pellets, where intragrain diffusion resistance may become so large that it will control the progress of the reaction process. Moreover, Galan et al. [235] investigated the permeability of the CaCO₃ layer on the surface of portlandite and reported that this layer provides significant protection against diffusion of Ca²⁺ and OH⁻ ions, which hinders further carbonation. However, in the case of ettringite, which is a fibrous-form material, the carbonates could form between its needles (see Figure 59) which would not

hinder the CO₂ diffusion or the CaO dissolution. Indeed, *Figure 64* shows that the CBC of ettringite is reached 18 days after portlandite's and the IBR remains constant for 20 days when ettringite is carbonated at 93% RH.

The carbonation of C-S-H is found to occur at a slower initial rate than the carbonation of CH because of the more rapid dissolution of CH [39][236]. This behavior reverses when the formation of microcrystalline CaCO₃ around reacting CH crystals inhibits further accessibility and slows down the portlandite dissolution, while the carbonation rate of C-S-H remains almost constant (very slow variation) even after 27 days of carbonation.

TGA and carbonation cell results show that the pure hydrates did not carbonate completely, their degree of carbonation did not exceed 45% in the present study (Table 35). In agreement with our results concerning portlandite's carbonation, Grandet [237] reported that the degree of carbonation of portlandite is limited to 50-60%. Concerning the carbonation of pure ettringite, Castellote [238] found that ettringite carbonates up to 50% under 0.03% CO₂ and 3% CO₂, and carbonates completely at 10% CO₂.

3.5.4 Application of the results of this work

Results from this work would help to enhance the understanding of the kinetics of carbonation at high RH on the reactivity of clinker phases (C₃S, C₃A, C₄AF) during storage in silos or bags for long periods under different RH levels, which is an important issue for the industrial field.

The developed test method could be used to compare the CO₂ binding capacity of existing or innovative binders to assess their actual environmental benefits of CO₂ uptake by carbonation and investigate the life cycle assessment of cementitious materials after their preparation (in the case of precast concrete), during their service life, and after the end of the service life (recycled concrete) [239]. The NF P19-839, NF EN 16757 standards [239] state that the degree of carbonation of concrete structures varies between 40% and 85% in a dry climate and under exposure to rain, respectively. However, our results in Table 35 reveal that even at 93% RH, the portlandite's degree of carbonation reached 39% only and the IBR varied very slightly after 7 days of carbonation. This suggests that higher RH or water content in addition to wetting drying cycle should be further investigated in terms of rate and maximum CO₂ uptake.

The results of this work could also improve the modeling of carbonation kinetics and the prediction of the shape of the carbonation front when the diffusion coefficient is also assessed. Since our results show that the CO₂-binding capacity of hydrates is reached after only 6 days (CH) or over 28 days (C-S-H) of exposure to carbonation, this means that the carbonation reaction could continue behind the carbonation depth determined by means of a pH indicator

results, which means that the carbonation front shape is not completely sharp [190][39][11].

3.6 CONCLUSIONS

In the present work, a new test method is developed to determine the carbonation kinetics of the main synthetic phases present in the cement. Results allow us to draw the following conclusions:

- An original experimental setup was developed in order to measure the instantaneous CO₂ binding rate (IBR) and determine the amount of bound CO₂ during all periods of carbonation. The test method is advantageous because of its simplicity and cost-efficiency. Results from this test method agree with TGA results, which is promising regarding the accuracy and reliability of the test method. However, the test method could be improved by using sensors with lower response time and by increasing the frequency of the CO₂-uptake measurements to minimize the errors of the integration step.
- The controlling factor of the amount of bound CO₂ is the surface water-adsorbed, since the CO₂ binding capacity is found to increase with the RH under which carbonation tests were undertaken.
- Portlandite carbonates significantly compared to other hydrates, even at low RH, and the only carbonate formed is calcite. Ettringite carbonates remarkably at 93% RH (DoC=45%) and only slightly at 55% and 33% RH. Even though the carbonation rate of C-S-H is initially lower than that of portlandite, its carbonation continues with a constant rate even after 28 days of exposure, especially at 93% RH.
- No significant carbonation of the anhydrous materials was noticed. The actual amount of bound CO₂ was found to be lower than the theoretical maximum binding capacity calculated for all powders. Only at 93% RH, C₃S powders were carbonated (DoC=14%), which could be due to the formation of C-S-H as intermediate reaction product at this high RH level.
- The maximum degree of carbonation (DoC = 45%) was observed for ettringite powder, followed by portlandite (DoC = 38%) carbonated at 93% RH, which highlights the important contribution of these two hydrates in the carbonation performance of aluminous cements and Portland cements, respectively.

Extended abstract in French

I- Introduction

La durabilité d'un ouvrage en béton armé est en grande partie liée à l'aptitude du béton à résister à la pénétration des agents agressifs. Le mécanisme de vieillissement des structures le plus courant, et qui touche toutes les structures en contact avec l'air atmosphérique, est sans aucun doute la carbonatation [240]. Ce processus physico-chimique entraîne la baisse du pH de la solution porale qui conduit à une dépassivation des aciers du béton armé [13]. Sans protection alcaline, les armatures sont exposées à un risque de corrosion.

Actuellement, les méthodes d'essais normalisées, couramment utilisées pour étudier la carbonatation du béton, s'appuient sur l'évaluation qualitative de la chute du pH de la solution interstitielle sur la section perpendiculaire à la surface d'un échantillon de béton exposé à des concentrations ambiantes ou très élevées de CO₂ (2% à 50% en volume). Ces méthodes sont souvent critiquées, soit parce qu'elles nécessitent beaucoup de temps (plus d'une année pour la carbonatation en conditions atmosphériques), soit parce qu'elles sont coûteuses et d'une faible fiabilité (la carbonatation en conditions accélérées, notamment quand la concentration en CO₂ est supérieure à 3% CO₂ [241]). Néanmoins, le test avec un indicateur coloré, comme la phénolphthaléine, reste une technique pratique pour déterminer une profondeur de carbonatation (qui correspond à un seuil de pH = 9), par comparaison à d'autres méthodes (XRD, TGA), mais ses limites doivent être gardées présentes à l'esprit.

Deux mécanismes principaux pilotent la carbonatation : le transport diffusif du dioxyde de carbone gazeux, qui est régi par le coefficient de diffusion effectif de cette molécule dans le milieu poreux, et la consommation du CO₂ une fois dissous par la masse de produits carbonatables. Ces deux phénomènes sont à prendre en compte dans les modèles scientifiques prédictifs de la durabilité des matériaux cimentaires [6][15].

Un manque de données expérimentales sur les propriétés que sont le coefficient de diffusion du CO₂ et la capacité de fixation du CO₂ par le matériau ressort particulièrement lorsqu'on veut utiliser des modèles de la littérature qui prennent en compte les conditions environnementales [45]. Ce manque est dû principalement à l'absence de méthodes d'essais simples et fiables pour la détermination de ces propriétés sous différents environnements [242].

Le présent travail a pour but de développer deux nouvelles méthodes d'essai pour évaluer, d'une part, le coefficient de diffusion effectif de gaz et, d'autre part, la masse de produits

carbonatables et la cinétique de fixation du CO₂ de matériaux cimentaires. En outre, notre objectif est de caractériser l'effet de différents paramètres sur ces deux propriétés, comme la composition du matériau, la durée d'hydratation, l'état de carbonatation et l'humidité relative ambiante. Toutes les données expérimentales ainsi obtenues sont analysées et discutées au regard de la littérature, pour être finalement intégrées comme entrées de deux modèles de prédictions de la profondeur de carbonatation [6][15].

II- Programme expérimental

2.1 Pâtes de ciments

Au cours de ce travail de thèse, le coefficient de diffusion effectif d'oxygène de neuf pâtes de ciment durcies a été déterminé sous différentes conditions environnementales et à différentes durées d'hydratation (Article I et II). Ce résumé présente un exemple de résultats obtenus sur trois pâtes de ciment les plus couramment utilisées (Tableau 1). La pâte de ciment contient l'essentiel de la porosité des mortiers et du béton ordinaire, et détermine ainsi dans une large mesure leurs propriétés de transport. Au premier ordre, la fraction volumique de la pâte de ciment permet le passage de la pâte au béton [173].

Pâtes de ciment	Type de ciment	Addition et pourcentage de remplacement	E/L	Humidité relative de pré-conditionnement
HD*_OPC_SF_W/B	OPC	10% silica fume	1.6 (%vol)	Sec (Étuvage à 80°C) 33%, 55%, 76% et 93%
PC6	CEM I 52.5 N	-	0.60	33%, 55% et 93%
SL6		60% slag	0.60	

Tableau 1: Trois pâtes de ciment testées au cours de ce travail

L'influence de la durée d'hydratation, l'humidité relative (HR) de pré-conditionnement, la composition (rapport volumique eau sur liant et type de liant) et la carbonatation accélérée sur le coefficient de diffusion effectif de l'oxygène est évalué. Pour ces matériaux à l'équilibre hydrique à une HR donnée, nous avons aussi déterminé le degré de saturation en eau, la distribution de la taille des pores et la porosité à l'eau, avant et après carbonatation accélérée.

La capacité de fixation du dioxyde de carbone de poudres des pâtes de ciments durcies et des principaux anhydres (C₂S, C₃S, C₃A) et hydrates (CH, C-S-H, AFt) a été déterminée à trois niveaux d'humidité relative en utilisant la méthode d'essai que nous avons développée. Les résultats obtenus sont comparés aux analyses thermogravimétrique (ATG) des mêmes

échantillons afin d'évaluer la fiabilité des résultats de la nouvelle méthode d'essai.

2.2 Bétons

Le coefficient de diffusion de trois bétons (Tableau 2) avant et après carbonatation accélérée (1% CO₂, 55% HR) a été déterminé après pré-conditionnement à 33%, 55% et 93% HR. La masse de produits carbonatables des pâtes de ciment durcies équivalentes (fabriquées en utilisant le rapport E/L effectif des bétons) a été déterminées avec la nouvelle méthode d'essai décrite dans la partie 3.2. Les échantillons de béton ont été découpés dans des éprouvettes de 22cm de longueur et 11cm de diamètre. Afin de pouvoir pré-conditionner et tester ces échantillons de béton dans un temps raisonnable, l'épaisseur des échantillons testés varie entre 8mm et 11mm. L'erreur liée à la dépendance de D_{e,O_2} à l'épaisseur de l'échantillon testé est prise en compte dans [90].

	C_PC	C_FA	C_LS
Rapport E/L	0.66	0.67	0.5
Air (%)	2	1.9	0.9
Type de ciment	CEM I 52.5 R	CEM I 52.5 R	CEM I 52.5 R
Type d'addition	-	30% Cendres volantes	40% Filler calcaire
Gravillon 6/20.8 mm (kg/m³)	830	782	771
Sable (0/4mm) (kg/m³)	906	946	706
Classe de résistance	C25/30	C25/30	C25/30
Ciment (kg/m³)	280	223	270

Tableau 2: Composition des trois des bétons testés

III- Méthodes d'essais développées

3.1 Cellule de diffusion d'oxygène

Le gaz choisi pour cette méthode d'essai est l'oxygène, puisque c'est un gaz inerte vis-à-vis des matériaux cimentaires. La diffusion de l'oxygène n'entraînera pas de modifications de la microstructure et permettra d'effectuer la mesure en un temps relativement court. La méthode d'essai que nous avons développée pour la détermination du coefficient de diffusion de l'oxygène consiste en la mesure de la concentration de l'oxygène de l'air qui diffuse à travers un disque de matériau à l'intérieur d'une cellule de diffusion. Dans le cas des pâtes de ciment, le disque a 4 mm de diamètre et 3 ± 0.5 mm d'épaisseur. Dans le cas du béton, les échantillons sont de 110 mm de diamètre et d'une épaisseur qui varie entre 5 mm et 50 mm [141]. Au cours de l'acquisition, la cellule est mise dans une chambre climatique à 20°C et à humidité relative contrôlée. L'équipement permet la lecture continue de la concentration en oxygène à l'intérieur de la cellule de diffusion. Le coefficient de diffusion de l'oxygène est calculé à partir de la courbe d'accumulation de la concentration de l'oxygène mesuré en fonction du temps jusqu'à atteindre l'état stationnaire, c'est-à-dire une concentration de 20% d'O₂ à l'intérieur de la cellule.

L'élément essentiel de ce dispositif est la cellule de diffusion (Figure 66 a) qu'on appelle aussi « chambre aval ». Il s'agit d'une cellule en polyéthylène haute densité (PEHD), étanche au gaz, séparée de l'air ambiant de la chambre climatique par l'échantillon. Cette cellule est purgée à l'azote en début d'essai, puis placée à l'intérieur d'une chambre climatique à 20°C. L'humidité relative à l'intérieur de cette « chambre amont » est maintenue constante et égale à celle de l'échantillon testé, afin de contrôler la saturation en eau de l'échantillon. Comme le volume de la chambre amont est beaucoup plus grand que le volume cumulé de la cellule de diffusion (68 ml et 209 ml pour les cellules pour pâtes de ciment et béton respectivement), le séchage de l'échantillon pendant l'essai est négligeable (variation de masse <0.02%). L'oxygène de l'air ambiant diffuse successivement à travers l'échantillon, puis dans la cellule remplie initialement d'azote. Un capteur à l'intérieur de la cellule permet de mesurer la concentration en oxygène en fonction du temps de façon continue.

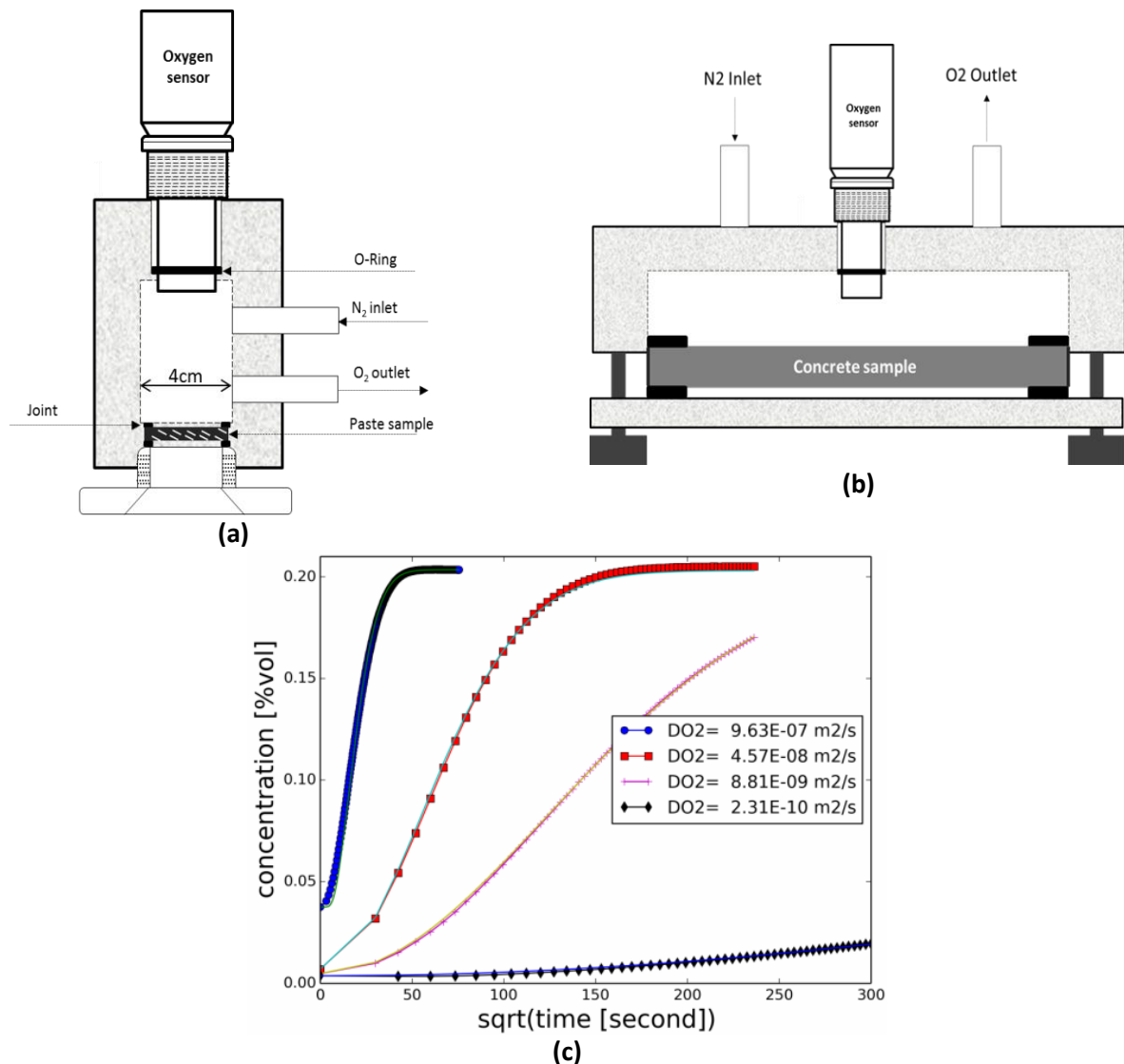


Figure 66. (a) Cellule de diffusion d'oxygène pour pâtes de ciments hydratée ; (b) cellule de diffusion pour béton (c) ; courbes d'accumulation expérimentales et théoriques après minimisation automatique.

L'essai fournit comme résultat une courbe de diffusion : concentration en O₂ en fonction du temps (Figure 66 c). Le coefficient de diffusion effectif est calculé automatiquement à partir de la courbe expérimentale à l'aide d'un programme en langage Python [178]. Ce dernier permet de calculer directement le coefficient de diffusion d'oxygène en minimisant l'écart entre les concentrations mesurées et celles calculées par résolution numérique de la deuxième loi de Fick (Équation 1). Les données d'entrée nécessaires au calcul de minimisation sont les concentrations en O₂, les échéances de temps, les paramètres de configuration relatifs à l'échantillon (saturation en eau, porosité et géométrie), à la cellule (géométrie, fuite), ainsi que les concentrations initiales et aux limites.

Seconde loi de Fick
$$\phi(1 - S_l) \frac{\partial C}{\partial t} = \frac{\partial}{\partial x} (D_{e,O_2} \frac{\partial C}{\partial x}) \quad \text{Équation 1}$$

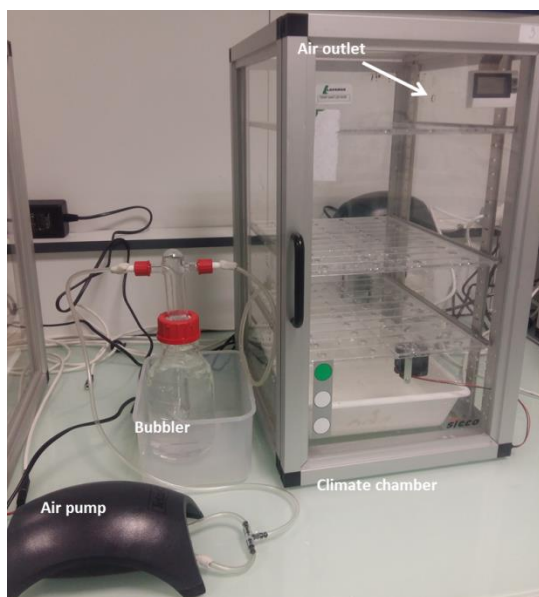
- Φ [-] et S_l [-] sont la porosité totale de l'échantillon et son degré de saturation en eau.

- D_{e,O_2} [m^2/s] et $C(\%)$ sont le coefficient de diffusion effective de l'oxygène et la concentration relative de ce gaz dans la cellule de diffusion.

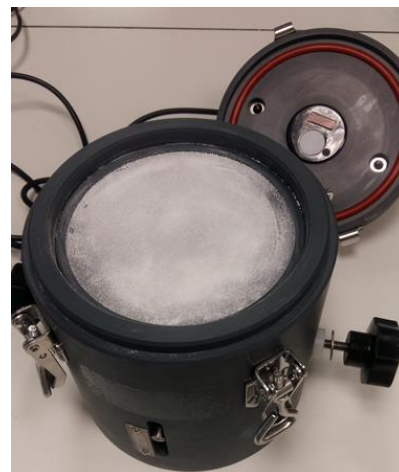
L'étanchéité du dispositif expérimental a été évaluée en réalisant un test de fuite. Il s'agit de mesurer la variation de concentration de l'oxygène à l'intérieur de la cellule en remplaçant l'échantillon par un disque étanche en PEHD. Sous l'hypothèse d'un débit de fuite linéaire en fonction du temps, nous avons mesuré un taux de fuite de 0.014% vol/heure, ce qui permet de déterminer avec le dispositif des coefficients de diffusion allant jusqu'à 10^{-11} m^2/s .

3.2 Capacité de fixation de CO_2

La méthode d'essai de la capacité de fixation du CO_2 consiste à exposer un échantillon en poudre à une carbonatation naturelle sous une humidité relative donnée. 1 g de poudre est uniformément et finement réparti sur un porte-échantillon (disque de 110 mm de diamètre (Figure 67 (b)) pour se carbonater dans une chambre climatique (Figure 67 (a)). La concentration en CO_2 et l'humidité relative pendant la carbonatation de la poudre sont maintenues constantes à l'aide d'un équipement qui permet la circulation de l'air ambiant régulé à l'humidité relative de l'essai dans la chambre de carbonatation (Figure 67 (a)).



(a)



(b)

Figure 67: (a) Chambre climatique utilisée pendant la carbonatation naturelle de l'échantillon de poudre, (b) cellule de carbonatation [151]

La vitesse de fixation instantanée de CO_2 par la poudre est mesurée dans une cellule fermée ponctuellement à différentes périodes de carbonatation. La durée de cette mesure doit être négligeable par rapport à la période de carbonatation globale de l'échantillon. Le temps de fixation de CO_2 étant proportionnel au volume de gaz, la cellule est équipée d'un piston qui

permet la variation de son volume interne de 10 ml à 285 ml. Pour les poudres très réactives avec le CO₂, le volume de la cellule est réglé à sa valeur maximale et inversement. La mesure totale avec la cellule fermée n'a pas dépassé 7 heures pour un temps total de carbonatation dans un système ouvert d'environ 28 jours. La fréquence de la mesure de la fixation de CO₂ est d'une fois par jour la première semaine et est ensuite adaptée en fonction de l'évolution temporelle du taux de carbonatation. La concentration de CO₂ à l'intérieur de la cellule est mesurée à l'aide d'un capteur d'absorption infrarouge qui mesure également l'humidité relative et la température.

La pente des courbes de fixation de CO₂ en fonction du temps est déterminée à l'aide d'un logiciel d'analyse de données (JMP). La pente mesurée (en ppm/s) est convertie en un taux instantané de fixation de CO₂ IBR (exprimée en g_{CO2}.g_{ciment}.s⁻¹) selon l'Équation 2, où P, M_{CO2}, Vg, R, T sont respectivement la pression ambiante, la masse molaire du dioxyde de carbone, le volume intérieur de la cellule de carbonatation, la constante des gaz parfaits, et la température ambiante. m₀ est la masse de l'échantillon testée sans CO₂ lié ni eau, corrigée par les résultats de l'ATG réalisés après le pré-conditionnement des poudres.

$$\text{IBR} = \frac{\text{Slope} * P * M_{\text{CO}_2} * Vg}{R * T * m_0} \quad \text{Équation 2}$$

$$B_{\text{CO}_2} = \int_{t=0}^T \text{IBR} dt \quad \text{Équation 3}$$

$$\text{carbonatable mass} = \frac{\text{CBC} * \text{cement dosage}}{M_{\text{CO}_2}} \quad \text{Équation 4}$$

La quantité de CO₂ fixé à différentes échéances d'exposition de carbonatation est déterminée selon l'Équation 3 en intégrant la valeur d'IBR sur la durée totale de carbonatation T. Ainsi, la masse de produits carbonatables est déduite de la quantité de CO₂ fixé à la fin des essais de carbonatation en utilisant Équation 4.

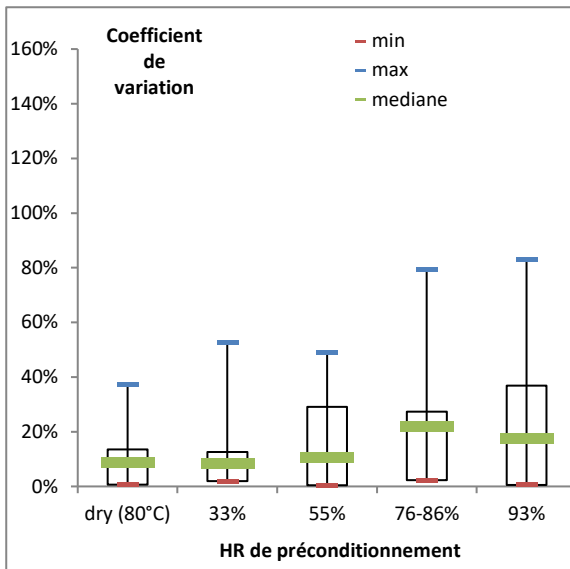
IV- Résultats principaux

4.1 Validation des méthodes d'essais

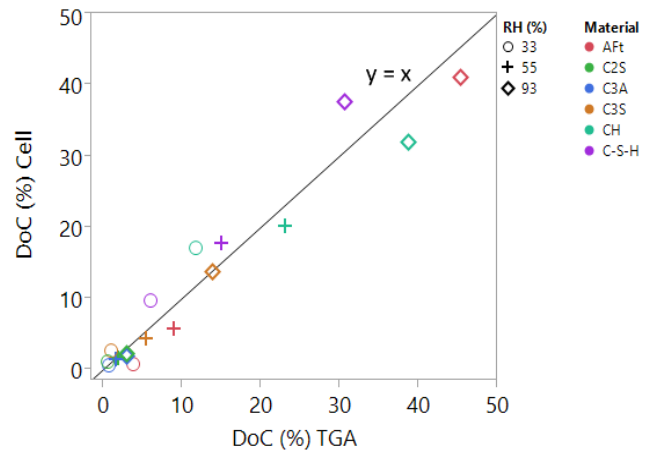
La Figure 68 (a) montre cinq boîtes à moustaches correspondant chacune au coefficient de variation des coefficients de diffusion déterminés expérimentalement après le pré-conditionnement des échantillons de pâtes de ciment dans cinq états: séchés au four (105 ° C), équilibrés à une humidité relative (HR) de 33% et à 55%, entre 76% et 86% et à 93% HR. Pour chaque catégorie, nous disposons des quantités de données suivantes d'échantillons de pâtes, c'est-à-dire respectivement 18, 30, 26, 24 et 21 valeurs.

L'espacement à l'intérieur de chaque boîte indique le degré de dispersion du coefficient de variation, qui dépend clairement de l'état de pré-conditionnement. La valeur moyenne du coefficient de variation varie de 9% à l'état sec à 48% lorsque l'échantillon de béton est pré-conditionné à 93% HR. Notons que la courte période de pré-conditionnement (en raison du critère d'équilibre de masse <0,05% sur une semaine) pourrait également entraîner une dispersion plus importante des données à cause d'une distribution hétérogène de l'eau dans l'espace poreux.

La Figure 68 (b) compare le degré de carbonatation (DoC) déterminé à l'aide de la méthode de suivi de la carbonatation développée dans nos travaux aux DoC déterminés par ATG. Les résultats sont cohérents, ce qui met en évidence la précision des mesures avec la méthode développée, car les résultats d'ATG sont une preuve de la réaction de carbonatation. Ce résultat est prometteur quant à l'exactitude et à la fiabilité de la nouvelle méthode d'essai. Cela prouve que l'analyse des courbes d'absorption de CO₂ correspond bien à la réaction de carbonatation.



(a)



(b)

Figure 68: (a) Coefficient de variation du coefficient de diffusion d'oxygène en fonction de l'humidité relative (b) Capacité de fixation du CO₂ déterminé avec la cellule de carbonatation en fonction de la capacité de fixation déterminée par ATG

4.2 Influence de la carbonatation et de l'hydratation sur les propriétés des matériaux testés

Sur la Figure 69, chaque valeur du coefficient de diffusion effectif de l'oxygène est la moyenne géométrique de trois coefficients de diffusion. La Figure 69 (a) montre que le coefficient de diffusion effectif de l'oxygène dépend à la fois du degré de saturation correspondant à l'humidité relative du préconditionnement et de l'état de carbonatation. D_{e,O_2} des pâtes PC6 diminue d'un facteur 3 à 33% et 55% d'humidité relative et augmente d'un facteur de 21 à 93% HR à l'état carbonaté. Alors que le coefficient de diffusion a augmenté après carbonatation d'un facteur de 4, 9 et 93 à 33%, 55% et 93% HR respectivement. La distribution de la taille des pores de ces matériaux a été évaluée dans l'article II. Une distribution de la taille des pores plus grossière est remarquée après carbonatation, ce qui cause une diminution du degré de saturation en eau des échantillons carbonatés notamment quand on les préconditionne à 93%HR. De plus, le coefficient de diffusion est bien corrélé au diamètre moyen des pores des pâtes de ciment testées, lorsque le degré de saturation en eau est inférieur à 30% (voir section 4.1.2 iv). Ce résultat est établi pour les pâtes de ciment carbonatées et non carbonatées, ce qui prouve la dépendance directe de la diffusivité de l'oxygène à la distribution de la taille des pores et au degré de saturation en eau.

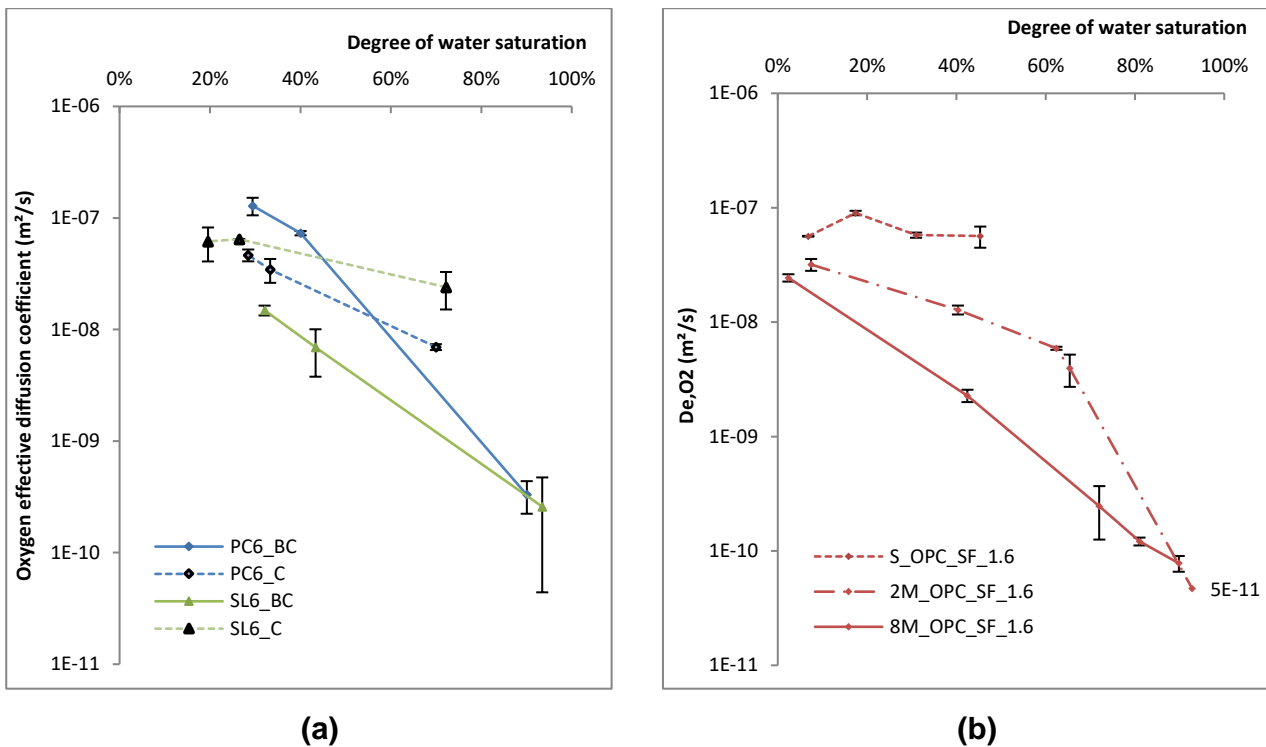


Figure 69: (a) Influence de la carbonatation sur D_{e,O_2} à différents degrés de saturation en eau et (b) influence de la durée d'hydratation sur D_{e,O_2} (S = 7 jours, 2M = 2 mois, 8M = 8 mois).

La Figure 69 (b) présente le coefficient de diffusion effectif de l'oxygène en fonction de l'humidité relative des échantillons hydratés pendant 7 jours (S), 2 mois (2M) et 8 mois (8M). Une durée de cure plus longue engendre une diminution significative du coefficient de diffusion de l'oxygène (D_{e,O_2} diminue jusqu'à trois ordres de grandeur). En effet, une cure plus longue favorise la formation d'une plus grande quantité d'hydrates (notamment les C-S-H) qui viennent combler et fractionner davantage la porosité capillaire [243]. Le coefficient de diffusion dépend fortement de l'humidité relative de l'échantillon. Cette dépendance est plus importante lorsque l'échantillon est bien hydraté. Plus l'humidité relative est élevée, plus les pores sont remplis d'eau ; le réseau poreux de l'échantillon accessible au transport de l'oxygène devient discontinu et l'échantillon est donc moins diffusif. L'influence du rapport eau sur liant sur le coefficient de diffusion de ces pâtes de ciment a été évaluée dans nos travaux précédents (Article I). D_{e,O_2} augmente avec le rapport eau/liant (E/L) (de 1,6 à 1,9 en volumique). Ce résultat est en accord avec les recherches de [158] qui explique que, pour un E/L plus faible, la porosité capillaire est constituée d'un réseau de pores plus fin et plus discontinu.

4.3 Capacité de fixation de CO_2 à différentes HR

La Figure 70 présente l'évolution de la vitesse instantanée de fixation du CO_2 (IBR) en fonction du degré de carbonatation (DoC) à trois niveaux d'humidité relative pour deux phases

synthétisées (CH et C₃S) et deux pâtes de ciment hydratées (PC6 et SL6).

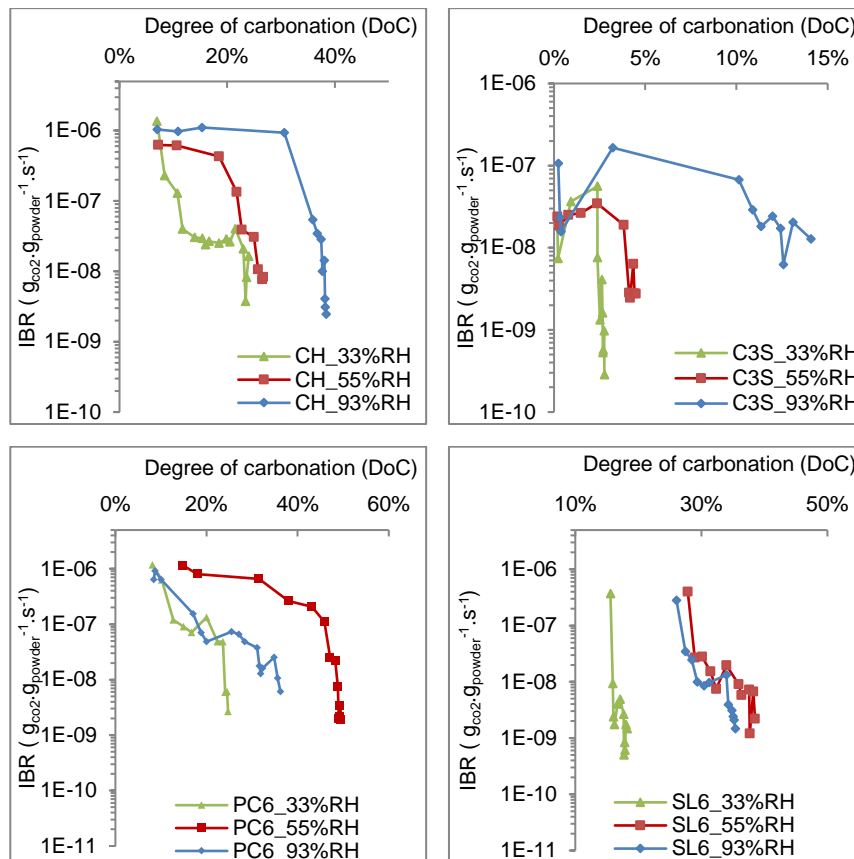


Figure 70: Variation de la vitesse instantanée de fixation du CO₂ (IBR) en fonction du degré de carbonatation à trois niveaux d'humidité relative.

La Figure 70 montre que le degré de carbonatation des matériaux synthétisés augmente avec l'humidité relative sous laquelle les essais de carbonatation sont effectués. Ce résultat est attendu car la cinétique de la réaction de carbonatation est contrôlée par la dissolution de CO₂ et du CaO. Dans le cas du C₃S, la carbonatation est très faible à 33% et 55% HR, alors qu'à 93%HR le degré de carbonatation atteint 14%. Cela pourrait être dû à une hydratation du C₃S à ce niveau d'humidité relative (voir article III).

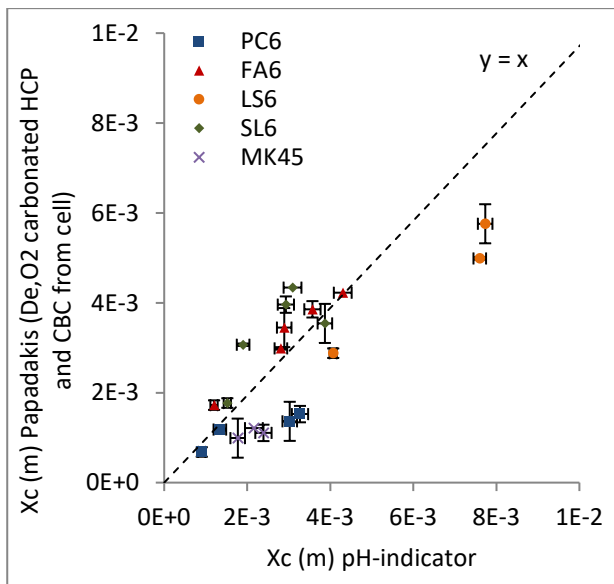
Le degré de carbonatation maximal est observé à 55% HR pour les pâtes de ciment hydratées. Notons aussi que le degré de carbonatation au début des mesures était non nul, à cause d'une carbonatation pendant le préconditionnement de ces matériaux pendant 15 jours, alors que de la chaux sodée avait été introduite dans la chambre climatique pour réduire au maximum la concentration en CO₂.

V- Modélisation de la profondeur de carbonatation

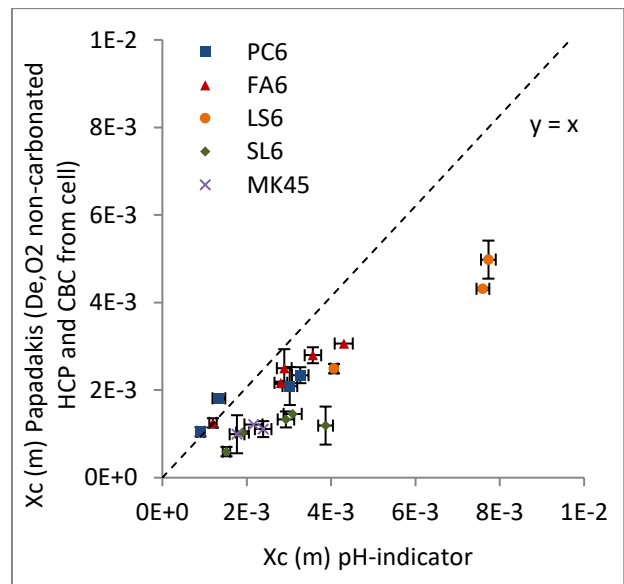
L'ensemble des données obtenues grâce aux essais de diffusion d'oxygène et de

détermination de la masse de produits carbonatés a été utilisé comme données d'entrée dans deux modèles de prédiction de la profondeur de carbonatation [6][15]. Les profondeurs ainsi calculées ont été comparées à des profondeurs de carbonatation déterminées expérimentalement sur des échantillons de pâte et béton, mis en carbonatation naturelle ou accélérée pendant plusieurs mois. Les profondeurs de carbonatation expérimentales ont été mises en évidence avec un indicateur de pH (phénolphtaléine).

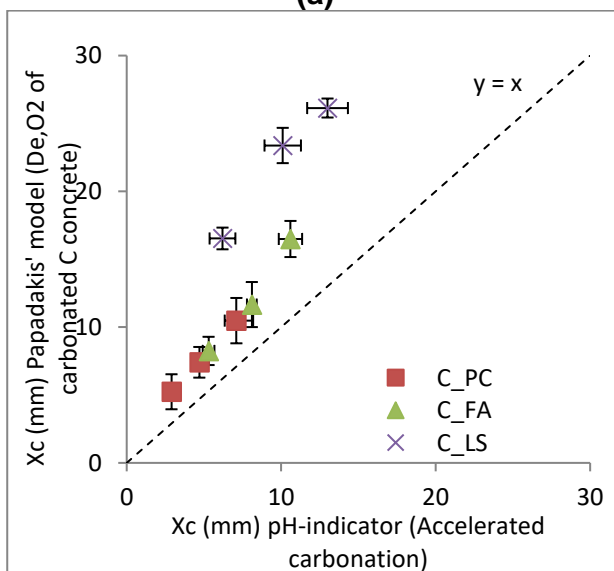
Les Figure 71 (a) et (b) comparent les profondeurs expérimentales aux résultats obtenus avec le modèle de Papadakis (section 5.4). Le modèle sous-estime les profondeurs obtenues expérimentalement. On note néanmoins une corrélation entre résultats d'essai et valeurs calculées (erreur 31% et 37% pour les résultats de la Figure 71 (a) et (b) respectivement). Cette corrélation est meilleure quand on utilise le coefficient de diffusion d'échantillons carbonatés plutôt que celui déterminé sur échantillons non carbonatés.



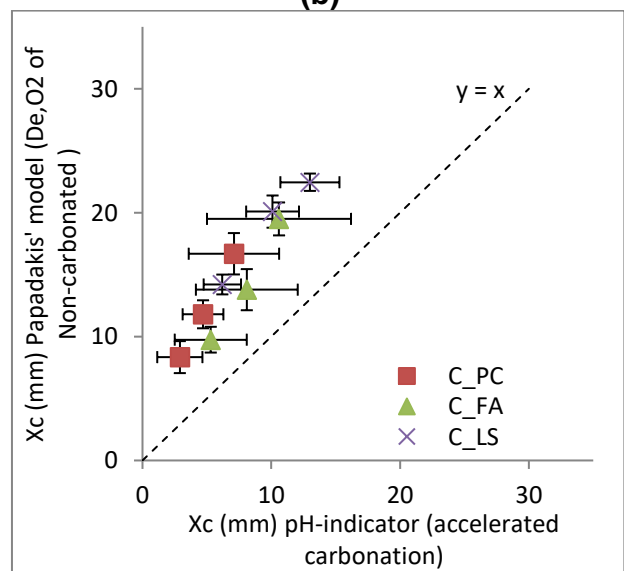
(a)



(b)



(c)



(d)

Figure 71: Comparaison de profondeurs de carbonatation déterminées expérimentalement (indicateur de pH) et de profondeurs calculés avec le modèle de Papadakis en utilisant nos résultats de D_{e,O_2} et produits carbonatables comme données d'entrée.

Les Figure 71 (c) et (d) comparent les profondeurs de carbonatation expérimentales aux résultats du modèle de Papadakis dans le cas de trois bétons exposée à une carbonatation accélérée (3% CO₂, 65% HR). On note cette fois que le modèle surestime la profondeur d'un facteur de 2.0 et 1.5, en utilisant les résultats des échantillons carbonatés et non carbonatés respectivement.

VI- Conclusion

Deux méthodes d'essai ont été développées pour déterminer la diffusivité de l'oxygène et la capacité de fixation du CO₂. Ces méthodes sont capables de reproduire des résultats de la littérature, comme une diminution de la diffusivité de l'oxygène avec le degré de saturation en eau et la durée d'hydratation, ou encore une dépendance de la quantité de produits carbonatables à l'humidité relative ambiante.

Les principaux résultats de nos travaux, peuvent être les suivants :

- Le coefficient de diffusion effectif de l'oxygène de matériaux carbonatés dépend moins de l'humidité relative du pré-conditionnement que le coefficient des mêmes matériaux avant carbonatation.
- La capacité et la vitesse de fixation du CO₂ par carbonatation dépendent fortement de l'humidité relative et de la composition du matériau. Le processus de carbonatation est fortement ralenti avant que les produits carbonatables ne soient consommés.

A l'aide des méthodes développées, la diffusivité de l'oxygène et la quantité de produits carbonatables peuvent être déterminées de manière fiable, sur une durée d'essai courte par comparaison aux essais de carbonatation naturelle (au plus 8 semaines au lieu de 1 an ou plus). Ces propriétés pourraient servir de données d'entrée à des modèles de prédiction de la profondeur de carbonatation basés sur la loi de Fick. Si prometteuse soit-elle, cette approche doit encore être confortée par une confrontation entre les résultats de tels modèles et des profondeurs de carbonatation naturelle obtenues sur des durées significatives.

REFERENCES

- [1] J. Olumuyiwa Ikotun, Effects of concrete quality and cover depth on carbonation-induced reinforcement corrosion and initiation of concrete cover cracking in reinforced concrete structures, PhD thesis. University of the Witwatersrand, Johannesburg, 2017.
- [2] L.J. Parrott, Some effects of cement and curing upon carbonation and reinforcement corrosion in concrete, *Mater. Struct.* 29 (1996) 164–173.
- [3] M.R. Jones, R.K. Dhir, M.D. Newlands, A.M.O. Abbas, A study of the CEN test method for measurement of the carbonation depth of hardened concrete, *Mater. Struct.* 33 (2000) 135–142.
- [4] Comité génie civil et bâtiment, Le patrimoine des ouvrages d’art en France : Entretien et surveillance, 2018.
- [5] AFNOR, Norme XP P18-458, Essai pour béton durci – Essai de carbonatation accélérée - Mesure de l’épaisseur de béton carbonaté, 2008.
- [6] V.G. Papadakis, C.G. Vayenas, M.N. Fardis, A reaction engineering approach to the problem of concrete carbonation, *AIChE J.* 35 (1989) 1639–1650.
- [7] M. Thiery, Modélisation de la carbonatation atmosphérique des matériaux cimentaires : Prise en compte des effets cinétiques et des modifications microstructurales et hydriques. PhD thesis, Ecole nationale des ponts et chaussées, 2005.
- [8] C.D. Lawrence, Transport of oxygen through concrete, in: *Br. Ceram. Proc.*, 1984: pp. 277–293.
- [9] J. Sercombe, R. Vidal, C. Gallé, F. Adenot, Experimental study of gas diffusion in cement paste, *Cem. Concr. Res.* 37 (2007) 579–588.
- [10] Y.F. Houst, F.H. Wittmann, Diffusion de gaz et durabilité du béton armé, in: *IABSE Symp. Durab. Struct.*, Lisbon, 1989: pp. 139–144.
- [11] L.J. Parrott, D.C. Killoh, Carbonation in a 36 year old, in-situ concrete, *Cem. Concr. Res.* 19 (1989) 649–656.
- [12] L. Bertolini, M. Carsana, M. Gastaldi, F. Lollini, E. Redaelli, Corrosion of Steel in Concrete and Its Prevention in Aggressive Chloride-Bearing Environments, in: *5th Int. Conf. Durability Concr. Struct.*, Shenzhen, China, 2016.
- [13] K. Tuutti, Corrosion of steel in concrete, PhD thesis, Royal Institute of Technology, Stockholm, 1982.
- [14] W. Ashraf, J. Olek, V. Atakan, Carbonation Reaction Kinetics, CO₂ Sequestration Capacity, and Microstructure of Hydraulic and Non-Hydraulic Cementitious Binders, in: *Fourth Int. Conf. Sustain. Constr. Mater. Technol.*, Las Vegas, USA, 2016.
- [15] C. Gehlen, Probabilistische Lebensdauerbemessung von Stahlbetonbauwerken- Zuverlässigkeitsbetrachtungen zur wirksamen Vermeidung von Bewehrungskorrosion, PhD thesis. RWTH Aachen, 2000.
- [16] S. Von Greve-dierfeld, C. Gehlen, Performance based durability design , carbonation part 1 – Benchmarking of European present design rules, *Struct. Concr.* 17 (2016) 309–328.
- [17] S.W. Webb, K. Pruess, The use of Fick’s law for modeling trace gas diffusion in porous media, *Transp. Porous Media.* 51 (2003) 327–341.
- [18] V.G. Papadakis, C.G. Vayenas, M.N. Fardis, Physical and chemical characteristics affecting the

durability of concrete, *ACI Mater. J.* 8 (1991) 186–196.

- [19] Y. Xi, Z.P. Bazant, L. Molina, H.M. Jennings, Moisture diffusion in cementitious materials, *Advn. Cem. Bas. Mat.* 1 (1994) 258–266.
- [20] M. Auroy, Impact de la carbonatation sur les propriétés de transport d'eau des matériaux cimentaires. PhD thesis, Université Paris-Est, 2014.
- [21] H.F.W. Taylor, *Cement Chemistry*, 2nd ed, Thomas Telford Publishing, 1997.
- [22] J. Sun, Carbonation Kinetics of Cementitious Materials Used in the Geological Disposal of Radioactive Waste, PhD thesis. University College London, 2010.
- [23] T. Grounds, H.G. Midgley, D.V. Nowell, Carbonation of ettringite by atmospheric carbon dioxide, *Thermochim. Acta.* 135 (1988) 347–352.
- [24] A. Morandeau, Carbonatation atmosphérique des systèmes cimentaires a faible teneur en portlandite, PhD thesis. Université Paris-Est, 2013.
- [25] P. López-Arce, L.S. Gómez-Villalba, S. Martínez-Ramírez, M. Álvarez de Buergo, R. Fort, Influence of relative humidity on the carbonation of calcium hydroxide nanoparticles and the formation of calcium carbonate polymorphs, *Powder Technol.* 205 (2011) 263–269.
- [26] Y.B. Hu, M. Wolthers, D.A. Wolf-Gladrow, G. Nehrke, Effect of pH and phosphate on calcium carbonate polymorphs precipitated at near-freezing temperature, *Cryst. Growth Des.* 15 (2015) 1596–1601.
- [27] A.V. Radha, T.Z. Forbes, C.E. Killian, P.U.P.A. Gilbert, A. Navrotsky, Transformation and crystallization energetics of synthetic and biogenic amorphous calcium carbonate, *Proc. Natl. Acad. Sci.* 107 (2010) 16438–16443.
- [28] M. Balonis, F.P. Glasser, The Density of Cement Phases, *Cem. Concr. Res.* (2009) 1–61.
- [29] E. Hamza, Contribution à l'étude des eaux géothermales du sud tunisien : etude des mecanismes et de la prevention des phenomenes d'entartrage, PhD thesis. L'Institut National des Sciences Appliquées de Toulouse, 1999.
- [30] Q. Phung, N. Maes, D. Jacques, E. Bruneel, I. Van Driessche, G. Ye, G. De Schutter, Effect of limestone fillers on microstructure and permeability due to carbonation of cement pastes under controlled CO₂ pressure conditions, *Constr. Build. Mater.* 82 (2015) 376–390.
- [31] B. Šavija, M. Luković, Carbonation of cement paste: Understanding, challenges, and opportunities, *Constr. Build. Mater.* 117 (2016) 285–301.
- [32] S. Zdenek, Carbonization of porous concrete and its main binding components, *Cem. Concr. Res.* 1 (1971) 645–662.
- [33] E.T. Stepkowska, J.L. Pérez-Rodríguez, M.J. Sayagués, J.M. Martínez-Blanes, Calcite, vaterite and aragonite forming on cement hydration from liquid and gaseous phase, *J. Therm. Anal. Calorim.* 73 (2003) 247–269.
- [34] G. Wolf, C. Günther, Thermophysical investigations of the polymorphous phases of calcium carbonate, *J. Therm. Anal. Calorim.* 65 (2001) 687–698.
- [35] V. Shah, K. Scrivener, B. Bhattacharjee, S. Bishnoi, Changes in microstructure characteristics of cement paste on carbonation, *Cem. Concr. Res.* 109 (2018) 184–197.
- [36] W. Soja, H. Maraghechi, F. Georget, K. Scrivener, Changes of microstructure and diffusivity in

blended cement pastes exposed to natural carbonation, in: MATEC Web Conf. ICCRRR, Cape Town, South Africa, 2018: p. 199.

- [37] P. Van den Heede, M. De Schepper, N. De Belie, Accelerated and natural carbonation of concrete with high volumes of fly ash: chemical, mineralogical and microstructural effects, *R. Soc. Open Sci.* 6 (2019).
- [38] S.T. Pham, W. Prince, Effects of Carbonation on the Microstructure and Macro Physical Properties of Cement Mortar, *Int. J. Civ. Environ. Eng.* 7 (2013) 434–437.
- [39] M. Thiery, G. Villain, P. Dangla, G. Platret, Investigation of the carbonation front shape on cementitious materials: Effects of the chemical kinetics, *Cem. Concr. Res.* 37 (2007) 1047–1058.
- [40] J.H. Seo, I.T. Amr, S.M. Park, R.A. Bamagain, B.A. Fadhel, G.M. Kim, A.S. Hunaidy, H.K. Lee, CO₂ uptake of carbonation-cured cement blended with ground volcanic ash, *Materials (Basel)*. 11 (2018).
- [41] R. Miragliotta, Modélisation des processus physico-chimiques de la carbonatation des bétons préfabriqués - prise en compte des effets de paroi, PhD thesis. La Rochelle université, 2000.
- [42] R.M. Lawrence, T.J. Mays, S.P. Rigby, P. Walker, D. D’Ayala, Effects of carbonation on the pore structure of non-hydraulic lime mortars, *Cem. Concr. Res.* 37 (2007) 1059–1069.
- [43] V.T. Ngala, C.L. Page, Effect of carbonation on pore structure and diffusional properties of hydrated cement pastes, *Cem. Concr. Res.* 27 (1997) 995–1007.
- [44] G. Villain, M. Thiery, Impact of carbonation on microstructure and transport properties of concrete, in: 10DBMC Int. Conférence Durab. Build. Mater. Components, Lyon , France, 2005.
- [45] M. Thiéry, P. Faure, A. Morandeau, G. Platret, J. Bouteloup, P. Dangla, V. Baroghel-Bouny, P. Dangla, Effect of carbonation on the microstructure and the moisture properties of cement-based materials, in: Int. Conf. Durab. Build. Mater. Components, Porto - Portugal, 2011.
- [46] M. Bertin, Impact du séchage au jeune âge sur la carbonatation des matériaux cimentaires avec additions minérales, PhD thesis. Université Paris-Est marne la vallée, 2017.
- [47] D.J. Anstice, C.L. Page, M.M. Page, The pore solution phase of carbonated cement pastes, *Cem. Concr. Res.* 35 (2005) 377–383.
- [48] O. Omikrine Metalsi, A. Aït-Mokhtar, P. Turcry, B. Ruot, Consequences of carbonation on microstructure and drying shrinkage of a mortar with cellulose ether, *Constr. Build. Mater.* 34 (2012) 218–225.
- [49] E. Brunauer, Stephen; Emmett, P. H.; Teller, Adsorption of Gases in Multimolecular Layers, *J. Am. Chem. Soc.* (1938) 309–319.
- [50] H. Ranaivomanana, Transferts dans les milieux poreux réactifs non saturés : application à la cicatrisation de fissure dans les matériaux cimentaires par carbonatation, PhD thesis. Université Toulouse III - Paul Sabatier, 2010.
- [51] M. Auroy, S. Poyer, P. Le Bescop, J. Torrenti, T. Charpentier, M. Moskura, X. Bourbon, Impact of carbonation on unsaturated water transport properties of cement-based materials, *Cem. Concr. Res.* 74 (2015) 44–58.
- [52] V. Dutzer, W. Dridi, S. Poyet, P. Le Bescop, X. Bourbon, The link between gas diffusion and carbonation in hardened cement pastes, *Cem. Concr. Res.* 123 (2019) 105795.
- [53] N. Hyvert, Application de l’approche probabiliste à la durabilité des produits préfabriqués en béton, PhD thesis. Université Paul Sabatier - Toulouse III, 2009.

- [54] P.H.R. Borges, J.O. Costa, N.B. Milestone, C.J. Lynsdale, R.E. Streatfield, Carbonation of CH and C-S-H in composite cement pastes containing high amounts of BFS, *Cem. Concr. Res.* 40 (2010) 284–292.
- [55] T. Tracz, T. Zdeb, Effect of hydration and carbonation progress on the porosity and permeability of cement pastes, *Materials (Basel)*. 12 (2019) 192.
- [56] H.S. Wong, M. Zobel, N.R. Buenfeld, R.W. Zimmerman, Influence of the interfacial transition zone and microcracking on the diffusivity, permeability and sorptivity of cement-based materials after drying, *Mag. Concr. Res.* 61 (2009) 571–589.
- [57] B. Huet, Comportement à la corrosion des armatures dans un béton carbonaté . Influence de la chimie de la solution interstitielle et d'une barrière de transport, PhD thesis. INSA Lyon, 2005.
- [58] A. Belda Revert, K. De Weerd, K. Hornbostel, M.R. Geiker, Carbonation-induced corrosion: Investigation of the corrosion onset, *Constr. Build. Mater.* 162 (2018) 847–856.
- [59] P.F. Marques, C. Chastre, Â. Nunes, Carbonation service life modelling of RC structures for concrete with Portland and blended cements, *Cem. Concr. Compos.* 37 (2013) 171–184.
- [60] T. El Maaddawy, K. Soudki, A model for prediction of time from corrosion initiation to corrosion cracking, *Cem. Concr. Compos.* 29 (2007) 168–175.
- [61] F. Hunkeler, L. Lammar, Anforderungen an den Karbonatisierungswiderstand von Betonen, Schweizerischer Verband der Strassen- und Verkehrsfachleute (VSS), 2012.
- [62] S. Lay, P. Schiessl, Service life models - Instructions on methodology and application of models for the prediction of the residual service life for classified environmental loads and types of structures in Europe, Report, cbm – Technische Universität München, 2004.
- [63] I.S. Yoon, O. Çopuroğlu, K.B. Park, Effect of global climatic change on carbonation progress of concrete, *Atmos. Environ.* 41 (2007) 7274–7285.
- [64] R.R. Hussain, T. Ishida, M. Wasim, Experimental investigation of time dependent non-linear 3D relationship between critical carbonation depth and corrosion of steel in carbonated concrete, *Corros. Eng. Sci. Technol.* 46 (2011) 657–660.
- [65] M. Limbachiya, M.S. Meddah, Y. Ouchagour, Use of recycled concrete aggregate in fly-ash concrete, *Constr. Build. Mater.* 27 (2012) 439–449.
- [66] R. Sander, Compilation of Henry's law constants (version 4.0) for water as solvent, *Atmos. Chem. Phys.* 15 (2015) 4399–4981.
- [67] R.K. Dhir, M.C. Limbachiya, M.J. McCarthy, A. Chaipanich, Evaluation of Portland limestone cements for use in concrete construction, *Mater. Struct.* 40 (2007) 459–473.
- [68] A. Leemann, P. Nygaard, J. Kaufmann, R. Loser, Relation between carbonation resistance, mix design and exposure of mortar and concrete, *Cem. Concr. Compos.* 62 (2015) 33–43.
- [69] Y. Yan, T. Guanbao, W. Ling, C. Suping, C. Yin, Difference between natural and accelerated carbonation of concrete at 2 % CO₂ and 20 % CO₂, *Rom. J. Mater.* 48 (2018) 70–75.
- [70] S.A. Bernal, J.L. Provis, D.G. Brice, A. Kilcullen, P. Duxson, J.S.J. Van Deventer, Accelerated carbonation testing of alkali-activated binders significantly underestimates service life: The role of pore solution chemistry, *Cem. Concr. Res.* 42 (2012) 1317–1326.
- [71] N. Hyvert, A. Sellier, F. Duprat, P. Rougeau, P. Francisco, Dependency of C-S-H carbonation rate on CO₂ pressure to explain transition from accelerated tests to natural carbonation, *Cem. Concr. Res.* 40 (2010) 1582–1589.

- [72] M. Castellote, C. Andrade, X. Turrillas, J. Campo, G.J. Cuello, Accelerated carbonation of cement pastes in situ monitored by neutron diffraction, *Cem. Concr. Res.* (2008).
- [73] M.R. Jones, M.D. Newlands, A. Abbas, Carbonation Testing Of Hardened Concrete And The Effect Of Cement Type, in: 9th Int. Conf. Durab. Build. Mater. Components, Brisbane, Australia, 2002.
- [74] A. Leemann, F. Moro, Carbonation of concrete - the role of CO₂ concentration, relative humidity and CO₂ buffer capacity, *Mater. Struct.* 50 (2017).
- [75] BS EN 14629, Products and systems for the protection and repair of concrete structures - Test methods - Determination of chloride content in hardened concrete, Br. Stand. (2007).
- [76] W. Le Tang, H.S. Lee, V. Vimonsatit, T. Htut, J.K. Singh, W.N.F.W. Hassan, M.A. Ismail, A.H. Seikh, N. Alharthi, Optimization of micro and nano palm oil fuel ash to determine the carbonation resistance of the concrete in accelerated condition, *Materials (Basel)*. 12 (2019).
- [77] Iso 1920-12:2015 (E), Determination of the carbonation resistance of concrete — Accelerated carbonation method, 2015.
- [78] SIA 262/1:2013, Concrete Structures Supplementary specifications. Appendix I Carbonation resistance, 2013.
- [79] NT Build 357, Concrete, Repairing Materials and Protective Coating: Carbonation resistance, (1984).
- [80] D. Cui, W. Sun, N. Banthia, Use of tomography to understand the influence of preconditioning on carbonation tests in cement-based materials, *Cem. Concr. Compos.* 88 (2018) 52–63.
- [81] EN 12390-12:2018-10, Determination of the carbonation resistance of concrete – Accelerated carbonation method, 2018.
- [82] N. Rafai, H. Hornain, G. Villain, V. Baroghel Bouny, G. Platret, T. Chaussadent, Comparaison et validité des méthodes de mesure de la carbonatation, *Rev. Française Génie Civ.* 6 (2002) 251–274.
- [83] V.G. Papadakis, C.G. Vayenas, M.N. Fardis, Experimental Investigation and Mathematical-Modeling of the Concrete Carbonation Problem, *Chem. Eng. Sci.* 46 (1991) 1333–1338.
- [84] International Federation for Structural Concrete, MC-SLD:2006. Model Code for Service Life Design, in: *Model Code Bull.* 34, 2006: p. 116.
- [85] C. Peretti, A. Leemann, R. Loser, P. Lura, Influence of Different Conditioning Regimes on the Oxygen Diffusion and Oxygen Permeability of Concrete, in: 2nd Int. Conf. Microstruct. Relat. Durab. Cem. Compos., Amsterdam, 2012.
- [86] H.S. Wong, N.R. Buenfeld, M.K. Head, Estimating transport properties of mortars using image analysis on backscattered electron images, *Cem. Concr. Res.* 36 (2006) 1556–1566.
- [87] Y.F. Houst, Diffusion de gaz, carbonatation et retrait de la pate de ciment durcie, PhD thesis. Ecole polytechnique federale de Lausanne, 1992.
- [88] K.D. Namouniara, Etude expérimentale de la diffusion du CO₂ et des cinétiques de carbonatation de matériaux cimentaires à faible dosage en clinker, PhD thesis. La Rochelle université, 2015.
- [89] F. Gendron, Carbonatation des matériaux cimentaires Étude de la diffusion du CO₂, PhD thesis. La Rochelle université, 2019.
- [90] F. Gendron, M. Boumaaza, P. Turcry, B. Huet, A. Aït-Mokhtar, Gas Diffusion in Cementitious Materials: Test Methods Review, in: SynerCrete'18 Int. Conf. Interdiscip. Approaches Cem. Mater. Struct. Concr., Funchal - Madeira, 2018.

- [91] A. Leemann, R. Loser, B. Münch, P. Lura, Steady-state O₂ and CO₂ diffusion in carbonated mortars produced with blended cements, *Mater. Struct.* 50 (2017) 247.
- [92] C. Boher, Etude expérimentale et modélisation de la diffusion gazeuse à travers des milieux poreux partiellement saturés en eau. Application aux verres Vycor, géopolymères et pâtes de ciment CEMV., Université de Toulouse, 2012.
- [93] T.-H. VU, Caractérisation de la phase solide et transferts de gaz dans les milieux poreux insaturés. Etude expérimentale et modélisation appliquées à la diffusion de l'hydrogène dans les matériaux cimentaires, PhD thesis. Université de Toulouse, 2009.
- [94] D. Benavente, C. Pla, Effect of pore structure and moisture content on gas diffusion and permeability in porous building stones, *Mater. Struct. Constr.* 51 (2018) 1–14.
- [95] K. Namouniara, P. Turcry, A. Aït-Mokhtar, Measurement of CO₂ effective diffusion coefficient of cementitious materials, *Eur. J. Environ. Civ. Eng.* 2016. 8189 (2016).
- [96] S.H. Jung, M.K. Lee, B.H. Oh, Measurement device and characteristics of diffusion coefficient of carbon dioxide in concrete, *ACI Mater. J.* 108 (2011) 589–595.
- [97] K. Soukup, P. Schneider, O. Šolcová, Wicke-Kallenbach and Graham's diffusion cells : Limits of application for low surface area porous solids, *Chem. Eng. Sci.* 63 (2008) 4490–4493.
- [98] K. Soukup, P. Schneider, O. Šolcová, Comparison of Wicke-Kallenbach and Graham's diffusion cells for obtaining transport characteristics of porous solids, *Chem. Eng. Sci.* 63 (2008) 1003–1011.
- [99] C. Villani, R. Loser, M.J. West, C. Di Bella, P. Lura, W.J. Weiss, An inter lab comparison of gas transport testing procedures: Oxygen permeability and oxygen diffusivity, *Cem. Concr. Compos.* 53 (2014) 357–366.
- [100] S. Peng, Q. Hu, S. Hamamoto, Diffusivity of rocks: Gas diffusion measurements and correlation to porosity and pore size distribution, *Water Resour. Res.* 48 (2012).
- [101] K.H. Yang, E.A. Seo, S.H. Tae, Carbonation and CO₂ uptake of concrete, *Environ. Impact Assess. Rev.* 46 (2014) 43–52.
- [102] R.J. Millington, Gas Diffusion in Porous Media, *Science*, 130 (1959) 100–102.
- [103] J.A. Currie, Gaseous diffusion in porous media Part 1. - A non-steady state method, *Br. J. Appl. Phys.* (1960).
- [104] D.N. Huntzinger, J.S. Gierke, L.L. Sutter, S.K. Kawatra, T.C. Eisele, Mineral carbonation for carbon sequestration in cement kiln dust from waste piles, *J. Hazard. Mater.* 168 (2009) 31–37.
- [105] R. Andersson, K. Fridh, H. Stripple, M. Häglund, Calculating CO₂ uptake for existing concrete structures during and after service life, *Environ. Sci. Technol.* 47 (2013) 11625–11633.
- [106] Y. Guo, C. Zhao, C. Li, Thermogravimetric analysis of carbonation behaviors of several potassium-based sorbents in low concentration CO₂, *J Therm Anal Calorim.* 119 (2014) 441–451.
- [107] G. Villain, M. Thiery, G. Platret, Measurement methods of carbonation profiles in concrete : Thermogravimetry, chemical analysis and gammadensimetry, *Cem. Concr. Res.* 37 (2007) 1182–1192.
- [108] N.C. Collier, Transition and decomposition temperatures of cement phases – a collection of thermal analysis data, *Ceramics-Silikaty.* 60 (2016) 338–343.
- [109] K.L. Scrivener, T. Füllmann, E. Gallucci, G. Walenta, E. Bermejo, Quantitative study of Portland

cement hydration by X-ray diffraction/Rietveld analysis and independent methods, *Cem. Concr. Res.* 34 (2004) 1541–1547.

- [110] E. Possan, W.A. Thomaz, G.A. Aleandri, E.F. Felix, A.C.P. dos Santos, CO₂ uptake potential due to concrete carbonation: A case study, *Case Stud. Constr. Mater.* 6 (2017) 147–161.
- [111] B. Lagerblad, Carbon dioxide uptake during concrete life cycle-State of the art, Swedish Cement and Concrete Research Institute. CBI report, 2005.
- [112] H.S. Lee, X.Y. Wang, Evaluation of the carbon dioxide uptake of slag-blended concrete structures, considering the effect of carbonation, *Sustain.* 8 (2016).
- [113] K. Van Balen, Carbonation reaction of lime, kinetics at ambient temperature, *Cem. Concr. Res.* 35 (2005) 647–657.
- [114] F. Georget, A Reactive Transport Simulator for Cement Pastes, PhD thesis. Princeton University, 2017.
- [115] I. Galan, C. Andrade, Comparison of Carbonation Models, in: 3rd Int. RILEM PhD Student Work. Model. Durab. Reinf. Concr., University of Minho, Guimarães, Portugal, 2009.
- [116] M.M.Y. Delmi, Etude de l'hydratation et du couplage carbonatation-échanges hydriques dans les mortiers et bétons, PhD thesis. La Rochelle université, 2004.
- [117] O. Omikrine Metalssi, Pour obtenir Étude des couplages hydratation-échanges hydriques-carbonatation dans les mortiers modifiés polymères Remerciements, PhD thesis. La Rochelle université, 2006.
- [118] A. Younsi, Carbonatation de bétons à forts taux de substitution du ciment par des additions minérales, PhD thesis. Université de La Rochelle, 2012.
- [119] O. Omikrine Metalssi, A. Aït-Mokhtar, P. Turcry, A proposed modelling of coupling carbonation-porosity-moisture transfer in concrete based on mass balance equilibrium, *Constr. Build. Mater.* 230 (2020) 116997.
- [120] S. Von Greve-dierfeld, C. Gehlen, Performance-based durability design , carbonation part 2 – Classification of concrete, *Struct. Concr. J. FIB.* 17 (2016) 523–532.
- [121] C. Galle, Effect of drying on cement-based materials pore structure as identified by mercury intrusion porosimetry A comparative study between oven- , vacuum- , and freeze-drying, *Cem. Concr. Res.* 31 (2001) 1467–1477.
- [122] Association Française de Normalisation (AFNOR), NF P18-459, Essai pour béton durci Essai de porosité et de masse volumique, 2010.
- [123] E. Berodier, K. Scrivener, Evolution of pore structure in blended systems, *Cem. Concr. Res.* 73 (2015) 25–35.
- [124] Z. Yu, G. Ye, The pore structure of cement paste blended with fly ash, *Constr. Build. Mater.* 45 (2013) 30–35.
- [125] O. Coussy, Surface Energy and Capillarity, in: *Mech. Phys. Porous Solids*, John Wiley, 2010: pp. 121–122.
- [126] F. Moro, H. Böhni, Ink-bottle effect in mercury intrusion porosimetry of cement-based materials, *J. Colloid Interface Sci.* 246 (2002) 135–149.
- [127] S. Meulenyzer, J. Chanussot, S. Crombez, J.J. Chen, Spectral-spatial image processing strategies for

classifying multispectral SEM-EDS X-Ray maps of cementitious materials, in: 14th Euroseminar Microsc. Appl. to Build. Mater., Helsingør, Denmark, 2013.

- [128] M.H.N. Yio, J.C. Phelan, H.S. Wong, N.R. Buenfeld, Determining the slag fraction, water/binder ratio and degree of hydration in hardened cement pastes, *Cem. Concr. Res.* 56 (2014) 171–181.
- [129] V. Kocaba, E. Gallucci, K.L. Scrivener, Methods for determination of degree of reaction of slag in blended cement pastes, *Cem. Concr. Res.* 42 (2012) 511–525.
- [130] D. Helsel, M. A., Ferraris, C. F., and Bentz, Comparative study of methods to measure the density of Cementitious powders, *J. Test. Eval.* 44 (2016) 2147–2154.
- [131] V. Baroghel-Bouny, Développement d’une approche globale, performantielle et prédictive de la durabilité des structures en béton (armé) sur la base d’indicateurs de durabilité Bilan et perspectives, LCPC, 2008.
- [132] M. Hamada, Carbonation of concrete, in: Princeton University Library, 1385: p. 302.
- [133] AFNOR, XP P18-463 Essai de perméabilité aux gaz sur béton durci, 2011.
- [134] J.J. Kollek, The determination of the permeability of concrete to oxygen by the Cembureau method—a recommendation, *Mater. Struct.* 22 (1989) 225–230.
- [135] Rilem TC 116-PCD, Permeability of concrete as a criterion of its durability, *Mater. Struct.* 32 (1999) 174–179.
- [136] F. Sorrentino, Upscaling the synthesis of tricalcium silicate and alite, *Cem. Wapno Bet.* 8 (2008) 177–183.
- [137] France, PerfDub project, (2015). <https://www.perfdub.fr/en/>.
- [138] W.Y. Chan, The effect of specimen size on the measured mass transport properties of concrete, in: 1st Civ. Environ. Eng. Student Conf. Imp. Coll. London, 2012.
- [139] NF EN 206/CN, Béton-Spécification, performance, production et conformité-Complément national à la norme NF EN 206, 2014.
- [140] T. Graham, On the law of the diffusion of gases, *London Edinburgh Philos. Mag. J. Sci.* 2 (1833) 269–351.
- [141] M. Boumaaza, B. Huet, P. Turcry, A. Aït-Mokhtar, C. Gehlen, D. Heinz, Gas diffusivity test method development : effect of cement paste saturation degree and concrete specimen thickness, in: 12th Fib Int. PhD Symp. Civ. Eng., Prague Czech republic, 2018.
- [142] R.L. Nuzzo, The Box Plots Alternative for Visualizing Quantitative Data, *PM&R.* 8 (2016) 268–272.
- [143] Y. Houst, F.H. Wittmann, Influence of porosity and water content on the diffusivity of CO₂ and O₂ through hydrated cement paste, *Cem. Concr. Res.* 24 (1994) 1165–1176.
- [144] P. Soongswang, M. Tia, D. Bloomquist, Factors affecting the strength and permeability of concrete made with porous limestone, *ACI Mater. J.* 88 (1991) 400–406.
- [145] L.J. Parrott, Moisture conditioning and transport properties of concrete test specimens, *Mater. Struct.* 27 (1994) 460–468.
- [146] D.N. Winslow, M.D. Cohen, D.P. Bentz, K.A. Snyder, E.J. Garboczi, Percolation and pore structure in mortars and concrete, *Cem. Concr. Res.* 24 (1994) 25–37.
- [147] T. Gardner, Chloride transport through concrete and implications for rapid chloride testing, PhD

thesis. University of Cape Town, 2006.

- [148] T.C. Powers, A Hypothesis on Carbonation Shrinkage, *J. Portl. Cem. Assoc. Res. Dev. Lab.* (1962) 40–50.
- [149] B.G. Salvoldi, H. Beushausen, M.G. Alexander, Oxygen permeability of concrete and its relation to carbonation, *Constr. Build. Mater.* 85 (2015) 30–37.
- [150] H.S. Fogler, From Elements of Chemical Reaction Engineering, in: I. Pearson Education (Ed.), *Simulating Ecol. Evol. Syst. C*, 2010: pp. 820–860.
- [151] M. Boumaaza, B. Huet, C. Le Galliard, P. Turcry, A. Aït-mokhtar, C. Gehlen, Experimental determination of carbonation related durability indicators : gas diffusivity and CO₂ binding capacity, in: *15th Int. Congr. Chem. Cem.*, Prague, Czech Republic, 2019.
- [152] M. Balonis, F.P. Glasser, The density of cement phases, *Cem. Concr. Res.* 39 (2009) 733–739.
- [153] Z. Wu, H.S. Wong, N.R. Buenfeld, Effect of confining pressure and microcracks on mass transport properties of concrete, *Adv. Appl. Ceram.* 113 (2014) 485–495.
- [154] W. Soja, Carbonation of low carbon binders, PhD thesis. Ecole polytechnique federale de Lausanne, 2019.
- [155] RILEM, GDP: Test Methods for Gas Diffusion in Porous Media, (2019). <https://www.rilem.net/groupe/gdp-test-methods-for-gas-diffusion-in-porous-media-386>.
- [156] V. Nikulshina, M.E. Gálvez, A. Steinfeld, Kinetic analysis of the carbonation reactions for the capture of CO₂ from air via the Ca(OH)₂ – CaCO₃– CaO solar thermochemical cycle, *Chem. Eng. J.* 129. 129 (2007) 75–83.
- [157] A. El-Turki, M.A. Carter, M.A. Wilson, R.J. Ball, G.C. Allen, A microbalance study of the effects of hydraulicity and sand grain size on carbonation of lime and cement, *Constr. Build. Mater.* 23 (2009) 1423–1428.
- [158] D.P.P. Bentz, O.M. Jensen, A.M. Coats, F.P.P. Glasser, Influence of silica fume on diffusivity in cement-based materials I. Experimental and computer modeling studies on cement pastes, *Cem. Concr. Res.* 30 (2000) 953–962.
- [159] V. Baroghel-Bouny, Water vapour sorption experiments on hardened cementitious materials. Part I: Essential tool for analysis of hygral behaviour and its relation to pore structure, *Cem. Concr. Res.* 37 (2007) 414–437.
- [160] N. De Belie, J. Kratky, S. Van Vlierberghe, Influence of pozzolans and slag on the microstructure of partially carbonated cement paste by means of water vapour and nitrogen sorption experiments and BET calculations, *Cem. Concr. Res.* 40 (2010) 1723–1733. doi:10.1016/j.cemconres.2010.08.014.
- [161] H.S. Wong, N.R. Buenfeld, J. Hill, A.W. Harris, Mass transport properties of mature wasteform grouts, *Adv. Cem. Res.* 19 (2007) 35–46.
- [162] M. Saillio, V. Baroghel-Bouny, M. Bertin, S. Pradelle, J. Vincent, Phase assemblage of cement pastes with SCM at different ages, *Constr. Build. Mater.* 224 (2019) 144–157.
- [163] M. Ben Haha, B. Lothenbach, G. Le Saout, F. Winnefeld, Influence of slag chemistry on the hydration of alkali-activated blast-furnace slag - Part II: Effect of Al₂O₃, *Cem. Concr. Res.* 42 (2012) 74–83.
- [164] V.G. Papadakis, C.G. Vayenas, M.N. Fardis, Fundamental modeling and experimental investigation of concrete carbonation, *ACI Mater. J.* 88 (1991) 363–373.

- [165] DIN EN 12390-10:2019-03, Prüfung von Festbeton - Teil 10: Bestimmung des Karbonatisierungswiderstandes von Beton bei atmosphärischer Konzentration von Kohlenstoffdioxid; Deutsche Fassung EN 12390-10:2018, Beuth, Berlin, 2018.
- [166] V. Baroghel-Bouny, K. Kinomura, M. Thiery, S. Moscardelli, Easy assessment of durability indicators for service life prediction or quality control of concretes with high volumes of supplementary cementitious materials, *Cem. Concr. Compos.* 33 (2011) 832–847.
- [167] K. Sakata, A study on moisture diffusion in drying and drying shrinkage of concrete, *Cem. Concr. Res.* 13 (1983) 216–224.
- [168] B. Huet, V. L'hostis, G. Santarini, D. Feron, H. Idrissi, Steel corrosion in concrete: Determinist modeling of cathodic reaction as a function of water saturation degree, *Corros. Sci.* 49 (2007) 1918–1932.
- [169] A.A. Hamami, P. Turcry, A. Aït-Mokhtar, Influence of mix proportions on microstructure and gas permeability of cement pastes and mortars, *Cem. Concr. Res.* 42 (2012) 490–498.
- [170] S. Demis, M.P. Efstathiou, V.G. Papadakis, Computer-aided modeling of concrete service life, *Cem. Concr. Compos.* 47 (2014) 9–18.
- [171] M.M. Mezedur, M. Kaviany, W. Moore, Effect of pore structure, randomness and size on effective mass diffusivity, *AIChE J.* 48 (2002) 15–24.
- [172] V.G. Papadakis, Effect of supplementary cementing materials on concrete resistance against carbonation and chloride ingress, *Cem. Concr. Res.* 30 (2000) 291–299.
- [173] Z. Bajja, W. Dridi, B. Larbi, P. Le Bescop, The validity of the formation factor concept from throughout diffusion tests on Portland cement mortars, *Cem. Concr. Compos.* 63 (2015) 76–83.
- [174] K.L. Scrivener, A.K. Crumbie, P. Laugesen, The interfacial transition zone (ITZ) between cement paste and aggregate in concrete, *Interface Sci.* 12 (2004) 411–421.
- [175] P. Termkhajornkit, R. Barbarulo, G. Chanvillard, Microstructurally-designed cement pastes: A mimic strategy to determine the relationships between microstructure and properties at any hydration degree, *Cem. Concr. Res.* 71 (2015) 66–77.
- [176] B. Jeffrey W., J. Hamlin M., L. Richard A., N. Andre, S. George W., S. Jeffrey S., S. Karen L., T. Jeffrey J., Mechanisms of cement hydration, *Cem. Concr. Res.* 41 (2011) 1208–1223.
- [177] T.E. Oliphant, SciPy: Open source scientific tools for Python, *Comput. Sci. Eng.* 9 (2007) 10–20.
- [178] J.E. Guyer, D. Wheeler, J.A. Warren, FiPy: Partial differential equations with python, *Comput. Sci. Eng.* 11 (2009) 6–15.
- [179] A. Abell, K. Willis, D. Lange, Mercury Intrusion Porosimetry and Image Analysis of Cement-Based Materials., *J. Colloid Interface Sci.* 211 (1999) 39–44.
- [180] A.C.A. Muller, Characterization of porosity & C-S-H in cement pastes by ¹H NMR, PhD thesis. Ecole polytechnique fédérale de Lausanne, 2014.
- [181] J.W. Bartlett, C. Frost, Reliability, repeatability and reproducibility: Analysis of measurement errors in continuous variables, *Ultrasound Obstet. Gynecol.* 31 (2008) 466–475.
- [182] T.C. POWERS, Structure and Physical Properties of Hardened Portland Cement Paste, *J. Am. Ceram. Soc.* 41 (1958).
- [183] H.M. Jennings, J.J. Thomas, J.J. Chen, D. Rothstein, Cement Paste as a Porous Material, *Handb.*

Porous Solids. (2002) 2971–3028.

- [184] X. Feng, E.J. Garboczi, D.P. Bentz, P.E. Stutzman, T.O. Mason, Estimation of the degree of hydration of blended cement pastes by a scanning electron microscope point-counting procedure, *Cem. Concr. Res.* 34 (2004) 1787–1793.
- [185] F. Jacobs, Permeability to gas of partially saturated concrete, *Mag. Concr. Res.* 50 (1998) 115–121.
- [186] T.R. Marrero, E.A. Mason, Gaseous Diffusion Coefficients, *J. Phys. Chem. Ref. Data.* 1 (1972).
- [187] Feldman R. F. and Cheng Yi. H., Properties of Portland cement - silica fume pastes, *Cem. Concr. Res.* 15 (1985) 765–774.
- [188] M. Rhamdhani, The Characterisation of Oxygen in Metal / Slag Reactions, in: *Electr. Furn. Conf. Proc.*, 2002: pp. 787–796.
- [189] W. Ashraf, Carbonation of cement-based materials: Challenges and opportunities, *Constr. Build. Mater.* 120 (2016) 558–570.
- [190] P. Turcry, L. Oksri-Nelfia, A. Younsi, A. Aït-Mokhtar, Analysis of an accelerated carbonation test with severe preconditioning, *Cem. Concr. Res.* (2014).
- [191] C. Thiel, C. Gehlen, Compliance testing for probabilistic durability design purposes, in: *Sixth Int. Symp. Life-Cycle Civ. Eng. (IALCCE 2018)*, Ghent, Belgium, 2018.
- [192] M. Boumaaza, B. Huet, G. Pham, P. Turcry, A. Aït-Mokhtar, C. Gehlen, A new test method to determine the gaseous oxygen diffusion coefficient of cement pastes as a function of hydration duration, microstructure, and relative humidity, *Mater. Struct.* 51 (2018) 1–31.
- [193] H. Jansson, R. Snibb, K. Bohlin, I. Lofgren, Carbonation of concrete with mineral additions, in: *Proc. XXIII Nord. Concr. Res. Symp.*, Aalborg, Denmark, 2017: pp. 101–104.
- [194] N. Issaadi, A. Nouviaire, R. Belarbi, A. Aït-Mokhtar, Moisture characterization of cementitious material properties: Assessment of water vapor sorption isotherm and permeability variation with ages, *Constr. Build. Mater.* 83 (2015) 237–247.
- [195] O. Amiri, A. Aït-Mokhtar, M. Sarhani, Tri-dimensional modelling of cementitious materials permeability from polymodal pore size distribution obtained by mercury intrusion porosimetry tests, *Adv. Cem. Res.* 17 (2005) 39–45.
- [196] C. Andrade, A.S. Miguel, Updating Carbon Storage Capacity of Spanish Cements, *Sustain.* 10 (2018) 4806.
- [197] EN 197-1, Cement Part 1: Composition, Specifications and Conformity Criteria for Common Cements, *Br. Stand.* (2011).
- [198] E.M.J. Berodier, Impact of the Supplementary Cementitious Materials on the kinetics and microstructural development of cement hydration, PhD thesis. Ecole polytechnique federale de lausanne, 2015.
- [199] C. Naber, S. Stegmeyer, D. Jansen, F. Goetz-Neunhoeffler, J. Neubauer, The PONKCS method applied for time resolved XRD quantification of supplementary cementitious material reactivity in hydrating mixtures with ordinary Portland cement, *Constr. Build. Mater.* 214 (2019) 449–457.
- [200] A.K. Schindler, K.J. Folliard, Influence of supplementary cementing materials on the heat of hydration of concrete, in: *Adv. Cem. Concr. IX Conf.*, Colorado, 2003: pp. 10–14.
- [201] M. Auroy, S. Poyet, P. Le Bescop, J.M. Torrenti, T. Charpentier, M. Moskura, X. Bourbon, Comparison

between natural and accelerated carbonation (3% CO₂): Impact on mineralogy, microstructure, water retention and cracking, *Cem. Concr. Res.* 109 (2018) 64–80.

- [202] Association Française de Normalisation (AFNOR), Determination of real and apparent densities, open and total porosities, in: AFNOR (Ed.), NF EN 1936, 2007.
- [203] K. Suzuki, N. Tadaihiro, S. ITO, Formation and carbonation of CSH in water, *Cem. Concr. Res.* 15 (1985) 213–224.
- [204] O. Metalssi, A. Aït-Mokhtar, A proposed methodology for a quantitative investigation of carbonation in polymer-modified mortars, *Exp. Tech.* 33 (2009) 59–65.
- [205] C. Andrade, Evaluation of the degree of carbonation of concretes in three environments, *Constr. Build. Mater.* 230 (2020) 116804.
- [206] A. Morandea, M. Thiéry, P. Dangla, Investigation of the carbonation mechanism of CH and C-S-H in terms of kinetics, microstructure changes and moisture properties, *Cem. Concr. Res.* 56 (2014) 153–170.
- [207] S.E. Pihlajavaara, Some results of the effect of carbonation on the porosity and pore size distribution of cement paste, *Mater. Struct.* (1968) 521–527.
- [208] S.E. Pihlajavaara, P. Esko, Effect of carbonation on microstructural properties of cement stones, *Cem. Concr. Res.* 4 (1974) 149–154.
- [209] B. Johannesson, P. Utgenannt, Microstructural changes caused by carbonation of cement mortar, *Cem. Concr. Res.* 31 (2001) 925–931.
- [210] A. Machner, M. Zajac, M. Ben Haha, K.O. Kjellsen, M.R. Geiker, K. De Weerd, Stability of the hydrate phase assemblage in Portland composite cements containing dolomite and metakaolin after leaching, carbonation, and chloride exposure, *Cem. Concr. Compos.* 89 (2018) 89–106.
- [211] L. Black, K. Garbev, I. Gee, Surface carbonation of synthetic C-S-H samples: A comparison between fresh and aged C-S-H using X-ray photoelectron spectroscopy, *Cem. Concr. Res.* (2008).
- [212] L. Black, K. Garbev, G. Beuchle, P. Stemmermann, D. Schild, X-ray photoelectron spectroscopic investigation of nanocrystalline calcium silicate hydrates synthesised by reactive milling, *Cem. Concr. Res.* 36 (2006) 1023–1031.
- [213] A.E. Morandea, M. Thiery, P. Dangla, C.E. White, Accelerated carbonation modelling of fly ash-blended cement paste, in: RILEM Int. Symp. Concr. Model., Beijing, China, 2014.
- [214] I.G. Richardson, The nature of C-S-H in hardened cements, *Cem. Concr. Res.* 29 (1999) 1131–1147.
- [215] Q.T. Phung, N. Maes, E. Jacobs, D. Jacques, G. De Schutter, G. Ye, Insights and issues on the correlation between diffusion and microstructure of saturated cement pastes, *Cem. Concr. Compos.* 96 (2019) 106–117.
- [216] F. Lollini, E. Redaelli, L. Bertolini, Effects of portland cement replacement with limestone on the properties of hardened concrete, *Cem. Concr. Compos.* 46 (2014) 32–40.
- [217] R. Bucher, P. Diederich, G. Escadeillas, M. Cyr, Service life of metakaolin-based concrete exposed to carbonation: Comparison with blended cement containing fly ash, blast furnace slag and limestone filler, *Cem. Concr. Res.* 99 (2017) 18–29.
- [218] C.J. Engelsens, H. Justnes, CO₂-binding by concrete – carbonation speed, degree and binding capacity, in: 13th NCB Int. Semin. Cem. Build. Mater., 2013: pp. 1–10.

- [219] S.-M. Shih, C.-S. Ho, Y.-S. Song, J.-P. Lin, Kinetics of the Reaction of Ca(OH)₂ with CO₂ at Low Temperature, *Ind. Eng. Chem. Res.* 38 (1999) 1316–1322.
- [220] T. Aono, Studies on the reactions between gas and solid, part II, absorption of CO₂ by CaO and Ca(OH)₂, *Bull. Chem. Soc. Jpn.* 6 (1931) 319–324.
- [221] R.J. Flatt, G.W. Scherer, J.W. Bullard, Why alite stops hydrating below 80% relative humidity, *Cem. Concr. Res.* 41 (2011) 987–992.
- [222] O. Regnault, V. Lagneau, H. Schneider, Experimental measurement of portlandite carbonation kinetics with supercritical CO₂, *Chem. Geol.* 265 (2009) 113–121.
- [223] I. Galan, F.P. Glasser, D. Baza, C. Andrade, Assessment of the protective effect of carbonation on portlandite crystals, *Cem. Concr. Res.* 74 (2015) 68–77.
- [224] T. Nishikawa, K. Suzuki, S. Ito, Decomposition of synthesized ettringite by carbonation, *Cem. Concr. Res.* 22 (1992) 6–14.
- [225] Q. Zhou, F.P. Glasser, Kinetics and mechanism of the carbonation of ettringite, *Adv. Cem. Res.* 12 (2000) 131–136.
- [226] G. Seishi, S. Kenzo, K. Takeshi, Calcium silicate carbonation products, *J. Am. Ceram. Soc.* 78 (1995).
- [227] V. Rostami, Y. Shao, A.J. Boyd, Z. He, Microstructure of cement paste subject to early carbonation curing, *Cem. Concr. Res.* (2012).
- [228] O. Shtepenko, C. Hills, A. Brough, M. Thomas, The effect of carbon dioxide on beta-dicalcium silicate and Portland cement, *Chem. Eng. J.* 118 (2006) 107–118.
- [229] J. Han, G.H. Pan, W. Sun, C.H. Wang, D. Cui, Application of nanoindentation to investigate chemomechanical properties change of cement paste in the carbonation reaction, *Sci. China Technol. Sci.* 55 (2012) 616–622.
- [230] G.Y. Marija Nedeljković, Bahman Ghiassi, Stefan Melzer, Chris Kooij, Sieger van der Laan, CO₂ binding capacity of alkali-activated fly ash and slag pastes, *Ceram. Int.* (2018).
- [231] T.L. Robl, U.M. Graham, D.N. Taulbee, W. Giles, on the long term stability of products made from dry FGD materials The effect of carbonation reactions, *ACS Div. Fuel Chem.* (1996).
- [232] J.F. Young, R.L. Berger, J. Breese, Accelerated Curing of Compacted Calcium Silicate Mortars on Exposure to CO₂, *J. Am. Ceram. Soc.* 5 (1974) 394–398.
- [233] D. Wang, Y. Fang, Y. Zhang, J. Chang, Changes in mineral composition, growth of calcite crystal, and promotion of physico-chemical properties induced by carbonation of β-C₂S, *J. CO₂ Util.* 34 (2019) 149–162.
- [234] H.Y. Sohn, J. Szekely, The effect of intragrain diffusion on the reaction between a porous solid and a gas, *Chem. Eng. Sci.* 29 (1974) 630–634.
- [235] I. Galan, C. Andrade, P. Mora, M.A. Sanjuan, Sequestration of CO₂ by concrete carbonation, *Environ. Sci. Technol.* 44 (2010) 3181–3186.
- [236] I.G. Richardson, G.W. Groves, A.R. Brough, C.M. Dobson, The carbonation of OPC and OPC/silica fume hardened cement pastes in air under conditions of fixed humidity, *Adv. Cem. Res.* 5 (1993) 81–86.
- [237] J. Grandet, Contribution à l'étude de la prise et de la carbonatation des mortiers au contact des matériaux poreux, PhD thesis. Université Toulouse III, 1975.

- [238] M. Castellote, L. Fernandez, C. Andrade, C. Alonso, Chemical changes and phase analysis of OPC pastes carbonated at different CO₂ concentrations, *Mater. Struct.* 515–525 (2009).
- [239] Association Française de Normalisation (AFNOR), NF P19-839, NF EN 16757, (2017).
- [240] S.O. Ekolü, A review on effects of curing, sheltering, and CO₂ concentration upon natural carbonation of concrete, *Constr. Build. Mater.* 127 (2016) 306–320.
- [241] C.A. García-González, A. Hidalgo, C. Andrade, M.C. Alonso, J. Fraile, A.M. López-Periago, C. Domingo, Modification of composition and microstructure of Portland cement pastes as a result of natural and supercritical carbonation procedures, *Ind. Eng. Chem. Res.* 45 (2006) 4985–4992.
- [242] DuraCrete, The European Union – Brite EuRam III. Compliance Testing for Probabilistic Design Purposes, 1999.
- [243] M. Hassoune, F. Ghomari, A. Khelidj, A. Bezzar, B. Touil, Influence des paramètres de composition et de cure sur la diffusivité des bétons à base de matériaux locaux, *Nat. Technol.* (2013) 2–9.

Appendices

1 Appendix of Paper I

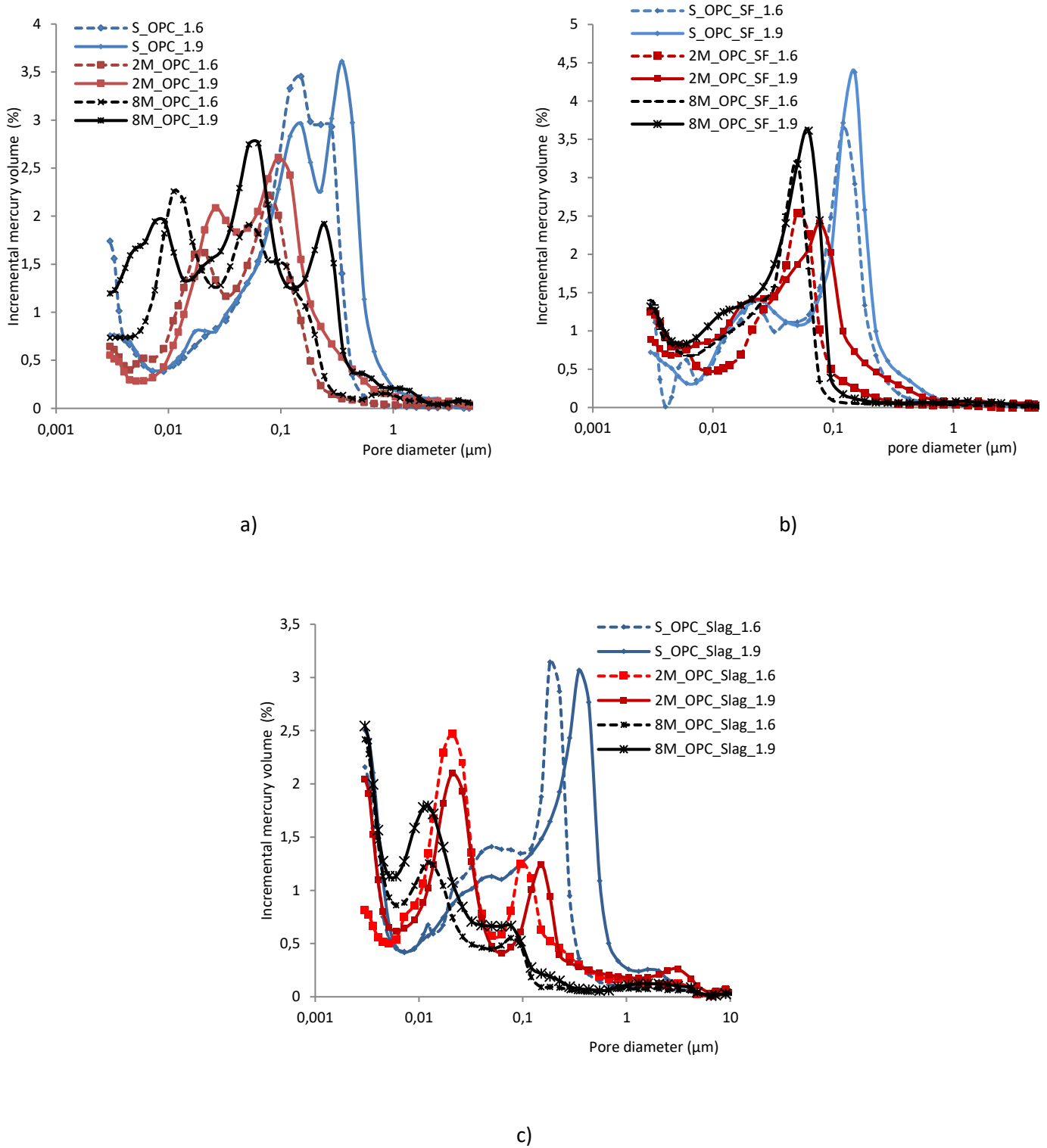


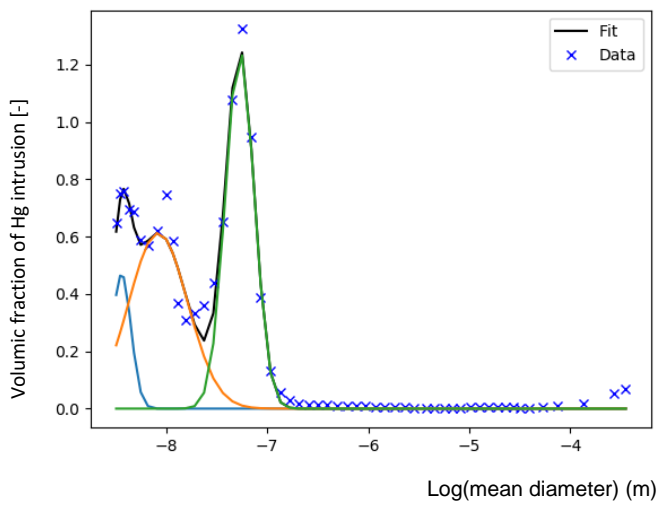
Figure 72: Pore size distribution from mercury intrusion: OPC samples. (b) OPC_Silica Fume samples and (c) OPC_Slag samples



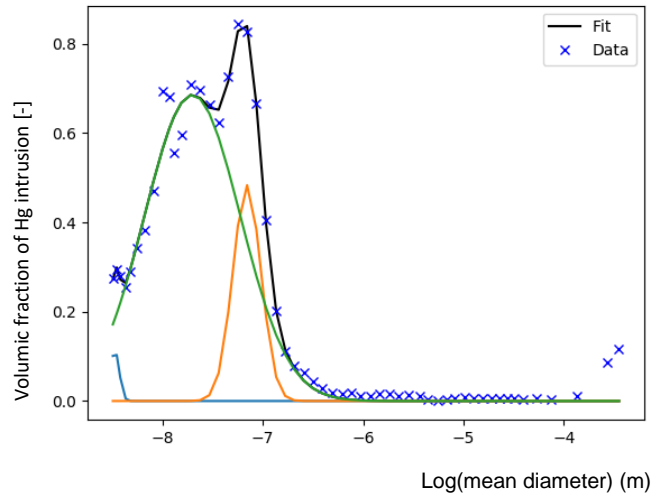
Figure 73: The preconditioning climate chamber (left) and the drying oven (80°C) (right)

2 Appendix of Paper II

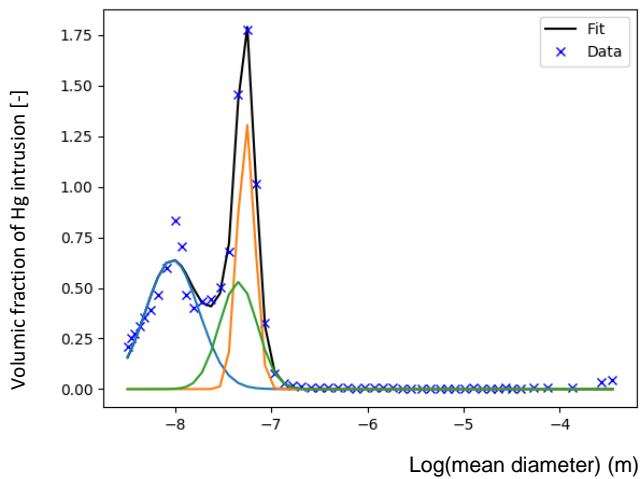
2.1 Results of the automatic fit of the MIP data



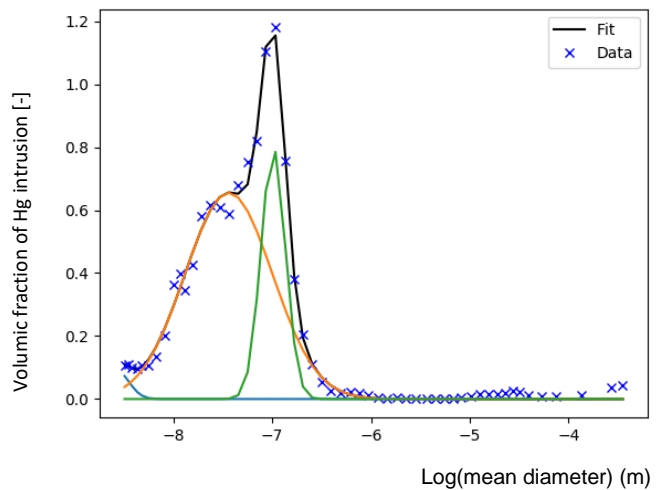
PC6_BC



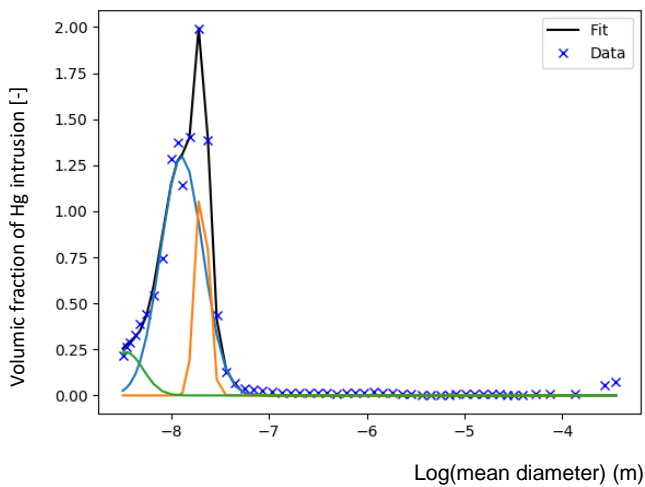
PC6_C



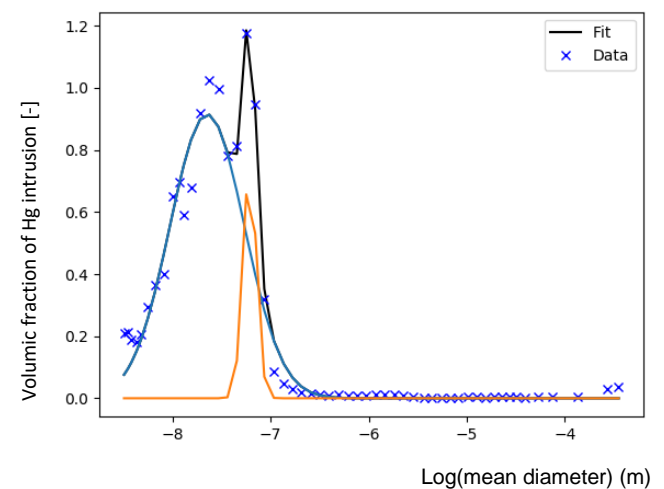
FA6_BC



FA6_C



SL6_BC



SL6_C

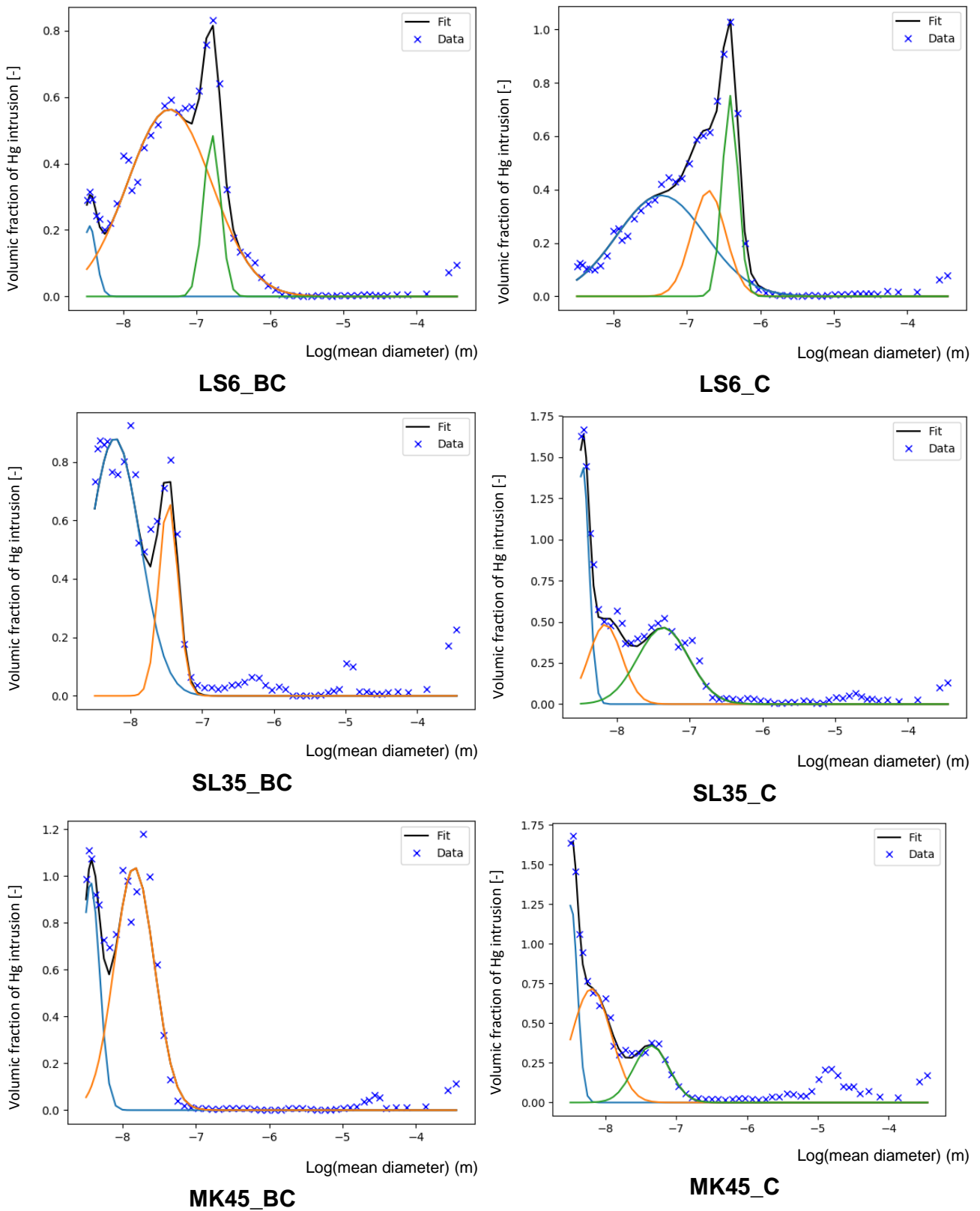


Figure 74: The automatic fit of the MIP raw data, before carbonation (BC) and after carbonation (C)

	diameter_1	diameter_2	diameter_3	Vol_fraction_1	Vol_fraction_2	Vol_fraction_3
	[m]	[m]	[m]			
S OPC_1.6	3.2 10 ⁻⁰⁹	3.2 10 ⁻⁰⁸	1.8 10 ⁻⁰⁷	0.07	0.33	0.60
S OPC_1.9	7.3 10 ⁻⁰⁹	1.7 10 ⁻⁰⁷	4.2 10 ⁻⁰⁷	0.24	0.63	0.13
S OPC+SF_1.6	3.3 10 ⁻⁰⁹	4.1 10 ⁻⁰⁸	1.4 10 ⁻⁰⁷	0.06	0.63	0.32
S OPC+SF_1.9	3.2 10 ⁻⁰⁹	4.9 10 ⁻⁰⁸	1.6 10 ⁻⁰⁷	0.05	0.65	0.30
S OPC+Slag_1.6	3.3 10 ⁻⁰⁹	6.1 10 ⁻⁰⁸	2.2 10 ⁻⁰⁷	0.18	0.62	0.20
S OPC+Slag_1.9	3.4 10 ⁻⁰⁹	9.2 10 ⁻⁰⁸	3.9 10 ⁻⁰⁷	0.18	0.59	0.23
2M OPC_1.6	3.3 10 ⁻⁰⁹	2.1 10 ⁻⁰⁸	9.3 10 ⁻⁰⁸	0.14	0.40	0.46
2M OPC_1.9	3.0 10 ⁻⁰⁹	2.6 10 ⁻⁰⁸	1.0 10 ⁻⁰⁷	0.16	0.26	0.58
2M OPC+SF_1.6	3.6 10 ⁻⁰⁹	3.9 10 ⁻⁰⁸	6.0 10 ⁻⁰⁸	0.29	0.53	0.18
2M OPC+SF_1.9	3.1 10 ⁻⁰⁹	3.5 10 ⁻⁰⁸	8.4 10 ⁻⁰⁸	0.07	0.77	0.15
2M OPC+Slag_1.6	4.4 10 ⁻⁰⁹	2.3 10 ⁻⁰⁸	1.2 10 ⁻⁰⁷	0.31	0.42	0.26
2M OPC+Slag_1.9	3.0 10 ⁻⁰⁹	2.3 10 ⁻⁰⁸	1.6 10 ⁻⁰⁷	0.31	0.49	0.20
8M OPC_1.6	3.7 10 ⁻⁰⁹	1.3 10 ⁻⁰⁸	6.6 10 ⁻⁰⁸	0.13	0.27	0.60
8M OPC_1.9	8.4 10 ⁻⁰⁹	6.4 10 ⁻⁰⁸	2.5 10 ⁻⁰⁷	0.49	0.33	0.18
8M OPC+SF_1.6	3.2 10 ⁻⁰⁹	1.7 10 ⁻⁰⁸	5.3 10 ⁻⁰⁸	0.10	0.57	0.33
8M OPC+SF_1.9	3.3 10 ⁻⁰⁹	2.1 10 ⁻⁰⁸	6.4 10 ⁻⁰⁸	0.11	0.55	0.34
8M OPC+Slag_1.6	3.3 10 ⁻⁰⁹	1.2 10 ⁻⁰⁸	8.1 10 ⁻⁰⁸	0.29	0.59	0.12
8M OPC+Slag_1.9	3.3 10 ⁻⁰⁹	1.1 10 ⁻⁰⁸	6.8 10 ⁻⁰⁸	0.24	0.57	0.19
LS6_C	3.9 10 ⁻⁰⁷	2.0 10 ⁻⁰⁷	4.5 10 ⁻⁰⁸	0.37	0.18	0.45
LS6_C	3.9 10 ⁻⁰⁷	2.0 10 ⁻⁰⁷	4.5 10 ⁻⁰⁸	0.37	0.18	0.45
LS6_NC	1.6 10 ⁻⁰⁷	4.3 10 ⁻⁰⁸	3.5 10 ⁻⁰⁹	0.32	0.64	3.8 10 ⁻⁰²
FA6_C	1.0 10 ⁻⁰⁷	3.6 10 ⁻⁰⁸	2.7 10 ⁻⁰⁹	0.40	0.57	2.2 10 ⁻⁰²
LS6_NC	1.6 10 ⁻⁰⁷	4.3 10 ⁻⁰⁸	3.5 10 ⁻⁰⁹	0.32	0.64	3.8 10 ⁻⁰²
SL6_C	6.1 10 ⁻⁰⁸	2.3 10 ⁻⁰⁸		0.32	0.68	
FA6_C	1.0 10 ⁻⁰⁷	3.6 10 ⁻⁰⁸	2.7 10 ⁻⁰⁹	0.40	0.57	2.2 10 ⁻⁰²
FA6_NC	5.4 10 ⁻⁰⁸	1.1 10 ⁻⁰⁸		0.59	0.41	
SL6_C	6.1 10 ⁻⁰⁸	2.3 10 ⁻⁰⁸		0.32	0.68	
PC6_C	2.0 10 ⁻⁰⁸	6.9 10 ⁻⁰⁸	3.4 10 ⁻⁰⁹	0.87	0.12	8.5 10 ⁻⁰³
PC6_NC	5.4 10 ⁻⁰⁸	8.3 10 ⁻⁰⁹	3.6 10 ⁻⁰⁹	0.62	0.31	7.5 10 ⁻⁰²
FA6_NC	5.4 10 ⁻⁰⁸	1.1 10 ⁻⁰⁸		0.59	0.41	
SL6_NC	1.5 10 ⁻⁰⁸			1.0		
LS6_C	3.9 10 ⁻⁰⁷	2.0 10 ⁻⁰⁷	4.5 10 ⁻⁰⁸	0.37	0.18	0.45
PC6_C	2.0 10 ⁻⁰⁸	6.9 10 ⁻⁰⁸	3.4 10 ⁻⁰⁹	0.87	0.12	8.5 10 ⁻⁰³
PC6_NC	5.4 10 ⁻⁰⁸	8.3 10 ⁻⁰⁹	3.6 10 ⁻⁰⁹	0.62	0.31	7.5 10 ⁻⁰²
SL6_NC	1.5 10 ⁻⁰⁸			1.0		
FA6_C	1.0 10 ⁻⁰⁷	3.6 10 ⁻⁰⁸	2.7 10 ⁻⁰⁹	0.40	0.57	2.2 10 ⁻⁰²
MK45_NC	1.5 10 ⁻⁰⁸	3.7 10 ⁻⁰⁹		0.85	0.15	
SL35_NC	3.4 10 ⁻⁰⁸	6.1 10 ⁻⁰⁹		0.55	0.45	
SL35_C	4.3 10 ⁻⁰⁸	7.0 10 ⁻⁰⁹	3.4 10 ⁻⁰⁹	0.77	0.11	0.12
MK45_C	4.5 10 ⁻⁰⁸	6.4 10 ⁻⁰⁹	3.3 10 ⁻⁰⁹	0.73	0.17	9.8 10 ⁻⁰²
LS6_NC	1.6 10 ⁻⁰⁷	4.3 10 ⁻⁰⁸	3.5 10 ⁻⁰⁹	0.32	0.64	3.8 10 ⁻⁰²
MK45_NC	1.5 10 ⁻⁰⁸	3.7 10 ⁻⁰⁹		0.85	0.15	
SL35_C	4.3 10 ⁻⁰⁸	7.0 10 ⁻⁰⁹	3.4 10 ⁻⁰⁹	0.77	0.11	0.12
PC6_C	2.0 10 ⁻⁰⁸	6.9 10 ⁻⁰⁸	3.4 10 ⁻⁰⁹	0.87	0.12	8.5 10 ⁻⁰³
SL6_C	6.1 10 ⁻⁰⁸	2.3 10 ⁻⁰⁸		0.32	0.68	
MK45_C	4.5 10 ⁻⁰⁸	6.4 10 ⁻⁰⁹	3.3 10 ⁻⁰⁹	0.73	0.17	9.8 10 ⁻⁰²
SL35_NC	3.4 10 ⁻⁰⁸	6.1 10 ⁻⁰⁹		0.55	0.45	
SL35_C	4.3 10 ⁻⁰⁸	7.0 10 ⁻⁰⁹	3.4 10 ⁻⁰⁹	0.77	0.11	0.12

PC6_NC	$5.4 \cdot 10^{-08}$	$8.3 \cdot 10^{-09}$	$3.6 \cdot 10^{-09}$	0.62	0.31	$7.5 \cdot 10^{-02}$
FA6_NC	$5.4 \cdot 10^{-08}$	$1.1 \cdot 10^{-08}$		0.59	0.41	
MK45_C	$4.5 \cdot 10^{-08}$	$6. \cdot 10^{-09}$	$3.3 \cdot 10^{-09}$	0.73	0.17	$9.8 \cdot 10^{-02}$
SL6_NC	$1.5 \cdot 10^{-08}$			1.0		
MK45_NC	$1.5 \cdot 10^{-08}$	$3.7 \cdot 10^{-09}$		0.85	0.15	
SL35_NC	$3.4 \cdot 10^{-08}$	$6.1 \cdot 10^{-09}$		0.55	0.45	

Table 39: Summary of the MIP results

2.2 Composition of the raw materials



ARGICAL™ - M 1000

METAKAOLIN (NORME NF P18-513)

ARGICAL-M 1000 is an artificial pozzolan (metakaolin). It is obtained by calcining and micronising a kaolinitic clay from the Charentes basin.

ARGICAL-M 1000 is a dehydroxylated aluminium silicate. Its general formula is $Al_2O_3 \cdot 2SiO_2$. It is an amorphous non-crystallised material, constituted of lamellar particles.

APPLICATION

Additive for concretes, mortars and coatings, made from Portland cement or lime.

CHEMICAL ANALYSIS (% on fired)

SiO ₂	55
Al ₂ O ₃	40
K ₂ O + Na ₂ O	0,8
Fe ₂ O ₃	1,4
TiO ₂	1,5
CaO + MgO	0,3
Loss on ignition	1

PHYSICAL PROPERTIES

Pozzolanic index (Chapelle test)	1100 mg Ca(OH) ₂ /g	
Brightness	L*: 90	
Specific area (BET)	17 m ² /g	
Specific gravity	2,4 g/cm ³	
Bulk density	LOOSE	TAMPED
	400 kg/m ³	800 kg/m ³

PARTICLE SIZE DISTRIBUTION

> 200 μm	0,5%
> 100 μm	3%
> 63 μm	10%
	d50 = 6 μm

Revision 1 - 2014 July

The technical information and specifications contained in this data sheet are only for information purposes. These information and specifications can be modified and do not constitute nor could be constitutive or be interpreted as a representation and/or as a warranty of the validity of the information and specifications specified. The general terms and conditions of sale, available on our website or upon request from our customer service, apply to the sale of our products.



IMERYS REFRACTORY MINERALS
17 270 Clérac - FRANCE

Tel: +33(0)5.46.04.17.11
E.mail: refractory.minerals@imerys.com



www.imerys-refractoryminerals.com

Figure 75: Metakaolin composition and properties

FICHE TECHNIQUE

Fabriqué à LUMBRES

Mise à jour du 19/12/2014

Ciment Portland

<i>NF EN 197-1/A1</i>	CEM I 52,5 N N° de certificat : 0333-CPR-2701	01/06/2001
<i>CE+NF</i>	CEM I 52,5 N CE CP2 NF	05/02/1998
<i>NF P15-318</i>	Ciments à teneur en sulfures limitée pour béton précontraint	CP2
<i>CE+BENOR</i>	CEM I 52,5 N CE HES BENOR N° de certificat : 15/33/239	13/09/2000
<i>NBN B12-110</i>	Ciment Portland à haute résistance initiale	HES

Disponibilités : Sac 25 kg, Vrac

COMPOSITION DÉCLARÉE (en %)

<u>Constituant</u>		<u>Régulateur de prise</u>	
Clinker (K)	97	Gypse	5,0
Laitier de haut-fourneau (S)	-	Anhydrite	-
Schiste calciné (T)	-	Autre sulfate de calcium	-
Sulfate de calcium (Cs)	-		
Pouzzolanes naturelles (P)	-	<u>Additif</u>	
Cendres volantes siliceuses (V)	-	Agent de mouture CXN2	0,06
Cendres volantes calciques (W)	-	Sulfate ferreux	0,25
Calcaires (L ou LL)	-		
Constituants secondaires	3		

RESISTANCES A LA COMPRESSION (en MPa)

1 jour **24** 2 jours **37** 7 jours **—** 28 jours **60**

CARACTÉRISATION PHYSIQUE

<u>Sur poudre</u>	<u>Sur pâte pure</u>	<u>Sur mortier</u>
Masse volumique (en g/cm ³) 3,09	Besoin en eau (en %) 30,5	Chal. hydr. 4h (en J/g) —
Surface massique (en cm ² /g) 4600	Stabilité (en mm) 0,5	
Indice de clarté 66,5	Début de prise (en min) 160	

CARACTÉRISATION CHIMIQUE (en %)

PAF	INS	SiO ₂	Al ₂ O ₃	Fe ₂ O ₃	CaO	MgO	SO ₃	K ₂ O	Na ₂ O	S ⁻	Cl ⁻	CO ₂	CaO _{libre}	Na ₂ O éq actif
1,8	0,5	20,1	5,2	3,3	64,1	0,8	3,0	0,76	0,28	0,01	0,07	1,0	1,7	0,78

Composition potentielle du clinker : C3A **8,6** C3S **61** C4AF **11,1**



La reproduction partielle ou intégrale de ce document est interdite sans accord préalable de notre part. Les résultats faisant l'objet du présent document sont basés sur des valeurs moyennes et sont donnés à titre purement indicatif. Etant susceptibles de varier dans les limites autorisées par les normes correspondantes, ils ne sauraient engager la responsabilité de Holcim France ou Holcim Belgique.

Figure 76: CEM I 52.5 N



FICHE TECHNIQUE CIMENT PERFORMAT

CIMENT

FTMO2.1522

Mise à jour : 01/02/2015

Page 1/1

Produit : **CEM I 52,5 N CE PM-CP2 NF**
Usine : **Montalieu (38)**

Caractéristiques physiques et mécaniques

	Masse Volumique (g/cm ³)	Finesse Blaine (cm ² /g) / Diamètre médian (µm)	Clarté L*	Demande en eau (%)	Temps de début de prise (min)	Expansion (mm)	Chaleur d'hydratation à 41h (J/g)	Résistance en compression (MPa)			
								1j	2j	7j	28j
Moyenne	3,13	4090 / 12,4	60,6	28,0	138	1,5	312	22	34	48	59
Ecart type	*	160 / 0,4	*	0,7	20	0,8	10	1,8	1,7	1,7	1,8
Limites	CE	*	*	*	≥ 40	≤ 10	*	*	≥ 18	*	≥ 50
	NF	*	*	*	≥ 60	≤ 5	*	*	≥ 18	*	≥ 50

Caractéristiques chimiques

(%)	Moyenne	Ecart type	Limites	
			CE	NF
Alcalins eq. actifs (Na ₂ O eq. actifs)	0,86	0,03	*	*
Perte au feu 950°C	1,99	*	≤ 5,0	≤ 5,0
MgO	2,01	*	*	≤ 3,0
Al ₂ O ₃	4,59	*	*	≤ 8,0
SO ₃	2,88	*	≤ 4,5	≤ 3,0
Cl ⁻	0,04	*	≤ 0,10	≤ 0,10
S ²⁻	0,01	*	*	≤ 0,2
Résidu insoluble	0,46	*	≤ 5,0	≤ 5,0
C ₃ A	6,4	*	*	≤ 8,0
C ₃ A+0,27x C ₃ S	20,8	*		≤ 23,5

Composition hors gypse et caractéristiques des constituants

Constituant	Teneur (%)	Caractéristiques (%)			
		C ₃ S	C ₂ S	C ₃ A	C ₄ AF
Clinker	99				
		53,1	21,6	7,2	10,8
Calcaire	*	*	*	*	*
Laitier	*	*	*	*	*
Constituants Secondaires	1	*	*	*	*

Certificat CE et Marque NF-LH

Certificat CE	N° 0333-CPR-3302
Marque NF-Liant Hydraulique	N°33.54 du 02.07.2014

Les valeurs indiquées sont des valeurs moyennes, elles peuvent varier légèrement dans les limites autorisées par les normes.
Le succès des travaux entrepris avec ce ciment reste naturellement conditionné par le respect des règles de bonne pratique en matière de préparation, de mise en oeuvre et de conservation des mortiers et bétons.
Le ciment contient un agent réducteur de chrome hexavalent soluble afin de satisfaire à la réglementation en vigueur.

VICAT - DIRECTION COMMERCIALE CIMENT - 4, RUE ARISTIDE BERGÈS - BP 137 - LES TROIS VALLONS
38081 L'ISLE D'ABEAU CEDEX TEL : +33 (0)4 74 18 41 00 - FAX : +33 (0)4 74 18 40 18

Figure 77: CEM I 52.5 N CE PM



Omya International AG
 P.O. Box 335
 CH-4665 Oftringen
 +41 62 789 29 29
 +41 62 789 20 77
 www.omya.com

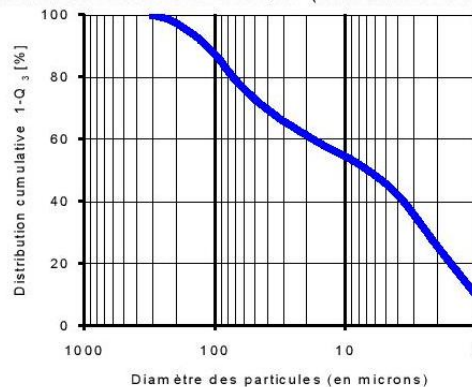
Betocarb® - GY

SITE:	GY, France	
DESCRIPTION DU PRODUIT:	Addition calcaire de catégorie A-FM selon la norme NF P 18-508 pour bétons hydrauliques. Utilisable en tant que filler pour bétons hydrauliques hautes performances (EN 12620+ A1).	
COMPOSITION DU PRODUIT:	CaCO ₃	95 %
	Carbonates totaux	96 %
	Chlorures	0.0008 %
	Sulfates	0.003 %
	Soufre total	0.05 %
	Matières organiques	0.05 %
	Essai au bleu de méthylène	1.5 g/kg
	Alcalins équivalents	0.02 %
	Silice totale	1 %
	Réactivité aux alcalins	NR
CARACTERISTIQUES TYPES DU PRODUIT:	Granulométrie:	
	- Particules < 2 mm	100 %
	- Particules < 0.125 mm	91 %
	- Particules < 0.063 mm	77 %
	Surface spécifique Blaine (DIN 66126)	596 m ² /kg
	Indice d'activité à 28 jours	0.77
	Taux d'humidité départ usine (ISO 787-2)	0.2 %
CARACTERISTIQUES GENERALES DU PRODUIT:	Densité (ISO 787-10)	2.7 g/ml
	Densité apparente tassée (ISO 787-11)	1.5 g/ml

APPLICATIONS PRINCIPALES:

- Produits en béton
 - Pavés
 - Blocs
 - Autres produits
- Béton prêt à l'emploi
- Éléments préfabriqués

REPARTITION GRANULOMETRIQUE (Malvern Mastersizer 2000):



CONDITIONNEMENT STANDARD:

- VRAC
- SAC (papier) de 25 kg sur palette

Les informations contenues dans cette fiche technique ne concernent que le matériel spécifique mentionné et ne concernent pas l'utilisation conjointement avec tout autre matériel ou dans tout procédé. Les informations fournies dans le présent document se basent sur des données techniques qui, à la connaissance de Omya, sont fiables, toutefois Omya ne fournit aucune garantie de complétude ou d'exactitude de ces informations, et Omya n'assume aucune responsabilité résultant de leur utilisation ou vis-à-vis de toutes réclamations, pertes ou dommages subis par une tierce partie. Toute personne recevant ces informations doit exercer son jugement propre en ce qui concerne leur utilisation appropriée et il incombe à l'utilisateur d'évaluer si le matériel convient (y compris en matière de sécurité) pour un usage particulier avant d'en faire usage.

édition : 04.05.2015
 Product Information :
 S08.03.01_FR_CORPFRGY
 I28002_02_F
 version : 14

Figure 78: Limestone addition composition

1. DEFINITION

Ecocem, le laitier granulé de haut fourneau moulu CE produit par ECOCEM France à Fos sur Mer (13), répond à la norme européenne NF EN 15167-1, 2006 : Laitier granulé de haut-fourneau moulu pour utilisation dans le béton, mortier et coulis - Partie 1 : définitions, exigences et critères de conformité.

Le certificat CE de constance des performances 1164-CPR-LGM001, a été renouvelé le 10 Janvier 2014, par le CERIB, organisme notifié n°1164.

Ecocem est un laitier moulu de classe A, suivant les distinctions faites dans la norme NF EN 206/CN, classe confirmée, en date du 28 Juin 2013, par le CERIB.

2. FABRICATION

Ecocem est produit par le séchage et le broyage du laitier granulé de haut-fourneau.

Le laitier granulé est obtenu par trempage à l'eau du laitier à la sortie des hauts-fourneaux de Fos sur Mer, au moyen de granulateur de nouvelle génération (INBA®).

Le taux de vitrification moyen obtenu est supérieur à 90% (mesure par diffraction de rayons X).

Ecocem est livré en vrac.

3. COMPOSITION CHIMIQUE (centésimale moyenne)

CaO	43,7	Fe₂O₃	0,5	Na₂O	0,25
SiO₂	37,4	TiO₂	0,6	K₂O	0,36
Al₂O₃	10,8	SO₃	0,1	Na₂O éq.	0,49
MgO	6,5	S²⁻	0,8	Cl⁻	0,01

Module chimique (CaO+MgO)/SiO₂ : > 1,25 (≥1,2 : classe A selon NF EN 206-1/CN)

4. CARACTERISTIQUES PHYSIQUES (valeurs indicatives représentatives)

FORMULATION		Résistances en Compression (MPa)			Indice d'activité			Temps de prise initial (min)
Ecocem	Ciment référence	7 jrs	28 jrs	90 jrs	7 jrs	28 jrs	90 jrs	
0%	100%	45	56	65	-			140
50%	50%	32	57	72	71%	102%	111%	165
<i>Limites de la Norme produit NF EN 15167-1</i>					≥ 45%	≥ 70%	-	< 2 × Tps Ciment
<i>Limites Classe A selon Norme NF EN 206/CN</i>					≥ 65%	≥ 85%	-	-

5. AUTRES CARACTERISTIQUES

Surface spécifique Blaine : 4450 ± 250 cm²/g
 ≥ 2750 cm²/g : NF EN 15167-1
 ≥ 4200 cm²/g : classe A selon NF EN 206/CN

Passant à 32 µm : ≥ 95%
 Diamètre médian indicatif (d50) : 11µm

Indice [CIE L*ab] avec CR410, L* = 89,5 ± 2
 Perte au feu (950°C) : < 1,5 %
 Humidité (100°C) : < 0,5%
 Masse volumique (g/cm³) : 2,90 ± 0,03
 Densité apparente : 0,8 ± 0,1

Les valeurs indiquées sont des valeurs moyennes, elles peuvent varier légèrement dans les limites autorisées par la norme de référence.

Figure 79: Slag composition

Silicoline®

Déclaration de performances


Centrale : **GARDANNE CENTRALE DE PROVENCE**
Dénomination et Tranche : **Silicoline® GARD 5**

- 1- Code d'identification du produit type : Cendres volantes pour béton **catégorie A - classe N**
- 2- Identification de produit de construction :
- 3- Usages prévus : Préparation de béton, coulis et autres mélanges destinés à la construction et à la fabrication de produits de construction.
- 4- Nom et adresse du fabricant : Centrale thermique du groupe ECN - 5 rue d'Athènes 75009 PARIS
Nom et adresse du fournisseur : Société SURSCHISTE - 33 rue Auguste Mariette- ZI la Croisette -62300 LENS
- 5- Nom et adresse du mandataire : -
- 6- Système d'évaluation et de vérification de la constance des performances : **système 1+**
- 7- Dans le cas de la déclaration des performances concernant un produit de construction couvert par une norme harmonisée :
L'organisme notifié de certification du produit Be-CERT (numéro d'identification N°. 0965), selon le système 1+, délivre le certificat de constance des performances du produit en réalisant la détermination du produit type sur la base d'essais type (y compris l'échantillonnage), une inspection initiale de l'établissement de fabrication et de contrôle de la production en usine, une surveillance et une appréciation permanentes du contrôle de la production en usine, des essais par sondage sur des échantillons prélevés avant de mettre le produit sur le marché.

Produit : Cendres Volantes silico-alumineuses issues de la combustion du charbon "houille" en Centrale Thermique

8 - Performance déclarée				
Suivi du produit selon les critères de la norme EN 450-1-2012				
Propriété	Fréquence minimale d'essai en période de disponibilité de produits	Norme d'essai utilisée	classe	Valeur
Finesse : (refus à 45 µm)	1/jour	EN 451-2 Tamisage humide NF X11-640 Méthode Alpine	N	< 40 %
masse volumique	1/mois	EN 196-6		+/-200 kg/m ³
Indice d'activité 28 j	2/mois	EN 196-1		> 75 %
Indice d'activité 90j	2/mois	EN 196-1		> 85 %
Perte au feu	1/jour	EN 196-2	A	< 5 %
Taux de carbone	base statistique	NF P 10 694	B	0 à 7 %
			C	0 à 9 %
Teneur en chlorures	1/mois	EN 196-2		< 0,10 %
Teneur en SO ₃	1/mois	EN 196-2		< 3 %
Teneur en oxyde de calcium	1/mois	EN 196-2 - ICP - fluorescence x		< 10 %
Teneur en oxyde de calcium réactif	si oxyde de calcium > 10 %	EN 197-1-2000 § 3.1		< 10 %
Teneur en CaO libre	1/semaine ou 1/mois*	EN 451-1		< 1 % et < 2,5 %
Stabilité	si CaO libre > 1%	EN 196-3		< 10mm

* si les 10 derniers < 0,5% et si le charbon ne varie pas

 <p>N° CERTIFICATION Be-CERT 0965-CPR-V-115</p>	CARACTÉRISTIQUES DU PRODUIT valeurs listées période du : 01/10/14 au 30/09/15	
	Valeurs	
FINESSE	CLASSE	N
PERTE AU FEU	CATEGORIE	A
MASSE VOLUMIQUE DECLARÉE = masse volumique réelle		2210 kg / m ³
pour info : masse volumique apparente (en vrac) = 700 à 900 kg/m ³		
FINESSE DECLARÉE refus à 45µm		26%
	Teneur en chlorures (en %)	0,009
	Teneur en SO ₃ (en %)	0,58
	Teneur en CaO libre (en %)	0,68
	Teneur en CaO Total (en %)	5,08
	Teneur en CaO réactif si CaO T > 10 %	-
	SiO ₂ -Al ₂ O ₃ -Fe ₂ O ₃ en %	83,45
	Stabilité (fait si CaO libre > 1%)	-
	Na ₂ O total équivalent (%)	1,51

- 9- Les performances du produit identifié aux point 1 et 2 sont conformes aux performances déclarées au point 8.
La présente déclaration des performances est établie sous la seule responsabilité du fournisseur identifié au point 4.

Informations commerciales :
Indices d'activité
(EN 206-1 § 5.2.5.2.2 - Règlement NF BPE chapitre 2.2.5.4 tableau 3)

en %	mars15	avril15	mai15	juin15	juil15	août15	sept15	Bilan alcalin mai 2015	ALCALINS			
									TOTAUX			Na ₂ O Solubles équivalents
								Na ₂ O %	K ₂ O %	Na ₂ O equiv		
i 28	89,00	88,10	91,40	90,40	91,60	89,60	89,30		0,31	1,66	1,40	0,0538
i 90	103,80	100,70	106,70	107,20	108,50							

Cette fiche technique est utilisable pour les contrôles qualité par nos clients utilisant nos produits, le bon de livraison faisant foi

Signé par le fabricant et en son nom par :
Service Technique : Mise à jour le 10/11/2015

SURSCHISTE SIEGE
ZI LA CROISSETTE
33 Rue Auguste Mariette
62 300 LENS

Tel. : 03 21 45 73 73
Fax. : 03 21 45 73 70
email : siege@surschiste.com
site internet : www.surschiste.com



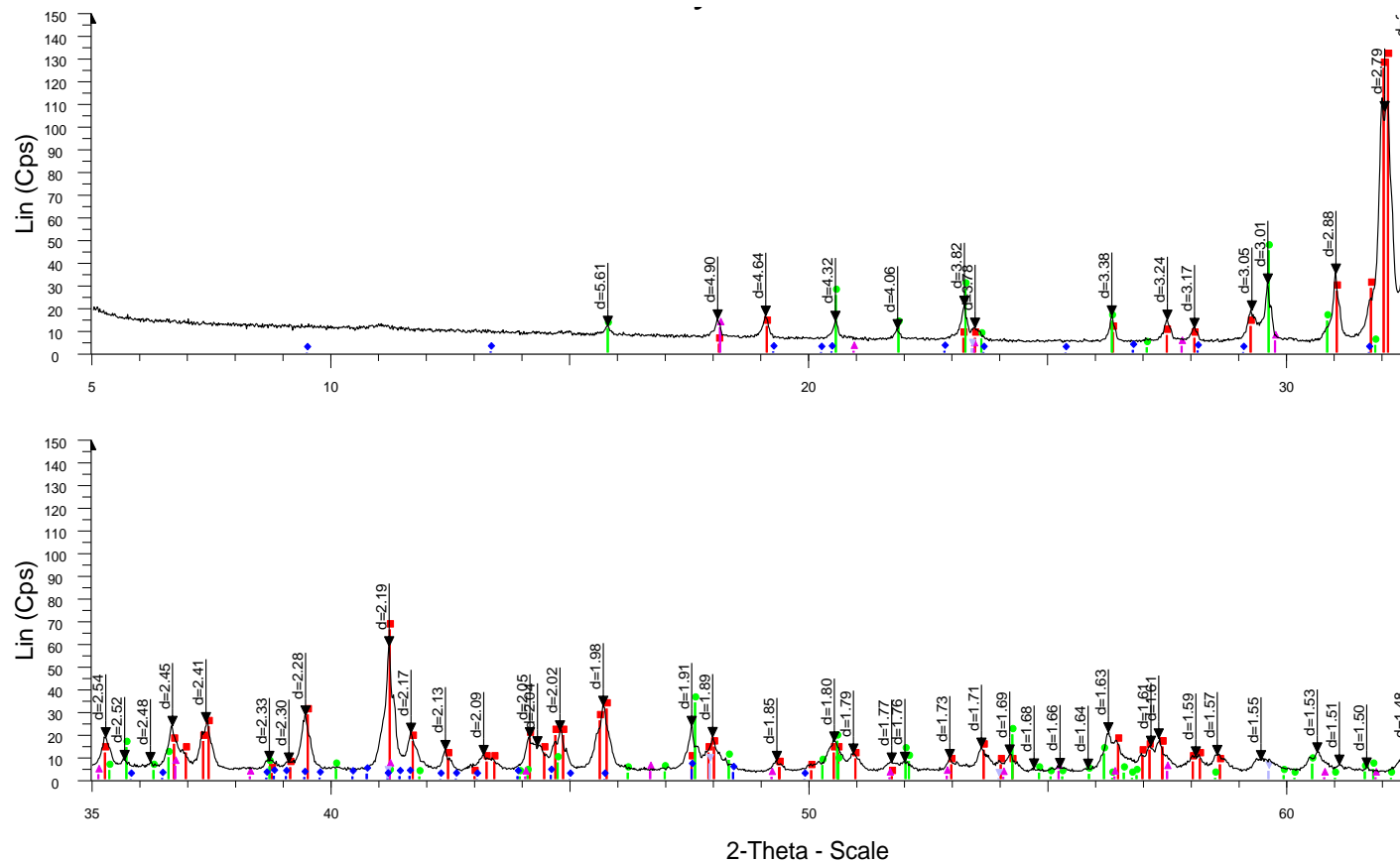
Figure 80: Fly ash composition

3 Appendix of Paper III

	Ca ₂ SiO ₄	Ca ₃ SiO ₅	Ca ₃ Al ₂ O ₆	CaSO ₄ .2H ₂ O	Ca(OH) ₂	Ca ₆ Al ₂ (SO ₄) ₃ (OH) _{1,2-2,6} H ₂ O	And / or	Ca ₆ (Al(OH) ₆) ₂ (SO ₄) ₃ (H ₂ O) _{2,5.7}	CaCO ₃	CaMg(CO ₃) ₂	SiO ₂	Al ₂ SiO ₅	CaCO ₃		Ca ₂ MgSi ₂ O ₇	KAlSiO ₄	₂ MgO· ₂ Al ₂ O ₃ -5SiO ₂	gamma-Ca ₂ SiO ₄	KFe ₃ (SO ₄) ₂ (OH) ₆	(Ca.Na)(Si.Al) ₄ O ₈	Na ₇ Al ₆ Si ₆ O ₂ ₄ S ₃	Ca(Fe _{1.4} Al _{0.6})SiO ₆		
	Larnite	Calcium Silicate	Calcium Aluminum Oxide	Gypsum	Portlandite		Ettringite		Calcite	Dolomite	Cristobalite	Sillimanite	Vaterite	tobermorite	Akermanite	Kaliophilite	Cordierite	Calcium Silicate	Jarosite	Anorthite	Lazurite	Esseneite	amorphous	
C3S triclinic	★	✓	-	-	-	-	-	★	★	-	-	-	-	-	-	-	-	-	-	-	-	-	-	-
C ₂ S Béta	✓	★	-	-	★	-	-	★	★	-	-	★	-	-	-	-	-	-	-	-	-	-	-	-
C3A Cubic	-	-	✓	-	-	-	-	-	-	-	-	★	-	-	-	-	-	-	-	-	-	-	-	-
Ettringite	-	-	★	★	★	✓	-	★	★	★	★	★	-	-	-	-	-	-	-	-	-	-	-	-
Portlandite	-	-	-	-	✓	-	-	-	-	-	-	-	★	-	-	-	-	-	-	-	-	-	-	-
C-S-H0.9	-	-	-	-	-	-	-	★	-	-	-	-	-	✓	-	-	-	-	-	-	-	-	-	✓

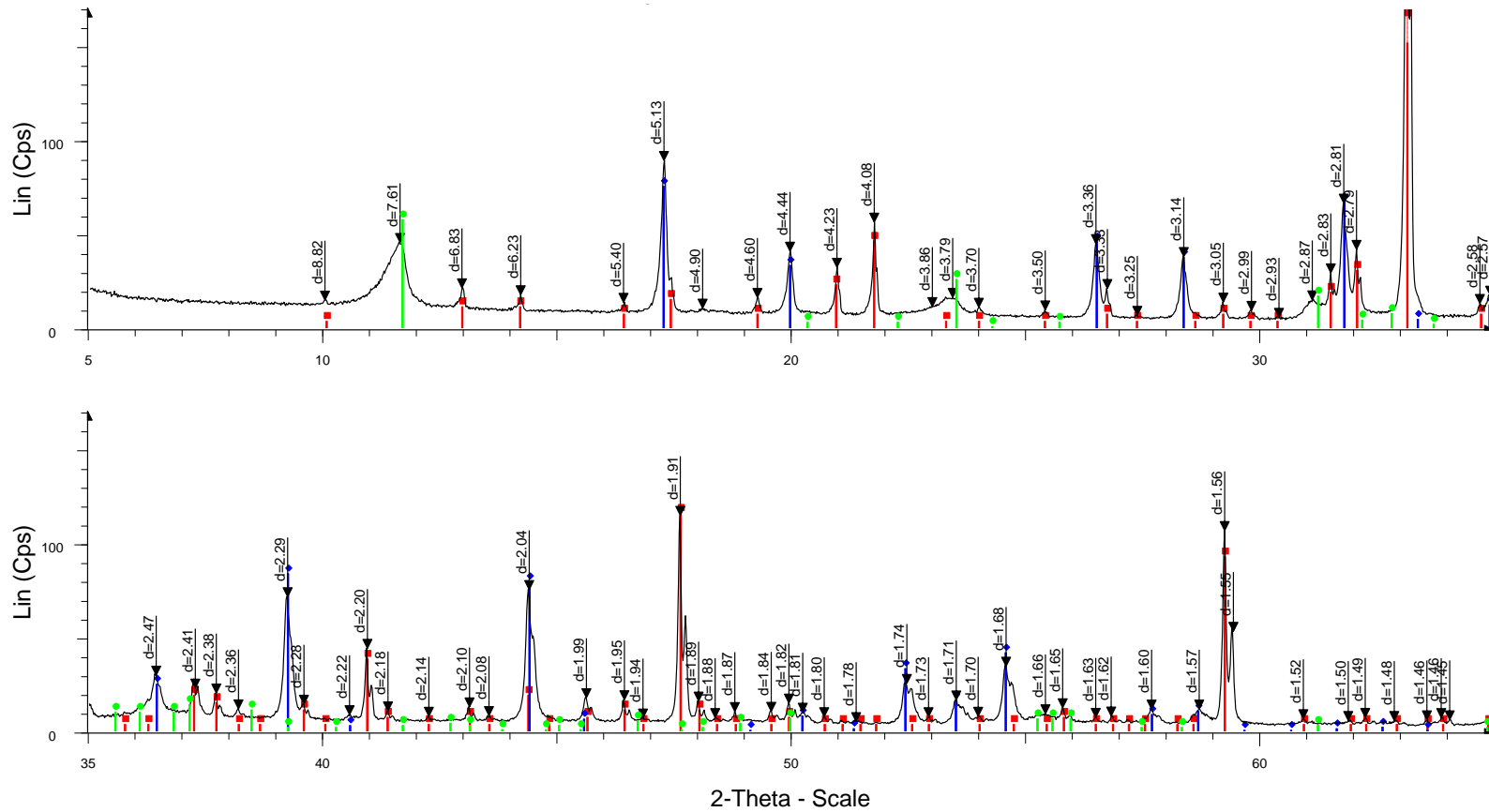
✓: Existing phase (very high probability) , ★: Possibly existing phase , -: Non-detected phase

Table 40 : XRD qualitative results after the synthesis of CH, C-S-H, Aft, C₃A, C₃S and C₂S



C2S hydraté à 93% - File: PLA-18-05154-T (1801169).raw - Type: 2Th/Th locked - Start: 5.000 ° - End: 64.993 ° - Step: 0.017 ° - Step time: 59.7 s - Temp.: 25 °C (Room) - Time Started: 0 s - 2-Theta: 5.00
 Operations: Import
 00-033-0302 (*) - Larnite, syn - Ca₂SiO₄ - Y: 98.24 % - d x by: 1. - WL: 1.54056 - Monoclinic - a 9.31000 - b 6.75650 - c 5.50590 - alpha 90.000 - beta 94.460 - gamma 90.000 - Primitive - P21/n (14) - 4 - 2
 00-031-0297 (*) - Calcium Silicate - Ca₂SiO₄ - Y: 42.76 % - d x by: 1. - WL: 1.54056 - 0 -
 00-035-0591 (*) - Merwinite, syn - Ca₃Mg(SiO₄)₂ - Y: 9.43 % - d x by: 1. - WL: 1.54056 - 0 -
 00-009-0413 (*) - Mayenite, syn - Ca₁₂Al₁₄O₃₃ - Y: 8.92 % - d x by: 1. - WL: 1.54056 - 0 -
 01-075-2100 (C) - Perovskite - CaTiO₃ - Y: 10.65 % - d x by: 1. - WL: 1.54056 - Cubic - a 3.79500 - b 3.79500 - c 3.79500 - alpha 90.000 - beta 90.000 - gamma 90.000 - Primitive - Pm-3m (221) - 1 - 54.6

Figure 81 : C₂S Experimental x-ray diffraction spectra obtained on anhydrous powders preconditioned at 93%RH during 32 days in low-CO₂ concentration



C3A hydraté à 95%RH - File: PLA-18-04989-T 1801119.raw - Type: 2Th/Th locked - Start: 5.000 ° - End: 64.993 ° - Step: 0.017 ° - Step time: 59.7 s - Temp.: 25 °C (Room) - Time Started: 0 s - 2-Theta: 5.000 ° - Theta:

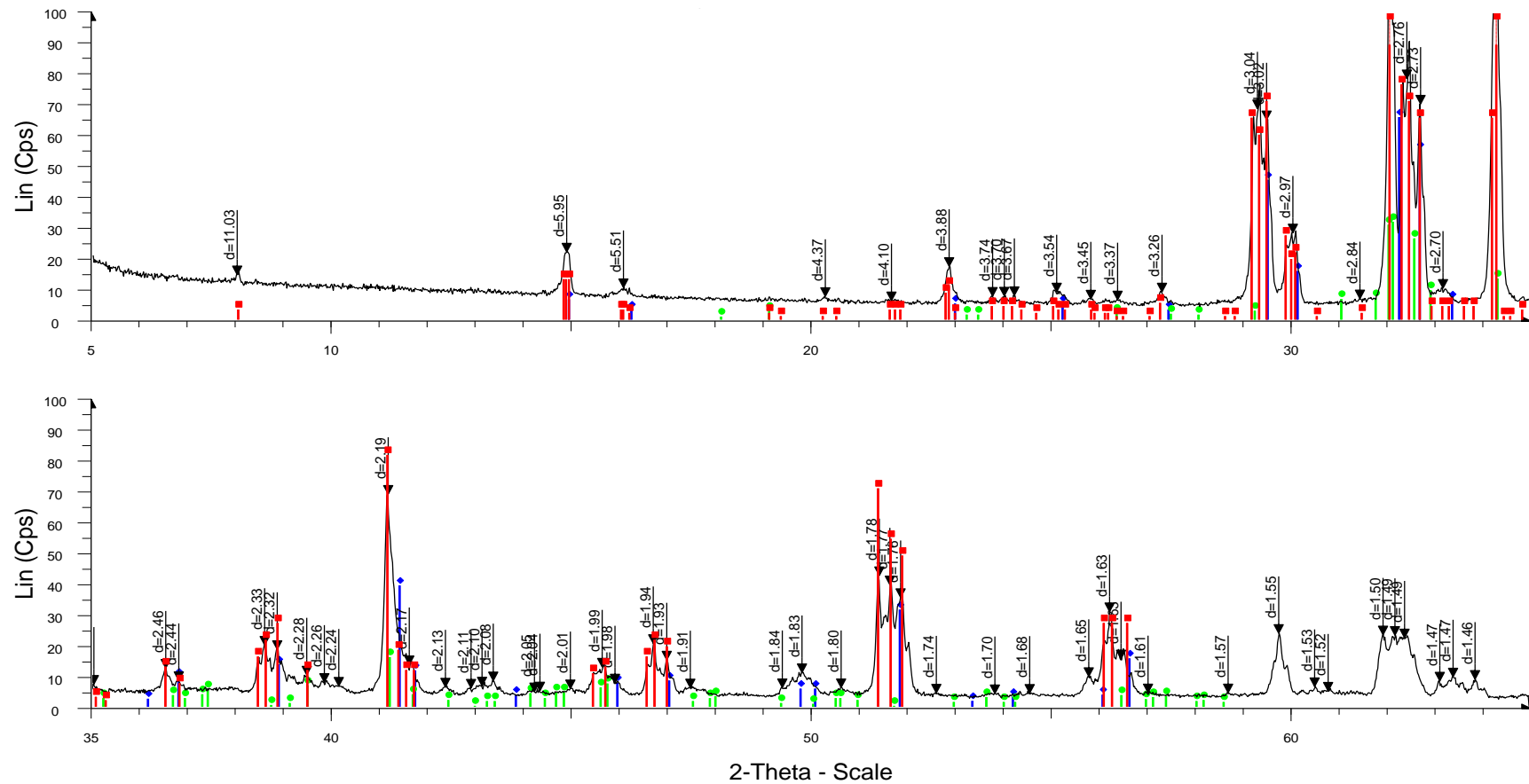
Operations: Import

00-038-1429 (*) - Calcium Aluminum Oxide tricalcium aluminate - Ca3Al2O6 - Y: 100.98 % - d x by: 1. - WL: 1.54056 - 0 -

00-024-0217 (*) - Katoite, syn - Ca3Al2(OH)12 - Y: 21.91 % - d x by: 1. - WL: 1.54056 - 0 -

00-014-0083 (D) - Calcium Aluminum Oxide Carbonate Hydrate - Ca4Al2CO9.11H2O - Y: 15.10 % - d x by: 1. - WL: 1.54056 - 0 -

Figure 82 : C₃A Experimental x-ray diffraction spectra obtained on anhydrous powders preconditioned at 93%RH during 32 days with low CO₂ concentration (lower than 10ppm)



C3S hydraté à 95% - File: ECH-1800126 (1801139).raw - Type: 2Th/Th locked - Start: 5.000 ° - End: 64.993 ° - Step: 0.017 ° - Step time: 59.7 s - Temp.: 25 °C (Room) - Time Started: 0 s - 2-Theta: 5.000 ° - Theta: 2.5
 Operations: Import
 00-031-0301 (*) - Calcium Silicate - Ca₃SiO₅ - Y: 65.39 % - d x by: 1. - WL: 1.54056 - 0 -
 99-090-0001 (U) - C3S MONOCLINIQUE - 3CaO.SiO₂ - Y: 39.37 % - d x by: 1. - WL: 1.54056 - 0 -
 00-033-0302 (*) - Larnite, syn - Ca₂SiO₄ - Y: 19.03 % - d x by: 1. - WL: 1.54056 - 0 -

Figure 83: XRD results of C₃S powder conditioned at different RH in a CO₂-low environment

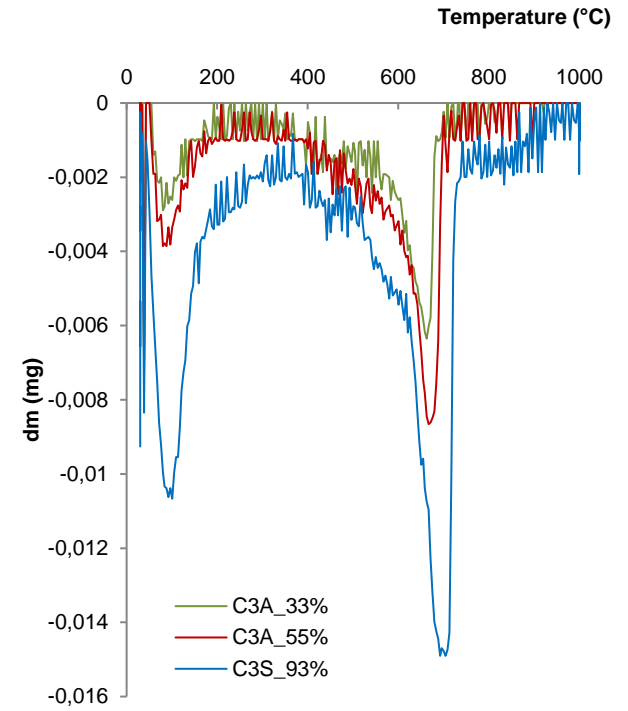
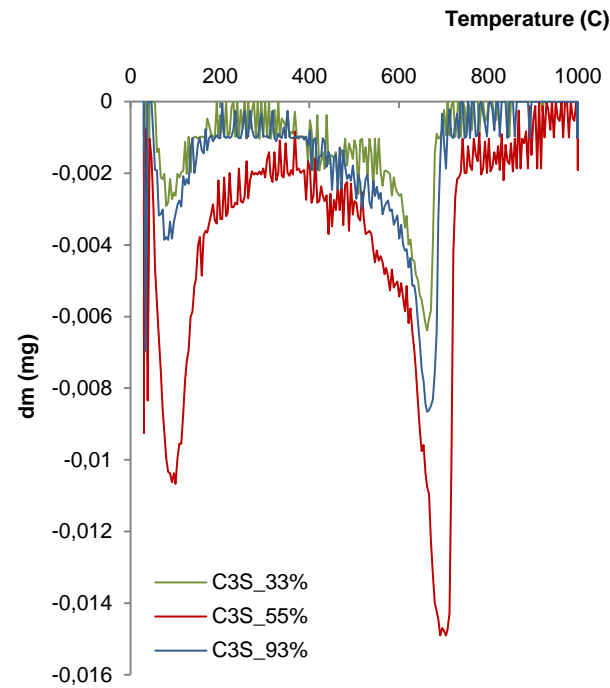
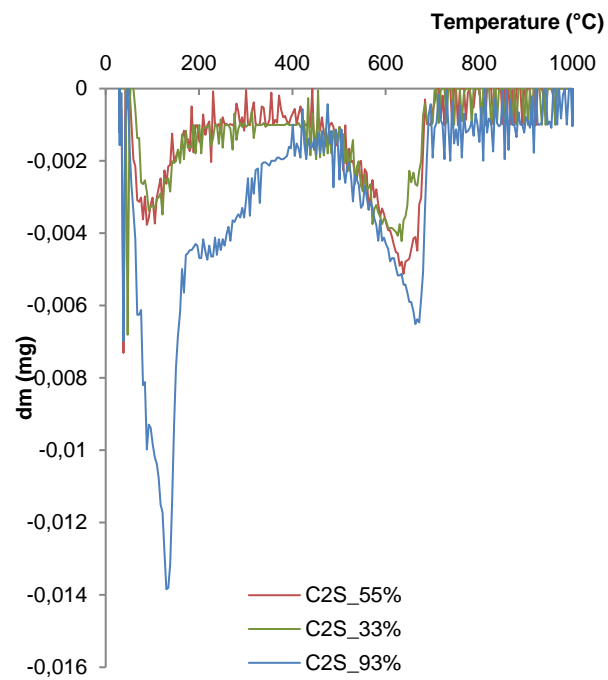
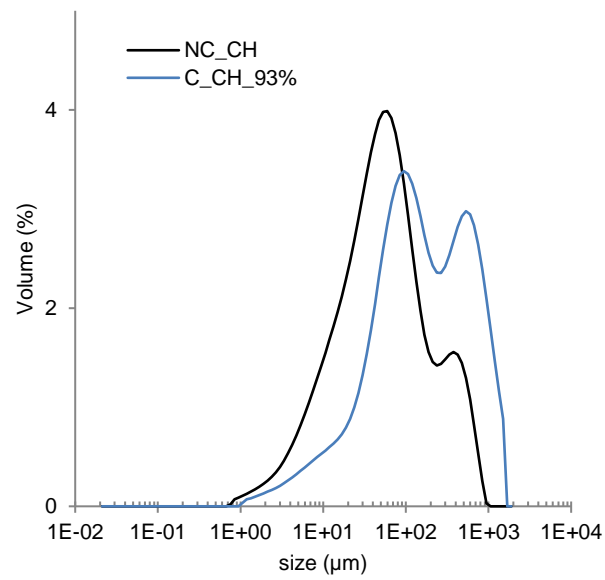
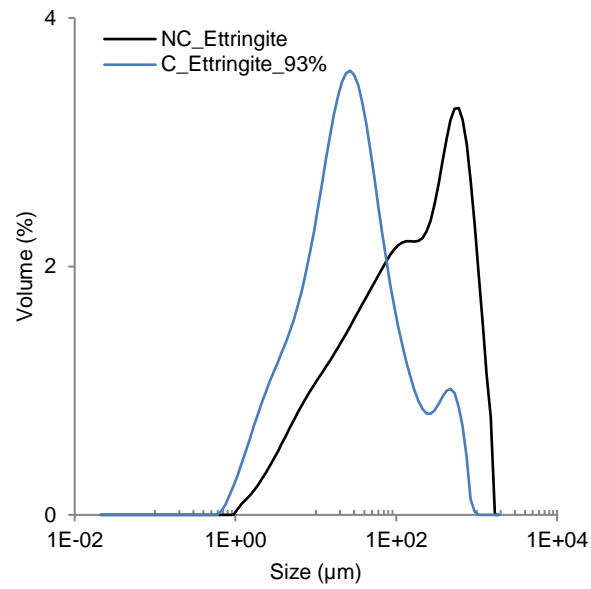


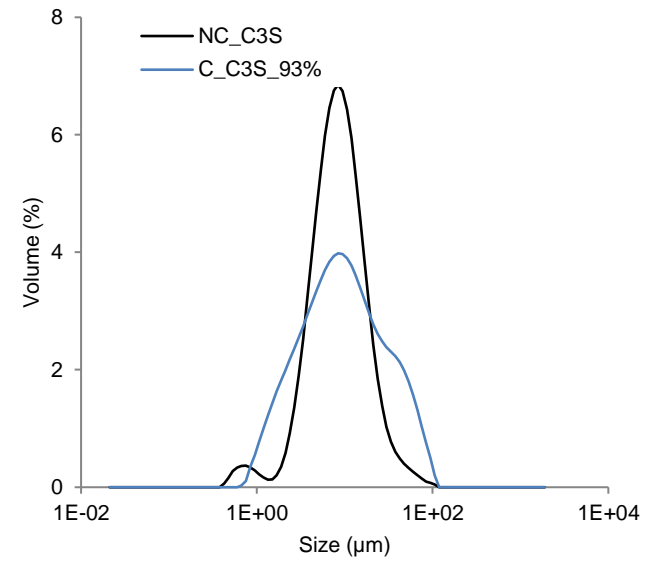
Figure 84: TGA results of anhydrous phases conserved at 3 RH during 32 days in an ambience with low CO₂ concentration (lower than 10ppm)



(a)

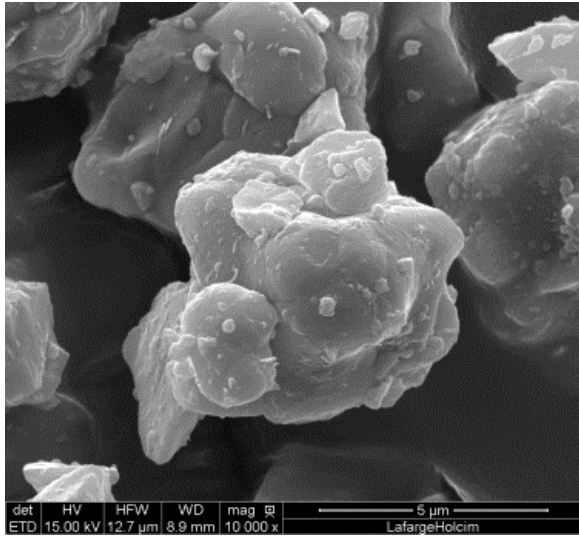


(b)

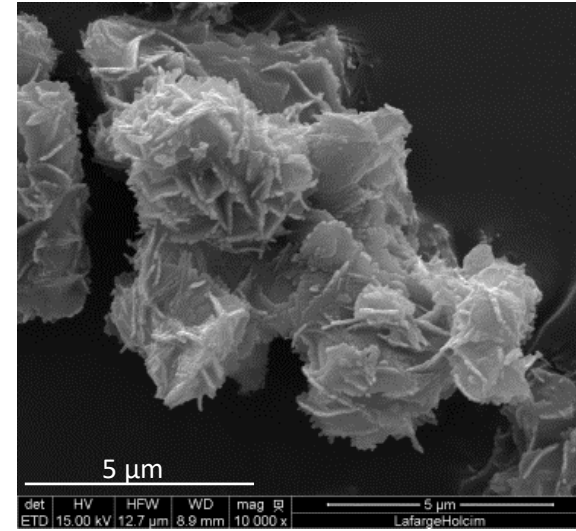


(c)

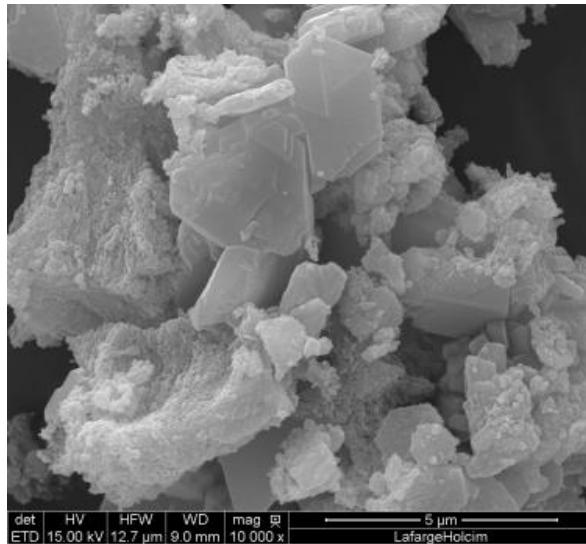
Figure 85 : grain size distribution of Portlandite (a), Ettringite (b) and C₃S (c) powders before carbonation (NC) and after exposure to ambient CO₂ at 93% RH (C_93%)



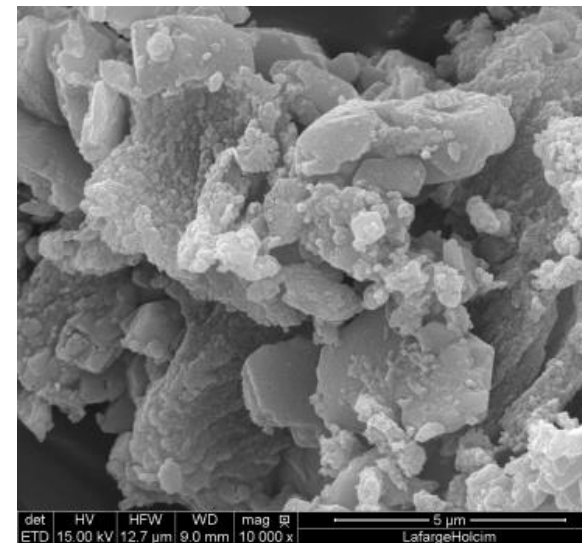
C₃S carbonated at 33%



C₃S carbonated at 55%



CH Carbonated at 33%



CH Carbonated at 55%

Figure 86 : SEM images of C₃S and CH powders after carbonation at 33% RH and 55% RH

